Characterisation of Thin-Film Semiconductors for Device Application

Vladimir Smirnov

A thesis submitted in partial fulfilment of the
requirements of the University of Abertay Dundee
for the degree of Doctor of Philosophy

This research programme was carried out in collaboration with
the Institute for Photovoltaics, Forschungszentrum Jülich GmbH (Germany)

March 2006

I certify that this thesis is the true and accurate version of the thesis approved by the examiners.

Signed ....[redacted].....
Date..21/6/06....

(Director of Studies)

To my parents

Acknowledgements

I am most grateful to my supervisors Dr. Steve Reynolds and Prof. Charlie Main for their constant interest, encouragement, enthusiasm and generosity with their time. I also wish to thank Dr. Steve Reynolds for support during 'writing-up' period and many discussions via the Internet.

I would like to thank research staff at the Institute for Photovoltaics, Forschungszentrum Jülich, Germany, for preparation and characterisation of microcrystalline silicon samples. Special thanks are due to Dr. Friedhelm Finger and Dr. Reinhard Carius for provision of the samples, their interest in the present research and many valuable discussions.

I am grateful to Dr. Colin Cartwright and Prof. Allan Gillespie for providing a possibility to complete 'writing up' phase in Dundee. Dr. Colin Cartwright is also acknowledged for supervising me during 'writing up' time and help with many things.

I wish to thank Dr. Amar Merazga, Dr. Ivica Zrinscak and Dr. Mariana Gueorguieva for friendship, many interesting discussions on the properties of thin films and the pleasure to share a laboratory with them. I thank Dr. Saydulla Persheyev, University of Dundee, for his advice and friendship.

I am grateful to academic and research staff at the EPICentre, most of all: Dr. Allan MacLeod, Dr. Elaine Billen, Robert Sharpe, Tudor Radulescu, Karen Wilson, Fu Yu and Zhao Tian for providing a supporting atmosphere and friendship.

Declaration

I declare that while registered as a candidate for the degree for which this thesis is presented I have not been a candidate for any other award. I further declare that except where stated the work contains in this thesis is original and was performed by the author.

Signed [redacted] ..... Date 21/06/2006.....

Vladimir Smirnov

Abstract

Microcrystalline silicon films prepared over a range of deposition conditions have been investigated using dark- and photo-conductivity measurements, constant photocurrent method and transient photoconductivity. The dark conductivity was measured as a function of temperature; the photoconductivity was measured with steady state and transient excitation as a function of temperature and excitation intensity. Microcrystalline silicon films deposited at high silane concentration, near the transition from microcrystalline to amorphous growth are found to have similar optoelectronic properties to undoped amorphous silicon films. In contrast, the properties of largely crystalline films, grown at low silane concentration bear some similarities to n-type amorphous silicon.

Transient photocurrent and post-transit time of flight measurements on coplanar and *pin* photovoltaic structures respectively have been interpreted in terms of a multiple trapping transport model. It appears that multiple trapping analysis is applicable to transitional materials, although in highly crystalline materials significant deviations occur, especially at low temperatures. From a comparison of transient photoconductivity and time of flight results, and variations in dark- and photo-conductivity with film thickness, anisotropy in electronic properties measured in the direction of, and perpendicular to, the direction of film growth may be inferred.

The effects of ambient atmosphere on optoelectronic properties have been investigated for films prepared over a range of deposition conditions, such as silane concentration, doping and film thickness. It was found that both irreversible and reversible changes may take place. Irreversible effects, associated with oxidation process, result in a shift of the Fermi level position towards the conduction band accompanied by irreversible changes in the density of states, together with increase in dark and photoconductivity and decrease in conductivity prefactor. Thinner films are found to show more rapid irreversible changes and for these films the activation energy was found to decrease by as much as 0.4 eV over a period of one month after deposition.

The reversible effect was found to result in decrease or increase in dark conductivity, depending on material microstructure. Reversible atmospheric

effects have been interpreted in terms of adsorption process that results in band bending and saturates in most cases over a period of few days. Changes in properties produced by evacuating the measurement chamber were more pronounced for films deposited at higher silane concentration, which may be explained in terms of material microstructure. A vacuum of 10^{-3} torr was however insufficient to prevent adsorption process. A correlation between changes in dark, steady state and transient photoconductivity over a period of time has been found and explained in terms of changes in the Fermi level position. Reversible conductivity changes measured on a series of boron-doped samples have demonstrated that the effect may be minimised or even reversed by doping. Computer simulation, which models the effect of atmospheric adsorption as a charge 'sheet' penetrating into the film close to the surface, gives good agreement with experimental results for the boron doped series.

Light soaking experiments on microcrystalline silicon prepared under optimal conditions for high-efficiency solar cells indicate little degradation at room temperature, while some degradation has been observed at a temperature of 50°C. The interpretation of these experiments is complicated by 'interference' from atmospheric effects that result in changes in dark and photoconductivity opposite in direction to light soaking. It was shown that these metastable effects may be separated using different annealing regimes.

Symbol and abbreviation list

C_n	electron capture coefficient
C_p	hole capture coefficient
C_R	recombination coefficient
d	film thickness
D^-	defect state occupied with two electrons
D^+	unoccupied defect state
D^0	defect state occupied with one electron
e	elementary charge
e_n	emission probability for electrons
e_p	emission probability for holes
E_a	dark conductivity activation energy
E_c	conduction band energy
E_f	Fermi energy
E_{fn}	free electron quasi Fermi level
E_{fp}	free hole quasi Fermi level
E_g	mobility gap / band gap
E_{MNR}	Meyer-Neldel characteristic energy
E_{th}	thermalisation energy
E_{tn}	trap quasi Fermi level for electrons
E_{tp}	trap quasi Fermi level for holes
E_v	valence band energy
$f(E_t)$	occupation function in non-equilibrium steady-state conductivity
$f_0(E_t)$	Fermi-Dirac occupancy function in a thermal equilibrium
FF	fill factor
g(E)	density of states distribution function
G_d	thermal equilibrium generation rate
G_{ss}	steady state photogeneration rate
G_ω	modulated generation rate amplitude
I(t)	transient photocurrent
$I_a = I_{480}$	integrated Raman intensity of amorphous phase
$I_c = I_{520} + I_{505}$	integrated Raman intensity of crystalline phase
I_{sc}	short circuit current

I_ω	modulated photocurrent amplitude
k	Boltzmann's constant
n	electron density
n_1	effective electron density at conduction band edge
n_d	thermodynamic equilibrium free electron density
n_{ss}	excess density of free electrons
n_t	trapped electron density
N_c	conduction band density of states
N_0	density of defects in the gap
N_t	trap density
p	hole density
p_1	effective hole density at valence band edge
p_d	thermodynamic equilibrium free hole density
p_{ss}	excess density of free holes
Q	charge due to molecular adsorption
R	recombination rate
t	time
t_{tr}	transit time
T	temperature
T_c	conduction band tail characteristic temperature
T_f	filament temperature
T_s	substrate temperature
T_v	valence band tail characteristic temperature
U	correlation energy
V	applied voltage
V_{oc}	open circuit voltage
ΔV	band bending due to molecular adsorption

α	absorption coefficient
γ	Rose factor
Δ	penetration depth
ε	dielectric constant

ε_0	dielectric constant in vacuum
η	quantum efficiency
μ_n	electron mobility
μ_p	hole mobility
σ_{dark}	dark conductivity
σ_{ph}	photoconductivity
σ_0	conductivity prefactor
σ_{00}	Meyer-Neldel rule constant
τ	electron lifetime
Φ	photon flux
Φ_ω	phase shift
ω	angular frequency

CVF	crystalline volume fraction
DOS	density of states
ESR	electron spin resonance
MNR	Meyer-Neldel rule
MPC	modulated photoconductivity
PT TOF	post transit time-of-flight
SC	silane concentration
TCO	transparent conductive oxide
TPC	transient photoconductivity
TSC	thermally stimulated current

Contents

Chapter 1. Thin- Film Silicon

1.1 Amorphous silicon

1.1.1 Introduction

Thin-film silicon (thickness of order 1 micrometre) offers a number of commercial and technological advantages over the conventional crystalline silicon wafer-based approach in photovoltaic and display applications. These are primarily associated with the ability to cover large areas cheaply and at comparatively low energy cost. This in turn has led to sustained efforts in research and development over the past 30 years to improve material quality and to seek out new formulations which may offer additional improvements in performance and cost advantage.

Although there are several distinct types of silicon film, their properties may be understood to a large extent in terms of the degree of ordering of silicon atoms, for which there are two extremes. In *crystalline* silicon, each atom is four-fold coordinated with its neighbours to give a tetrahedral crystal structure, in which there is a regular periodicity. Electronically, this gives rise to a classical semiconductor with conduction and valence bands separated by a forbidden gap. Ideally, the band edges are discontinuous and there are no electronic states in the forbidden gap.

Amorphous silicon is a disordered semiconductor and its optoelectronic properties are determined by the significant number of imperfections present in its atomic structure. The covalent bonds between the silicon atoms in amorphous silicon are similar to the bonds in crystalline silicon. The silicon atoms have the same number of neighbours and on average the same bond lengths and bond angles. A perfect crystal is completely ordered to large pair distances, while amorphous materials tend to show only short-range order, as the bonds are strained and distorted such that there is no extensive periodic arrangement of atoms. The arrangements of atoms in crystalline and amorphous silicon are illustrated in figure 1.1.

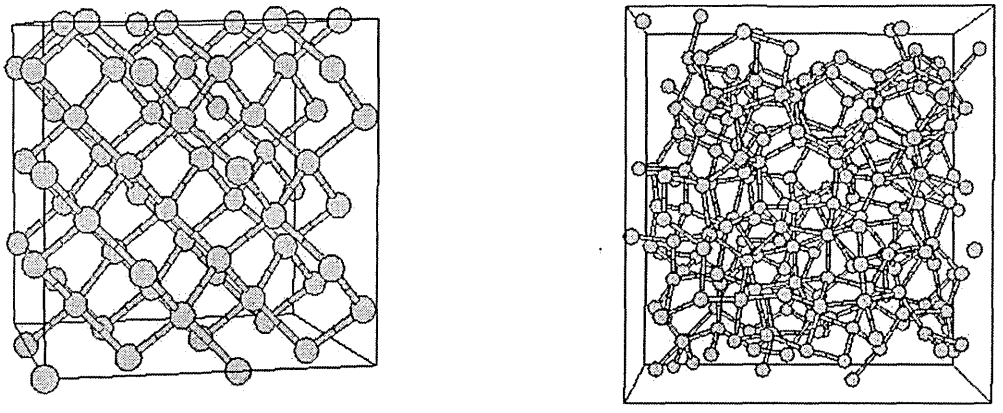

Figure 1.1. Schematic diagram of crystalline (left) and amorphous silicon (right).

At some points bond deformation can lead to a formation of so-called dangling bonds, where no orbital overlap is possible. As a result, pure amorphous silicon, for example deposited in early period of amorphous silicon research, has a high defect density, around 10^{20} cm^{-3} [Street 1991] which is around one dangling bond for every 500 silicon atoms. Trapping of carriers in these states prevents effective doping and greatly reduces the mobility of carriers as discussed below. Such amorphous silicon can be called unhydrogenated. The positive role of hydrogen introduction during amorphous silicon deposition is the ability to passivate defects, greatly improving photoelectrical properties and enabling for doping. Hydrogenation to a level of 10 at.% profoundly reduces the defect density, by about 4 orders of magnitude [Fritzsche 1977].

Hydrogenated amorphous silicon is not a homogeneous material. Its structure may include morphological inhomogeneties, such as initial nucleation region, columnar growth regions and voids (which are the low density areas) of varying sizes, embedded in an amorphous matrix [Meiling *et al.* 1990, van Sark *et al.* 1997, van Sark 2002]. The material morphology is determined by deposition chemistry and growth process. Poor quality amorphous silicon may have up to 20% of voids fraction, while the 'device quality' amorphous silicon may contain around 1% of voids.

1.1.2 Electronic structure and transport

The presence of short range order gives electronic energy level structure similar to crystalline silicon, forming extended mobile states, defined by conduction and valence band edges (E_c and E_v), separated by a mobility gap E_g (see figure 1.2). The long-range disorder results in the presence of band tail localized states. Coordination defects (dangling bonds) introduce deep electronic states around the midgap. Carrier transport in amorphous silicon also takes place within conduction and valence bands, but is very strongly influenced by the presence of band tails and defects.

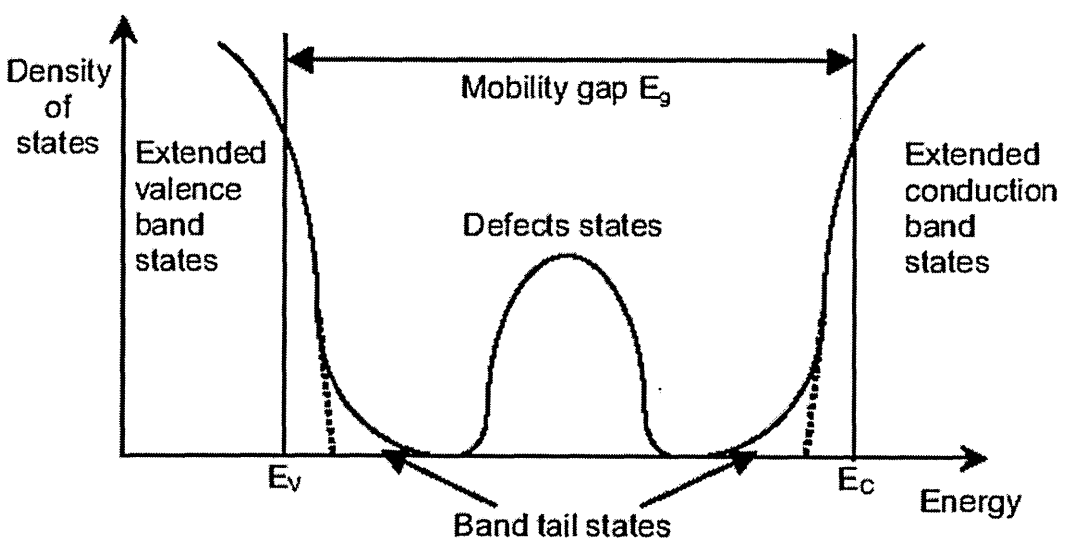

Figure 1.2. Schematic diagram of the density of states distribution in a disordered semiconductor (taken from van Sark 2002).

The defect states affect electronic properties by controlling trapping and recombination processes. When a carrier is captured by such localised states it cannot respond to an electric field and thus, is not available for conduction, until it is thermally released to the band. This greatly reduces the mobility of carriers.

The conductivity in a-Si:H is usually thermally activated and for electron transport one can write the following expression [Street 1991] for the conductivity σ:

$$\sigma(T)=\exp\left(-\frac{E_C-E_f}{kT}\right) \tag{1.1}$$

$$\sigma(T)=\exp\left(-\frac{E_a}{kT}\right)$$

where E_a is a conductivity activation energy, E_f denotes the Fermi energy, σ_0 conductivity prefactor, k Boltzmann's constant, and T the temperature. The correlation between conductivity prefactor σ_0 and the activation energy E_a, can be described as:

$$\sigma_0=\sigma_{00}\exp\left(\frac{E_a}{E_{MNR}}\right) \tag{1.2}$$

where σ_{00} is a constant and E_{MNR} is the Meyer-Neldel characteristic energy. Equation (1.2) is known as the Meyer-Neldel rule.

The activation energy E_a, defined as E_c-E_f for conduction band, depends on the quality of the material and on the presence of impurities. The impurities can be incorporated due to intentional doping during deposition process, or unintentionally, during deposition and also post deposition. If the material contains impurities, the Fermi level shifts towards the conduction or valence bands depending on whether impurities act as donors or acceptors. For undoped amorphous silicon, the typical activation energy E_a value is about 0.8 eV and the Fermi level is close to the midgap position.

1.1.3 Metastability of amorphous silicon

1.1.3.1 Light- induced degradation

Metastability of amorphous silicon is a key issue in applications such as solar cells. The effect of metastable changes due to prolonged exposure to light was first observed by Staebler and Wronski in 1977 [Staebler and Wronski, 1977]. A decrease in both photoconductivity during illumination and dark conductivity after exposure to light, frequently referred to as 'light soaking' was

observed. The effect is associated with an increase of dangling bond defects, which act as recombination centres, which results in a decrease of carrier lifetime, and a decrease in the conductivity. The increase of defect concentration can be detected by Electron Spin Resonance (ESR, see section 1.3.1) or by measuring the optical absorption coefficient, where it appears as a 'shoulder' below about 1.3 eV. Prolonged illumination of amorphous silicon is able to produce around 10^{17} cm^{-3} of defects. Most reports conclude that the defects created due to light soaking are indistinguishable from unilluminated amorphous silicon that has initially high defect density due to non-optimal growth conditions. Annealing can restore the initial condition of the material. Several hours are needed to completely anneal the defects at temperature around 130°C, while only several minutes are required at 200°C [Street 1991].

The Staebler Wronski effect has been studied extensively for more than 20 years, however the microscopic aspects explaining the effect are still under discussion. It is widely accepted that the mechanism originates from light induced carrier recombination and involves breaking of Si-Si bonds and hydrogen diffusion.

The weak bond breaking model of Stutzmann *et al.* [Stutzmann *et al.* 1985] considers the Staebler-Wronski effect as an intrinsic bulk effect, that does not depend on the concentration of impurities (below a value of around 10^{19} cm^{-3}). The mechanism of light induced degradation is assumed to be as follows: the dangling bonds are created by recombination of electrons and holes at weak bonds. The recombination energy enables an H atom to be bonded to one of the Si that prevents a restoration of the bond. The schematic diagram of the light induced defect creation is presented in figure 1.3. The process of defect creation is self-limited. When the defect density increases, the additional recombination through new states reduces the concentration of band edge carriers and suppresses the mechanism of defect creation. During annealing the hydrogen atom moves back to its original position.

Later models explaining the Staebler-Wronski effect do not consider a close spatial correlation between the hydrogen and dangling bond, and involve long range diffusion of hydrogen. Godet *et al.* [Godet *et al.* 1998] have suggested a model involving a metastable H trapping. It assumes that metastable H atoms are weakly bonded in Si-H-Si configurations, which are the mobile species in

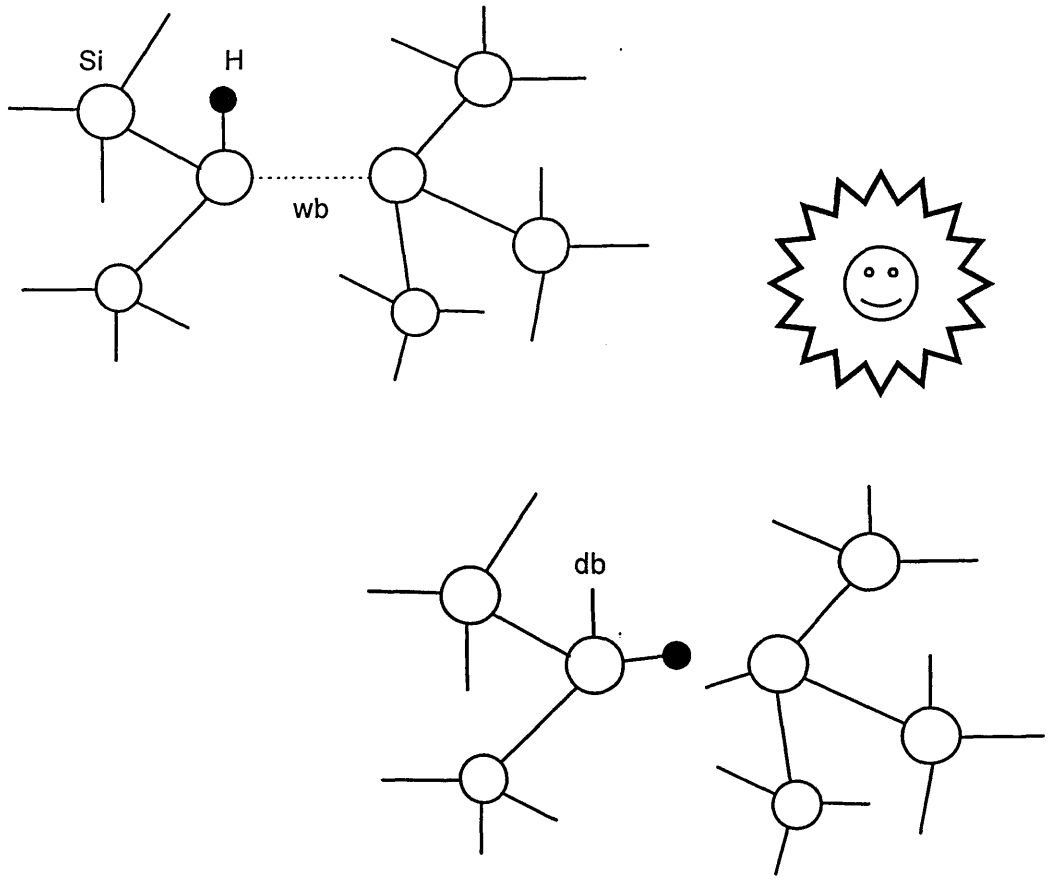

Figure 1.3. A schematic diagram of light induced defect creation.

amorphous silicon. The hydrogen collision model of Branz [Branz 2000] suggests that a defect is created by recombination at Si-H bonds and recombination energy is used to lift hydrogen to a transport state. The mobile hydrogen atom is represented by a mobile complex of Si-H bond and a dangling bond. This mobile complex diffuses in the material by breaking one Si-Si bond after another, but each broken bond is reformed after the complex passes it. When two hydrogen mobile complexes meet, a metastable Si-HH-Si complex is formed, resulting a creation of two dangling bonds that are not spatially correlated with hydrogen atoms.

1.1.3.2 Atmospheric effects

Another aspect of metastability is related to reversible post deposition atmospheric effects. The adsorbed atmospheric molecules can influence the

electronic transport, affecting dark and photoconductivities. Several works in the early 1980s [Tanielian *et al.* 1980, Solomon 1981, Tanielian 1982] reported conductivity changes in amorphous silicon films that can be as large as 3 orders of magnitude when exposed to different atmospheres. These effects are considered to be associated with band bending, induced by adsorbed molecules. Particularly it was proposed that an adsorbed water molecule can act as a donor, resulting an effective shift of the Fermi level towards the conduction band. Such changes were found to be reversible by annealing the sample at temperatures above 100°C. These aspects are discussed in more detail in chapter 2, where both reversible and irreversible atmospheric effects are reviewed.

1.1.4 Deposition of amorphous silicon

The techniques used for deposition of amorphous silicon films are based on the decomposition of silane gas (SiH_4) at relatively low substrate temperatures. These techniques are readily scaleable allowing large areas on flexible substrates such as stainless steel roll to be covered cheaply and at low energy cost. The hydrogen present also serves to passivate to a large extent the broken or 'dangling' bond defects. This is extremely important in the production of electronic quality material and without it no useful devices or doped layers could be produced.

1.1.4.1 Plasma Enhanced Chemical Vapour Deposition (PECVD)

At present the most common method of depositing device quality a-Si:H is plasma enhanced chemical vapour deposition (PECVD), based on plasma decomposition of silane gas (SiH_4). In the standard technology silane dissociates between two parallel electrodes in a radio frequency (13.56 MHz) glow discharge (GD). Dissociation of SiH_4 creates different SiH_x (where x=1, 2, 3) radicals. Some radicals, such as SiH_3 are assumed to be mainly responsible for the film growth, while some other radicals can participate in the subsequent (secondary) dissociation reactions. It is believed that the dominant presence of SiH_3 radicals results in a deposition of good quality amorphous silicon [van Sark 2002], the possible reaction of the radical formation following:

$$SiH_4 + H \rightarrow H_2 + SiH_3 \quad (1.3)$$

The plasma containing ions and other reactive species allow silicon to be deposited on the substrate at temperatures of 200-300 °C, so hydrogen may be incorporated in amorphous silicon structure during the growth process.

In order to produce controlled n-type or p-type materials, phosphine gas (PH_3) and diborane gas (B_2H_6) respectively are commonly added to silane during the deposition process. These molecules are dissociated by plasma, forming radicals that bond to the growing layers and incorporate active donors or acceptors.

1.1.4.2. Hot Wire Chemical Vapour Deposition (HW CVD)

In hot wire chemical vapour deposition (HWCVD), material growth takes place by thermal decomposition of the silane (or silane + hydrogen mixture) gas at the surface of a hot filament heated at temperatures in the range of 1500-2000 °C. At these temperatures silane is decomposed into a gaseous mixture of silicon and hydrogen atoms. Device quality amorphous silicon was reported to be obtained at high deposition rate up to 20 Å/s [Mahan 2003]. Ultra high deposition rates of amorphous silicon solar cell i-layer have been reported [Mahan *et al.* 2001, Mahan *et al.* 2002, Mahan 2003]. However, an increase of deposition rate to ultra high values (>100 Å/s) results in reduction of cell efficiency and material quality, particularly a significant increase (up to 2 orders of magnitude) in void fraction was reported [Mahan *et al.* 2001, Mahan 2003]. In general, for the films deposited by HWCVD one can expect lower hydrogen content and higher voids fraction comparatively to PECVD material [van Sark 2002]. An important difference between the HWCVD and the PECVD process is the absence of ions, and the smaller number of species in the gas phase [van Sark 2002, Mahan 2003].

The advantages of HWCVD over PECVD are claimed to be less interface damage due to lack of ion bombardment during deposition, high deposition rates and low equipment cost. However, high deposition rate may not always result in deposition of high quality material.

Depending on the deposition conditions, such as silane concentration (which is a ratio of silane/ silane + hydrogen), temperature and gas pressure, silicon films of varying properties may be prepared. For example, the amount of incorporated hydrogen depends on the deposition temperature, with the hydrogen content decreases with increasing substrate temperature [Itoh *et al.* 2001]. The deposition rate is also varying and, for example, increases with silane concentration increase. The typical deposition rate expected at silane concentration of 2% is about 1 Å/ s, while at 8% gas ratio one can expect 5 Å / s rate or higher [Wyrsch *et al.* 2000].

Silane concentration is a convenient parameter to use to control microstructure of deposited films. Usually at high silane concentration values one can expect to grow materials with large amorphous fraction, while at lower concentrations larger crystalline fraction is expected [Finger *et al.* 2001]. In the latter case the long-range order persisting over centimetres, associated with silicon wafers, is absent, and it is more usual for grains of crystalline material of varying dimensions, often grouped together in columnar structures and separated by voids or amorphous silicon, to occur. These *microcrystalline* silicon films, which possess properties intermediate between amorphous and single-crystal material, remain relatively poorly understood and form the focus of a substantial part of the present study. Amorphous silicon has been studied extensively since the early 1970's, however microcrystalline silicon films have only received significant attention since their improved stability to light exposure and voltage bias and desirable light absorption characteristics began to be fully appreciated some 10-15 years ago.

1.2 Microcrystalline Silicon

Hydrogenated microcrystalline silicon is a promising material for applications in thin film solar cells, photosensors and thin film transistors. It is composed of microcrystallities of varying sizes, regions of low density (voids) and an amorphous phase [Finger *et al.* 1998, Luysberg *et al.* 1997, Houben *et al.* 1998a, Luysberg *et al.* 2001, Shah *et al.* 2003]. Microcrystalline silicon can be prepared

using a standard plasma enhanced chemical vapor deposition (PECVD) which is widely used for deposition of hydrogenated amorphous silicon with only small modification of deposition condition parameters [Finger *et al.* 1998]. Important advantages of microcrystalline silicon comparatively to amorphous silicon are an improved stability [Finger *et al.* 1998] against light induced degradation and improved optical absorption [Vetterl *et al.* 2000]. The properties of microcrystalline silicon are discussed in details below.

1.2.1 Microstructure

Microstructure is one of the most relevant properties of microcrystalline silicon material, it describes the volume fractions and spatial distribution of crystalline and amorphous phases in the material. The microstructure of microcrystalline silicon is strongly dependent on deposition conditions and can significantly modify electronic properties, thus it is important to understand and to control it.

A convenient way to obtain microstructural changes in thin silicon films is to vary silane concentration (SC) in the process gas mixture during deposition. This will affect crystalline and amorphous volume fractions, size of crystals, presence of low density regions - voids or grain boundaries and nucleation layer. Changes of silane concentration will also affect the growth rate of microcrystalline silicon films [Finger *et al.* 1998]. In general, deposition rate increases with increasing silane concentration. Details of the microcrystalline silicon morphology are considered below.

1.2.1.1 Crystalline content

As was mentioned, by variation of deposition conditions highly crystalline or almost amorphous structures can be prepared. The crystalline regions have a periodic and well-determined columnar microstructure. Columns consist of crystallites of same orientation, placed parallel to the direction of growth [Finger *et al.* 1998, Shah *et al.* 2000, Shah *et al.* 2003]. Such microstructure can be obtained if materials are deposited at low silane concentration (less then 2%). A columnar microstructure parallel to the direction of growth is typical for the materials

produced at low silane concentrations [Finger *et al.* 1998, Houben *et al.* 1998a]. For the materials with dominant crystalline fraction, the individual crystal diameter is around 25 nm (see figure 1.4). The crystals are surrounded by grain boundaries. Grain boundaries are usually considered as disordered regions of high defect densities, that also can contain high amount of hydrogen that is hardly to incorporate into the crystals [Houben *et al.* 1998a]. Increasing the silane concentration in the PECVD process will cause a decreasing of crystalline phase and formation of amorphous fractions. The individual crystal diameter also decreases and depending on deposition properties is found to be in the range of 20 nm [Finger *et al.* 1998, Siebke *et al.* 1998, Lips *et al.* 1998, Ruff *et al.* 1998]. The columnar structure is also observed in the materials deposited around 4% silane concentration. A further increase in silane concentration will lead to a noticeable degradation in a columnar growth. The crystalline volume fraction decreases, especially close to the interface between the substrate and the film. The materials deposited at silane concentration of about 7%-9% are considered as transitional structures [Brüggemann *et al.* 2000, Vetterl *et al.* 2000, Shah *et al.* 2003]. They are not purely amorphous, and contain a number of randomly placed small crystallites of irregular shape, incorporated into an amorphous matrix. The schematic diagram of microstructure in microcrystalline silicon is presented in figure 1.4.

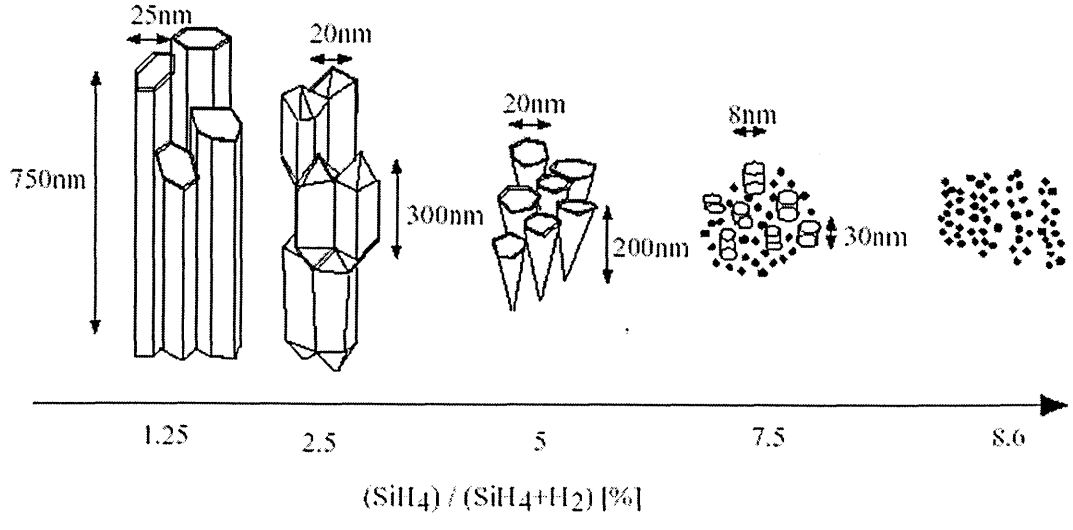

Figure 1.4. Schematic evolution of microstructure in microcrystalline silicon with a variation in hydrogen dilution (from Shah *et al.* 2003).

On the left hand side of the figure a strong columnar microstructure of microcrystalline silicon, that is expected to appear at low silane concentration, is shown. The columnar growth degrades when the silane concentration increases. Microstructure of transitional microcrystalline silicon is presented on the right hand side of the figure.

1.2.1.2 Voids

Two types of voids [Luysberg *et al.* 1997, Houben *et al.* 1998a] are observed in microcrystalline silicon: crack-like cavities and nearly spherical cavities. The crack-like cavities are found to vary in width and length, and appear to be in parallel to the direction of material growth. The size of spherical cavities can be up to 14 nm in diameter [Houben 1998a]. In the case of strong columnar growth, crack-like cavities are normally appear in between columnar structures and also in the close to the substrate region. In contrast, if the columnar growth is not observed, the crack-like voids do not appear close to the substrate. Spherical voids are commonly observed in the case of more amorphous structures, incorporated into the amorphous phase. The mechanism of void formation still remains unclear. A possible explanation of voids formation is related to the soaking of hydrogen into the growth zone with subsequent chemical reactions and structural rearrangements. [Houben *et al.* 1998a]

1.2.1.3 Nucleation region

Usually deposition of microcrystalline silicon does not result in homogeneous layer growth. The presence of the nucleation layer in microcrystalline silicon films is widely accepted [Luysberg *et al.* 1997, Tzolov *et al.* 1997, Finger *et al.* 1998, Houben *et al.* 1998a, Houben *et al.* 1998b, Shah *et al.* 2003, Kocka *et al.* 2003, Fujiwara *et al.* 2004, Ross *et al.* 2005]. The formation of a nucleation layer is mainly affected by deposition conditions, first of all plasma, and also morphology and type of substrate. Growth conditions for initial growth (close to substrate) and bulk growth are different. Even for the materials deposited at low silane concentration, showing a strong crystal growth, the appearance of an

incubation layer containing a mixture of both crystalline and amorphous fractions was reported [Houben *et al.* 1998a, Shah *et al.* 2003]. The crystalline growth starts at nucleation centers close to the interface between film and substrate. During the growth the diameter of "successful" crystallites increases, forming crystallites of conical shape close to the substrate region. The space between crystallites is filled with amorphous material and/or voids [Houben *et al.* 1998a].

The thickness of the nucleation layer varies depending on deposition conditions and substrate type; typically the nucleation layer thickness is around 30~50 nm for materials showing strong columnar growth [Houben *et al.* 1998a]. Less crystalline material can show an initial dominance of amorphous growth and have a nucleation layer more then 100 nm [Roca i Cabarrocas *et al.* 1996, Shah *et al.* 2003] where the crystal formation starts far from substrate.

The presence of incubation layer and frequently observed conical crystal formation could result in noticeable thickness dependence of the properties of microcrystalline silicon. An increase in crystalline volume fraction and dark conductivity with film thickness has been shown in a number of reports [Roca i Cabarrocas *et al.* 1996, Andoh *et al.* 2001, Moutinho *et al.* 2003, Kocka *et al.* 2003].

A schematic picture of possible microstructure of microcrystalline silicon is shown in figure 1.5. The diagram displays the changes in material microstructure upon decrease of crystalline volume fraction. It should be pointed out that microcrystalline silicon microstructure strongly depends on technological parameters, such as reactor properties, type of substrate, deposition condition and film thickness, so various structural compositions are strongly dependent on these. Thus the presented diagram is a simplified view to outline basic features of microstructure that includes grain size, voids and nucleation layer. The figure shows schematically the variations in crystalline volume fraction and in the nucleation region thickness. The material on the left hand side is characterized by high crystalline volume fraction and large grain sizes; crystalline columns are separated by deep cracks. In the transition from highly to lower crystalline growth, the column size decreases, while the amorphous volume fraction increases. The material presented on the right hand side includes small crystals incorporated into amorphous phase, and thus is not "typical" amorphous silicon as obtained for example from RF PECVD of 100% silane.

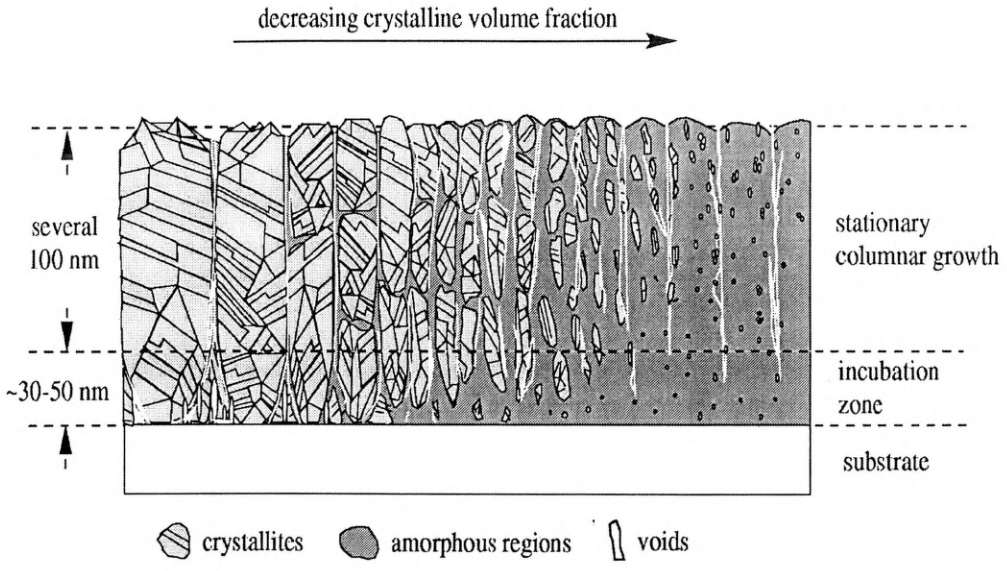

Figure 1.5. Schematic diagram of microcrystalline silicon composition: change from highly crystalline to transitional structures is shown. (from Vetterl *et al.* 2000)

1.2.1.4 Film inside solar cell *vs.* film deposited on substrate

In the present work both coplanar microcrystalline silicon films and photovoltaic *pin* structures (see section 1.4 for basic description) with microcrystalline silicon i-layer have been investigated. This section aims to underline the presence of differences between the properties of an intrinsic film inside a solar cell and coplanar film grown on a glass substrate.

It has been reported [Bailat *et al.* 2002, Houben *et al.* 2002, Edelman *et al.* 2003] that the structure of microcrystalline silicon films could be different when incorporated in a solar cell instead of deposited on glass substrate. For microcrystalline silicon films the presence of the incubation largely amorphous sublayer has been frequently observed [Luysberg *et al.* 1997, Tzolov *et al.* 1997, Finger *et al.* 1998, Houben *et al.* 1998a, Shah *et al.* 2003, Kocka *et al.* 2003]. Although the thickness and microstructure of the nucleation layer depend on deposition conditions, even for the films grown at low silane concentration conditions, showing a strong crystal growth, the appearance of an incubation layer containing a mixture of both crystalline and amorphous fractions was reported [Houben *et al.* 1998a, Shah *et al.* 2003]. In contrast to the films, the microstructure

of the intrinsic microcrystalline silicon incorporated into photovoltaic structure is different. The intrinsic layer of photovoltaic structure, grown at the same deposition conditions as films, shows significant reduction in nucleation layer thickness [Bailat *et al.* 2002, Houben *et al.* 2002] or no nucleation layer [Edelman *et al.* 2003] over a range of silane concentrations. The second difference is that the crystallinity is larger in the intrinsic layer of the cell than in the film. It was suggested that an explanation of these facts is related to the difference during material growth on a substrate (for example glass) from an intrinsic layer deposited on doped film in a *pin* subsequence.

The differences mentioned above should be taken into account when, for example, a comparison of transport properties in coplanar and photovoltaic structures is being made.

1.2.1.5 Raman spectroscopy

Raman spectroscopy is a frequently used technique which may provide detailed information on vibrational properties of solids, which may be linked to their physical structure and composition. Raman scattering in solid state is described as inelastic scattering of a photon under emission (Stokes process) and under absorption (anti-Stokes process) of a phonon. A detailed discussion of the method can be found in the literature [see for example Cardona 1982]. Raman spectroscopy can be applied to microcrystalline silicon to estimate the crystalline volume content of the material [Finger *et al.* 1998].

A typical Raman spectrum of microcrystalline silicon is shown in figure 1.6. The spectra is a convolution of a crystalline and an amorphous spectrum. Spectra of crystalline silicon is dominated by a peak at 520 cm^{-1}. Due to the finite grain size and internal stress in microcrystalline silicon this peak shifts to lower values (usually found at 518 cm^{-1}) and the peak width increases [Richter *et al.* 1981]. A broad band centered at 480 cm^{-1} characterizes the Raman spectrum of amorphous silicon.

In order to quantify the crystalline volume fraction, the Raman spectrum of microcrystalline silicon shown in figure 1.6 may be deconvoluted into three

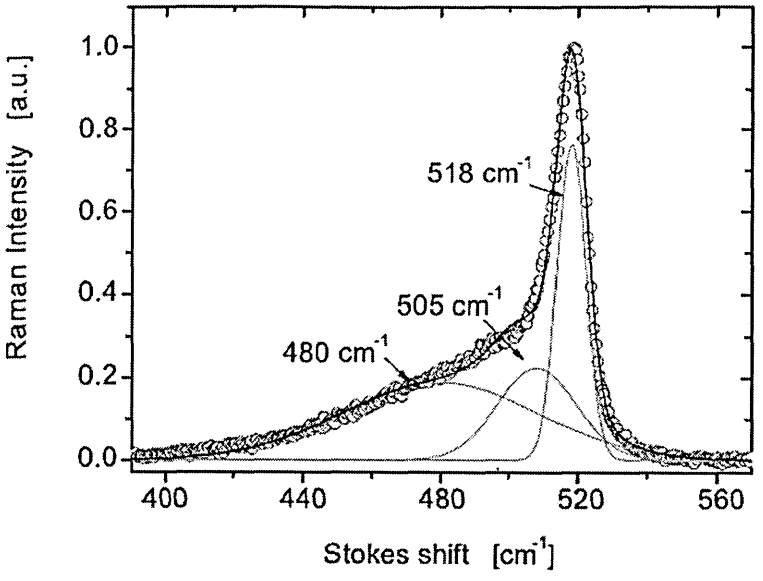

Figure 1.6. Typical Raman spectrum of PECVD microcrystalline silicon. [from Dylla 2005]

Gaussian lines. The integrated Raman intensity of the crystalline phase is fitted by two Gaussian lines at 520 cm^{-1} and 505 cm^{-1} to account for asymmetry, thus $I_c = I_{520} + I_{505}$. The ratio of the Raman intensity of the crystalline phase I_c to the total scattering intensity ($I_a + I_c$) is taken as a measure of the crystalline volume fraction:

$$I_{CVF} = (I_{520} + I_{505}) / (I_{520} + I_{505} + I_{480}) \qquad (1.4)$$

The evaluation of the integrated Raman intensity from equation 1.4 should be performed with caution. In highly crystalline materials a contribution of grain boundaries to 480 cm^{-1} Raman mode may lead to overestimation of the amorphous phase [Veprek *et al* 1987]. On the other hand in largely amorphous materials an underestimation of the crystalline phase could take place [Houben *et al* 1998a] as evident from comparison with X-ray diffraction results. Later, a lack of correlation between Raman intensity ratio and crystalline volume fraction obtained from X-ray diffraction measurements was pointed out by Ossadnik *et al* [Ossadnik *et al* 1999]. Thus, the Raman measurements can be useful to determine the

trends in crystallinity variations of a series of microcrystalline silicon samples, but could not provide a quantitative determination of the crystalline volume fraction.

1.2.2 Optical and electronic properties of microcrystalline silicon

1.2.2.1 Optical absorption

One of the applications of microcrystalline silicon is as the absorber layer of thin film solar cells. The basic principles of thin film solar cell operation are discussed in some detail in section 1.4. There are 2 key points related to active layer properties, which are of key significance for industrial applications: the layer thickness and the absorption coefficient. A minimization of the absorber layer thickness is desirable, taking into account the typical deposition rates of PECVD process are in the range of few Å/s. However, the layer thickness must be sufficient to enable sufficient absorption of light.

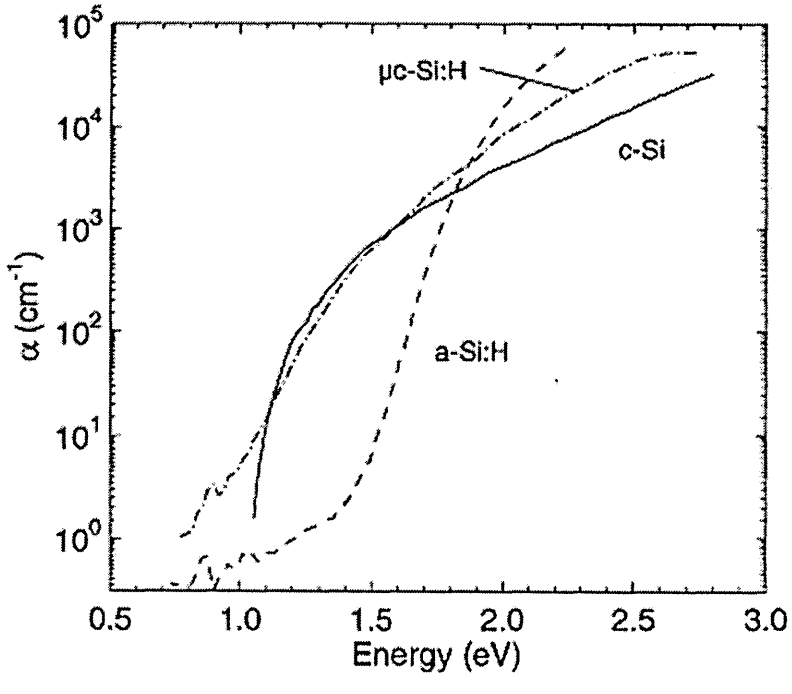

Figure 1.7. Absorption coefficient of crystalline, microcrystalline and amorphous silicon. (from Vetterl *et al.* 2000).

Figure 1.7 shows the absorption coefficient of intrinsic microcrystalline silicon material. One can see that the optical absorption of microcrystalline silicon is higher in the visible spectrum then for crystalline silicon. For energies below 1.7 eV the absorption of microcrystalline silicon is significantly higher comparatively to amorphous silicon. The increased absorption of microcrystalline silicon is an important advantage in photovoltaic applications and makes it possible the use of this material as an active layer of the solar cell, reducing the solar cell thickness.

An important development resulting in improvement of solar cell efficiency is a combination of amorphous and microcrystalline silicon active layers for capturing wider spectrum of light [Meier *et al.* 1997, Shah *et al.* 2000, Guha 2000, Shah *et al.* 2003, van Veen *et al.* 2004]. These so-called 'micromorph' (microcrystalline / amorphous silicon) or tandem cells consist of a microcrystalline silicon bottom cell and an amorphous silicon top cell. Stabilized micromorph solar cell efficiencies around 11%-12% have been achieved [Shah *et al.* 2003].

1.2.2.2 Electronic conductivity

Due to the presence of crystalline and amorphous phases, the electronic transport in microcrystalline silicon depends strongly on structural composition. Although the values of coplanar dark conductivity may vary depending on deposition techniques [Brüggemann *et al.* 2001, Vetterl *et al.* 2002, Ray *et al.* 2002b, Kocka *et al.* 2003], the general trend shows that dark conductivity increases with increasing material crystallinity. One explanation could be that an increase in dark conductivity could be related to a reduction of defect density, however, the ESR measurements [Finger *et al.* 2000, Baia Neto *et al.* 2002] show that the highest spin density value is obtained for the materials prepared at highly crystalline growth regime. Defect density decreases by more than an order of magnitude under a transition to low crystalline growth. The highest dark conductivity values, around 10^{-5} S/cm, are found in the highly crystalline films, while highly amorphous structures show dark conductivity around 10^{-10} S/cm. The transition between highly crystalline and amorphous growth is observed at silane

concentration SC around 6~7%. Figure 1.8 shows the changes in spin density and dark conductivity as a function of silane concentration.

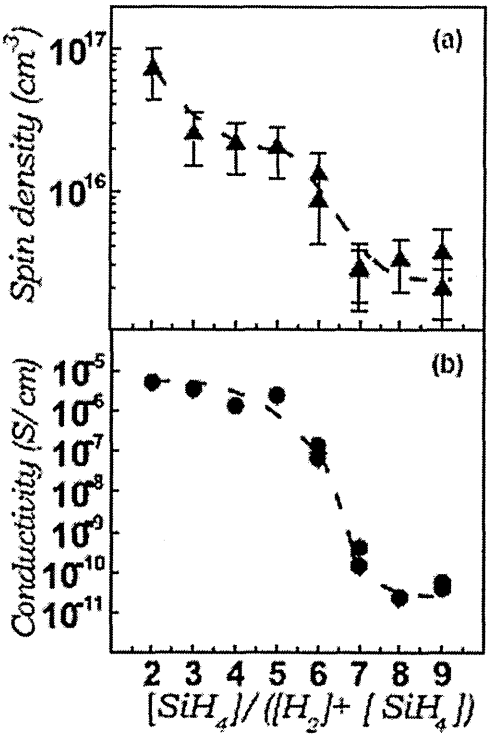

Figure 1.8. Changes in spin density and dark conductivity depending on silane concentration (from Baia Neto *et al.* 2002).

At present, there is no explanation that could correlate an observed decrease in dark conductivity with decrease of defect density. A possible reason for dark conductivity increase with crystallinity is related to unintentional doping [Finger *et al.* 1998, Shah *et al.* 2000, Baia Neto *et al.* 2002].

Shimakawa [Shimakawa 2000] attempted to explain the electronic transport in microcrystalline silicon in terms of effective-medium approximation. The proposed model considered microcrystalline silicon material as a mixture of particles of two different conductivities, close to conductivities of amorphous and crystalline silicon. The calculation suggested that the percolation threshold should take place at crystalline volume fraction around 0.3, while experimental results [Baia Neto *et al.* 2002] indicate the threshold takes place at higher crystalline volume fractions. On the other hand the model does not explain observed

changes in defect density with crystallinity, that suggests the transport in microcrystalline silicon is determined not only by a ratio of crystalline to amorphous fractions and could be more likely related to reasons stated above.

1.2.3 Instabilities

1.2.3.1 Light induced degradation

As described earlier, in amorphous silicon material, additional (metastable) defects are readily produced by the breaking of weak bonds under light illumination (the Staebler-Wronski effect), resulting in greater loss of photogenerated carriers by recombination and a subsequent reduction in energy conversion efficiency, amongst other things. The mechanism of the Staebler-Wronski effect is discussed in more detail in section 1.1.3. Microcrystalline silicon thin films and solar cells with microcrystalline silicon active layer, in general, provide more stable photoelectrical properties under prolonged light illumination compared with amorphous silicon [Goerlitzer *et al.* 1997, Kleider *et al.* 2001, Finger *et al.* 2003, Klein *et al.* 2003]. Particularly, it was found that microcrystalline silicon structures with significant crystalline fraction (more then 50 %) show almost no degradation of photoelectrical properties after prolonged light soaking. It should be noted that the properties of microcrystalline silicon materials significantly vary with microstructure and some types of microcrystalline silicon structures may suffer from light induced degradation. It is proposed that the observed light induced degradation in these structures is associated with the presence of the amorphous phase, which could result in light induced metastability. The light induced degradation of microcrystalline silicon structures containing amorphous volume fractions has been reported in several works [Ray *et al.* 2002a, Klein *et al.* 2003, Finger *et al.* 2003].

For the solar cell applications, an active layer of microcrystalline silicon with high crystalline volume fraction will result in a high stability against light soaking. However, such solar cell will not yield the highest efficiency. On the other hand, to

use a highly amorphous structure as an active layer will result in at least some light induced degradation.

It was suggested that the optimal microcrystalline silicon material for use as an active layer of high performance solar cells should be grown near the transition between microcrystalline and amorphous growth [Vetterl *et al.* 2000]. Solar cells using an active layer of microcrystalline silicon grown near the transition between microcrystalline and amorphous growth cell show an improved stability against light soaking compared to amorphous silicon and in addition a reasonable efficiency of about 7%. However, the observation of some light induced degradation was still reported for such structures. [Klein *et al.* 2003, Finger *et al.* 2003]

1.2.3.2 Atmospheric instabilities

Another source of instabilities arises from the influence of atmospheric gases that can influence the material surface or, due to the porous structure, diffuse into microcrystalline silicon bulk, resulting in changes of electrical properties. The atmospheric effects can be irreversible, normally associated with so-called 'post-oxidation' process, and also reversible one, normally associated with adsorption of atmospheric components on materials. This point of concern is particularly pronounced in regard to microcrystalline silicon films (coplanar structures), while photovoltaic structures are found to be less affected by atmosphere [Meier *et al.* 1998]. This could be because of encapsulation effects, provided by TCO (transparent conductive oxide) layer on one side and metallic contact layer on the other side of photovoltaic structure. However, changes of optoelectronic properties of solar cell structures due to atmospheric effects are reported [Wang *et al.* 2003, Klein *et al.* 2003].

Irreversible effect (Post deposition oxidation)

The effect of post deposition oxygen incorporation into microcrystalline silicon films has been reported by several groups. [Veprek *et al.* 1983, Meier *et al.* 1998, Shah *et al.* 2003, Finger *et al.* 2003]. It is proposed that oxygen atoms can play a role of donors, causing a shift of the Fermi level position toward the

conduction band, resulting the material slightly n-type. The corresponding dark conductivity changes up to 3 orders of magnitude have been reported [Meier *et al.* 1998]. The effect of oxygen incorporation is not reversible up to annealing temperature of 200 °C. Veprek *et al.* reported a removal of oxygen only at temperatures above 1050 °C.

The recent work of Jülich group on investigation of atmospheric effects in microcrystalline silicon films has demonstrated that the oxidation process depends on material microstructure [Finger *et al.* 2003]. Based on FTIR spectroscopy, it was shown that highly crystalline materials are more sensitive to oxygen contamination, while the structures with high amorphous volume fraction are less affected by this process. The possible explanation for this fact is that crystalline structures are generally, but not exclusively found to be more porous, which together with presence of cracks-like voids, makes the process of oxygen contamination more efficient.

Reversible effect (adsorption)

The effect of gas adsorption in microcrystalline silicon films was first reported by Veprek and co-workers in 1983 [Veprek *et al.* 1983] for the materials deposited with facilities available at that time. It was proposed that the reversible atmospheric effects are associated with molecule adsorption processes that result in band bending and the effective shift of the Fermi level position. Only few reports mentioning an adsorption effect on present microcrystalline silicon materials can be found (see chapter 2 for details). The recent work of Finger *et al* [Finger *et al.* 2003], conducted in parallel to the work of our group, attempts to correlated observed instabilities with microcrystalline silicon morphology. In this work two categories of materials were identified: type I and type II microcrystalline silicon materials based on microstructural differences. Type I materials, or *porous*, are usually the structures with high crystalline volume fraction and large grain sizes, deposited at low silane concentration. After exposure to air, such materials are found to show a reversible decrease in dark conductivity, by up to 3 orders of magnitude. Type II materials, or *compact,* are usually prepared under conditions of close to amorphous growth, containing a significant amorphous fraction. For

this type of microcrystalline silicon one can usually expect a reversible increase of dark conductivity on air exposure.

The effects of atmosphere on thin film properties are discussed in more detail in chapter 2.

1.2.4. Deposition and impurities

As was pointed out above, microcrystalline silicon films are sensitive to unintentional incorporation of impurities. These might happen not only after deposition (post-deposition effects) as discussed above, but also during the material growth. A small amount of impurities can adsorb on the walls of chamber after previous deposition processes, remaining in the deposition reactor [Finger *et al.* 1998]. Upon the process of sample loading, water vapour and oxygen also can be adsorbed, diffusing into the chamber. These residual gases will desorb during the deposition process and may be incorporated as impurities in the material structure. Depending on the chamber performance and history, the presence of impurities can result in p or n type unintentional doping to occur. The influence of impurities remaining from previous depositions can be minimized by frequent cleaning of the reactor, while to completely avoid a presence of atmospheric gases is more complicated. These atmospheric impurities, especially oxygen, are considered to be donors [Finger *et al.* 1998, Liu *et al.* 2001, Kondo *et al.* 2002] in microcrystalline silicon. This results in the shift of the Fermi level away from the midgap position towards the conduction band. It was proposed that the deposition rate has a strong influence on the incorporation of impurities during material growth. The process of unintentional doping is more pronounced in the case of low deposition rates, because these rates will allow more impurities to be incorporated. Due to reasons stated above, undoped microcrystalline silicon is often n type.

To shift the Fermi level in the midgap position the procedure of compensation should be performed during a deposition process. The compensation can be achieved by adding a small amount of diborane gas B_2H_6, that varies depending on deposition conditions. For example in the case of highly crystalline materials (with crystalline volume fraction about 90%) grown by

HWCVD, the compensation can be achieved by adding about 0.1% of [diborane/ diborane + silane] gas ratio [Brüggemann *at al* 1998a].

1.3 Defect spectroscopy methods

The electronic quality of amorphous and microcrystalline silicon depends greatly on the number of electronic defects. These defects control electronic and transport properties of thin silicon materials and are involved in the processes of light induced metastability and doping. To obtain a device quality material it is important to investigate the defect density, with an aim to produce materials with as low defect density as possible. In the present section the experimental techniques that can provide information about the defects are reviewed. These are *Electron Spin Resonance* (ESR), *Constant Photocurrent Method* (CPM), *Photothermal Deflection Spectroscopy* (PDS), *Transient Photoconductivity* (TPC), *Time-of-Flight* (TOF) and *Modulated Photoconductivity* (MPC) measurements.

1.3.1 Electron Spin Resonance (ESR)

The ESR technique is based on the interaction of spins with magnetic fields and with each other. When a single electron occupies a quantum state the two states of the Pauli pair are normally degenerate, but are split by a magnetic field [Street 1991]. Paramagnetism and ESR are the result of the transition between the split energy levels. The transition occurs at microwave frequencies for the usual magnetic fields. The strength of the microwave absorption gives information about the local bonding structure. The density of spins measured by ESR is equal to the defect density. ESR is only sensitive to defects occupied by one electron (D^0) because defects occupied by two electrons (D^-) or unoccupied defects (D^+) are not paramagnetic [Street 1991].

1.3.2 Constant Photocurrent Method (CPM)

Constant photocurrent method (CPM) on silicon films is able to provide information on the defect density distribution in the lower portion of the gap. The CPM technique was firstly used to investigate defect density in amorphous silicon by Vanecek *et al* [Vanecek *et al.* 1981]. The method is based on the measuring of the absorption coefficient of the material α. During the experimental procedure the photocurrent is kept constant while the photon energy E_{ph} is varied. The inverse value of photon flux Φ needed to keep to photocurrent constant is then proportional to the absorption coefficient $\alpha(E_{ph})$ and can be expressed [Vanecek *et al.* 1981] as:

$$\alpha(E_{ph}) = C / \Phi(E_{ph}) \tag{1.5}$$

where C is a constant. The expression is valid for photoconductivity index γ $0.5 < \gamma < 1$ and $\alpha d << 1$, where d is the thickness of material.

A simple method to obtain a density of states distribution from a CPM spectrum is based on differentiation of $\alpha(E_{ph})$ over photon energy range that can be written as [Hata and Wagner 1991]:

$$N(E)\,f(E) = \left[\frac{\partial \alpha}{\partial E_{ph}}\right]_{E_{ph}=E_c-E_{ph}} \tag{1.6}$$

where N(E) the density of states and f(E) is the occupation function. Other methods to obtain the density of states from a CPM spectrum may be found in the literature [Marshall *et al.* 1991, Poruba and Schauer 1994].

1.3.3 Photothermal Deflection Spectroscopy (PDS)

Photothermal Deflection Spectroscopy (PDS) is a technique similar to CPM used to measure the optical absorption of amorphous [Jackson and Amer 1982] and microcrystalline [Finger *et al.* 2001] silicon. The PDS experiment is based on the measuring the temperature rise in the sample due to absorbed radiation, that

is proportional to αd ($\alpha d << 1$) [Ley 1998]. The temperature rise of the sample is measured through the temperature gradient produced in a gas or liquid immediately in front of the sample surface. A gradient in the refractive index of the liquid or gas, connected with temperature gradient, is detected by deflection of the laser probe beam. The deflection of the probe laser is proportional to the absorption.

1.3.4 Transient Photoconductivity (TPC) and Time-of-Flight (TOF) measurements

Transient photoconductivity (TPC) experiment is used to study energy resolved distribution of defects in thin silicon samples of coplanar configuration. In the experiment the sample is illuminated with short laser pulse. Photocurrent decay occurs before recombination due to interaction between injected carriers and the traps. Thus the transient photoconductivity decay contains information on the distribution of localized states in conduction band tail and also deep defects. Time-of-Flight (TOF) experiment is similar to TPC and is used to study samples with sandwich electrode configuration. In this case strongly absorbed light can create carriers close to illumination surface and subsequently carriers of one or other sign can be drawn across the specimen by an applied electric field. The experiment provides a simple method to calculate carrier drift mobility. A more detailed discussion of the underlying physics and methods of DOS extraction is given in chapter 3.

1.3.5 Modulated Photoconductivity (MPC)

Modulated photoconductivity (MPC) and TPC experiments are closely related. In the MPC experiment the sample is illuminated with light, intensity of which is modulated with a sine wave [Brüggemann *et al.* 1990]. The response to sinusoidal excitation is a phase shifted sinusoidal photocurrent and thus MPC data contains information about photocurrent, angular frequency and phase shift. Compared to TPC experiment, the energy range of MPC is limited. The limitation arises from the splitting of the quasi Fermi levels by the steady state generation

rate and thus the states below quasi Fermi levels can not be probed. TPC experiment does not lead to splitting of the quasi Fermi levels and thus can "see" the states down to the Fermi level.

1.4 Basic Aspects of Thin Film Solar Cells

Photovoltaic power is one of the major applications of thin film materials. The operational principal of a solar cell is based on absorption of light with subsequent generation of charge carrier pairs, and separation of charge carriers by an internal electric field. Separation of electrons and holes is required in order to contribute to the current of the device. While in crystalline semiconductor the internal field of p-n junction is able to prevent recombination of photogenerated electrons and holes, in amorphous semiconductors this would yield poor efficiency because photogenerated electrons carriers cannot diffuse for long distances due to high defect densities of p- and n-type layers. Thus the intrinsic layer with lower defect density should be used as an absorber layer in photovoltaic device (*pin* structure) to enable efficient carrier separation to take place.

The intrinsic layer should be thick enough to absorb the maximum amount of photons. The p and n layers provide the built-in potential and do not contribute to the charge collection, thus they should not be too thick. Because of high absorption of thin films, the thickness of solar cell can be significantly reduced, compared to crystalline materials. The typical thickness values for thin film solar cells are in the order of 1 μm for the intrinsic layer and around 50 nm for doped layers.

The schematic cross section of a *pin* solar cell is presented in figure 1.9. The cell is deposited on transparent substrate (usually glass) that serves as a window to the cell. The top electrode consists of a transparent conductive oxide (TCO), while bottom electrode is usually metal, made from Al or Ag.

It is possible to improve absorption of photons by increasing the optical path through the active layer. In the ideal case the light is repeatedly reflected

within solar cell until it is completely absorbed in the active layer. This so-called 'light trapping' may be achieved by introducing textured front and/ or back surfaces, that provide random scattering, increasing path length [Kluth *et al.* 1999, Guha 2000, Mueller *et al.* 2001, Shah *et al.* 2003]. Introduction of textured surfaces allows the thickness of a solar cell active layer to be reduced.

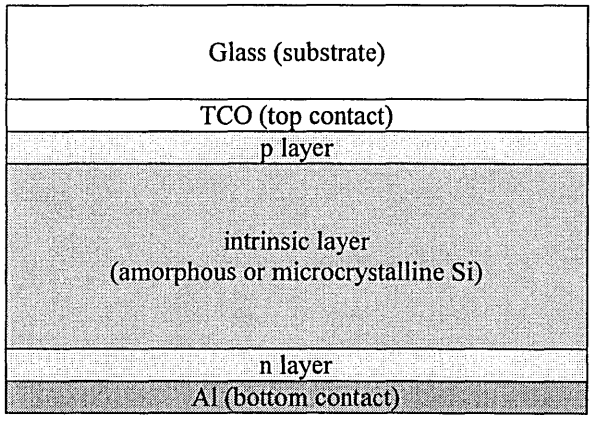

Figure 1.9. Cross section of the *pin* photovoltaic structure.

The efficiency of a solar cell η is determined by the following parameters: the fill factor FF, the open circuit voltage V_{oc} and the short circuit current I_{sc}. The open circuit voltage V_{oc} and the short circuit current Isc are defined as the values of the voltage and current at I (V) = 0 and V = 0, respectively. The fill factor FF is defined as the ratio of the maximum power and the product of I_{sc} and V_{oc}. The solar cell efficiency η is defined as the ratio of the maximum delivered power and the power of the incident light and can be presented as:

$$\eta = \frac{I_{SC} V_{OC} FF}{100 mW / cm^2} \qquad (1.7)$$

Illumination of a solar cell with amorphous silicon active layer results in a decrease of efficiency η and fill factor FF due to light induced degradation (Staebler-Wronski effect, see section 1.1.3). Creation of new defects enhances the electrons and holes trapping process; thus the solar cell efficiency decreases because of collection reduction and decrease of the internal electric field due to charged dangling bonds. The efficiency reduction tends to stabilise after few hundreds of hours illumination time at a level below initial efficiency. The solar cell properties can be recovered by annealing at temperatures below 200 °C [Shah *et al.* 1995].

To avoid light-induced degradation of the solar cell, an active layer of microcrystalline silicon can be used. Microcrystalline silicon with high crystalline volume fraction is known to show improved stability against light induced degradation [Goerlitzer *et al.* 1997, Kleider *et al.* 2001, Finger *et al.* 2003, Klein *et al.* 2003]. The correlation between a solar cell performance and the active layer properties of microcrystalline silicon has been reported in a detailed study by Vetterl *et al* [Vetterl *et al.* 2000]. It was found that V_{oc} continuously increases with decreasing crystallinity. Deposition conditions with low silane concentration also lead to decrease of fill factor FF and short circuit current I_{sc}. Thus, a solar cell with highly crystalline active layer will show a lowest efficiency. On the other hand, the lowest crystallinity is not the best choice for the active layer material, because a *decrease* in fill factor FF and short circuit current I_{sc} is observed if the active layer crystallinity decreases below a certain value. A complete physical model explaining such behavior has not yet been established. Possible suggestions include the influence of grain boundary recombination/ passivation effects or interface effects between doped and intrinsic layers. As a result, it was suggested [Vetterl *et al.* 2000] that an optimal solar cell performance could be achieved if the active layer is grown near the transition between microcrystalline and amorphous growth, and the microcrystalline silicon films with highest crystalline volume fraction are probably not the most suitable for solar cell applications.

Chapter 2. Review of work on ageing

Stability against light-induced degradation is an important advantage of microcrystalline silicon materials with significant crystalline volume fraction. However, microcrystalline silicon materials are sensitive to post deposition atmospheric effects, including atmospheric gases adsorption and oxidation. The present section reviews the reports, showing the influence of atmosphere on both coplanar and sandwich configuration structures of amorphous and microcrystalline silicon materials.

First reports on the effects of atmospheric gases on the electronic properties of amorphous and microcrystalline silicon materials appeared in the 1980s [Solomon 1980, Tanielian *et al.* 1980, Tanielian 1982, Veprek *et al.* 1983]. These reports concerned coplanar sample configurations. Atmospheric components, such as water or oxygen molecules, may interact with a semiconductor surface in two ways – physical and chemical [Gregg and Sing 1967, Avetard and Haydon 1973, Morrison 1990]. The physical interaction, referred to as *adsorption* is the process of weak binding of molecules to a surface, that involves "weak" van der Waals forces. In this case adsorbed species become ionised and could capture or inject electrons from the material [Morrison 1990]. This interaction assumes *no sharing* of electrons, as would be in the case of, for example, covalent bonding. Atmospheric components, physically adsorbed on a semiconductor surface can be removed, for example, by vacuum drying, and thus adsorption is a reversible effect [Morrison 1990].

The process of "charge transfer" may result in a band bending effect that influences the electronic properties of the material. For example the reversible effect of dark conductivity changes reported for amorphous and microcrystalline silicon was associated with band bending on the material surface [Solomon 1980, Tanielian *et al.* 1980, Tanielian 1982, Veprek *et al.* 1983]. These works will be considered in detail later in the text. The schematic diagram of the band bending effect due to adsorption of atmospheric species is presented in figure 2.1.

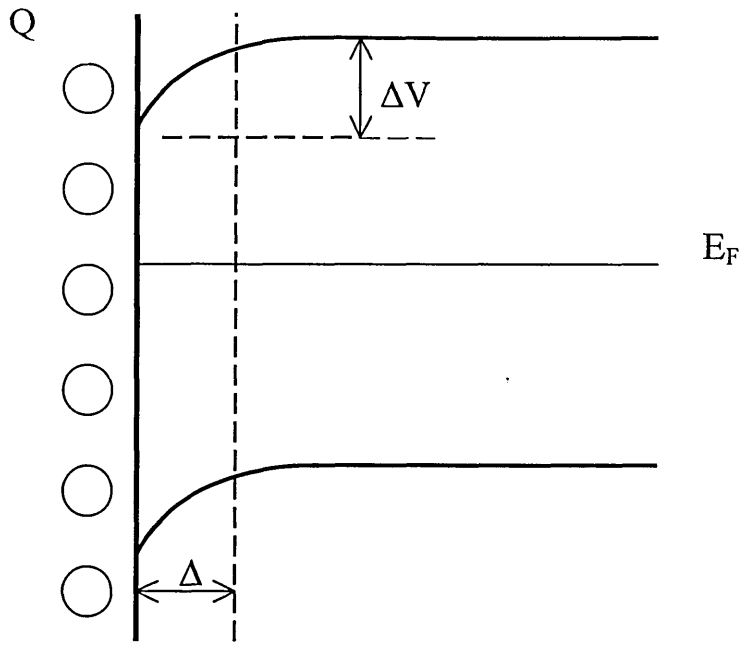

Figure 2.1. Schematic diagram of band-bending at the film surface. The description of parameters is given later in the text.

The circles in the figure schematically show atmospheric gas molecules adsorbed on the film surface. The molecules cause a charge at the surface that is compensated by an equal and opposite charge in the film. This would be equivalent to the shift of the Fermi level that could be large enough to cause conductivity changes. As schematically shown in the figure for the water molecules, the water adsorption process results in an electron accumulation layer formation close to the surface that effectively shifts the Fermi level position towards the conduction band for the value ΔV, that results in changes of dark conductivity.

Another way of interaction of atmospheric components with a semiconductor is chemical bonding, that results in forming of chemical bonds between material and "foreign" atoms [Avetard and Haydon 1973, Morrison 1990]. In the case of silicon, this type of interaction with atmospheric species referred to as *oxidation*, that is the process of chemical reaction of oxygen with silicon material. This leads to incorporation of oxygen into the material and the possible chemical reactions [Morrison 1990] could be written as:

$$Si + O_2 \rightarrow SiO_2 \qquad (2.1)$$
$$Si + 2H_2O \rightarrow SiO_2 + 2H_2$$

Oxidation of silicon could take place in a wide temperature range up to 700 K [Morrison 1990]. Even at temperatures below room temperature a formation of Si-O bonds has been observed [Morrison 1990].

In the 1980s several groups [Solomon 1980, Tanielian *et al.* 1980, Tanielian 1982, Veprek *et al.* 1983] reported on investigation of atmospheric effects in amorphous and microcrystalline silicon films. Below the results of these investigations are reviewed. It should be noted that these reports were produced in the early days of amorphous and microcrystalline silicon research and the materials could be possibly considered as non-optimised silicon films from today's viewpoint.

Solomon [Solomon 1980] reported on the study of atmospheric and band bending effects in amorphous silicon films. The band bending could be described by the penetration depth Δ, which is the Debye length in the material, and the value of the band bending ΔV (see figure 2.1). The values of the band bending ΔV at the surface and the penetration depth Δ can be estimated using equations:

$$\Delta V = - Q / e\,(\varepsilon\,\varepsilon_0\,N_o)^{1/2} \qquad (2.2)$$

$$\Delta = 1/e\,(\varepsilon\,\varepsilon_0 / N_o)^{1/2} \qquad (2.3)$$

where e is the elementary charge, ε is the dielectric constant of the material, ε_0 is the vacuum permittivity and N_o is the density of states near the Fermi level. Q is the density of charges at the surface.

Rough estimation of the band bending value at the surface ΔV suggests that it can be of the order of few tenths of eV, considering a concentration value Q on the film surface at least 10^{10}-10^{11} elementary charges per cm^2. The penetration depth Δ will be in the order of a fraction of micron. This means that for film

thickness around 1 micron the surface conductivity could dominate the bulk conductivity. Solomon concluded that as a result, in many cases the surface conductivity of amorphous silicon could be by 3 or more orders of magnitude higher than bulk conductivity.

In early 1980's Tanielian and co-workers [Tanielian *et al.* 1980, Tanielian 1982] presented very detailed works on the relation between water adsorption effects and dark conductivity of hydrogenated *amorphous* silicon. An overview of these two papers is presented below.

The coplanar samples of amorphous silicon were prepared in a 13.6 MHz SiH_4 glow-discharge system, the silane gas was diluted with Ar at ratio 1:9, the samples thickness was varied between 0.2~2 μm. Such deposition conditions could promote the growth of columnar microstructures of the materials.

Nominally undoped amorphous silicon films show an increase of dark conductivity when the films are exposed to water vapour. The effects of atmospheric adsorption were investigated depending on the sign of the majority carriers. It was found that for n type samples dark conductivity *normally* increases, when the samples are exposed to water vapour. The opposite behaviour was observed for the p-type samples: dark conductivity *normally* decreases on water vapour exposure. However, it was pointed out that in some cases the behaviour is different from described above, where non–monotonic increase/ decrease of conductance could be observed.

The time dependence of dark conductivity changes as a function of partial pressure. It was found that for the majority of samples, time needed to reach the saturation decreases with increase of adsorbate partial pressure. It was also suggested that the water does not penetrate amorphous silicon films used in the study, while for sputtered amorphous silicon the penetration could take place.

The sample thickness was found to affect the adsorption processes relatively weakly. In some cases, but not always, thinner films demonstrated faster response. It was suggested that the speed of adsorption processes was dependent on the sample surface properties, which may vary with thickness and also on the sample history. The interpretation of these results is based on the suggestion that water molecule behaves as an electron donor, when adsorbed on the amorphous silicon film surface, or electron acceptor, when the water

adsorption process takes place on the oxidised film surface. The model suggested by Tanielian *et al.* was aimed to explain observations of both monotonic and non-monotonic dark conductivity changes. It was proposed that two different reactions between adsorbed water and hydrogenated amorphous silicon could be distinguished: a fast process, associated with formation of donor-like state, close to the conduction band, by weakly bound water on the surface of amorphous silicon film, and a slow process, that can be associated with a slow formation of an acceptor-like state close to the middle of the gap. The last process was suggested to arise from more strongly bonded compound formed by the reaction of water with oxidised surface, equivalent to Si-OH. It was suggested that on annealing at temperatures about 100°C such compounds could be removed from silicon film surface. The fast process was suggested to donate electrons to the material, increasing the conductance, while the slow process can result in electron extraction from the material, decreasing the dark conductivity. Thus, these processes were able to explain monotonic or non-monotonic conductance changes.

An investigation of atmospheric effects in *microcrystalline* silicon films was presented by Veprek and co-workers in 1983 [Veprek *et al.* 1983]. Microcrystalline silicon films were prepared by chemical transport deposition process, at deposition temperatures between 100°C and 450°C. By varying deposition temperature and other deposition parameters, the average crystal size was typically varied between 3 and 20 nm.

Two different atmospheric effects were identified: reversible and irreversible effects. The reversible atmospheric effect resulted in dark conductivity decrease over a period of several days and was related to the oxygen adsorption process. It was suggested that adsorbed oxygen could behave as an electron acceptor, resulting in a decrease of dark conductivity. The irreversible atmospheric effect was associated with oxidation process. Irreversible changes in dark conductivity were correlated with changes of spin densities, revealing changes in oxygen content. It was demonstrated that irreversibly incorporated oxygen could be removed only at temperatures above 1050 °C.

It was reported that the reversibly adsorbed oxygen species could not be detected by infrared absorption measurements. The adsorbed oxygen could be

removed by annealing the sample at temperatures about 200°C - 220°C. A dark conductivity time dependence on partial pressure gave similar results to the work of Tanielian *et al.*

It should be noted that both works (Tanielian *et al.* and Veprek *et al.*) observed an effect of dark conductivity decrease on air exposure. Tanielian *et al.* attempt to explain the observed decrease as a process of reaction involving water adsorption on oxidised silicon surface. Veprek *et al.* suggested that the dark conductivity decrease is due to reversible effect of oxygen adsorption on the film surface. Although both described mechanisms could take place, the mechanism suggested by Tanielian requires an appearance of silicon oxide that should be detected by infrared absorption measurements. However it was reported by Veprek *et al.* that the reversible atmospheric effects did not produce changes in the infrared absorption spectra. It suggests that the mechanism involving oxygen adsorption process could be more appropriate to describe the effect of dark conductivity decrease on exposure to atmosphere.

The following key conclusions may be drawn from the above overview:

- atmospheric effects in amorphous silicon films are associated with water adsorption process. The water adsorption results in increase of dark conductivity
- atmospheric effects in microcrystalline silicon films are associated with oxygen, and are both reversible or irreversible
- reversible oxygen adsorption in microcrystalline silicon films results in dark conductivity decrease
- the reversibly adsorbed atmospheric components could be removed by annealing at temperatures below 220°C, irreversibly incorporated oxygen could only be removed at temperatures above 1050 °C.

These conclusions are drawn from results obtained from materials grown more than 20 years ago by deposition techniques available at that time. Since then, only a few reports of *post deposition* atmospheric instabilities in silicon thin film materials have appeared. In 1998 Goerlitzer *et al.* [Goerlitzer *et al.* 1998] reported an observation of an increase in dark conductivity values of GD

microcrystalline silicon films measured 4 months after deposition. It was proposed that the effect could be related to oxygen contamination process, where the oxygen could be considered as a donor. The oxygen concentration was measured as a function of film thickness, revealing a gradient of oxygen content. The concept of donor properties of oxygen in thin silicon films was later widely accepted for impurities incorporated during material deposition process [Finger *et al.* 1998, Liu *et al.* 2001, Kondo *et al.* 2002]. Brüggemann *et al.* [Brüggemann *et al.* 1998b] and Schubert *et al.* [Schubert *et al.* 1998] reported an investigation of ambient atmosphere effect in hot wire nanocrystalline silicon films. A decrease of coplanar dark conductivity on air exposure and an increase of dark conductivity on annealing the samples were observed. It was suggested that the effect of conductivity changes could have the same origin of effects reported by Veprek *et al.* and be related to the oxygen adsorption process.

In parallel to the investigations of the atmospheric effects conducted in Dundee, the relevance of instabilities study in microcrystalline silicon films was underlined in the recent work of Jülich group [Finger *et al.* 2003]. Finger and co-workers investigated microcrystalline silicon samples optimised for photovoltaic applications. The samples around 1 micron thick were deposited at varying silane concentration to obtain the materials changed from highly crystalline to amorphous. It was suggested that depending on microstructure, the microcrystalline silicon films could be distinguished into 2 categories: type I (porous) and type II (compact) materials. Type I materials are more crystalline structures with large grain sizes, generally deposited at low silane concentration; crystal columns are separated by cracks. Type II materials are prepared at close to amorphous growth and have smaller grain sizes. The basic features of type I and type II materials are summarized in table 2.1.

The work pointed out that the compact materials could be more beneficial for photovoltaic applications giving a higher efficiency values, while porous materials are more stable to light induced degradation. On the other hand, these films are more sensitive to atmospheric effects.

The work distinguishes, in a similar way to Veprek, between reversible and irreversible atmospheric effects. Porous (type I) microcrystalline silicon structures

are found to be more sensitive to irreversible oxygen incorporation, increasing the number of Si-O bonds, while compact structures are less affected by oxidation process.

Type I 'porous'	Type II 'compact'
Poor efficiency	**High efficiency**
High crystallinity	**Low crystallinity**
Conductivity decreases on air exposure	**Conductivity increases on air exposure**

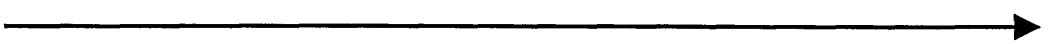

Silane concentration

Table 2.1. Basic features of type I/ type II microcrystalline silicon materials.

The Si-O bonds are stable, resulting the oxidation process is irreversible up to 200°C annealing. This is in agreement with observations reported by Veprek, who observed removal of oxygen only around 1050°C.

The reversible effects of atmospheric gases adsorption are reported for both porous and compact materials. It was demonstrated that a typical porous microcrystalline silicon film, that is a highly crystalline material, could show a conductivity decrease about 3 orders of magnitude while exposed to air, similar to the results observed by Veprek and co-workers. Typical compact film (type II) with large amorphous volume fraction demonstrated an opposite behavior, where dark conductivity increased on air exposure by some 3 orders of magnitude that is similar to the effect reported by Tanielian for amorphous silicon films. The proposed explanation of observed effects considered the corresponding changes in dark conductivity as shift of the Fermi level that changes occupation of states. The Fermi level shift arises from band banding due to adsorption of water and/ or

oxygen. For type I materials, the adsorption of an electron acceptor molecule creates a depletion layer at the material surface, decreasing the conductivity. This is equivalent to the shift of the Fermi level away from the conduction band. The changes in conductivity in type II microcrystalline silicon films on air exposure were proposed to have a similar origin as undoped amorphous silicon, which is associated with creation of accumulation layer due to water molecules adsorption.

Another recent work focused on the investigation of atmospheric effects in both *solar cells* and coplanar structures. In 2003 Wang *et al.* [Wang *et al.* 2003] presented a study of degradation of hot wire CVD amorphous silicon films and solar cells. The changes in dark conductivity and corresponding decrease of dark conductivity activation energy due to the influence of atmospheric gases were reported for coplanar sample configurations. It was shown that the atmospheric gases could also affect the photovoltaic structures: the degradation of solar cells, particularly the decrease of open circuit voltage and the solar cell efficiency due to storage on air was reported. It was suggested that the degradation mechanisms of thin films and solar cells structures could have the same origin and be related to the process of adsorption/ incorporation of water or oxygen. Similarly to this work, an effect of atmosphere on the solar cell properties has been observed by Klein *et al.* [Klein *et al.* 2003]. Particularly it was found that after annealing the solar cells at 160°C for 1 hour, an improvement of the solar cells efficiencies could take place.

Summarising this review, it must be underlined that the electronic properties of coplanar amorphous and microcrystalline film structures are significantly affected by the atmospheric effects. For microcrystalline silicon films the effect of atmospheric gases could be dominant over deposition parameters, which complicates a proper comparison and optimisation of various structures. As was demonstrated, a significant degradation of thin film solar cells could take place not only due to Staebler-Wronski effect, but also due to influence of atmospheric gases. This fact underlines the relevance of investigation of atmospheric related effects on thin film materials. Given the problem of reversible and irreversible effects and the wide range of morphologies of thin film materials,

it is clear that stability to atmosphere in present-day thin film silicon requires more attention. Thus the significant part of the present study was focused on the investigation of the influence of atmospheric gases on the properties of microcrystalline silicon films.

Chapter 3. Photoconductivity

3.1 Steady state photoconductivity

In a semiconductor at thermal equilibrium, the free carrier generation rate is equal to the recombination rate, and the resulting equilibrium carrier concentrations of electrons and holes give rise to a dark conductivity σ_{dark}. Illumination of a semiconductor with light of energy greater than the band gap results in carriers being optically excited to conducting states and a consequent increase in carrier concentrations above the thermal equilibrium values. If the illumination is constant with time, a new quasi-equilibrium, or 'steady-state', condition is obtained. The resulting photoconductivity σ_{ph} is expressed as the difference between the conductivity observed under illumination and the dark conductivity:

$$\sigma_{ph} = \sigma - \sigma_{dark} \tag{3.1}$$

Under steady-state conditions the recombination and generation rates are equal. If we assume that electron are the dominant carriers the following equation for the steady state photogeneration rate is obtained:

$$G_{ss} = n_{ss} / \tau \tag{3.2}$$

where n_{ss} is the density of free electrons and τ is the electron lifetime, which is the time that an excess electron spends in extended states before recombination. Measurements of the steady state photoconductivity $\sigma_{ph} = n_{ss}\, e\, \mu$ yield the mobility-lifetime product:

$$\mu\tau = \frac{\sigma_{ph}}{G_{ss}\, e} \tag{3.3}$$

The rate of change of free electron and hole concentrations is

$$dn/dt = dp/dt = G_d + G_{ss} - R \tag{3.4}$$

The recombination rate is given by

$$R = (n_d + n_{ss})(p_d + p_{ss})C_R = G_d + G_{ss} \quad (3.5)$$

where n_d and p_d are the thermodynamic equilibrium free carrier densities, C_R is the probability per second that an electron will recombine with a hole. The thermal generation rate $G_d = n_d\, p_d\, C_R$. If the material is electrically neutral and trap-free, then n = p and $n_d = p_d$. Substituting into equation (3.5) we obtain:

$$G_{ss} = (2\, n_d\, n_{ss} + n_{ss}^2)\, C_R \quad (3.6)$$

This equation exhibits two regimes depending on the magnitude of the generation rate.

Under conditions of low light the carrier generation rate is much smaller than the thermal generation rate $G_{ss} << G_d$ and thus $n_{ss} << n_d$. The probability of an electron recombining is therefore determined by a fixed density of thermally generated holes. So (3.6) becomes

$$G_{ss} = 2 n_d\, n_{ss}\, C_R \quad (3.7)$$

In this regime the photoconductivity is proportional to the optical generation rate and the lifetime is constant. This regime, in which the recombination rate depends on the excess density of only one type of carrier is called *monomolecular* recombination.

When the generation rate is high, $G_{ss} >> G_d$ and $n_{ss} >> n_d$ and we have

$$n_{ss} = (G_{ss} / C_R)^{1/2} \quad (3.8)$$

In this case the recombination rate depends on the densities of both recombining species and the photocurrent varies as a square root of the optical generation rate. This regime is called *bimolecular* recombination and results in a decrease of the carrier lifetime with increasing optical generation rate

Recombination in amorphous silicon is however more likely to take place through the significant number of gap states, which act as trapping centres. As was mentioned earlier, the emission probability of deeply trapped carriers is lower in comparison with carriers trapped close to band edges, so the deep states in the gap behave as recombination centres. The Shockley-Read mechanism [Shockley and Read 1952] considers two separate transitions from the mobility edges. This is shown schematically in figure 3.1. For low generation rates such that the total density of recombination centres N_t is much larger than the steady state density of electron occupied centres n_t recombination is monomolecular because $\tau = C_n N_t$, where C_n is the electron capture coefficient for the centre, is independent of the steady state photogeneration rate G_{ss}.

Figure 3.1 shows the states in the gap that behave as recombination centres and also states close to the band edges that act as 'temporary' traps of charge. Carriers captured by these shallow states are more likely to be thermally re-emitted than to capture a free carrier of opposite sign.

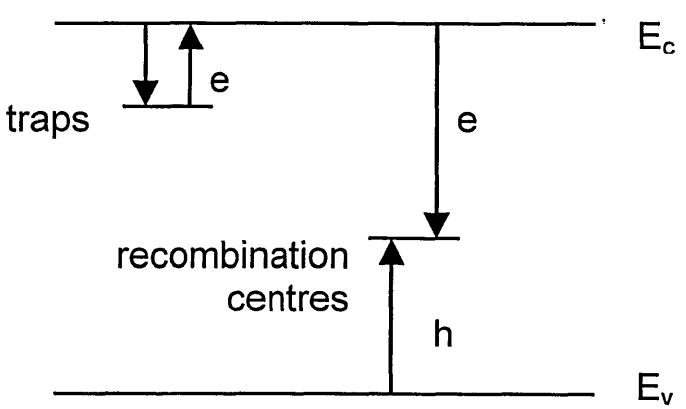

Figure 3.1. Shockley-Read recombination mechanism.

The presence of traps profoundly affects time-resolved conductivity measurements, for example transient photoconductivity, which is described later in the text.

The probability of thermal re-emission of a trapped carrier can be obtained by invoking the *principle of detailed balance*, that in thermodynamic equilibrium forward and reverse rates of all processes are equal. Thus with reference to figure 3.1 for electrons in thermodynamic equilibrium

rate of capture = rate of re-emission

$$C_n n_d N_t (1 - f_0(E_t)) = e_n N_t f_0(E_t) \qquad (3.9)$$

Where f_0 is the Fermi-Dirac distribution function and e_n is the emission probability per second. Substituting for f_0 gives

$$e_n = \nu_n \exp\left(-\frac{E_c - E_t}{kT}\right) \qquad (3.10)$$

This has the form of an attempt to escape frequency $\nu_n = C_n N_c$ multiplied by the probability of an electron finding the energy from the thermal background to make the transition to E_c. A similar expression can be written for the hole emission probability e_p. We note that equation 3.10 has been derived for so-called one electron states.

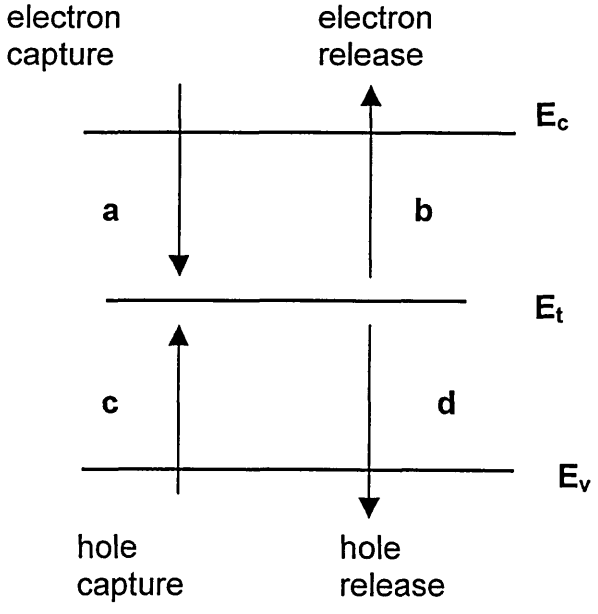

Figure 3.2. Electron and hole transition controlling the occupation of a localized state.

The Shockley – Read analysis obtains the occupation f under illumination of a single electron state in the gap by considering all possible transitions that can

occur for a given set of states (fig. 3.2) In the steady state the principle of detailed balance may again be applied and the sum of rates (a) and (d) must equal the sum of (b) and (c). Manipulation yields

$$f(E_t) = \frac{nC_n + pC_p}{(n + n_1(E_t))C_n + (p+p_1(E_t))C_p} \qquad (3.11)$$

where $n_1C_n = e_n$ and $p_1 C_p = e_p$. Note that this expression does not depend on N_t. Simmons and Taylor showed this could be applied to arbitrary distributions of states [Simmons and Taylor 1972].

The Shockley-Read statistics may be used to determine whether a gap state acts as a trap or recombination centre. For the traps the electron release rate is much greater than the hole capture rate ($n_1C_n >> pC_p$) so from equation 3.11

$$f(E) \approx \frac{n}{n_1} = \frac{n}{N_c \exp\left(-\frac{E_c - E_t}{kT}\right)} \qquad (3.12)$$

The occupation of traps at depth E is related to that of free states at E_c by a Boltzmann ratio and is thus temperature-dependent. For recombination centres the capture rates are much larger than the release rates so equation 3.11 becomes

$$f(E) \approx \frac{nC_n}{nC_n + pC_p} \qquad (3.13)$$

Considering a case of simple symmetry where n=p and C_n=C_p then f(E)=0.5 i.e. the occupation is constant. Figure 3.3 shows the form of the occupation in a semiconductor with a continuous distribution of localised states in the gap.

It is useful to define the electron quasi-Fermi level, which is related to the increased electron density under illumination by

$$n = N_c \exp\left(-\frac{E_c - E_{fn}}{kT}\right) \qquad (3.14)$$

where E_{fn} is the electron quasi-Fermi level. When a semiconductor is illuminated, the dark Fermi level splits into two quasi-Fermi levels which move towards the band edges with increasing excitation intensity. The occupation of traps is more appropriately described using *trap* quasi-Fermi level, E_{tn}, defined as the energy at which the occupation is half the occupation of equation 3.13 and thus E_{tn} marks the transition between traps and recombination centres. Figure 3.3 illustrates the occupation function f(E) in the dark condition and under illumination.

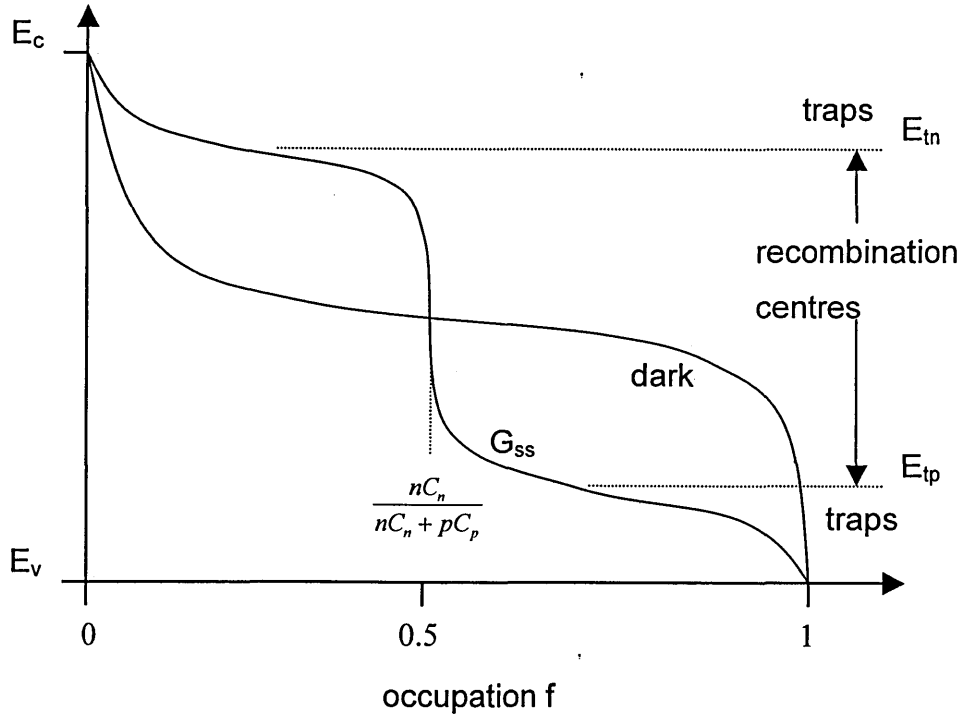

Figure 3.3. Occupation function for localized states in an amorphous semiconductor in the dark and under illumination.

In general trap quasi Fermi level E_{tn} is only slightly above E_{fn} in n type semiconductor and behaves similarly under illumination. Thus as the light intensity is increased, E_{tn} and E_{tp} move towards their respective bands signifying a conversion of traps into recombination centres.

The increase in the density of recombination centres with increase of generation rate forms the basis of a model developed by Rose [Rose 1963] to

explain the frequently observed phenomenon of a "power-law" photoconductivity excitation dependence intermediate between mono- and bimolecular, $n_{ss} \propto G_{ss}^{\gamma}$, $0.5 < \gamma < 1$. The deviation from the monomolecular or bimolecular regimes is cause by the gap states and the resulting γ will depend on the particular distribution of states. The Rose model assumes a semiconductor with an exponential density of states described by

$$g(E) = g_C \exp\left(-\frac{E_c - E}{kT_C}\right) \tag{3.15}$$

where kT_c is termed the characteristic band tail energy and T_C the band tail temperature. g_c is the extrapolation of g(E) to E_c and is termed the band edge DOS. The analyses performed by Rose demonstrate that for an exponential DOS $\gamma = T / (T_c + T)$.

In general, recombination in amorphous silicon via dangling bonds is more complex process then described above for one electron state by the Shockley-Read mechanism and involves three possible charge conditions: empty (D^+), singly occupied (D^0) and doubly occupied (D^-) [Street 1991]. There are two possible recombination paths that are illustrated in figure 3.4.

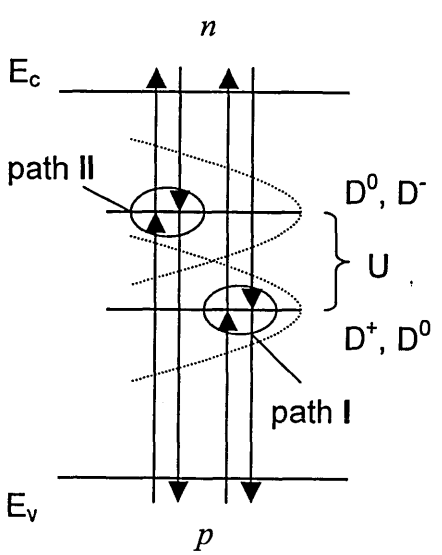

path I: $e + D^+ \rightarrow D^0$ and $h + D^0 \rightarrow D^+$
path II: $e + D^0 \rightarrow D^-$ and $h + D^- \rightarrow D^0$

Figure 3.4. Transition diagram for recombination via dangling bonds.

The occupation of the dangling bonds depends on the position of the Fermi level, usually the position of D^- states is found to be above midgap, while D^+ states are found below, the neutral defects D^0 are usually found around midgap. The energy of the D^0 state from path I is not the same from path II because of Coulomb interaction between the electrons of the singly occupied states. The energy difference between these two states is referred as the *correlation energy* U which is in the case of amorphous silicon is positive [Street 1991].

The correlation energy is defined as $U = q^2 / 4\pi\varepsilon\varepsilon_0 r - W$, where the first term describes the Coulomb interaction, with q as the elementary charge, r the effective separation of the two electrons, and the second term arises from lattice relaxation energy at the defect which is described by W.

3.2 Transient photoconductivity

Transient photoconductivity may be used to investigate density of states distributions and recombination kinetics in disordered semiconductors. A short flash of light creates free carriers which then interact with the localised states to give a current decay which bears the 'fingerprint' of their distribution in energy. It can be applied to either sandwich or coplanar electrode configurations. In the transient photoconductivity (TPC) experiment, coplanar, ohmic electrodes are used and thus the secondary photocurrent is investigated. If a sample with sandwich electrode configuration is studied, carriers may be generated close to illumination surface when strongly absorbed (short wavelength) light is used. The carriers of one sign may be drawn across the material by a suitable applied electric field F as a primary photocurrent, provided that there is no carrier injection from the contacts. Suitable conditions for this 'time-of-flight' (TOF) experiment can be achieved by applying a reverse bias to *pin* configuration. Figure 3.5 schematically shows the set-ups for the TPC and TOF experiments.

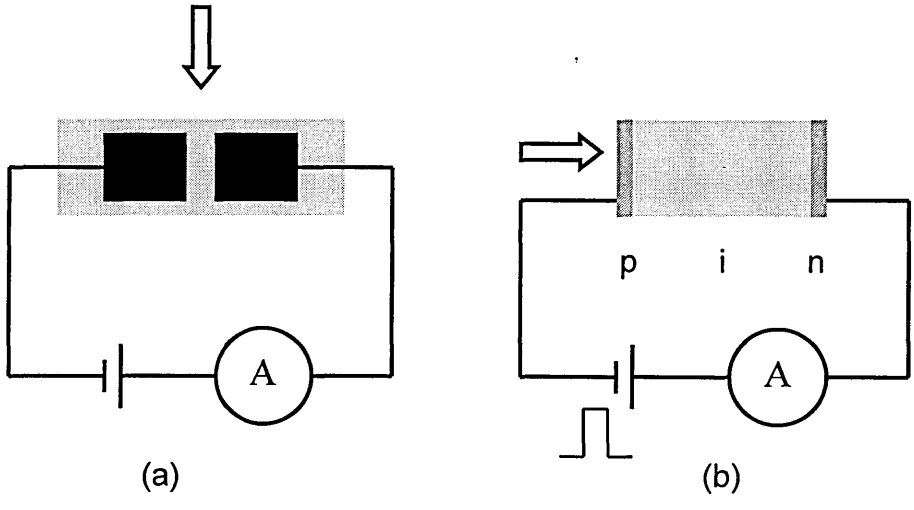

Figure 3.5. Schematic diagrams for (a) transient photoconductivity (TPC) and (b) time-of-flight (TOF) experiments.

The time-of-flight experiment provides a simple method for obtaining a carrier drift mobility μ_d. In the TOF configuration the pre-transit current in the

external circuit reflects the transit of charge across the sample. If the transit time t_{tr} and sample thickness L at a given field F are known, then the mobility is given by:

$$\mu_d = L / t_{tr} F \qquad (3.16)$$

In the idealised case, in the absence of trapping and recombination, the sheet of charge will drift across the sample, giving a constant current until it is extracted at the other side. In practice the current does not drop immediately to zero after the transit time because the carriers assume a gaussian distribution of velocities due to diffusion, so when the first carrier reaches the back contact, the current starts to drop. Decays of this type are known as *gaussian*, or *conventionally dispersive*. In this case the transit time of the drifting carriers t_{tr} may be identified as the time at witch the current falls to 50% of its plateau value [Marshall 1988]. Gaussian decay and transit time t_{tr} are shown schematically in figure 3.6 a.

Although the transit pulse of gaussian shape can be observed experimentally in many crystalline and some amorphous materials [Marshall 1977, Marshall 1988], for disordered materials it is very frequently the case that the transit pulse is different from described above and has an *anomalously dispersive* (or simply "dispersive") form, shown in figure 3.6 b.

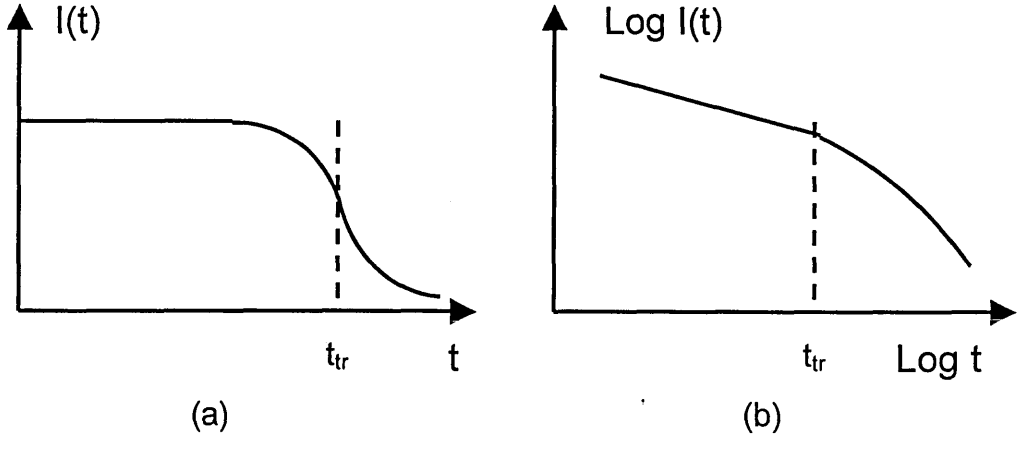

Figure 3.6. Gaussian (a) and anomalously dispersive (b) decays.

For anomalously dispersive decays the current decreases over the whole time range of the measurement. In the particular case of an exponential distribution of states the presentation of the decay with double logarithmic current and time axes establishes two power law slopes. The transition between these slopes takes place at time t_{tr}, where the fastest carriers begin to reach back electrode. At short times the charge carriers become trapped in localized states at various depth and the distribution of trapped carriers will move toward greater depth as time progresses. This 'thermalization' process causes a progressive reduction of the pre-transit photocurrent with time (so-called pre-transit regime). In post-transit regime the photocurrent is controlled by eventual release of deeply trapped carriers which are extracted before they without significant thermalization. A number of studies of anomalously dispersive behaviour [Scher and Montroll 1975, Schirmacher 1981, Orenstein *et al.* 1982] have demonstrated that the relationship between current I(t) and time t can be expressed as:

$$I(t) \propto t^{-(1-\alpha_1)} \qquad t < t_{tr} \tag{3.17a}$$

$$I(t) \propto t^{-(1+\alpha_2)} \qquad t > t_{tr} \tag{3.17b}$$

where α_1 and α_2 are dispersion parameters. While the first experiments suggested that $\alpha_1 = \alpha_2$, the later works have demonstrated that in general case $\alpha_1 \neq \alpha_2$ [Overhof and Thomas 1989]. To explain the anomalously dispersive transport, two mechanisms have been proposed.

In amorphous semiconductors photoconductivity decays are usually interpreted in terms of the multiple trapping model. Several reports in 1977 [Marshall 1977, Silver and Cohen 1977, Noolandi 1977, Schmidlin 1977] showed that the anomalously dispersive behaviour can arise from trap limited band transport. The mechanism of multiple trapping transport can be described as following. Charge carriers participate in conduction only in the extended states of the bands. If a carrier is trapped in a localized state it becomes immobilised. Later the trapped carrier will be thermally excited to the band where it again contributes to the electric current until it is trapped again. The schematic diagram of multiple trapping conduction mechanism is shown in figure 3.7.

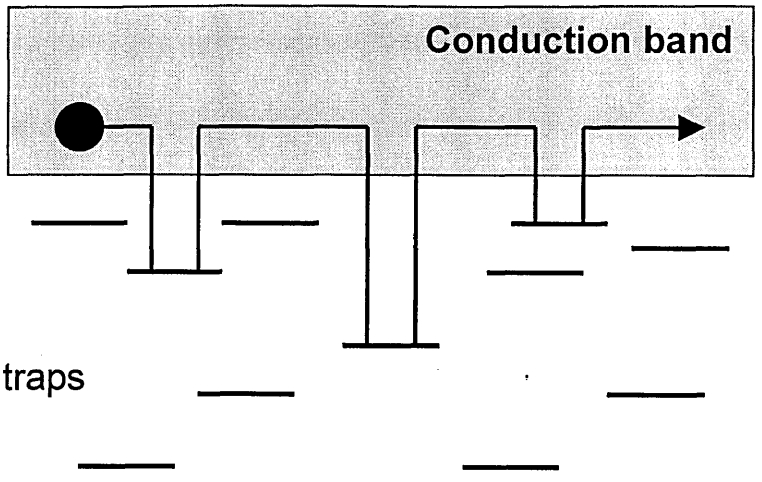

Figure 3.7. Multiple-trapping transport.

Unless the defect concentration is high or the temperature low (typically bellow 100 K), this transport mechanism tends to be dominant in amorphous silicon materials. Another transport mechanism, that could take place in amorphous or microcrystalline silicon at low temperatures [Carius *et al.* 1999, Godet 2000], is based on hopping or tunnelling of the carriers between states, introduced by Scher and Montroll [Scher and Montroll 1975]. At low temperatures the carriers do not reach extended states and electrical transport occurs via localized states near a so-called "transport level" E_t. In the case of hopping transport, the activated Arrhenius behaviour is replaced by a power law relationship between the logarithm of conductivity and temperature. The hopping conductivity can be stated as [Godet 2002]

$$\sigma = \sigma_{0h} \exp[-(T_0/T)^{1/4}] \qquad (3.18)$$

where σ_{0h} and T_0 are material dependent constants.

3.3 Model of Tiedje, Rose, Orenstein and Kastner (TROK)

A model explaining main features of dispersive transport was separately introduced by Tiedje and Rose and Orenstein, Kastner and Vaninov and is usually referred to as the "TROK" model [Tiedje and Rose 1980, Orenstein, Kastner and Vaninov 1982]. The model assumes multiple trapping transport mechanism and an exponential density of states. The model considers a pulsed carrier density being rapidly trapped by localized states, so the trapped electron distribution reflects the density of states. The approach in this model is to define the demarcation energy that varies with time of experiment and separates the carriers into two groups:

(i) carriers in thermal equilibrium with extended states
(ii) carriers too deep to have been released within the measurement time

The energy level separating these two groups is known as the *thermalization energy* E_c- E_{th}.

The demarcation energy E_{th} separating these two groups is given by [Orenstein *et al.* 1982]:

$$e_n(E_{th})\, t = 1 \qquad (3.19)$$

where e_n (E) is the release rate from states of energy E, that means that at energy E_{th} traps have on average released carriers only once at time t. Recall that e_n is given by equation 3.10, thus

$$E_{th} = kT \ln(\nu t) \qquad (3.20)$$

The same concept was proposed by Arkhipov and Rudenko [Arkhipov and Rudenko 1978]. Electrons in traps which are shallower than E_{th} are excited to the mobility edge and trapped many times, but electrons in states deeper than E_{th}

have very low probability of release within the time t. Thus the states deeper than E_{th} are occupied in proportion to the density of states, that decrease exponentially, on the other hand the states above E_{th} had time to equilibrate. Thus the electron distribution (so-called "charge packet") has a peak at E_{th}. As time progresses, the thermalisation energy will move deeper into the gap. A diagram showing electron thermalization is given in figure 3.8.

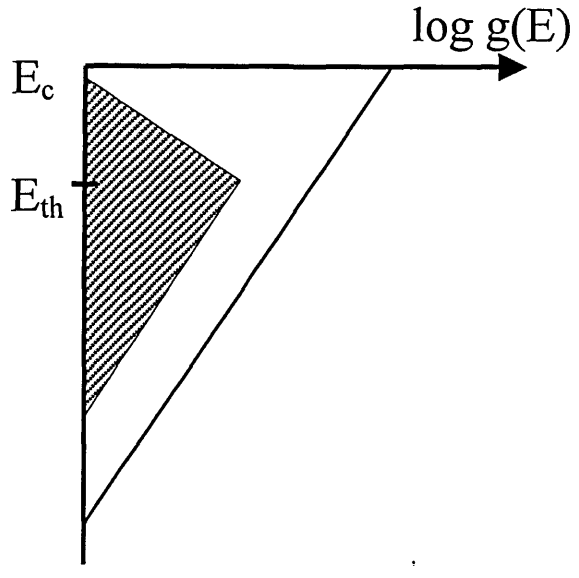

Figure 3.8. Electron thermalisation in an exponential conduction band tail.

3.4 Application of TROK to an exponential DOS

An analytical form can be derived from the TROK model for the transient free carrier density dependence on time δn(t) for a charge packet thermilizing in an exponential tail. Once initial trapping of the transient density of carriers has occurred, we can write by consideration of the transient occupation function:

$$\delta N_t \approx \delta f_d \left\{ \int_{E_c - E_{th}}^{E_c} g(E) \exp\left(-\frac{E_c - E}{kT} \right) dE + \int_{E_V}^{E_c - E_{th}} g(E)\, dE \right\} \qquad (3.21)$$

where δN_t is the total transient trapped density, δf_d is the transient occupation of the deep states, and g(E) is given by equation (3.15). δN_t is approximately equal

to the initial pulse generation of free charge density. The transient occupancy of free states is related to that at by

$$\delta n / \delta N_C = \delta f_d \exp\left(-\frac{E_{th}}{kT}\right) \tag{3.22}$$

Combining equations (3.21) and (3.22) to eliminate δf_d and substituting for g(E) and E_{th} gives

$$\delta n = \delta N_t \, \alpha(1-\alpha)(\nu t)^{(1-\alpha)} \tag{3.23}$$

where $\alpha = T/Tc$. Thus the model predicts a power law decay of index $-(1-\alpha)$, that is frequently observed in amorphous semiconductors.

Equation 3.21 can be re-written in an approximate form if it is assumed that the majority of charge is close to E_c-E_{th}:

$$\delta N_t \approx kT\delta f_d g(E_c - E_{th}) \tag{3.24}$$

Eliminating δf_d with equation 3.22 and substituting for E_{th} we can get

$$g(E_C - E_{th}) = \frac{\delta N_t \, N_C}{\nu \, kT \, \delta n} \tag{3.25}$$

Thus from a TPC data point ($\delta I(t)$,t) a DOS point {$g(E)\,(\delta I(t)t)^{-1}$, E_c-E=$kT\ln(\nu t)$} can be obtained for the specific case of an exponential DOS.

3.5 Fourier transform method

The TROK model shows in a simple way the relation between the transient photocurrent decay I(t) and the density of states at the thermalisation energy $g(E_{th})$ for an exponential density of states distribution. In this case the peak of carrier density is at the thermalisation energy at all times during the decay.

However, if the charge packet is not located at the thermalisation energy at all times, equation 3.25 gives an incorrect g(E). This would happen, for example, if the density of states consists of an exponential with a bump of states at a deep energy, which is frequently observed for amorphous silicon. In this case, at a certain time the peak in the carrier density will shift from E_{th} in the exponential, to the bump in the density of states. The thermalisation energy will thus shallower than the peak in the carrier density, *i.e.* states in the bump would control the current, not the states at E_{th}. Thus in general, if the density of states has more complicated structure than exponential, the TROK method of extracting the density of states from photoconductivity data would give an incorrect density of states. Marshall and Main [Marshall and Main 1983] demonstrated that this would be the case in the density of states consisting of three discrete levels. Using the above method Marshall and Main calculated the density of states from a simulated current decay: the reconstructed density of states gave incorrect values for the density of levels and placed them at the wrong energies.

The analyses based on the TROK model attempts to calculate a g(E) point from a single I(t) point. The realisation that the TROK model will not give reliable results led to development of so-called "multi time-point" methods for extraction of the density of states from photoconductivity decays.

A method which is based on Fourier transformation, can take into account I(t) data over a range of times and is able to deal with structured density of states. Such method has been developed by the group at the University of Abertay Dundee [Main *et al.* 1992]. The method combines the features of transient photoconductivity and modulated photoconductivity (MPC) experiments. The MPC experiment is equivalent to a TPC experiment in the frequency domain. The advantage of MPC in the current context is that within certain approximations, a *single* MPC data point (I_ω, Φ_ω, ω) does give a correct DOS point [Brüggemann *et al.* 1990]. In the MPC experiment the specimen, which may be in coplanar or sandwich configuration, is illuminated with light of an appropriate wavelength, the intensity of which is modulated with a sine wave. The generation rate thus can be represented as a steady state term G_{ss} and an altering component of angular frequency ω and amplitude G_ω (see figure 3.9).

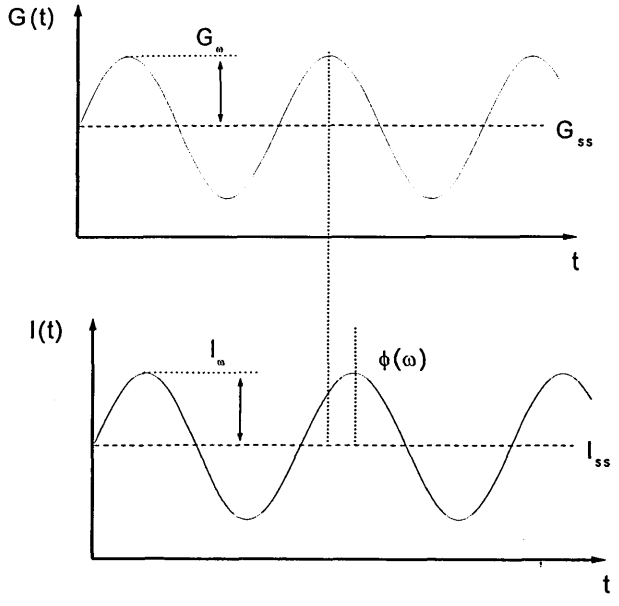

Figure 3.9. Generation rate and resulting photocurrent in the MPC experiment.

The response to sinusoidal excitation is a sinusoidal photocurrent which is phase shifted by a frequency dependent angle $\Phi_\omega(\omega)$ with respect to the generation and has a complex amplitude $I_\omega(\omega)$ which is also a function of frequency. A detailed analysis of the solution to the multiple trapping equations in the frequency domain may be found in the papers by Oheda and Brüggemann *et al.* [Oheda 1981, Brüggemann *et al.* 1990]. With some approximations the equation for determining the density of states from the experimental data is:

$$g(E_\omega)= 2(\pi kTC_n)^{-1} \{ G_\omega e\mu EA \sin\Phi / I_\omega - \omega\} \qquad (3.26)$$

where A is a conduction cross-section, μ is the free carrier mobility and Φ is the phase shift [Brüggemann *et al.* 1990]. The analysis leads to a similar to TROK expression in the frequency domain:

$$E_\omega = kT \ln(\nu/\omega) \qquad (3.27)$$

However, the definition for E_ω is obtained without making any assumptions about the shape of the density of states.

The procedure developed by Main *et al.* [Main *et al.* 1992] uses the Fourier transformation method to convert time domain TPC I(t) data into frequency domain $I(\omega)$, $\Phi(\omega)$ data. The density of states can then be obtained from an MPC analysis of the data. The strengths of the method have been well tested using computer simulated and experimental data [Main *et al.* 1993, Webb 1994, Main 1997, Main 2002] and found to be accurate and applicable to amorphous semiconductors.

3.6 Post-transit spectroscopy

The photocurrent in the post-transit regime is controlled by thermal emission of carriers that have been trapped in states deeper than the value of E_{th} at the transit time. Under these conditions it can thus be assumed that re-trapping of the carriers other then at shallow energies does not take place. The equation for the energy distribution is given by [Seynhaeve *et al.* 1989]:

$$N(E_{th})=C' I(t)t \tag{3.28}$$

where $C'=2N(E_c)/(eN_0\nu t_{tr})$ and t_{tr} is the free carrier transit time. In practice, some of the parameters in equation (3.28) may not be known. However, providing that ν does not vary significantly with trap depth [Marshall 2000] this only influences the absolute value of the localized state concentration and does not affect its shape as a function of energy.

Summary

Photoconductivity techniques used to study the electronic properties of silicon thin films have been reviewed. These include steady-state and transient photoconductivity, the TROK model used in the case of a simple exponential DOS, the more general method of Fourier transformation of current-time data, and finally, post-transit analysis of time-of-flight data.

Chapter 4. Experimental methods

This chapter describes materials and characterisation techniques used in this work. Firstly, the details of material preparation and configuration of samples are presented. This is followed by details of the experimental set-ups and characterisation techniques used.

4.1 Materials and sample preparation

The materials studied in the present work are microcrystalline silicon structures of various compositions. Deposition of the materials was carried out by technical staff at the Institute for Photovoltaics, Forschungszentrum Jülich GmbH (Germany). The materials studied were prepared by two techniques: plasma enhanced chemical vapour deposition (PECVD) and hot wire chemical vapour deposition (HWCVD). These techniques are described in outline in the chapter 1 and references therein.

PECVD microcrystalline silicon films were deposited on borosilicate glass substrates in a UHV system operating at 95 MHz, with total gas pressure of 0.3 torr and RF power of 5 W. Because microcrystalline silicon is sensitive to residual gas impurities, the deposition system was pumped to a base pressure of less than 10^{-9} torr. The temperature of the substrate was held at 185°C or 200°C. Variations of the microstructure were obtained by changing the silane/ hydrogen gas ratio. To deposit doped layers, phosphine gas (PH_3) and diborane gas (B_2H_4) were added to the process gas to create n-type and p-type materials respectively.

The i-layer of *pin* photovoltaic structures was deposited by HW CVD technique with a filament temperature of 1650 °C and substrate temperature below 220 °C, while p- and n-layers were prepared using UHV PECVD.

The crystalline volume fractions (CVF) were calculated from Raman intensity ratio at the IPV Juelich. Variations of the microstructure were obtained by changing the silane/hydrogen gas ratio.

4.2 Sample configuration

In the present work samples with 2 types of electrode configuration have been studied: coplanar gap cell and *pin* sandwich. The cross sections of the structures used are shown in Fig 4.1. Sandwich structures were deposited in the sequence glass substrate/TCO/*pin*/TCO/1 mm^2 silver dot contact. In this configuration (Fig 4.1 a) an electric field is applied during measurement in the direction of material growth. The thickness of intrinsic layer of sandwich samples was 1 and 1.6 μm.

In the case of coplanar (Fig 4.1 b) structures the field is applied parallel to the substrate. The thickness of coplanar structures was less 1 μm. A series of films was produced by varying gas ratio between 3.0% and 7%. For the coplanar structures the contacts were usually made from silver. The contact length is 1 cm separated by 0.05 cm gap.

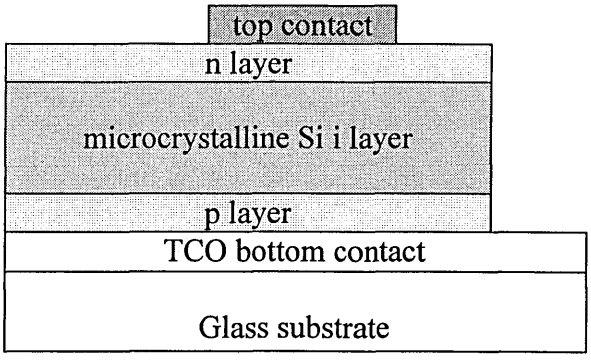

Figure 4.1 a. Cross section of the *pin* structure used in the study.

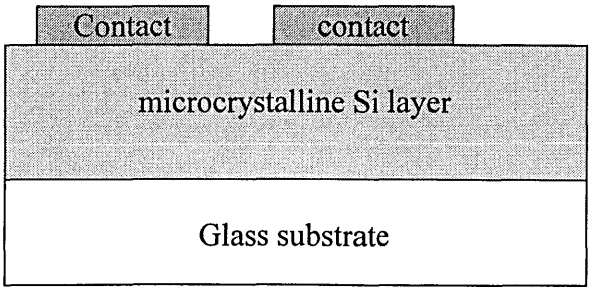

Figure 4.1 b. Cross section of coplanar structures used in the study.

The Ohmic nature of the contacts was checked by performing current-voltage measurements, which were found to be linear over the range of fields examined, indicating that the applied voltage appeared across the bulk film. Connections to the external circuit were made using thin aluminium wires and silver conductive paint.

The details of the samples used in the present study are presented in Table 4.1

Table 4.1. Sample details.

Coplanar microcrystalline silicon films

Sample	T_s(°C)	SC (%)	CVF	d (μm)	Doping (ppm)
00c341	185	3.7	0.72	0.55	-
00c345	185	6.3	0.50	0.80	-
00c348	185	4.3	0.65	0.60	-
00c354	185	3.0	0.70	0.41	-
00c385	185	5.6	0.60	0.73	-
02b299	200	3.0	0.7 – 0.8	0.34	-
02b306	200	3.0	0.7 – 0.8	0.34	5 B_2H_6
02b307	200	3.0	0.7 – 0.8	0.42	10 B_2H_6
02c452	200	7.0	0.48	0.31	-
03b173	200	5.0	-	0.09	-
03b170	200	5.0	-	0.26	-
03b189	200	3.0	-	0.083	-
03b188	200	3.0	-	0.320	-

Microcrystalline silicon *pin* photovoltaic structures

Sample	T_s/T_f(°C)	SC (%)	CVF	d (μm)
02C049	220 / 1650	7.0	0.32	1
01C218	185 / 1650	5.6	0.37	1.6
02C078	220 / 1650	6.0	0.4	1
02C083	220 / 1650	4.0	0.6	1

4.3 Sample delivery and storage

A large part of the present study was focused on the investigation of the influence of atmospheric effects on material properties. Because such experiments are time and ambience sensitive, a series of samples was delivered in sealed 'bubble pack', filled with an inert gas. The samples were packed in such containers in Juelich immediately after deposition and contact evaporation to minimise unmonitored material changes due to atmospheric processes. Opening the container initiated material changes, so in our laboratory the samples were stored sealed and unopened unless they were being measured.

4.4 Sample measurement chamber and sample holder

The simplified diagrams of the measurement chamber and sample holder are presented in figures 4.2a and 4.2b.

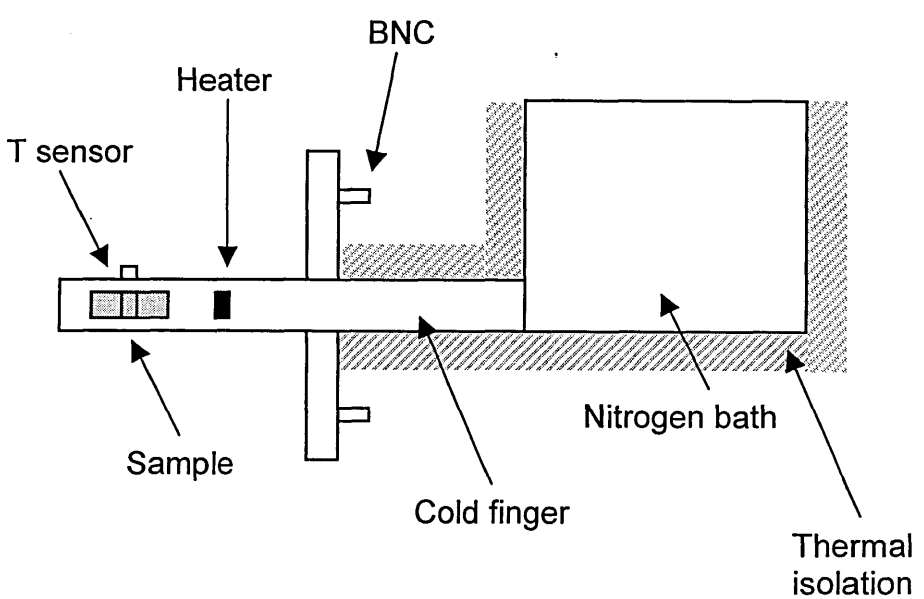

Figure 4.2a. Simplified diagram of the sample holder used in this work.

The experimental setup enabled measurements to be made at different temperatures under vacuum. Most experiments were performed in a vacuum chamber at a pressure of about 10^{-3} torr. For the majority of the experiments on atmospheric degradation the vacuum was not used since it can modify the effect of atmosphere. All annealings were performed under vacuum.

The sample was held vertically on a stage by means of silicone grease. Connections to the external circuit were made using BNC connectors and co-axial cable. The sample stage was connected to a cold finger, and cooled by a liquid nitrogen bath. Heating was applied by means of 2 heaters placed on the sample stage. The temperature sensor was placed in a small hole drilled in the sample stage close to the sample. The temperature was controlled by means of Oxford ITC601 intelligent temperature controller, which allowed temperature changes from about 100K to 480K. The sample was illuminated via a port on one side of the vacuum chamber either through a quartz window or a light pipe.

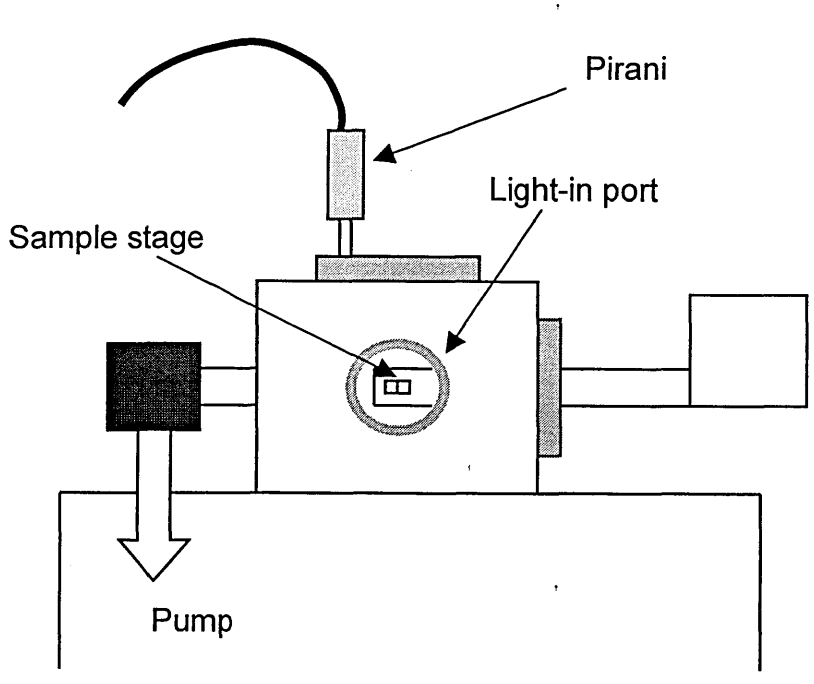

Figure 4.2b. Diagram of the vacuum chamber used in this work.

4.5 Light soaking procedure

For light soaking experiments a light source of AM1 simulated radiation was used. The solar simulator consists of General Electric 250W halogen lamp connected with a cooler. Light soaking was performed in measurement chamber under vacuum of about 10^{-3} torr. This allowed fluctuations of the sample temperature to be minimized and on reduced the effect of atmospheric gases on

photoconductivity data recorded during experiment. Light soaking was carried out at two temperatures: room temperature and 50 °C.

4.6 Annealing procedure

The diagram of setup used for temperature annealing measurements is shown in figure 4.3.

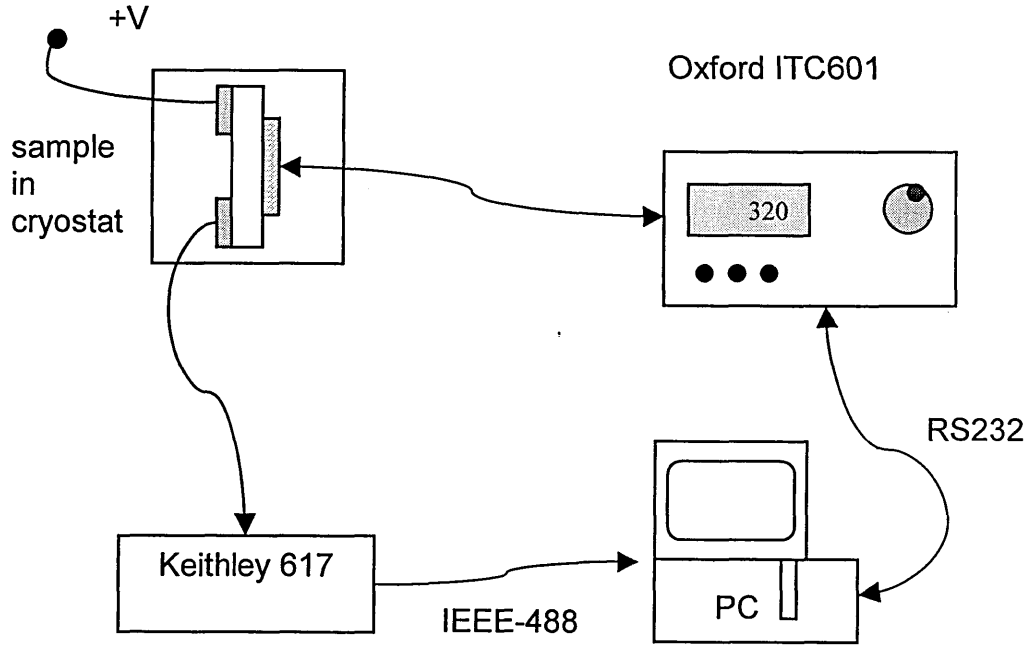

Figure 4.3. Experimental setup used for temperature annealing.

A Brandenburg model '477' high voltage power supply was used as a voltage source. The measurements were performed at 300 V bias. The setup was partially computer controlled via an IEEE-488 interface to a Keithley 617 Multimeter, and a RS 232 line that links a computer and an Oxford ITC601 temperature controller. The measurement procedure was controlled by software written by the author in the programming language TestPoint® version 3.0 for Windows.

A significant part of the present work was dedicated to a study of the effects of atmosphere, thus it was important to get an accurate picture of material behavior during high temperature treatments. During a measurement cycle the

temperature controller was programmed to enable various heating (and cooling) rates to be set as required, the time intervals between each reading could also be selected. The typical heating rate was 5K/min with 10 seconds time interval between each reading, providing around 360 data points for each annealing cycle. In some cases the time interval between readings was decreased to 2 sec to investigate some specific features. The set-up could be configured for steady state and transient photoconductivity measurements (described below) without breaking vacuum.

4.7 Steady state photoconductivity measurements

Steady state photoconductivity measurements (except CPM) were performed using a Ledtronics LED, emission peak 620 nm. The LED output was directed onto a sample through a quartz light pipe (length 125 mm and diameter 7 mm). The end of the light pipe was positioned about 10 mm above the sample gap. A Thurlby PL320 power supply was used to drive the LED, and a Keithley 175 Autoranging Multimeter was used to determine the LED current. The circuit for the steady state measurements is shown in figure 4.4.

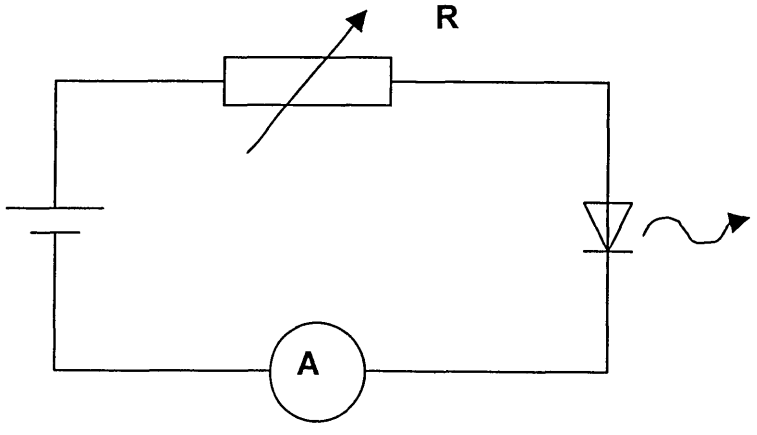

Figure 4.4. LED drive circuit for steady state illumination.

The LED output was measured with a BPX-65 *pin* photodiode that was calibrated for sensitivity vs. wavelength [Merazga 1990]. Thus it was possible to obtain a

calibration graph of photon flux vs. LED current by measuring the photodiode current and using a photodiode sensitivity reading to convert from photodiode current to incident flux.

When calibrating the LED the light pipe was kept at a similar distance from the photodiode as from a studied sample (z-axis). The photodiode current (measured with the Keithley 175) was then maximised at this distance by adjusting the LED in the x-y plane. Figure 4.5 shows the calibration graph for the LED used in the present work.

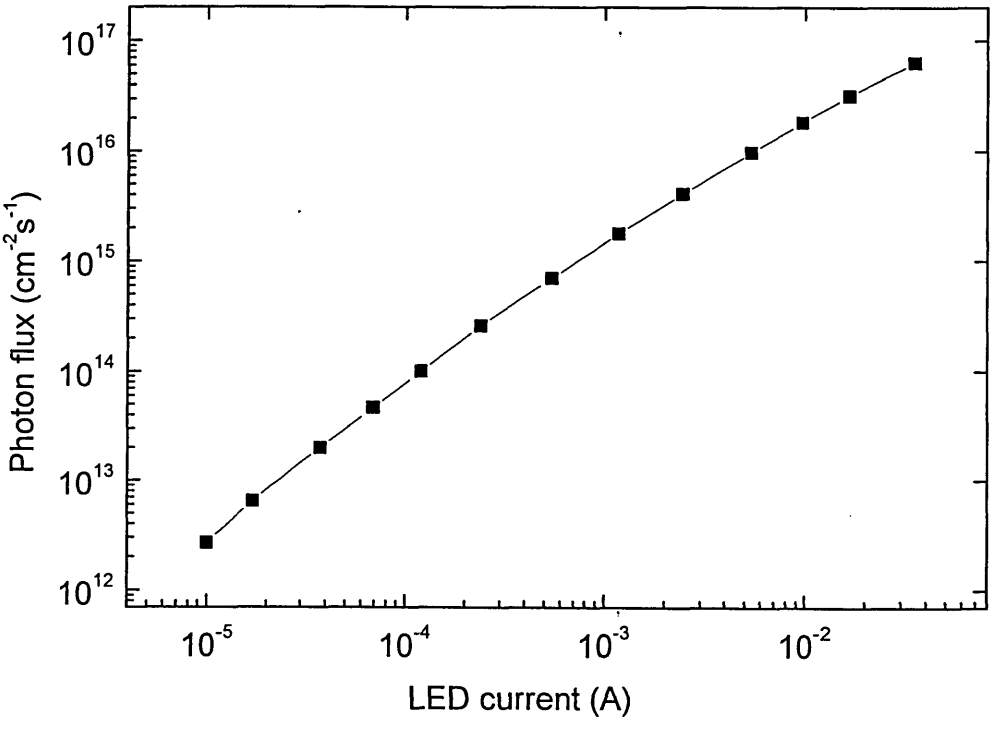

Figure 4.5. Calibration curve for Ledtronics red LED, λ = 620 nm.

4.8 Constant Photocurrent Method (CPM)

A number of samples has been characterised using Constant Photocurrent Method (CPM), that has already been mentioned in the chapter 1. A schematic diagram of the experimental setup for the CPM technique is shown in figure 4.6. The monochromatic light source consists of a 75 W halogen lamp connected to a software controlled power supply from 'Thurlby Thunder' model 'TSX 3510P' and a software controlled double monochromator from 'Jobin-Yvon' model 'SPEX DH10' with two 600 lines per millimetre mirror-gratings covering the wavelength range from 400 nm (3.1 eV) up to 1600 nm (0.775 eV).

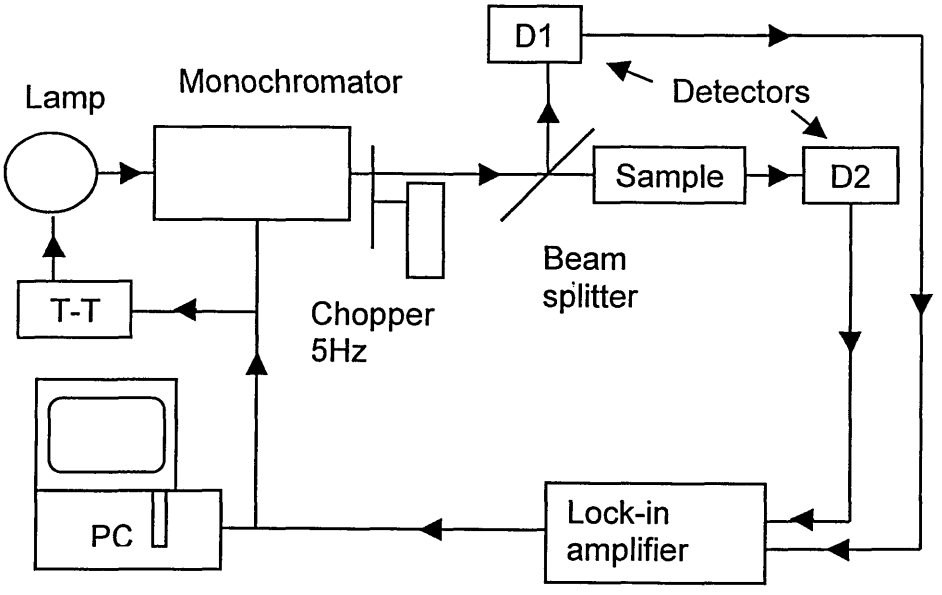

Figure 4.6. CPM experimental set-up.

To minimize 2nd and higher orders and scattered light, edge filters were used in a filter wheel placed at the exit of the monochromator. The edge filters were moved into the beam at following wavelength positions: 540 nm (RG490), 750 nm (RG750), 850 nm (RG850) and 1350 nm (RG1000). From 400 nm to 540 nm no edge filter was required.

The CPM setup was operated in AC mode, in which case a 'Scitec B640' chopper wheel was placed immediately after the monochromator running at a frequency of 5 Hz. A biconvex lens with 25 mm focal length was used to focus the probe beam onto the sample. A quartz slide beam splitter was placed between the lens and the sample to redirect a small part of the probe beam towards the detector measuring the magnitude of the incident flux. The detector for the photon flux consists of a 'Hamamatsu' two-colour SiGe detector and a 'Stanford Research' lock in amplifier model 'SR530'. In the case of transmission CPM (also referred to as absolute CPM) measurements a second SiGe detector was placed behind the sample, which measures the transmitted photon flux through the sample. This detector connects to the SR530 lock in amplifier too. A Brandenburg model '477' high voltage power supply was used to apply a bias voltage to the sample. The sample photocurrent was measured by a digital DSP lock in amplifier model 'EG&G 7260' also remote controlled by software. The setup was calibrated using a pyroelectric detector from 'Scitec' - model 'P2613M-06' with built-in pre-amplifier. The response of a pyroelectric detector is sensitive to the incident radiation power and not the number of absorbed photons. This enables calibration of a spectrally dependent detector like the SiGe detectors to measure the true photon flux $\Phi(E_{ph})$ of the probe beam at all wavelengths.

4.9 Transient Photoconductivity (TPC) and Time-of-Flight (TOF) experiments

Figure 4.7 presents a simplified diagram of the partially automated system used for transient photoconductivity measurements. A nitrogen pumped dye laser (Laser Science VSL337) is used to generate the pulse of photocarriers. The laser battery powered and enclosed in a Faraday cage to minimize interference. The system is partially computer controlled vie an IEEE-488 line that is connected to a digital storage oscilloscope (Tektronix TDS3052), and a RS 232 line that is used to trigger a pulse generator. The laser is triggered via an optical fiber and the oscilloscope trigger is initiated by a second optical fiber which samples the output of the laser. In this way the entire laser system is optically isolated and electrically screened, minimizing any electromagnetic coupling.

The sample signal is pre-amplified with a current to voltage amplifier and then displayed on the oscilloscope. The obtained data set is then passed to the computer for processing and storage. For a particular decay time range an appropriate feedback resistor is chosen for the amplifier and an appropriate time base and voltage range on the oscilloscope should be set manually. Several decays are averaged by the oscilloscope to minimise the effect of noise. The programme can overlap measurements at different time ranges to create a composite decay over many orders of time. The typical time range of resulting decay is from 10^{-9} to 1s.

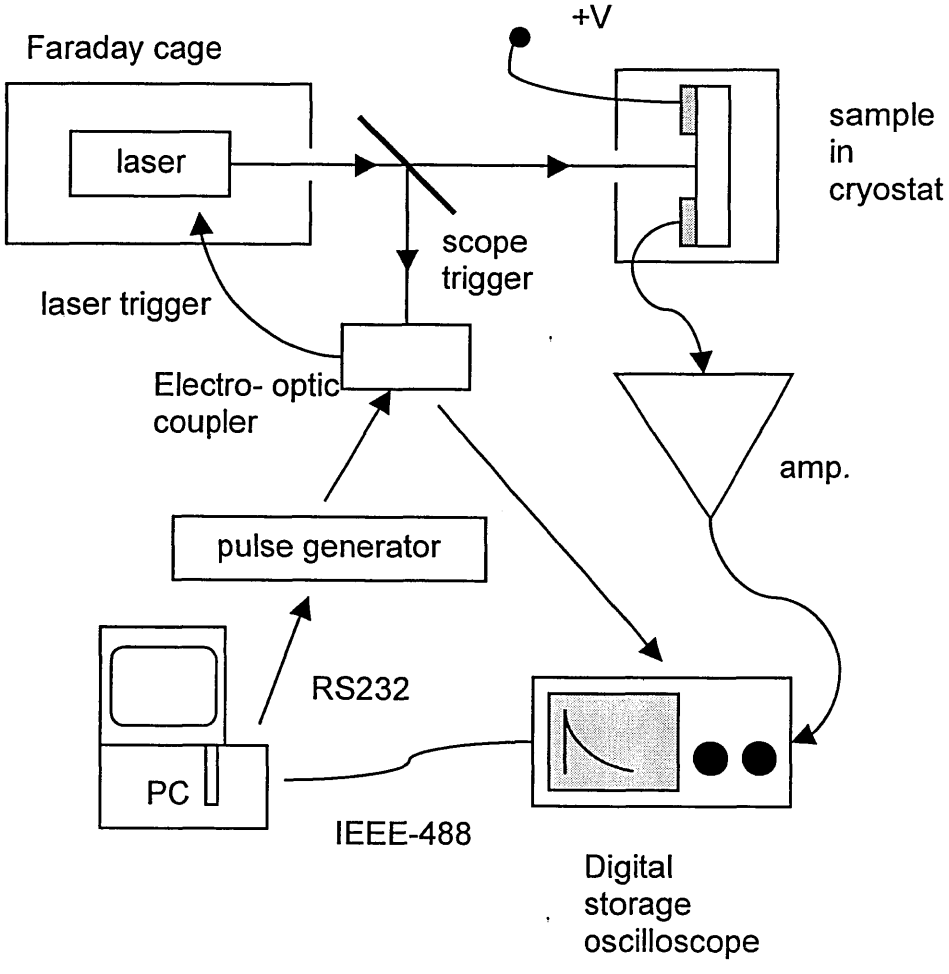

Figure 4.7. Schematic diagram of TPC experimental setup.

4.9.1 Dye laser

A nitrogen pumped dye laser (Laser Science inc VSL 337) was used as a light source in both TPC and TOF experiments. For transient photoconductivity measurements, the red dye used with the laser was Rhodamin 101 that gives an emission peak at 655 nm (1.9 eV). For Time-of-Flight experiments strongly absorbed light produced by Coumarin dye was used, with emission peak at approximately 500 nm (2.49 eV). The intensity of the laser beam can be attenuated by means of neutral density filters placed in the light path. The laser output from a single unattenuated pulse was equal to 2.1×10^{14} cm^{-2} [Webb 1994].

4.9.2 Pre-amplifier

The sample photocurrent response is a signal of low level that requires amplification. The sample response signal introducers a difficulty for amplification because the current may be large at short times, but very small at longer times. In this case the required amplifier should have a varying gain and bandwidth over a large range. At short times only a small gain and fast response are required, while at longer times the amplifier should provide a high gain, however the amplifier should not be overloaded.

The preamplifier system used for TPC measurements is based on a Burr-Brown OPA637 DIFET amplifier. The configuration of the current to voltage amplifier is shown in figure 4.8. The circuit acts so that the output voltage V_{out} is given by $V_{out} = -I_{in}R_f$ where I_{in} is the current through the sample. The limiting bandwidth of the circuit is $1/R_fC_f$, where C_f is a capacitance associated with the R_f and the circuit layout. The circuit allows variable current gain to be used by changing plug-in resistors. An adjustable offset current in the range 10^{-11} to 10^{-5} A can be combined with the incoming signal. The offset was used in cases when the dark current is substantially larger than the photocurrent recorded in a transient photoconductivity measurements, particularly at longer times. For sufficiently large magnitude of the signal at short times (<100 ns) a 50Ω sampling resistor was used to detect the current instead of the current amplifier.

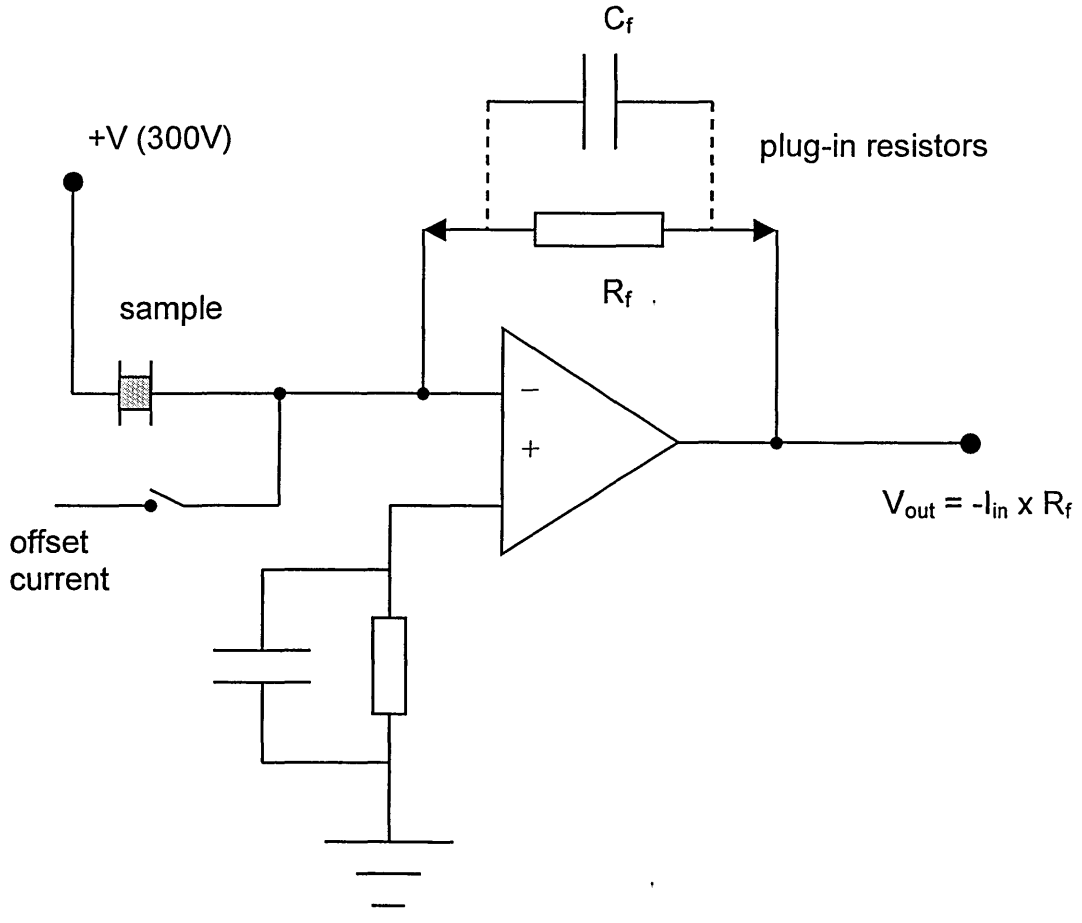

Figure 4.8. Current-to-voltage pre-amplifier. The output voltage $V_{out} = -I_{in}R_f$ where I_{in} is the current through the sample.

The response speed of the amplifier for various feedback resistors R_f is shown in figure 4.9. It can be seen that an increase in the amplifier gain increases the amplifier response time.

4.9.3. Signal capture and processing

For each sampling resistor used in the pre-amplifier, the oscilloscope voltage sensitivity and time base should be set manually to obtain an appropriate signal. After each laser pulse the oscilloscope captures both the signal from the sample and the signal from an electro-optic coupler that is used as the oscilloscope trigger. Both channels of data are then averaged the number of

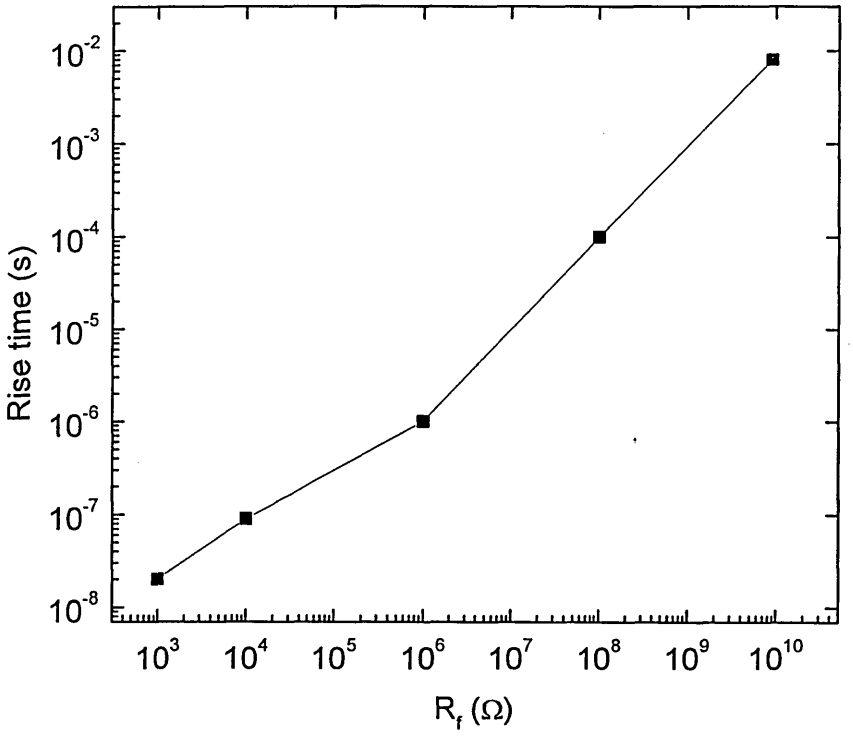

Figure 4.9. Measured rise time of the pre-amplifier vs. feedback resistor value R_f. [Shepherd 1998]

times, specified by the user. When a suitable number of decays have been averaged, the computer interrogates the oscilloscope to determine the voltage sensitivity and the time base, and calculates the current and sample time. The user supplies the value of the sampling resistor used in the pre-amplifier. The transient part of the signal is calculated by subtracting the steady state part, which is determined from 150 of the 200 samples recorded before the laser trigger is received. The program requires the user to determine the start of the transient decay and then reduces the number of data points (typically to 62) for plotting logarithmically by variable bandwidth digital filtering. The technique consists of replacing the data points in the time interval t-Δt to t+ Δt, where $\Delta t \propto t$, by a single data point at t with a current which is the average of the replaced data.

For the samples used in the present work the transient response can be measured from 5ns to 10s. Normally around 30 decays are averaged for each

time range setting. When the multiple pulses are used, care should be taken to allow material to relax in between each measurement, thus at longer times the pulse rate was reduced.

4.10 Experimental difficulties

During the experimental work it was discovered that materials are very sensitive to the effects of atmosphere that complicates the study and correct comparison of samples. Thus the first section of experiments aimed to investigate the properties of materials of different compositions has been carried out after annealing and under vacuum. The second section is focused on investigation of ageing effects. Due to variations in the extent of ageing and the time-scale of experiments, it was difficult to organize work on several samples at the same time. Difficulties also arise from the speed of effect. For some samples the speed of ageing effect could be comparable with the time required for measuring the sample. For example, during TPC measurements, that takes around 1 hour, the sample properties could be significantly changed. This results in lack of overlapping of decays at various time intervals, or DC offsets that are impossible to control due to the rapid changes in dark current.

Chapter 5. Transport properties of microcrystalline silicon

In this chapter the experimental results obtained on microcrystalline silicon films and photovoltaic structures are presented. First section of the chapter is focused on the studies of transport properties of coplanar microcrystalline silicon films of varying crystallinity by means of dark and steady state photoconductivity measurements. The results of transient photoconductivity measurements are presented in the second section. The information on the density of localised states (DOS) in the upper portion of the band gap obtained from transient photocurrents is correlated with steady state results and material morphology. The third section is dedicated to the investigation of defect distribution in the *pin* photovoltaic structures by means of post transit time-of-flight spectroscopy. The results obtained from coplanar and photovoltaic structures are compared and correlated with microstructural differences in the samples of coplanar and sandwich configurations.

5.1 Dark and steady state photoconductivity

Silane concentration is a convenient parameter to vary in order to achieve materials with different microstructure. There is a good agreement between variations in silane concentration during deposition process and material morphology, particularly crystalline and amorphous volume fractions of obtained materials [Vetterl *et al.* 2000, Shah *et al.* 2003]. Although crystalline volume fraction (CVF) could possibly be considered as more convenient variable to describe variations in material crystallinity, as was pointed out previously (see chapter 1) the detailed interpretation of material crystallinity remains under discussion [Houben *et al.* 1998, Ossadnik *et al.* 1999]. In this thesis SC will be used to identify the samples, in conjunction with Raman crystallinity data where these are available.

5.1.1 Dark conductivity

The results of dark conductivity measurements obtained for the series of microcrystalline silicon films are presented in figure 5.1.

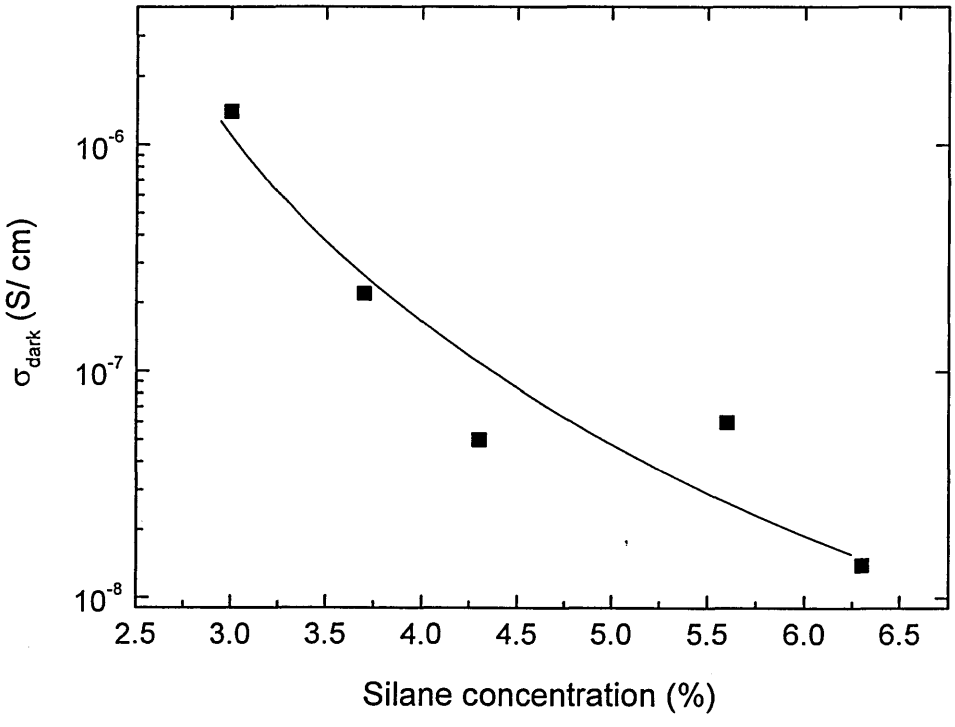

Figure 5.1. Dark conductivity of microcrystalline silicon films vs. silane concentration. The line is to guide the eye.

The general trend shows that the dark conductivity decreases with increasing silane concentration. For the samples deposited at silane concentration between 3% and 6.3% the conductivity decreases by more than two orders of magnitude. For the 'transitional' microcrystalline silicon film deposited at 6.3% silane concentration, where the amorphous fraction is 50% (see chapter 4, table 1) dark conductivity is about 3~4 orders of magnitude higher in compare with dark conductivity value of annealed high quality amorphous silicon material. A slightly high dark conductivity value, measured for the film with SC = 5.6% could possibly be related to the presence of adsorbed water, that can increase the conductivity (see chapter 6) or due to variation in microstructure that can take place with film thickness (see chapters 1 and 7).

The variations in activation energies for the series of films are presented in figure 5.2. The activation energies were calculated from the slope of Arrhenius plot and measured in the temperature region between 290K and 380K.

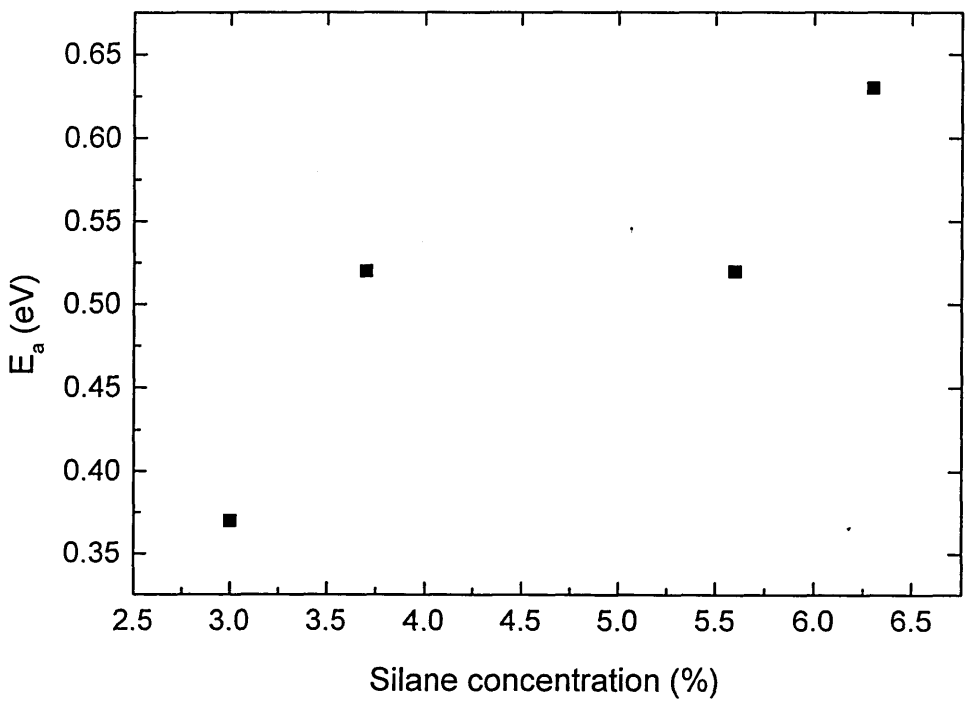

Figure 5.2. Dark conductivity activation energy of microcrystalline silicon films vs. silane concentration.

It should be noted that the data of SC = 4.3% film is not included in activation energy graph because large conductivity fluctuations upon annealing of the film have been observed. Although a reason that such unexpected behaviour may be related to a quality of the particular film could not excluded, it was the first time a possible influence of atmospheric components was suspected. The reports on the effects of atmospheric gases adsorption in amorphous silicon materials go back to early 1980s. [Solomon 1980, Tanielian *et al.* 1980, Tanielian 1982] have demonstrated that in amorphous silicon films coplanar dark conductivity can be changed up to 3 orders of magnitude due to band bending effects induced by gas adsorption on the films (see also chapter 2 of the present thesis for detailed review). An observation of this effect in the recently deposited microcrystalline

silicon films led us to explore this phenomenon in detail, because our purpose was to investigate transport properties of these film and it is important to understand to what extent the adsorption process can influence transport properties. Thus a significant part of experimental results is dedicated to the study of the effects of atmosphere on the properties of microcrystalline silicon materials. These results are presented in chapters 6,7 and 8.

The observed changes of the dark conductivity could be linked to the changes in the material microstructure and Fermi level position, which are known to take place with variations of silane concentration [Finger *et al.* 1998, Baia Neto *et al.* 2002]. As was pointed out in chapter 1, a physical model explaining variations of dark conductivity with silane concentration does not exist up to now. Changes in dark conductivity activation energies could arise from the changes in the mobility gap and/or shift in the Fermi level position. However, no increase in the mobility gap was observed if silane concentration varies between 2% and 6% [Vetterl *et al.* 2000]. The reasons for the shift in the Fermi level position are still under discussion. One of the possible explanations is related to the unintentional doping [Finger *et al.* 1998, Wyrsch *et al.* 2000, Baia Neto *et al.* 2002], for example oxygen, that could behave as n-type dopant. The efficiency of such doping could be more pronounced in the case of highly crystalline growth, because the deposition rate noticeably decreases with decrease of silane concentration [Finger *et al.* 1998, Vetterl *et al.* 2000]. In this case, a low deposition rate will result in the greater shift of the Fermi level toward the conduction band, decreasing the activation energy.

The general trend of our observations is in a good agreement with results reported for microcrystalline silicon films obtained at various deposition conditions. Figure 5.3 presents a comparison of our results with literature data. The reference data [Wyrsch *et al.* 2000, Vetterl *et al.* 2000, Ray *et al.* 2002] correspond to microcrystalline silicon films deposited by same technique as samples studied here (UHV PECVD). The general trend shows that dark conductivity decreases with increasing silane concentration ratio. The best agreement is achieved with the data of Jülich group [Vetterl *et al.* 2000], that may be simply connected to the fact that IPV samples are studied in the present work.

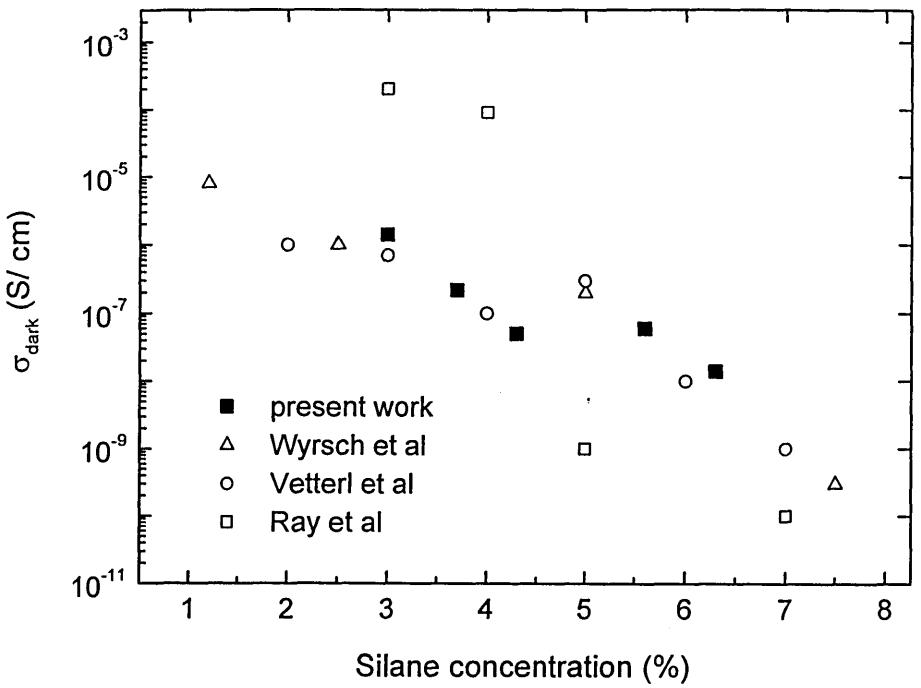

Figure 5.3. Comparison of present results with literature data. The reference data are taken from [Wyrsch *et al.* 2000, Vetterl *et al.* 2000, Ray *et al.* 2002].

5.1.2 Steady state photoconductivity

Figure 5.4 shows the $\mu\tau$ products of the series of microcrystalline silicon films measured at photon flux 10^{14} $cm^{-2}s^{-1}$. Although the point SC=5.6% is exceptional, the general trend indicates that mobility-lifetime product decreases with increasing silane concentration. It was suggested [Brüggemann and Main 1998] that the changes in $\mu\tau$ product in doped microcrystalline silicon films are determined by the shift of the Fermi level position. A shift of the Fermi level will result in changes in thermal occupation of recombination centres in the band gap. For example, if the Fermi level shifts close to the conduction band, most defects will be thermally occupied by electrons and inaccessible for excess electrons. This will increase electron lifetime and lead to rise of $\mu\tau$ product. This suggests that an increase of mobility-lifetime product could be due to increase in lifetime and so be correlated with dark conductivity and the Fermi level position.

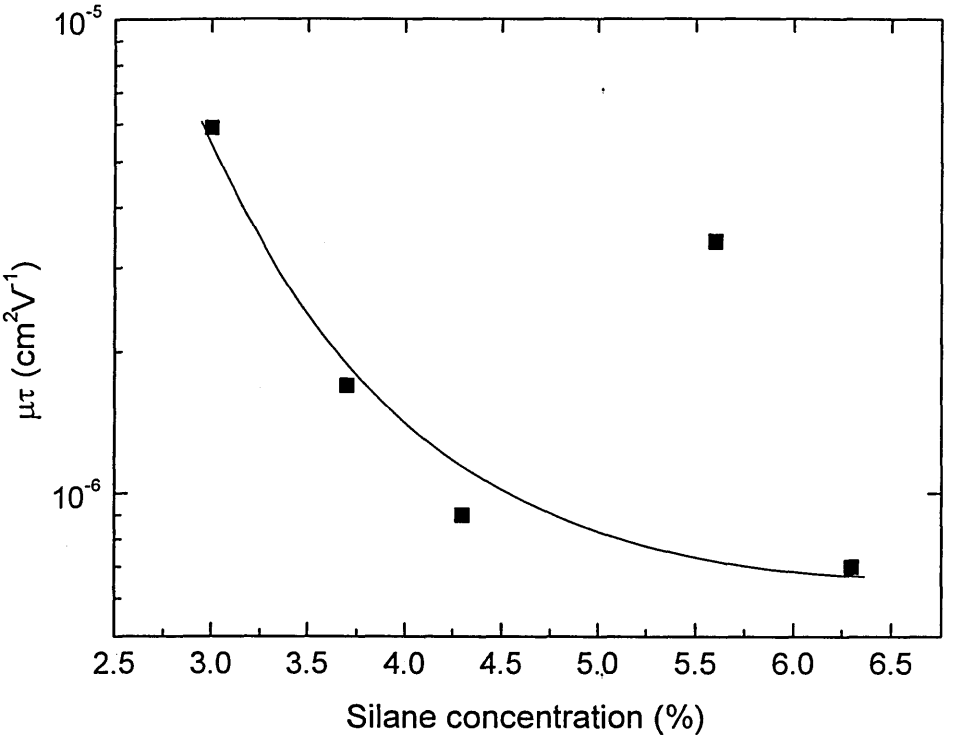

Figure 5.4. Mobility-lifetime product of microcrystalline silicon films vs. silane concentration ($\Phi=10^{14}$ $cm^{-2}s^{-1}$). The line is to show the trend.

Our results demonstrate that the highest value of the mobility lifetime product is obtained for highly crystalline sample, deposited at 3% silane concentration. Although this sample is nominally undoped, it shows the highest dark conductivity value and small activation energy. This suggests that the high $\mu\tau$ product value could be due to the shift of the Fermi level position closer to the conduction band; a correlation between the Fermi level position and the mobility lifetime product has been discussed above.

The similarity between the behaviour of nominally undoped microcrystalline silicon films deposited at various silane concentration ratios and different doping levels in amorphous silicon films is striking. N-type doping of amorphous silicon would lead to the shift of the Fermi level position toward the conduction band, that would be reflected in a decrease of dark current activation energy value and increased dark- and photoconductivity values. Similar behaviour is observed in

microcrystalline silicon on decreasing of silane concentration ratio (increasing crystallinity).

Because of the dependence on the Fermi level position, the mobility lifetime product by itself is not a reliable indicator of the material quality, as was pointed out by Brüggemann and Main [Brüggemann and Main 1998]. For solar cell applications, the material photosensitivity, that takes into account the ratio of photo and dark conductivities, is a parameter, frequently used as an indicator of absorber layer properties [Vetterl *et al.* 2000, Ito *et al.* 2001, Middya *et al.* 2001, Soppe *et al.* 2005]. It is generally believed that high photosensitivity of the absorber layer is an essential property of device quality photovoltaic material, because it indicates low recombination rate of carriers through midgap states and a low σ_{dark} leads to a stronger field in the solar cell, see for example Gordijn [Gordijn 2005]. Photosensitivity of the series of microcrystalline silicon films is presented in figure 5.5.

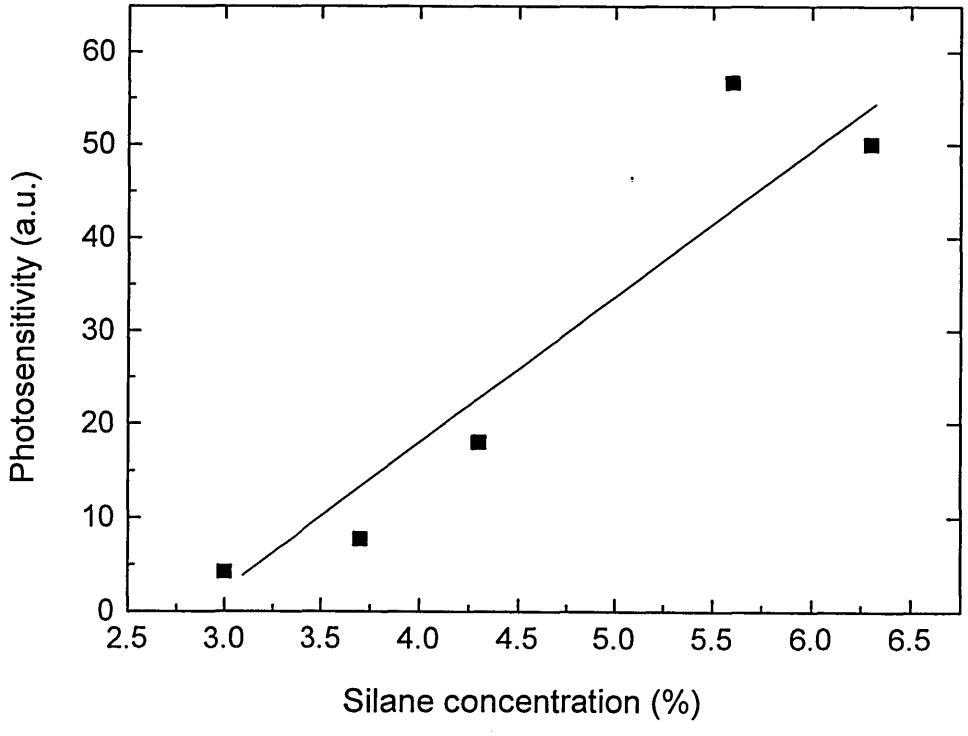

Figure 5.5. Photosensitivity of microcrystalline silicon films vs. silane concentration ($\Phi=10^{14}$ $cm^{-2}s^{-1}$). The line is to guide the eye.

As one can see, photosensitivity increases by one order of magnitude when silane concentration ratio changes from 3% to 6%. Our results suggest that the materials deposited at higher silane concentration could be more beneficial for solar cell applications.

As was described in chapter 1, one of the key properties of thin film material optimised for photovoltaic application is its ability to absorb maximum amount of photons. Figure 5.6 shows the absorption coefficient spectra for microcrystalline silicon films deposited 3% and 6.3% silane concentration, obtained by CPM measurements.

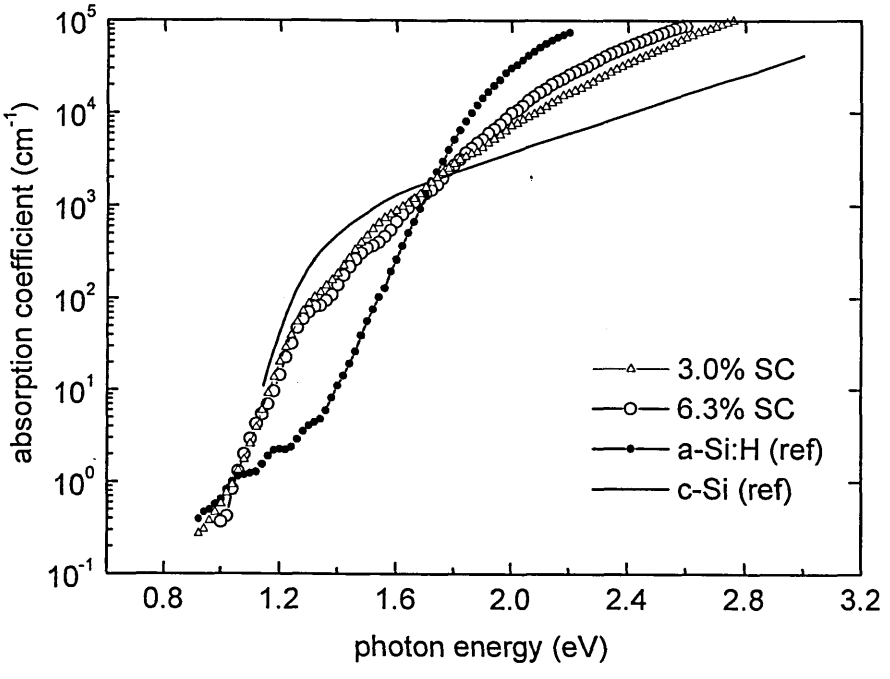

Figure 5.6. Absorption coefficient curves for 3% and 6.3% silane concentration microcrystalline silicon films. Amorphous silicon data taken from [Zrinscak *et al.* 2001], crystalline silicon data from [Hulthen 1975].

To enable comparison, the figure includes data of amorphous and crystalline silicon taken from literature [Zrinscak *et al.* 2001, Hulthen 1975]. For energies below 1.8 eV the absorption coefficient of both microcrystalline silicon films is similar to crystalline silicon and significantly higher than absorption coefficient of amorphous silicon. At higher photon energies the absorption of

microcrystalline silicon is higher than absorption of crystalline silicon. These results are in agreement with data reported in literature [Shah *et al.* 2000, Vetterl *et al.* 2000].

It can be seen that at energies below 1.9 eV both microcrystalline silicon films follow a similar curve. At higher photon energy the absorption coefficient of film deposited at 6.3% silane concentration is higher then of 3% silane concentration film.

Both photosensitivity and optical absorption measurements suggest that 6.3% silane concentration microcrystalline silicon film is more beneficial to use as an active layer of a solar cell, than the film deposited at 3% silane concentration. This is in agreement with results of Jülich and Neuchatel groups [Vetterl *et al.* 2000, Shah *et al.* 2002], that demonstrated that microcrystalline silicon grown under 'transitional' conditions yields highest solar cell efficiency.

Finally, the dependence of the steady state photoconductivity on illumination intensity was investigated. Photoconductivity is related to illumination intensity as:

$$\sigma_{ph} \propto \Phi^{\gamma} \qquad (5.1)$$

where Φ is the photon flux. A double logarithmic plot of σ_{ph} vs. Φ yields a line of the slope γ. To investigate the dependence two microcrystalline silicon films, representing highly crystalline and transitional compositions, have been selected. The dependence of photoconductivity on photon flux for two microcrystalline silicon films (SC=3% and SC=6.3%) is presented in figure 5.7.

Figure 5.7 shows that the photoconductivity index increases with increase of silane concentration: for microcrystalline silicon film deposited at 3% silane concentration photoconductivity index γ is about 0.59. For both films, photoconductivity remains sublinear for low and high photon fluxes. The model of Rose (see chapter 3) explains photoconductivity index gamma between 0.5 and 1, however, at low excitation ($\sigma_{photo} < \sigma_{dark}$) the model predicts a linear relationship (gamma=1).

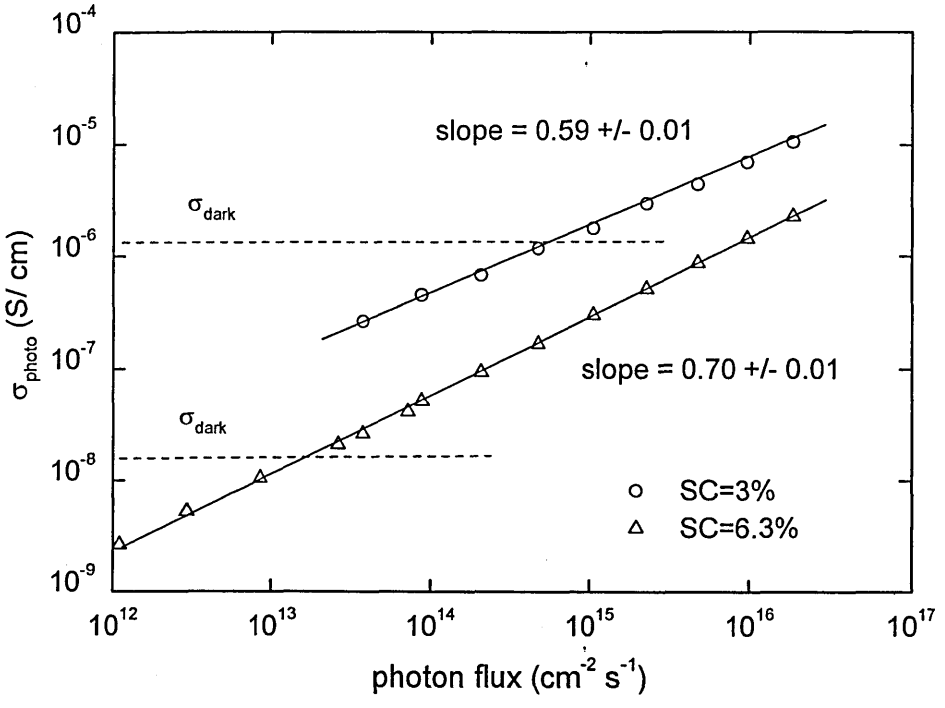

Figure 5.7. Photoconductivity σ_{photo} vs. photon flux, samples 00c354 and 00c345.

Our results do not follow linear excitation dependence in $\sigma_{photo} < \sigma_{dark}$ region. It has previously been demonstrated [Dick 1994, Main *et al.* 1996] that a dependence of the photoconductivity index on the Fermi level position takes place in n-type amorphous silicon films, where a sublinear dependence at low excitation has been observed. The observed changes of photoconductivity index γ in microcrystalline silicon films are remarkably similar to previously reported for n-type amorphous silicon [Merazga 1991, Dick 1994]. Figure 5.8 shows a comparison of the present results with data of n-type amorphous silicon films.

It can be seen that for both microcrystalline and amorphous silicon films a shift of the Fermi level position towards the conduction band results in a decrease of photoconductivity index γ. It was suggested that a decrease of photoconductivity index for n-type doped amorphous silicon films is related to the trapping of holes into deep defects [Merazga 1991, Dick 1994, Main *et al.* 1996], so called "safe hole traps". The concept of "safe hole traps" in amorphous silicon has been considered by MacMahon and Crandall [MacMahon and Crandall 1990].

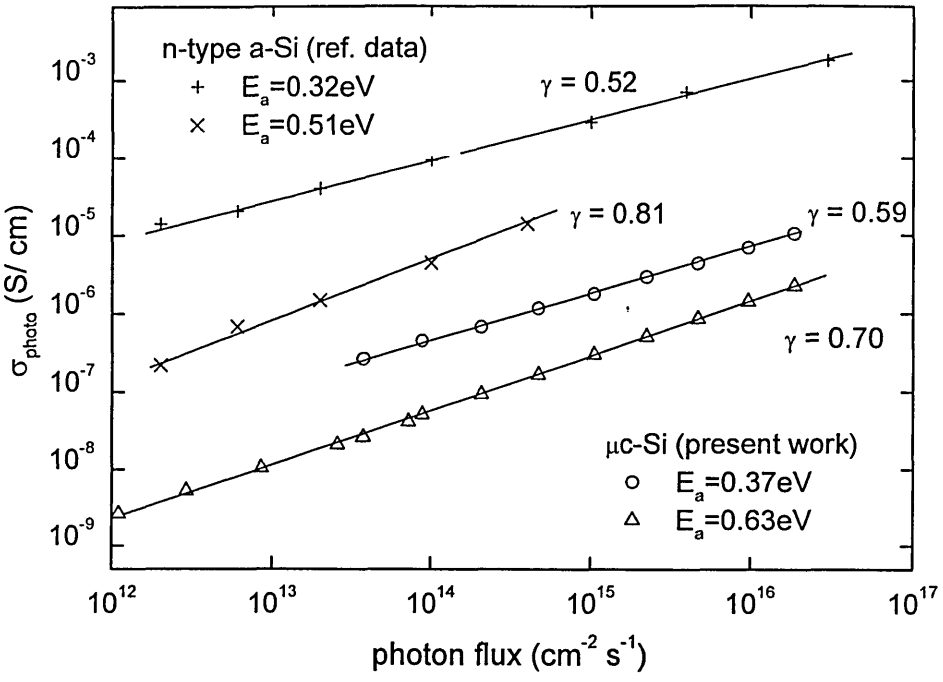

Figure 5.8. Comparison of results for microcrystalline and n-type amorphous silicon films. The reference data are taken from [Dick 1994].

They proposed that the safe hole traps are spatially isolated from other tail states and/or dangling bond defects (so that a tunnelling of trapped holes is unlikely) and a capture coefficient for electrons to such states is much smaller than the rate coefficient for electron capture to dangling bonds. The decrease of photoconductivity index observed in doped amorphous silicon is consistent with the changes of the Fermi level position observed upon variation of silane concentration.

Summary

The above section was dedicated to the study of dark and steady state photoconductivity properties of microcrystalline silicon films prepared over a range of silane concentrations. A decrease in silane concentration results in shift of the Fermi level position toward the conduction band. It is generally believed that the

shift of the Fermi level position is related to unintentional doping, for example oxygen, that would be more prevalent at low deposition rates, expected at low silane concentration. As a result of the Fermi level shift, dark conductivity and mobility-lifetime product decrease with increasing silane concentration. However, the photosensitivity of the material increases with increasing silane concentration, suggesting that although mobility lifetime product is highest for 3% silane concentration film, 'transitional' microcrystalline silicon is more appropriate for solar cell applications. The observed changes in the Fermi level position, dark and photoconductivity, and also photoconductivity index with variations of silane concentration ratio are remarkably similar to those reported for n-type amorphous silicon films.

5.2 Transient photoconductivity

Transient photoconductivity decays from the series of microcrystalline silicon film deposited at silane concentration varied between 3% and 6.3% are presented in figure 5.9.

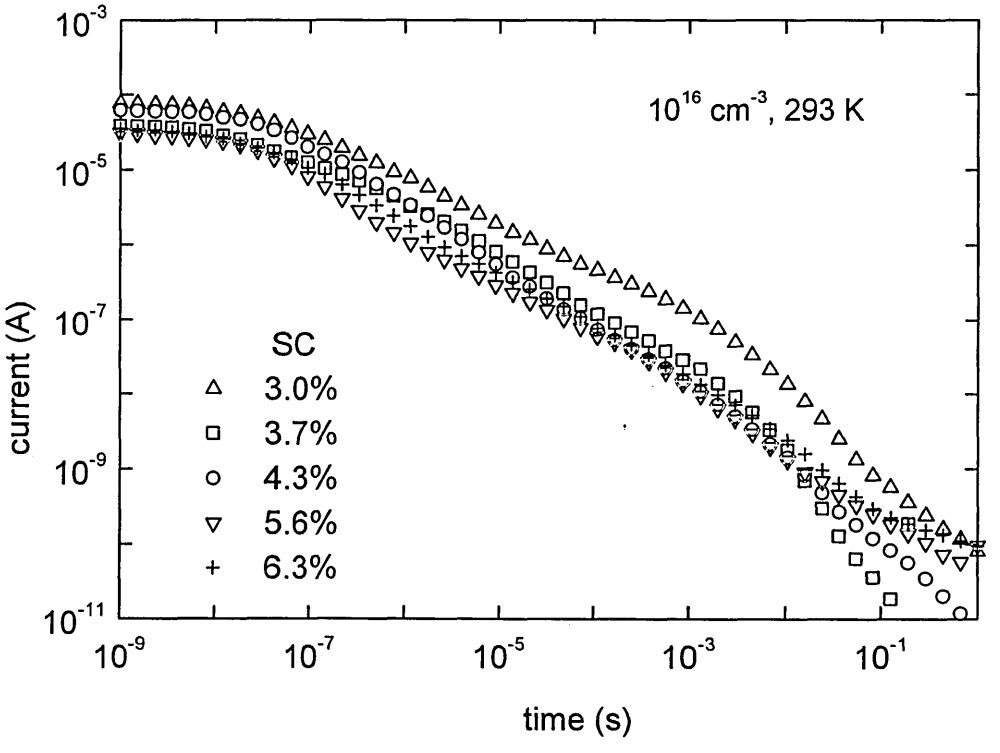

Figure 5.9. TPC decays for μc-Si:H films vs. gas ratio.

A trend in the shape of the decays can be identified. For the film deposited at 3% silane concentration there is a shallow fall in the photocurrent ($t^{-0.5}$ or less) from 10^{-7} s to 10^{-3} s, followed by a more rapid fall (typically t^{-1}) extending to the limits of our measurements. As silane concentration approaches 6%, the initial current is somewhat lower and the first power law section becomes steeper. This may signify an increase in carrier trapping into a larger density of deep states, as observed in amorphous silicon [Reynolds *et al.* 2000], or a wider range of electron thermalization as discussed below.

To quantify the differences in detailed behaviour two films, representing the highly crystalline and the transitional phases, were selected for detailed study: transitional sample deposited at SC= 6.3% and highly crystalline sample grown at SC= 3%. Figure 5.10 illustrates pulse density variations in TPC decays for the highly crystalline film.

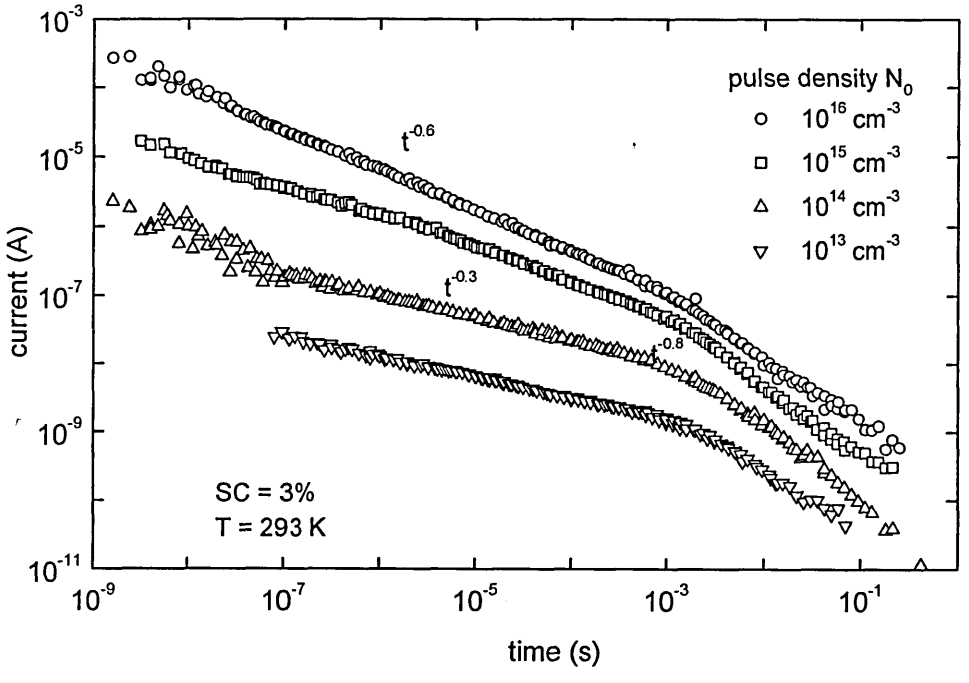

Figure 5.10. Pulse density N_0 variations in TPC decay for microcrystalline silicon film deposited at 3% silane concentration.

Figure 5.10 shows the strong variation in the power law index with pulse density N_0 in the range 10^{-7} s to 10^{-3} s, from $t^{-0.6}$ at $N_0 = 10^{16}$ cm^{-3} to $t^{-0.3}$ at $N_0 = 10^{13}$ cm^{-3}. The excitation dependence of transient photocurrent data for amorphous silicon films has been reported previously [Webb 1994, Reynolds *et al.* 2000]. A significant change in the photocurrent profile for pulse densities below 10^{15} cm^{-3} is observed. The rapid fall in photocurrent decay at low excitation densities is associated with a process of capture into deep defects. At pulse densities higher than 10^{15} cm^{-3} the

fall is reduced showing a strong pulse density dependence, when the deep defect states become saturated. However, the highly crystalline film studied here shows a strong excitation density dependence even for pulse densities below 10^{15} cm^{-3}. It is unlikely that this feature is associated with filling electron traps as proposed in the case of amorphous silicon films at densities above 10^{15} cm^{-3} because the dependence observed here occur even when pulse density is well below the reported spin defect density [Baia Neto *et al.* 2002].

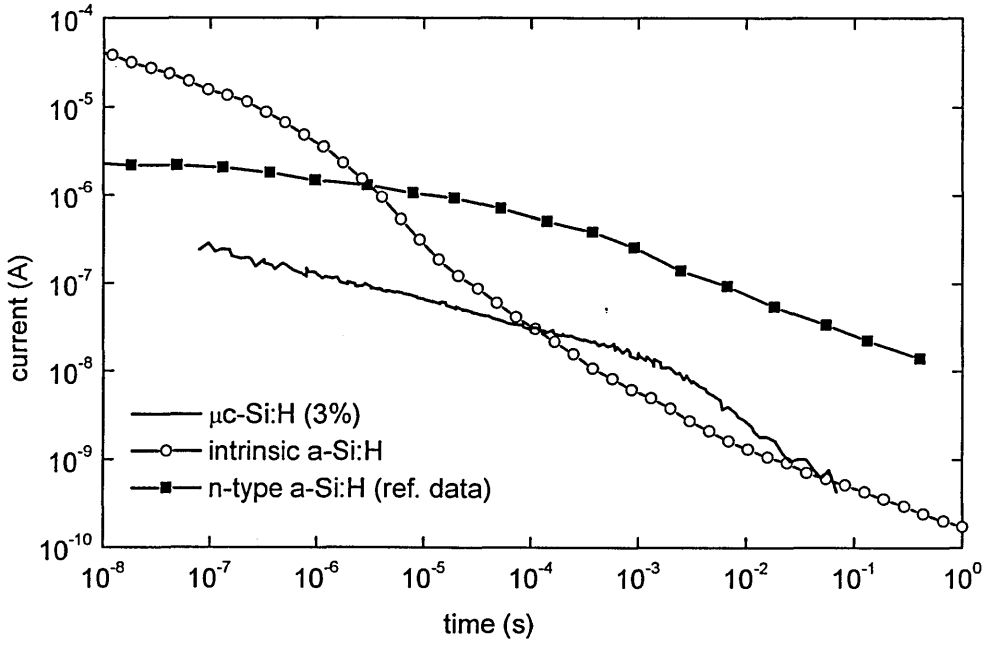

Figure 5.11. Comparison of TPC decays for μc-Si:H deposited at 3% silane concentration with intrinsic and n-type a-Si:H. The data for n-type a-Si:H are taken from [Merazga 1991].

Figure 5.11 shows the TPC decays for microcrystalline silicon film deposited at 3% silane concentration compared with TPC decays intrinsic amorphous silicon film obtained from an industrial PECVD reactor and for n-type amorphous silicon film. The n-type sample has dark conductivity activation energy similar to that of the microcrystalline silicon sample (0.37 eV). The purpose of presenting these curves is to enable a comparison between the TPC behaviour of the microcrystalline

silicon film deposited at 3% silane concentration with high quality intrinsic amorphous silicon and n-type amorphous silicon. The comparison suggests that behaviour of highly crystalline microcrystalline silicon sample is more closely resembles n-type amorphous silicon, as was also pointed out by Brüggemann [Brüggemann 2003]. In the section of steady state results similarities between highly crystalline microcrystalline silicon film and n-type amorphous silicon were also found.

The temperature dependence of transient photocurrent decays is shown in figure 5.12. The value of dark current activation energy for this sample is 0.37 eV, representing the Fermi level relative to an assumed transport energy.

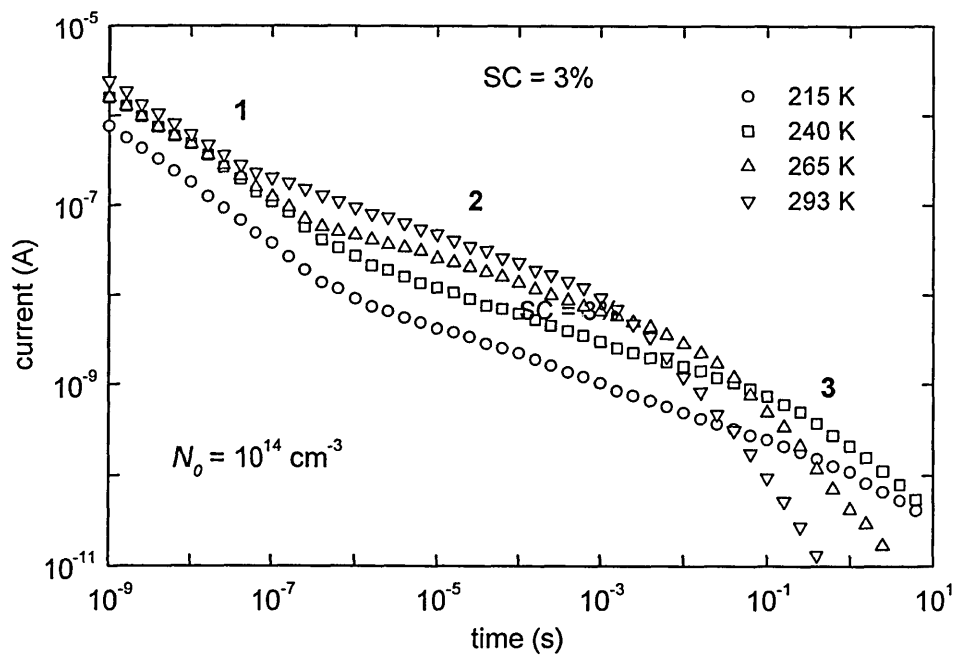

Figure 5.12. Temperature dependence of photocurrent decays for microcrystalline silicon film deposited at 3% silane concentration.

Using equation 3.20 with attempt-to-escape frequency 10^{12} s^{-1} this suggests that electron thermalization should be complete after about 1 μs, which can be ascribed

to section 1 in figure 5.12. The remainder of the decay consists of a weakly dispersive section (2) extending over some 4 orders of magnitude of time, and a steeper power law section (3) whose index is temperature-dependent. Similar behaviour has been observed in n-type a-Si:H, and explained in terms of a model [Main *et al.* 1987] where recombination is controlled by emission of holes from 'safe hole traps' in the valence band tail. Under such conditions the power law index of section 3 is predicted to equal T/T_V, where T_V is the characteristic temperature of the *valence* band tail. Our results show a reduction in the index with decreasing temperature in broad agreement with this, and a value $T_V \approx 30$ meV. This is somewhat steeper than suggested by CPM and PDS measurements on this material [Finger *et al.* 2001], but is in excellent agreement with recent hole TOF studies [Dylla *et al.* 2005].

Figure 5.13 is an Arrhenius plot of the turn-over time, *i.e.* the transition from region 2 to region 3. Within this model, the slope suggests the onset of significant recombination occurs when holes have thermalized to a depth of 0.63 eV and, from the intercept at $1/T = 0$ the attempt-to-escape frequency is of order 3×10^{13} s^{-1}.

TPC decays from films prepared at the crystalline to amorphous transition scale quite linearly with pulse density in the range $10^{14} - 10^{16}$ cm^{-3}, although a departure similar to that described above is evident at higher excitations. This is illustrated in figure 5.14.

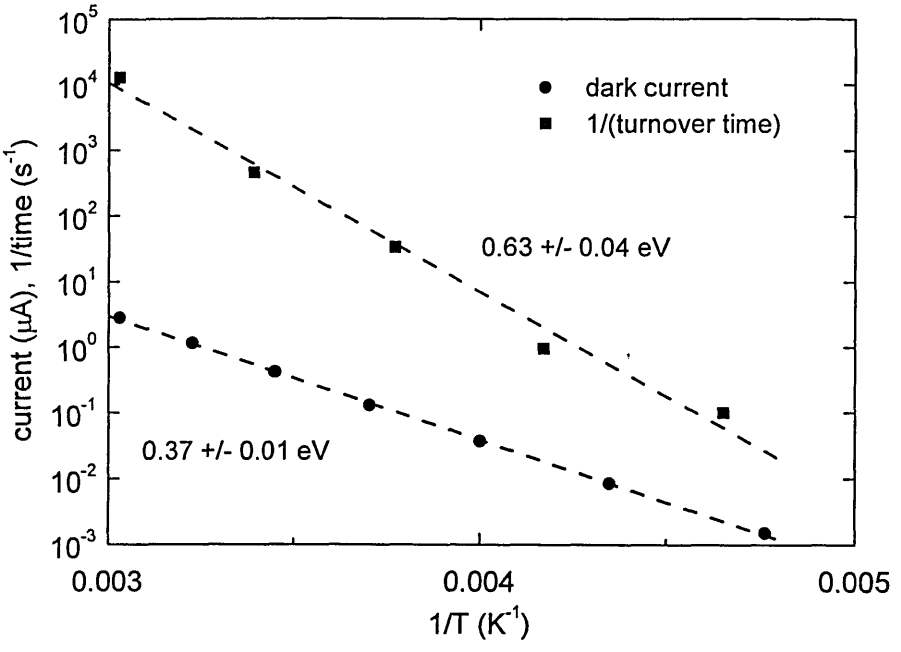

Figure 5.13 Arrhenius plots of dark current and reciprocal turnover time for highly crystalline film (SC=3%).

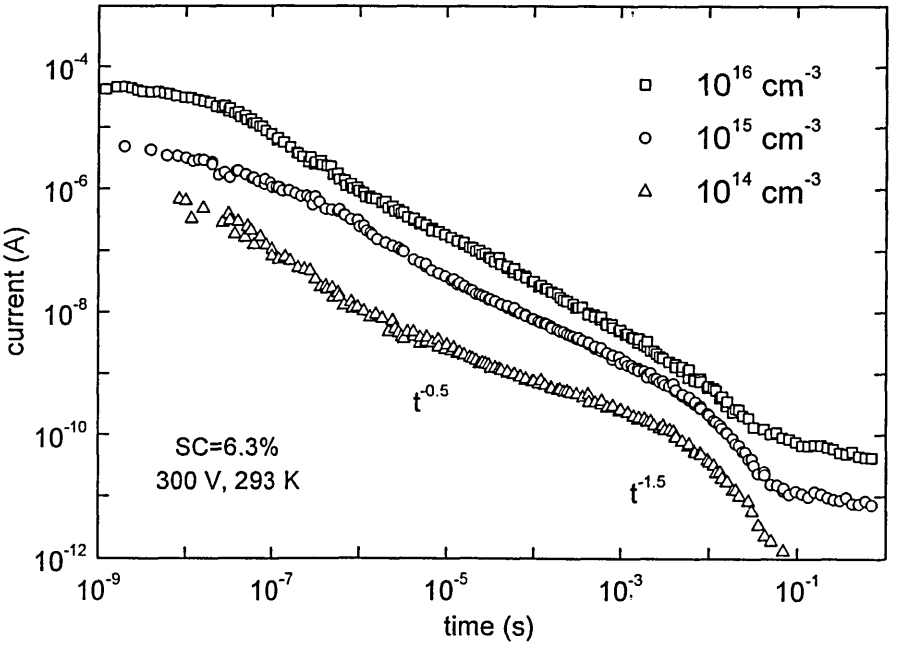

Figure 5.14. Pulse density variations in TPC decay for 'transitional' microcrystalline silicon film deposited at 6.3% silane concentration.

The conductivity activation energy value for the transitional sample is 0.63 eV, and if this corresponds to the Fermi level position it should be possible to apply DOS spectroscopy based on electron multiple-trapping to probe the localized state distribution in the upper portion of the band gap. TPC decays obtained in the temperature range from 215K to 390K and corresponding DOS are presented in figures 5.15 and 5.16.

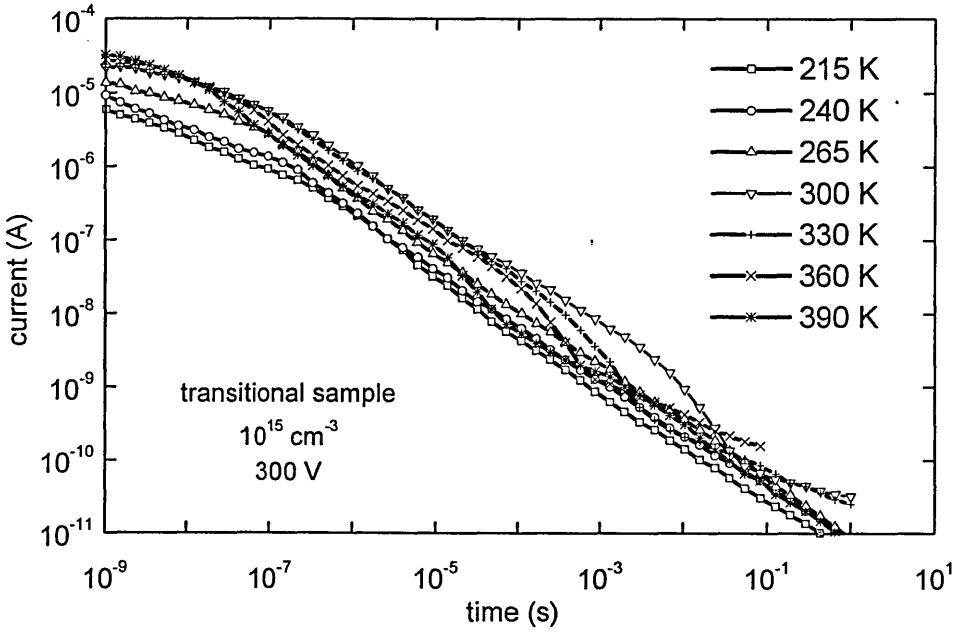

Figure 5.15. TPC decays for transitional sample.

The procedure used to obtain the DOS from the photocurrent decay is based on a Fourier transform technique described previously (see chapter 3), and assumes an attempt-to-escape frequency of 10^{12} s^{-1}. The curves have been aligned by shifting the DOS scaling so that the band tails overlap, and the intercept at the band edge has been positioned at 4×10^{21} cm^{-3} eV^{-1} to provide an indicative scaling. The 'best fit' shown in Figure 5.17 is obtained by overlapping the DOS plots obtained at different temperatures, such that the lowest temperature section is given greatest priority.

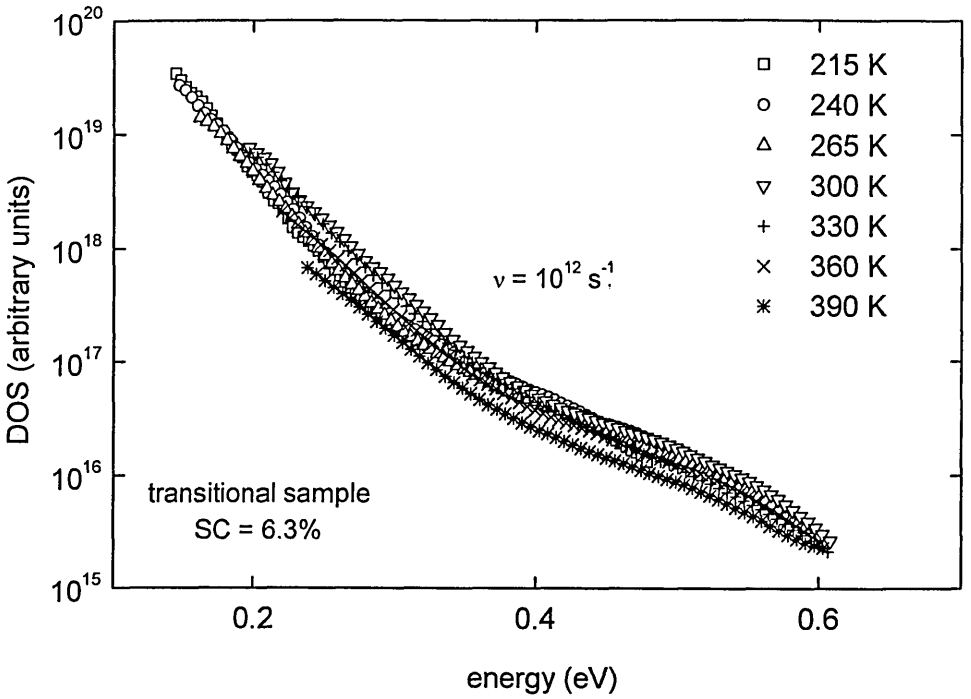

Figure 5.16. DOS for transitional film at various temperatures.

By projecting an exponential tail to the band edge an integrated density between 0.4 and 0.6 eV of 4×10^{15} cm^{-3} can be obtained, five times lower than the measured spin density. This suggests that one or more of the above assumptions could be invalid, for example the tail may not be exponential at shallow energies [Main *et al.* 1987]. It was found that the conduction band tail slope, at 30 meV, is somewhat broader than that in optimised amorphous silicon, and the defect density between 0.4 and 0.6 eV is substantially higher. The density at 0.6 eV is comparable to that in light-soaked a-Si:H.

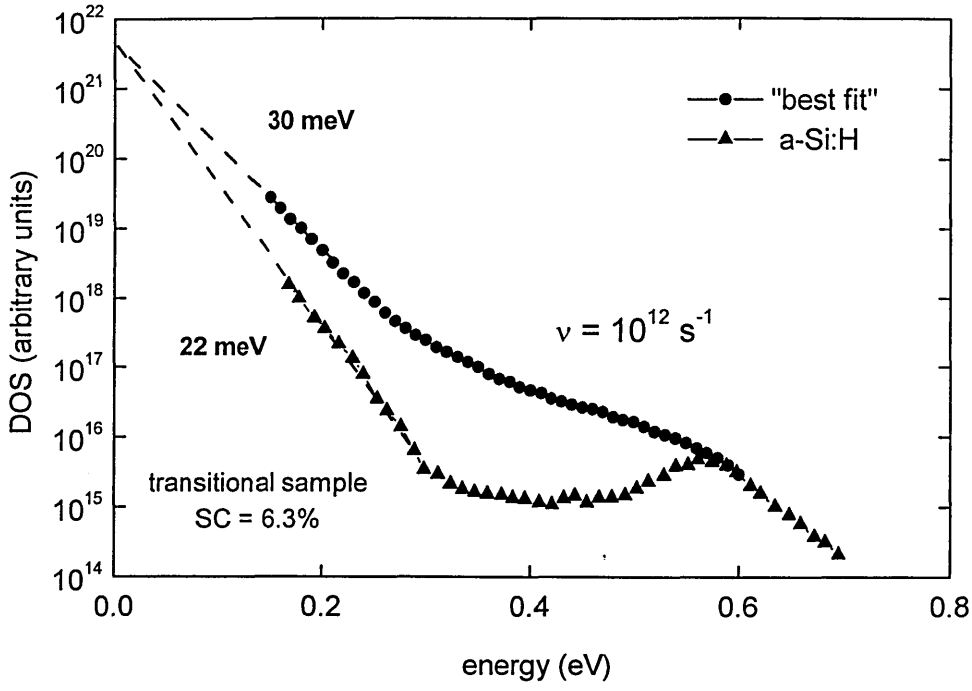

Figure 5.17. DOS for transitional μc-Si:H film (SC=6.3%), a-Si:H shown for comparison.

It should be determined whether a DOS analysis similar to that described above can be used for films deposited at lower silane concentration conditions, where crystalline volume fraction increases. Figure 5.18 suggests that the films with large crystalline volume fraction show lower deep defect density. However this result contradicts ESR measurements [Baia Neto *et al.* 2002]. A possible explanation is related to variations in the Fermi level position when crystallinity is varied. For the series of microcrystalline silicon films studied here the dark conductivity activation energy is in the range from about 0.6 eV (transitional film) to 0.35 eV (highly crystalline film). States deeper than the Fermi level position are largely occupied, resulting in an underestimate of the true DOS, that is particularly well pronounced for the case of highly crystalline samples.

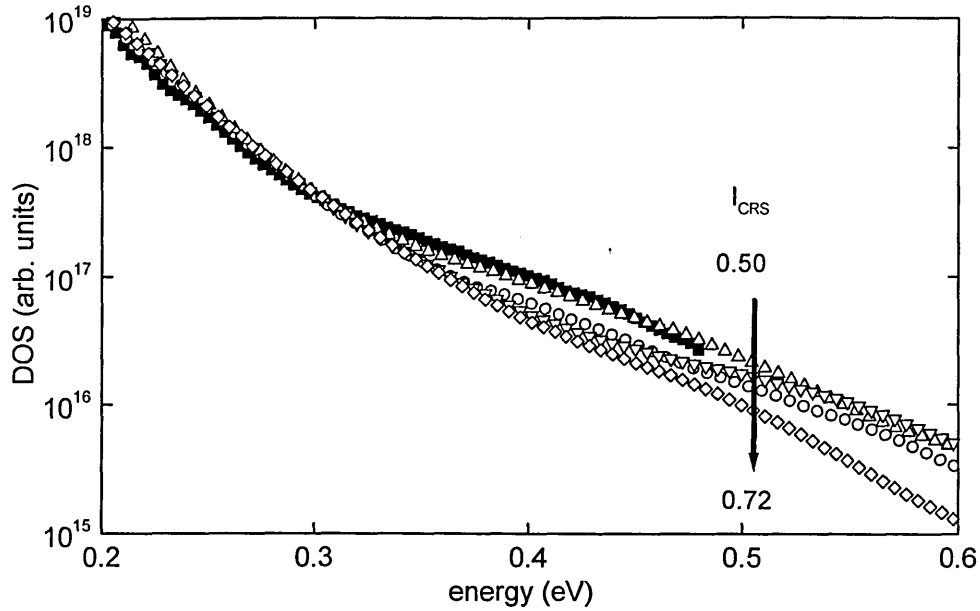

Figure 5.18. DOS plots for μc-Si:H films of varying crystallinity.

Thus, the apparent reduction in the DOS may simply reflect an increased *occupancy* of deep states, suggesting that that DOS spectroscopy should be used with caution when studying highly crystalline microcrystalline silicon films [Reynolds *et al.* 2002].

To illustrate this point the result of analysing the decay from a highly crystalline film are shown. Figure 5.19 shows the apparent DOS distribution obtained from the photocurrent decays presented in figure 5.12. There is little overlap between the decays at different temperatures except at shallow energies, which is to be expected given the Fermi level position [Reynolds *et al.* 2002]. The deep DOS values appeared to be unrealistically low. Similar results have been reported by Brüggemann [Brüggemann 2003]. It was demonstrated that in n-type thin silicon films an extraction of the density of states from transient photoconductivity data results in poor overlapping of curves at various temperatures and the density of states values were found to be too low. Similarly to the reasoning given in the present work, Brüggemann explained the results in term of position of the Fermi level and occupancy of defects.

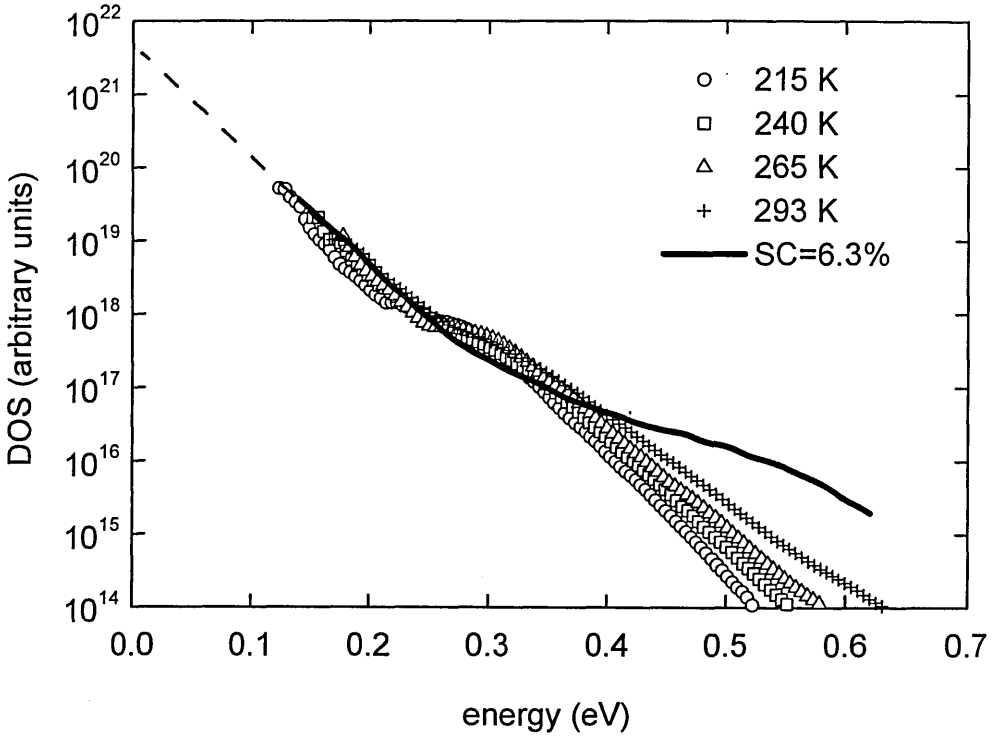

Figure 5.19. DOS analysis of highly crystalline μc-Si:H film (SC=3%). Data for 'transitional' sample presented for comparison.

5.3 Post transit Time-of-Flight (PT TOF) spectroscopy

In the previous section, the application of transient photocurrent spectroscopy (TPC) to the study of coplanar μc-Si:H films having varying degrees of crystallinity was described. In those experiments the electric field has been applied perpendicularly to the direction of film growth, suggesting that the transport properties parallel to the substrate have been monitored. The present section is dedicated to the study of the transport properties of *pin* photovoltaic structures with varying crystalline volume fractions of absorbing layer. The post-transit time-of-flight (PT TOF) measurements monitor the primary photocurrent decays in a reverse-biased device following the initial rapid transit of carriers, which may be related directly to the emission of carriers from deep traps. Following emission these carriers will be extracted before deep re-trapping can occur, and as the contacts are blocking they cannot be replenished by the external circuit. Since the electric field is applied perpendicular to the substrate, the technique is believed to monitor the transport properties along the direction of growth. This provides a possibility to examine the morphological anisotropy of microcrystalline silicon materials.

Firstly the *pin* sample with low crystallinity of i layer will be examined. Post transit time-of-flight decays from the sample with i layer deposited at 7% silane concentration are shown in figure 5.20 and the corresponding density of states in figure 5.21.

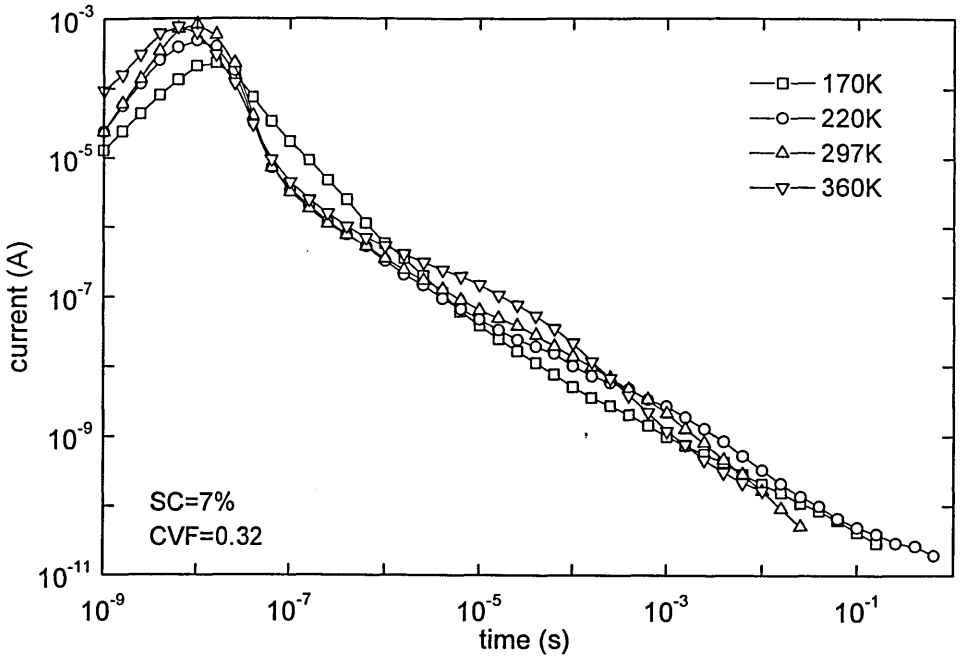

Figure 5.20. Photocurrent decays from μc-Si:H *pin*, i layer SC=7%.

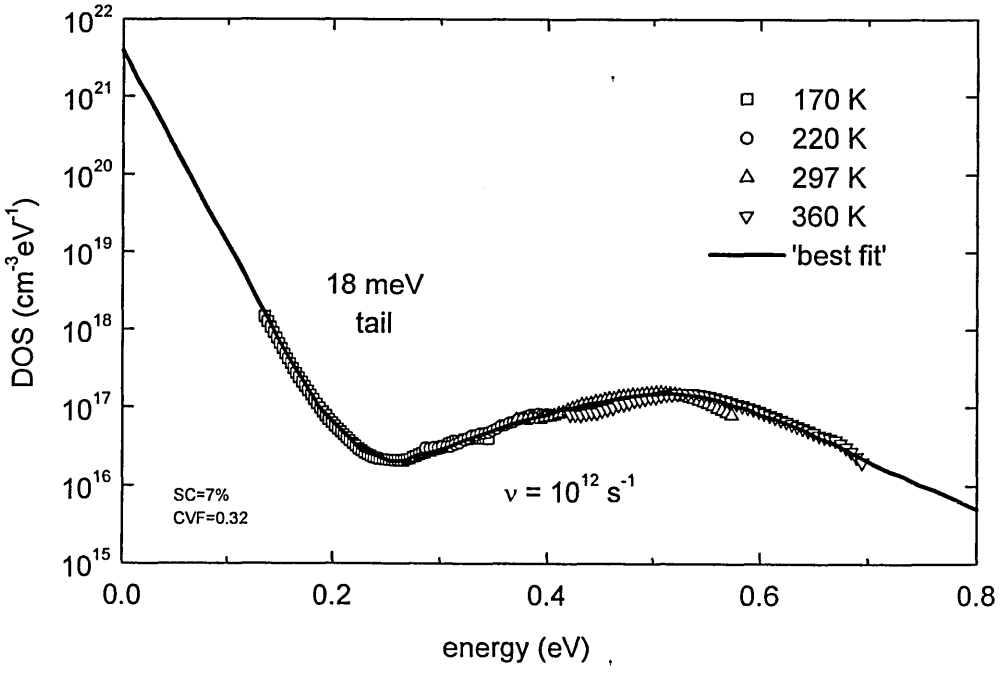

Figure 5.21. DOS from μc-Si:H *pin*, i layer SC=7%.

The data have been processed assuming the attempt-to-escape frequency ν_0 = 10^{12} s^{-1}, and it is evident that there is a good degree of overlap between the DOS sections calculated at different temperatures. This indicates an appropriate choice has been made for ν_0. At sufficiently low temperatures (< 200 K) it is possible to observe a section of the conduction band tail. Based on this evidence the tail slope is quite steep, some 18 meV. An approximate scaling of the DOS may be achieved by extrapolating this section to an assumed band edge density of 4×10^{21} cm^{-3} eV^{-1}. This yields a maximum value of 2×10^{17} cm^{-3} eV^{-1}, and an integrated density of about 5×10^{16} cm^{-3}, for deep defects.

Figure 5.22 presents density of states obtained for 'transitional' microcrystalline silicon sample in compare with fully amorphous sample. At energy < 0.15 eV the data points are plotted by extrapolation of the tail section to an assumed band edge density of 4×10^{21} cm^{-3} eV^{-1}.

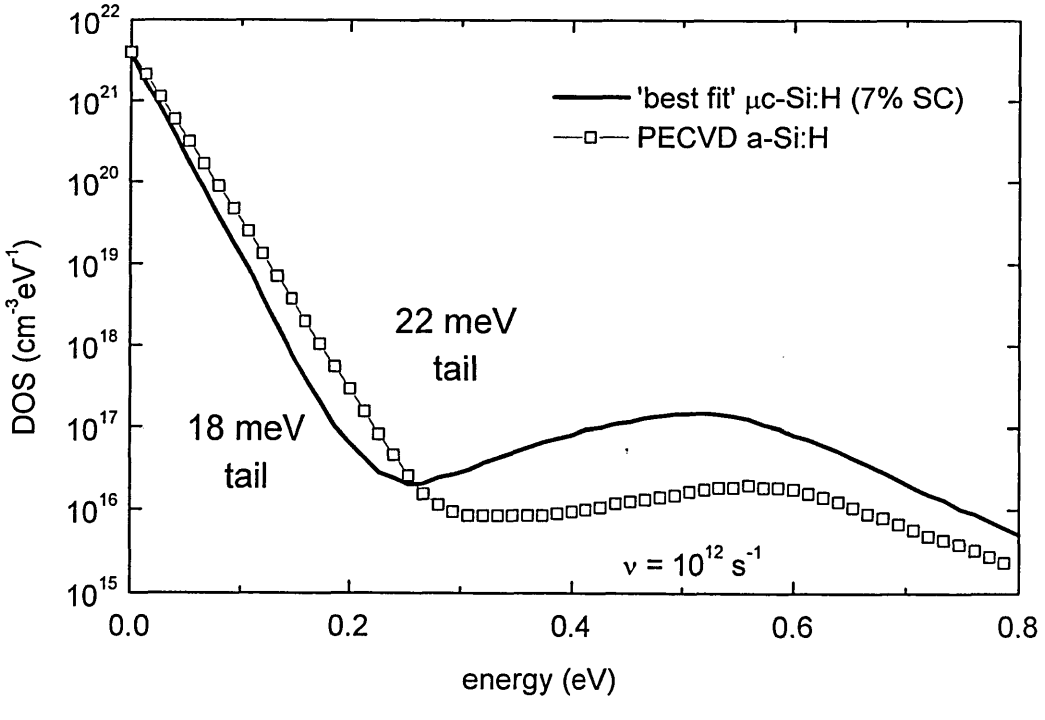

Figure 5.22. Comparison of DOS for μc-Si:H and a-Si:H *pin* structures.

It can be seen that the DOS is quite similar in shape, though the defect density is lower and the band tail slope slightly larger than for the μc-Si:H device. This

suggests that at low crystalline volume fraction the transport process prevailing in microcrystalline silicon structure is similar to observed in amorphous silicon, and is consistent with multiple-trapping in tail and defect states.

The effect of temperature on the photocurrent decays with decreasing i-layer silane concentration ratio (increasing crystallinity) is illustrated in figures 5.23 and 5.24. There is a tendency for the curves to become temperature-independent for samples with i layer CVF > 0.5, although an increase in gradient is apparent at times longer than 10^{-4} s. However, in more highly crystalline samples the reverse leakage current is several orders higher than the photocurrent in this region. Even though the leakage component is nulled out, results below 10^{-10} A should be viewed with caution.

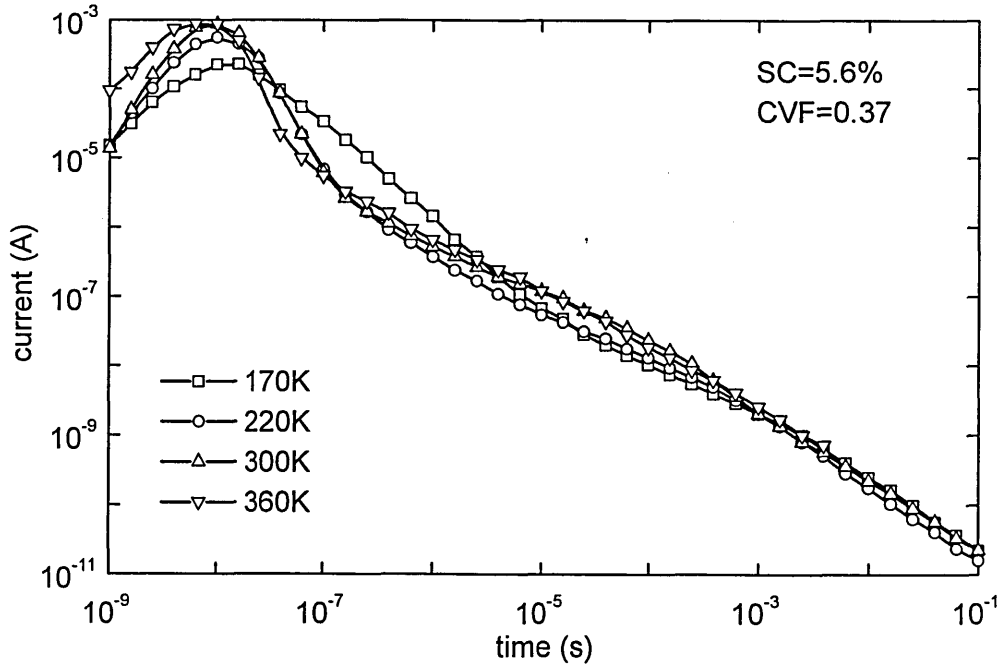

Figure 5.23. Temperature–dependence of photocurrent decays from μc-Si:H *pin*, i layer SC=5.6%.

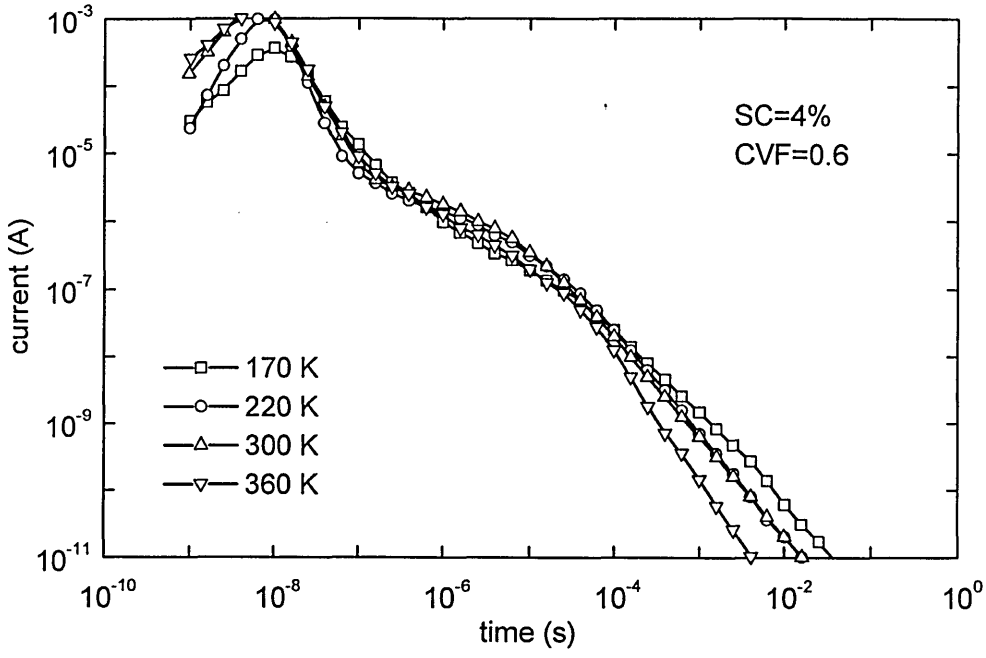

Figure 5.24. Temperature–dependence of photocurrent decays from μc-Si:H *pin*, i layer SC=4%.

In the context of multiple-trapping theory it is not possible to construct a realistic DOS that results in a temperature-independent photocurrent decay. However this does not necessarily mean that MT is not taking place, it could be that its manifestations within the post-transit current are obscured by other effects that should be considered. It was previously shown (see paragraph 5.2) that the transient photocurrent decay in highly-crystalline *coplanar* films more closely resembles behavior observed in n-type a-Si:H. In that case, the photocurrent decay is controlled by the release of the deeply-trapped *holes* required for recombination to proceed. For highly crystalline microcrystalline silicon films a shift of the Fermi level position toward the transport level has been reported [Ruff *et al.* 1998] for temperatures between 400 K and 200 K. This could account for the temperature-independent break-point at 10^{-5} s in figures 5.23 and 5.24 because although the thermalisation energy sinks more slowly at lower temperatures it reaches the (raised) Fermi level at much the same time. The increased gradient at

longer times might also be anticipated, reflecting a sharper Boltzmann tail. There is also evidence to suggest that transport below room temperature in highly crystalline films is by hopping [Kocka *et al.* 2002, Fejfar *et al.* 1998], and the presence of a distribution of states at potential barriers between crystalline clusters or columns and the surrounding amorphous tissue has also been inferred from ESR [Finger *et al.* 1998]. If transport is proceeding via these pathways then the causes of the shape of the photoconductivity decay is a matter for speculation.

Although the results presented above cannot be consistently interpreted in terms of MT theory, this transport mechanism may still prevail at room temperature (and above). If so, comparing room temperature photocurrent decays as the crystalline volume fraction is increased could give an insight into how the defect distributions evolve. Photocurrent decays for *pin* structures with different i-layer crystallinity obtained by variations in silane concentration ratio between 4% and 7% are shown in the figure 5.25.

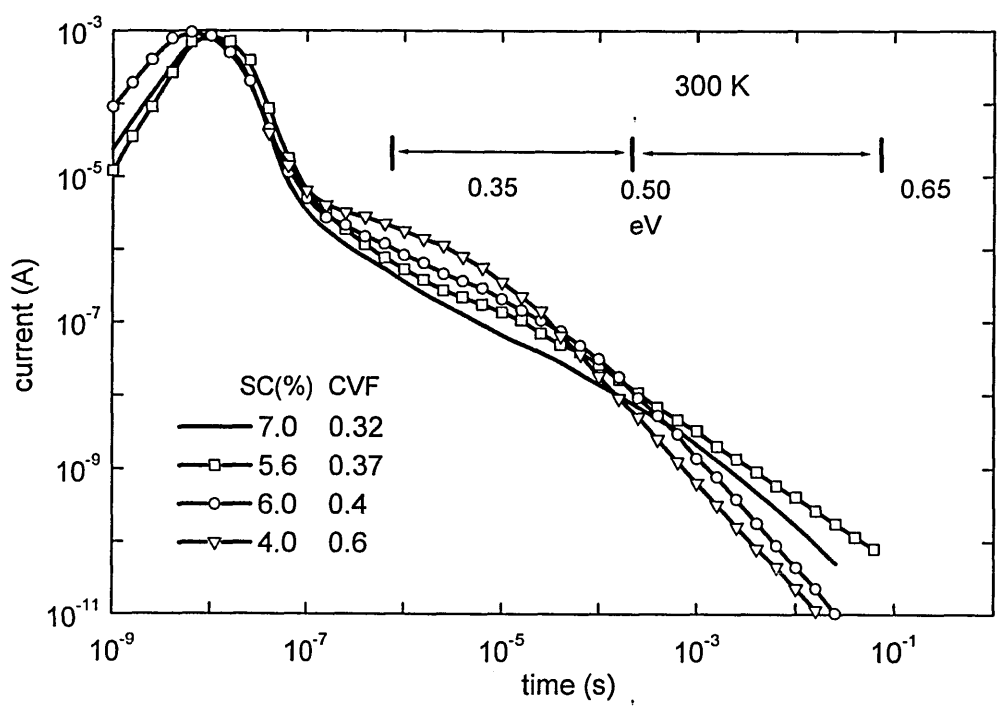

Figure 5.25. Photocurrent decays obtained over a range of SCs at 300 K.

The general trend demonstrates that as crystalline volume fraction increases, the current increases below 10^{-4} s and decreases at longer times. Through the post- transit analysis developed by Seynhaeve *et al.* [Seynhaeve *et al.* 1989] this may be interpreted as an increasing shallow DOS, and decreasing deep DOS, with increasing crystallinity. Linking this to structural changes, it is tempting to suggest that the shallow defects (0.35-0.5 eV) are associated with an increase in crystalline columns or granular clusters and their boundaries, and deeper defects (0.5-0.65 eV) with the amorphous tissue. The DOS plots obtained from photoconductivity data at room temperature as crystallinity is increased are presented in figure 5.26.

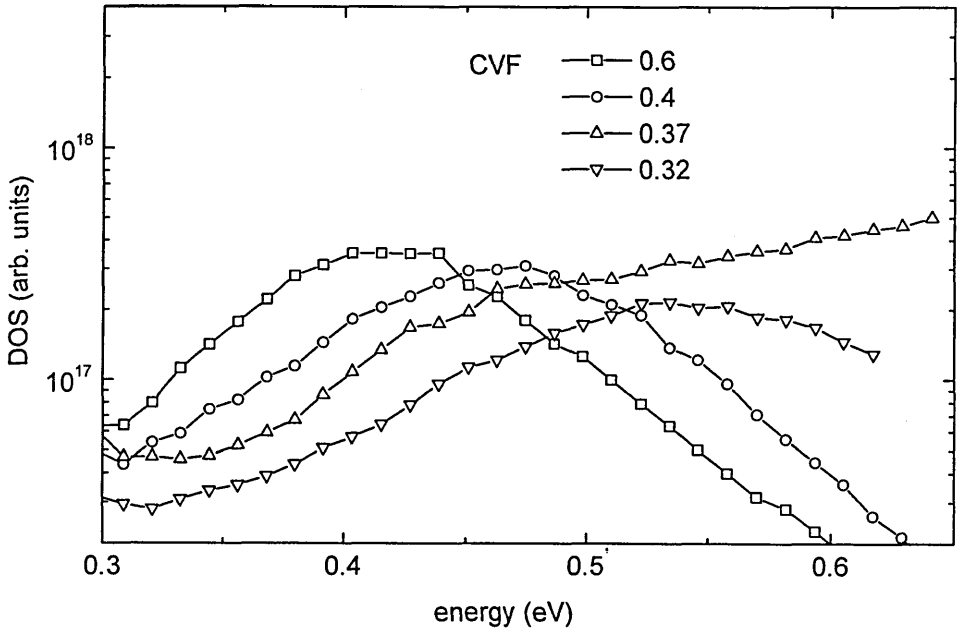

Figure 5.26. DOS calculated from photoconductivity curves at 300K.

It can be seen that there is a systematic trend for the peak in the DOS to move to shallower energies as the degree of crystallinity is increased. This may indicate that localized states specific to the crystalline phase, for example at column boundaries, occur at energies 0.4 eV below the transport energy, and the 'usual'

dangling-bond defects found in the amorphous tissue are located somewhat deeper in the region of 0.6 eV.

5.4 Comparison of TPC and TOF results

Figure 5.27 is a compilation of a number of DOS plots presented in the previous sections, obtained using transient photoconductivity and post transit time-of-flight techniques.

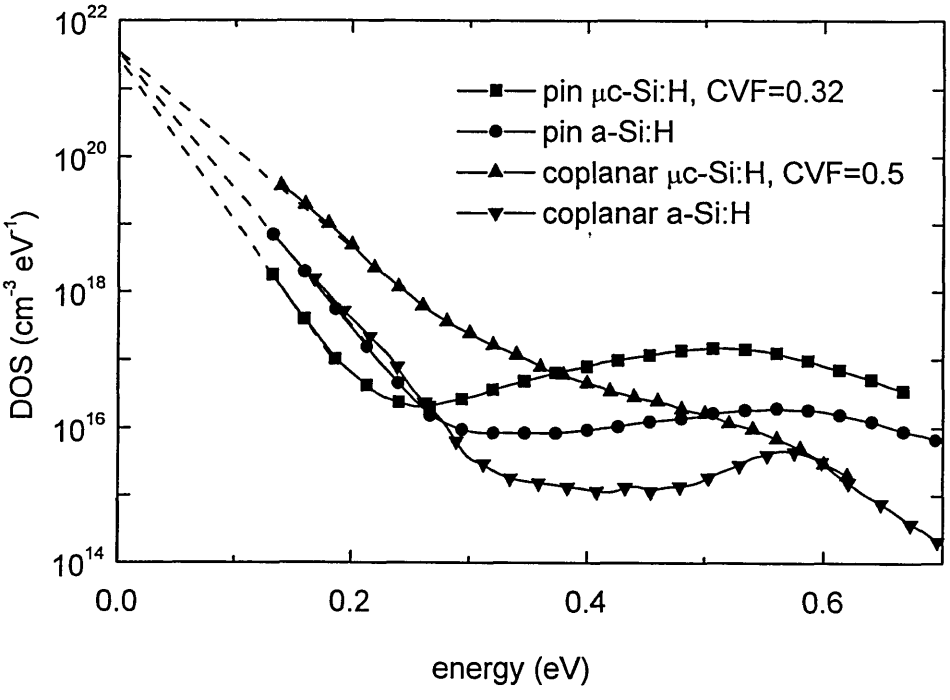

Figure 5.27. Comparison of DOS plots for μc-Si:H and a-Si:H in coplanar and *pin* configurations.

Each curve is composed of the overlap of DOS segments from measurements made over a range of temperatures, revealing both defect and tail state distributions. The distributions are normalised by extrapolating an assumed

exponential band tail to a value of $4x10^{21}$ cm^{-3} eV^{-1} at the band edge. A comparison suggests:

(i) The CB tail slope for μc-Si:H deduced from *pin* structures (albeit rather less crystalline) is considerably steeper than that deduced from coplanar samples.

(ii) The CB tail slopes for a-Si:H are similar in both coplanar and *pin* - slightly shallower than for μc-Si:H *pin* samples, but somewhat steeper than for coplanar μc-Si:H.

(iii) The deep (>0.6 eV) defect density for coplanar μc-Si:H is lower than that from *pin*.

(iv) The deep defect density for a-Si:H is lower than for μc-Si:H.

The results of our observations demonstrate that microcrystalline silicon films are electrically as well as structurally anisotropic. This result is in agreement with anisotropy concept reported for microcrystalline silicon [Luysberg *et al.* 1997, Finger *et al.* 1998, Houben *et al.* 1998, Unold *et al.* 2000, Shah *et al.* 2003, Kocka *et al.* 2003, Liu *et al.* 2004]. For the coplanar sample configuration, the TPC experiments may be expected to monitor transport in parallel to the substrate (perpendicular to the direction of material growth). Since the crystalline columns or aggregated structures are usually found to be surrounded by amorphous tissue [Finger *et al.* 1998, Shah *et al.* 2003, Kocka *et al.* 2003], in the case of TPC measurements the carriers may travel through the both crystalline and amorphous fractions. The PT-TOF measurements enable transport in the direction of growth (perpendicular to the substrate) to be measured. In this case the presence of columnar structures could play a significant role, dominating the carrier path. The sharper conduction band tail sampled by carriers travelling along the direction of growth (PT-TOF on *pin* samples), rather than in the plane of the film (in TPC on coplanar samples), is consistent with a greater degree of order, as might be found within the crystalline columns. This also suggest that amorphous nucleation region typically observed close to substrate for films grown under low silane concentration

condition is negligible for the case of i-layer of *pin* structure. This is because the material morphology is sensitive to the type of substrate used [Luysberg *et al.* 1997, Finger *et al.* 1997, Houben *et al.* 1998] and thus films grown on a layer of amorphous silicon could show stronger columnar growth. A similar effect, of increased crystallinity and an absence of nucleation layer for the intrinsic layer of photovoltaic cell, has been reported [Edelman *et al.* 2003, Ross *et al.* 2005].

The higher defect density in the PT-TOF DOS as against the TPC DOS suggests that trapping for energies between 0.37 eV and 0.5 eV is more prevalent at the column boundaries than within the amorphous tissue. This is in agreement with the view [Baia Neto *et al.* 2002, Kocka *et al.* 2003] that defects in microcrystalline silicon could be located at the column boundaries. Higher deep defect density (for energy > 0.5 eV) in the PT-TOF DOS (CVF=0.32) compared to TPC DOS of more crystalline material (CVF=0.5) suggests that amorphous phase could be responsible for these defects, in agreement with our previous observation (see figure 5.25).

High-quality a-Si:H appears to have a somewhat lower deep defect density than μc-Si:H, whichever of the two techniques is used to measure it. This suggests that the amorphous tissue in mixed-phase μc-Si:H is of poorer quality than single-component a-Si:H. This may be because passivating hydrogen is locked into grain boundaries [Finger *et al.* 1998] and is therefore less readily available to terminate dangling bonds. ESR evidence supports this view: For PECVD material, spin densities as high as 10^{17} cm^{-3} have been reported [Baia Neto *et al.* 2002] for highly crystalline samples, falling below 10^{16} cm^{-3} for fully amorphous material.

Summary

Paragraph 5.2 presented the results of the study of transport properties in microcrystalline silicon films by TPC. Photoconductivity decays in highly crystalline films show strong dependence on pulse density. The form of the transient decays is broadly similar to n-type amorphous silicon. The decays cannot be explained

solely in terms of electron multiple trapping model and require minority carrier contribution to be taken into account.

Transport in 'transitional' microcrystalline films is consistent with multiple trapping mechanism. The conduction band tail slope was found to be 30 meV, broader than in device quality amorphous silicon.

Deep defect density was found to decrease with increasing crystallinity, that is a subsequence of movement of the Fermi level away from the midgap. Thus the defect density in highly crystalline structures is believed to be underestimated by transient photoconductivity measurements.

The results of post-transit time-of-flight measurements on *pin* structure were presented in paragraph 5.3. At i layer crystalline volume fractions below 0.4 the results suggest the density of states is broadly similar in form to that of amorphous silicon, however, higher deep defect density was found. An increase in i layer crystalline volume fraction results in observation of temperature independent decays, suggesting that at least below room temperature multiple trapping transport does not take place. A comparison of the DOS obtained from I-t data at room temperature suggests that defects are associated with amorphous material and shallow defects are associated with crystalline content.

A comparison of results obtained on coplanar and sandwich configurations of microcrystalline silicon of similar quality suggests that electronic transport is anisotropic. Our results suggest greater structural order along the direction of film growth and a higher defect density within the amorphous tissue than is usual in good-quality 'homogeneous' amorphous silicon films.

Chapter 6. Atmospheric effects - part I: Dark and photo-conductivity, and computer simulation

Although microcrystalline silicon has attracted the attention of researchers for more than 20 years, few reports have considered atmospheric instabilities. In this chapter experimental results on instability of microcrystalline silicon films prepared at varying deposition conditions are presented. The effects of ambient atmosphere may result in both reversible and irreversible changes of microcrystalline silicon photoelectrical properties. This chapter mainly focuses on the study of reversible atmospheric effects.

6.1 Effect of atmospheric adsorption on dark conductivity

6.1.1 Variations in silane concentration

Figure 6.1 illustrates the effect of exposure to atmosphere on dark conductivity of microcrystalline silicon films grown at varying silane concentrations.

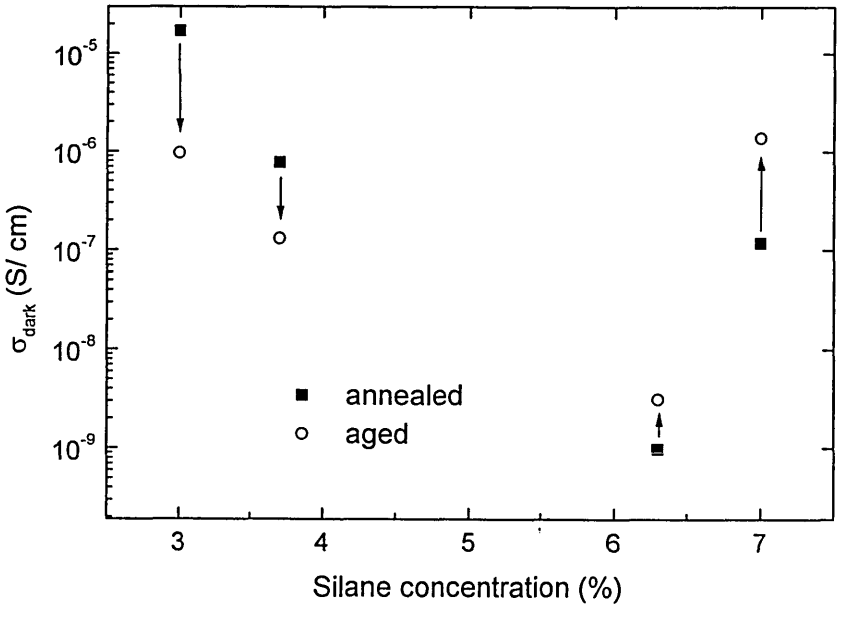

Figure 6.1. Dark conductivity σ_{dark} for ageing – annealing cycles *vs.* silane concentration. $\sigma_{dark}^{(aged)}$ recorded after 7 days of ageing.

Ageing was performed by exposure of samples to ambient air at room temperature. After several days of exposure to air, dark conductivity tends to remain unchanged and these conductivity values are recorded as "aged" condition (open circles in figure 6.1). Most significant changes in dark conductivity usually take place after 2 days of ageing when dark conductivity reaches at least 50% of $\sigma_{dark}^{(aged)}$ value, thus, the values given in the figure, after 7 days, are close to saturation. Variations in dark conductivity values in annealed condition (solid squares) with changes in silane concentration follow a trend commonly observed [Finger *et al.* 2001, Baia Neto *et al.* 2002, Kocka *et al.* 2003] for microcrystalline silicon, where at low silane concentration higher values of dark conductivity are expected (see also part I of results). The slightly high value of annealed dark conductivity for SC = 7% film may be due to fluctuations within the deposition system, but may also be related to thickness of the film, which is the lowest from the series presented. There is an indication from our work [Reynolds *et al.* 2005] that thinner films are more sensitive to post deposition oxidation process that can influence the Fermi level position and lead to dark conductivity increase. This effect is discussed in more detail in chapter 7 of results section.

Two different types of behaviour are observed on exposure to atmosphere. At low silane concentration (type I materials), where crystalline, more porous films are expected [Vetterl *et al.* 2000], dark conductivity *decreases* on ageing. At higher silane concentration the so-called type II materials deposited close to the transition from microcrystalline to amorphous growth [Vetterl *et al.* 2000], films behave in the opposite sense, show an *increase* in dark conductivity on exposure to atmosphere. Our results are in agreement with dark conductivity changes on exposure to air reported for type I/ type II microcrystalline silicon films [Finger *et al.* 2003]. In both cases, the initial conductivities of the samples can be restored by 10 minutes annealing under vacuum at 160 °C. These conductivity cycles can be repeated many times without any significant changes from cycle to cycle. The explanation of observed reversible conductivity changes can be related to adsorption of water or oxygen, resulting in a band bending effect. The mechanism of atmospheric adsorption effects is described in detail in chapter 2. An increase of dark conductivity in amorphous silicon films [Tanielian *et al.* 1980, Solomon 1980, Tanielian 1982] or microcrystalline silicon films [Finger *et al.* 2003] is usually associated with the adsorption of water molecules, that are known to donate

electrons to the material. In contrast, the adsorbed oxygen molecule behaves as an acceptor [Veprek *et al.* 1983, Finger *et al.* 2003], and thus the dark conductivity decrease is usually associated with the process of oxygen adsorption.

For the films deposited at SC=3% and SC=7% the changes in dark conductivity on ageing are more than 1 order of magnitude. A greater conductivity change observed for these films relative to SC=3.7% and SC=6.3% films can be explained due to morphological changes, particularly void fraction [Luysberg *et al.* 1997] with film thickness. This point is discussed in more detail in section 6.1.2.

In order to understand the annealing mechanism and to investigate the differences between type I and type II microcrystalline silicon films in more detail, the detailed behaviour of the samples during annealing as a function of time has been investigated. Annealing experiments were performed under vacuum of 10^{-3} torr. Two different types of behaviour have been observed in microcrystalline silicon films on annealing.

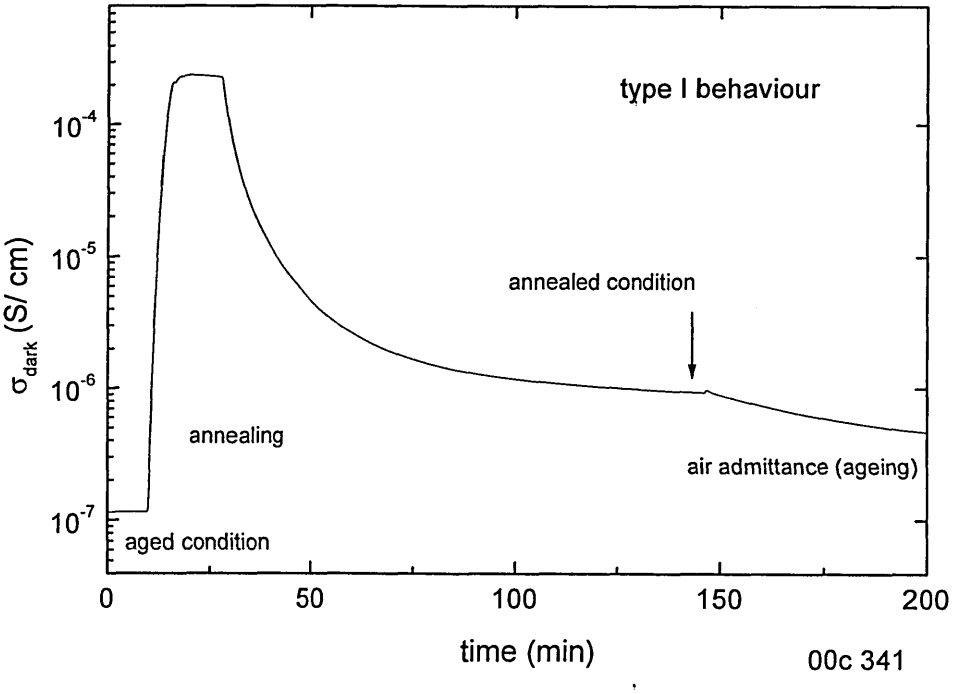

Figure 6.2a. Typical annealing curve for type I microcrystalline silicon film.

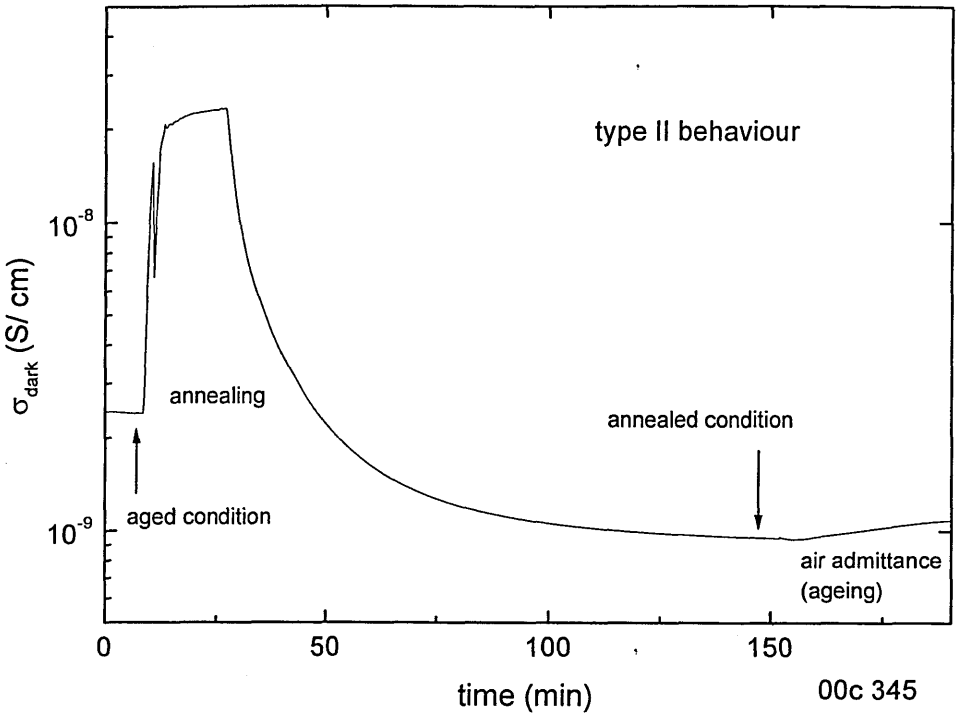

Figure 6.2b. Typical annealing curves for type II microcrystalline silicon film.

Figures 6.2a and 6.2b illustrate typical dark conductivity changes in microcrystalline silicon films observed during ageing-annealing cycles as a function of time. Figure 6.2a represents a typical behaviour of a film with significant crystalline volume fraction, while figure 6.2b shows the curve for a transitional film. After storage of type I samples in ambient air, the dark conductivity decreases with time and reaches a saturation level in several days. In figure 6.2a this level corresponds to the dark conductivity value of about 10^{-7} S/cm and marked as "aged condition". On annealing adsorbed atmospheric species are removed, resulting in an increase of dark conductivity back to the initial value. This level is indicated in the figure by "annealed condition" arrow. The conductivity decreases again when the sample is exposed to air.

Type II samples show a different behaviour. When the annealed sample is exposed to atmosphere, the dark conductivity increases (see figure 6.2b). Annealing of the sample results in removal of adsorbed atmospheric components, which restores the dark conductivity. During the heating of the sample a narrow

peak of conductivity is observed. This peak could be associated to the rapid removal of adsorbed atmospheric components when the temperature reaches a certain level, which results in a conductivity drop. The subsequent increase in conductivity is related to increase of the temperature before it reaches a constant value. The observed peak is a specific feature of type II materials on annealing, suggesting in principle, that the feature can be used to distinguish between highly crystalline and transitional (or amorphous) silicon films. To the author's knowledge such experiments have not been reported previously for any kind of thin silicon films. The peak has not been observed during annealings of type I materials, because both removal of adsorbed atmospheric species and heating of the sample result in conductivity increase. The presence of the peak suggests that the majority of adsorbed components can be removed rapidly if fast temperature pulses are applied to the sample. This is an important result because such rapid annealings can be used, for example, to distinguish between different types of metastabilities. For instance, rapid annealing can be applied to light soaked materials (Smirnov *et al.* 2004b) to remove adsorbed component without affecting light induced defects. The results of this series of experiments are described in chapter 8.

6.1.2 Effect of film thickness and vacuum treatment on atmospheric adsorption

As was noted in section 6.1.1, some films appeared to be more sensitive to atmospheric adsorption, showing a dark conductivity change on ageing more than 1 order of magnitude. To investigate this point in more detail, an *ageing sensitivity* parameter was introduce. The ageing sensitivity is determined as a ratio of maximum to minimum dark conductivity values obtained during ageing – annealing cycles. Such definition allows to compare structures grown under different deposition conditions, where the ageing process results in both directions of conductivity changes. Ageing sensitivity has been investigated on a series of

microcrystalline silicon films of thickness varied between 0.09μm and 0.8μm. Figure 6.3 shows the dependence of atmospheric ageing effect on film thickness.

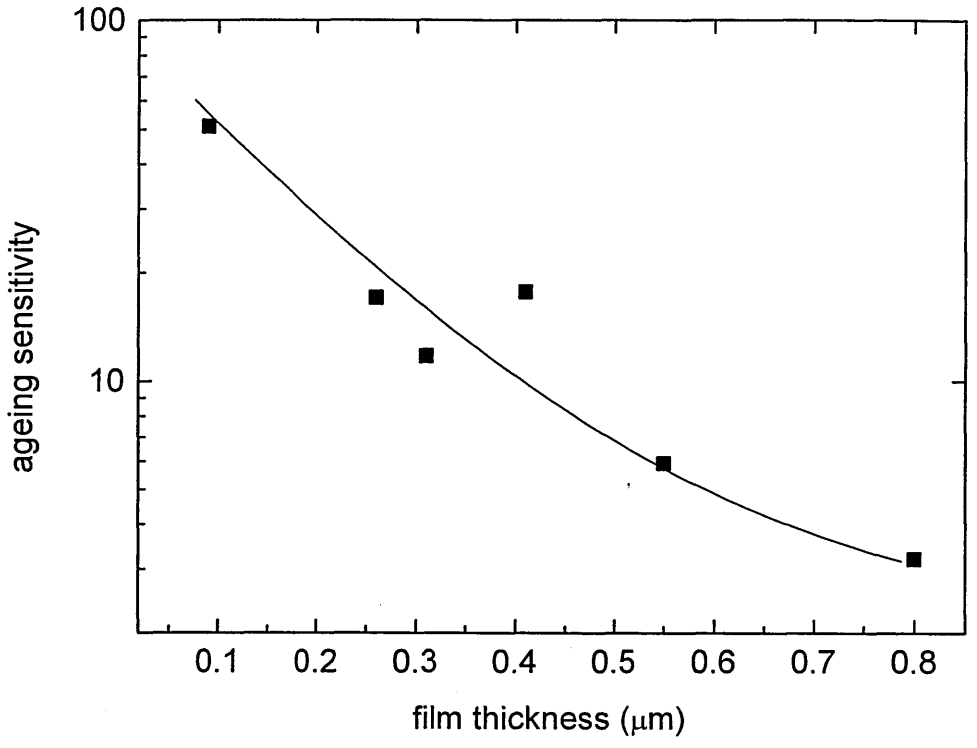

Figure 6.3. A dependence of atmospheric ageing process on film thickness. The line is to guide the eye.

The general trend clearly demonstrates that thinner films are found to be more sensitive to the ageing process. The sensitivity to atmospheric ageing may be linked to the material microstructure [Smirnov *et al.* 2005]. As was described in detail in chapter 1, the microstructure of microcrystalline silicon films significantly changes with film thickness. Even for optimised deposition conditions, the initial growth layers are found to contain large voids fraction (Luysberg *et al.* 1997, Houben *et al.* 1998), especially in the case of low silane concentration growth. The voids fraction, in general, reduces with film thickness (Houben *et al.* 1998). These voids could promote the process of atmospheric gases adsorption, which results in high conductivity changes. Thus for the thicker films the effect of exposure to atmosphere is reduced.

In the experiments described above annealing of aged films has been performed in a vacuum chamber. Typically heating of samples started in 5 minutes after the pressure went down to a level of 10^{-3} torr, because it was found that *room temperature* vacuum treatment is not able to remove completely adsorbed atmospheric species in any type of microcrystalline silicon even if applied for several days.

Figure 6.4 shows an effect of vacuum on room temperature dark conductivity of 10 days aged microcrystalline silicon films.

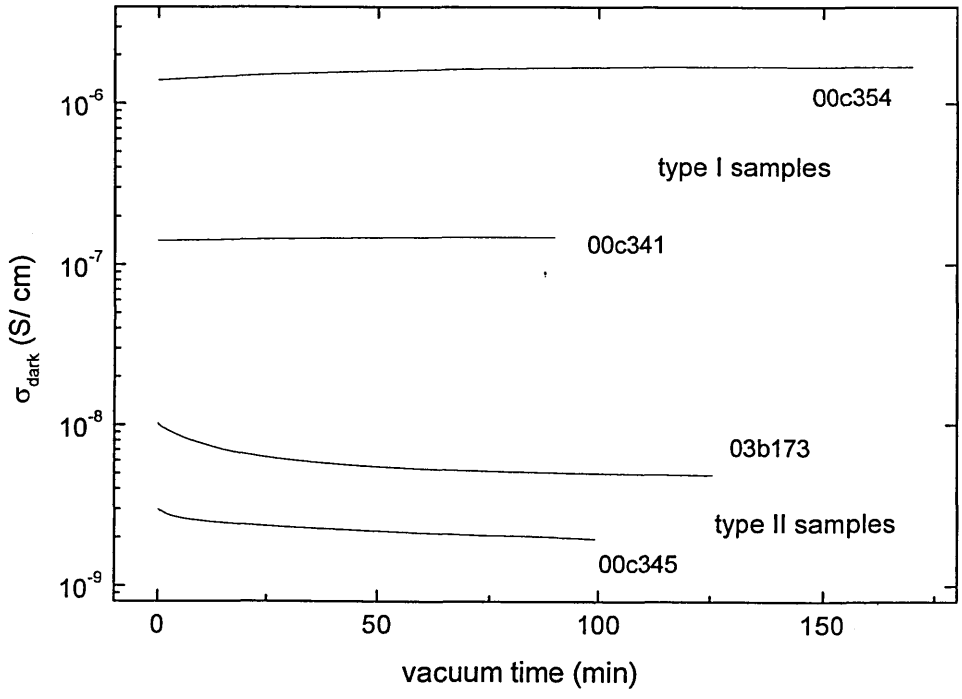

Figure 6.4. The effect of vacuum (10^{-3} torr) on dark conductivity of aged microcrystalline silicon films.

As one can see, room temperature vacuum treatment is able to reduce the effect of ageing. The figure suggests that room temperature vacuum has a smaller fractional effect on type I materials, while type II samples appear to be more sensitive. The possible explanation is related to morphological differences between type I and type II microcrystalline silicon. Type I samples, deposited at low silane concentration, are usually highly crystalline structures with large

number of *crack-like* voids [Luysberg *et al.* 1997, Houben *et al.* 1998, Finger *et al.* 2003] placed between crystalline grains. The adsorbed atmospheric components can diffuse through these voids into material bulk, resulting a higher resistance to vacuum. Type II materials are usually found to be more compact, containing spherical voids and less crack-like voids [Luysberg *et al.* 1997, Finger *et al.* 2003]. In this case the adsorbed atmospheric components would generally less diffused into the material bulk, and thus can be more easily removed from the surface by vacuum.

Based on discussion given above a distribution of voids in microcrystalline silicon films may be viewed as schematically drawn in figure 6.5. The figure shows a decrease of void fraction with film thickness and crack-like voids in highly crystalline (left) silicon film.

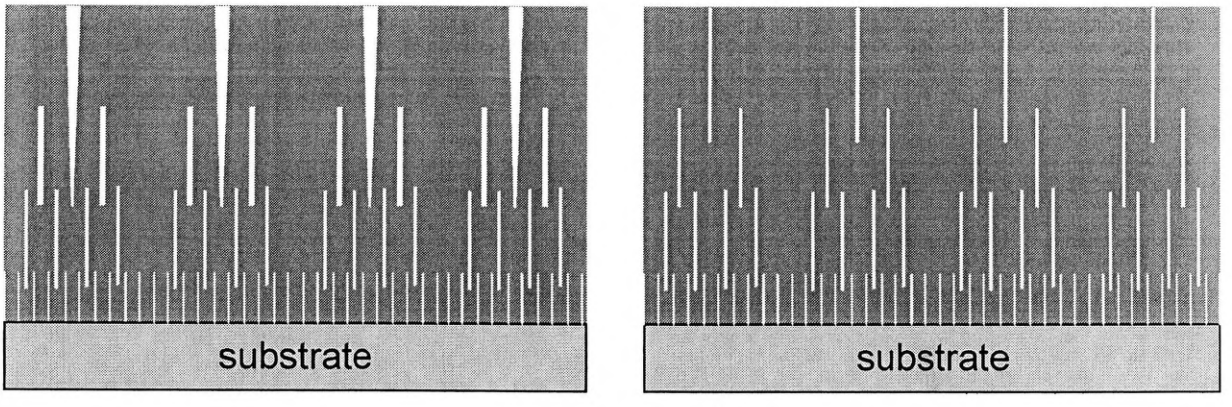

Figure 6.5 Schematic diagram of void distribution in highly crystalline (left) and transitional (right) microcrystalline silicon films.

6.1.3. Relationship between boron doping and atmospheric adsorption

The effect of atmosphere on dark conductivity of the series of boron doped microcrystalline silicon films is presented in figure 6.6. In annealed condition, dark conductivity increases with increase of doping, as expected. The series was

deposited at 3% silane concentration and estimated crystalline volume fraction from Raman scattering measurements was found to be 0.7-0.8 for all films. Considering nominally undoped film, the dark conductivity value in annealed condition σ_{dark}=1.6x10^{-8} S/cm which is several orders of magnitude below expected value for a given crystallinity [Vetterl *et al.* 2000]. This suggests the film may have some residual compensating doping.

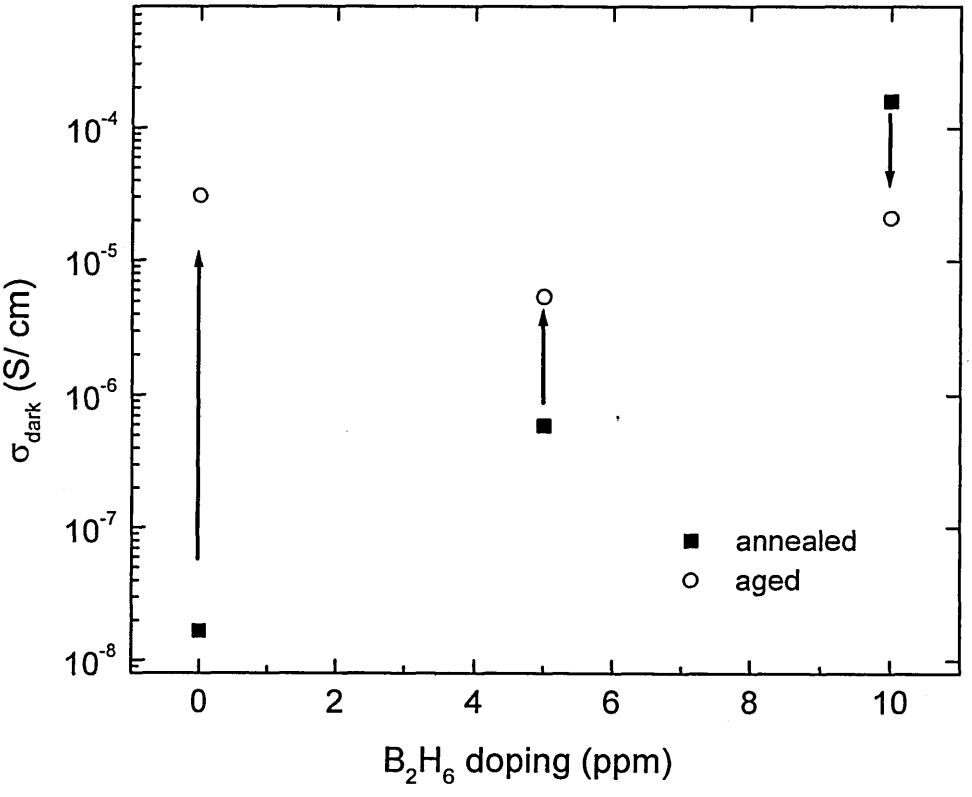

Figure 6.6. Dark conductivity σ_D for ageing – annealing cycles *vs.* boron doping.

Although the boron-doped series was found to be highly crystalline, a strong *increase* in conductivity was exhibited by the nominally undoped film (sample 02b299) on ageing. Such behaviour is more commonly associated with more compact films grown at higher silane concentration [Finger *et al.* 2003], however an increase of dark conductivity on air exposure has been reported [Finger *et al.* 2003] for the films deposited at low silane concentration.

It can be seen that addition of diborane to the process gas can reduce or even reverse the effect of ageing. Greater effect on exposure to atmosphere is observed for a nominally undoped film. The 10 days' ageing is able to increase the dark conductivity values by some 3 orders of magnitude. At a diborane gas concentration of 5 vppm, the dark conductivity increase after ageing is reduced by two orders of magnitude to a factor of 10. The film doped with 10 vppm of B_2H_6 shows a *decrease* in dark conductivity of about one order of magnitude. This can be explained if suggest that boron doping shifts the Fermi level so as to oppose the effects of ageing [Smirnov *et al.* 2004a], which would compensate the build-up of an electron accumulation layer. At 10 vppm film boron doping dominates and the initial conduction path is p-type. Adsorption of atmospheric species results in bending of valence band away from midgap, however the conduction path still remains p-type, albeit with a reduced carrier density. It should be also noted that the 10 vppm film is slightly thicker then two other films, which may influence its microstructure and the effect of ageing, as discussed in section 6.1.2.

The film deposited with a diborane concentration of 5 vppm shows a reduced conductivity increase in comparison with nominally undoped sample. The following suggestion is to explain the reduction in conductivity change on exposure to air by 2 orders of magnitude. At 5 vppm film, the initial (in annealed condition) conduction path is p-type. Ageing results in banding of conduction band to midgap and finally the conduction path becomes n-type when the process of atmospheric adsorption dominates. To check our suggestion have investigated the conductivity changes of 5 vppm sample during ageing process were investigated in more detail. If our reasoning is correct, the dark conductivity should reveal a dip as ageing proceeds, as the Fermi level effectively traverses the band-gap. The time dependence of ageing/ annealing cycle for 5 vppm B_2H_6 film is presented in figure 6.7.

Annealing process reduces the dark conductivity value. It should be noted that the sharp peak is observed in the beginning of annealing, associated with rapid removal of adsorbed atmospheric components, which is the characteristic feature of type II materials (see figure 6.2b). On air admittance, the dark conductivity initially decreases, which is opposite to what is expected for type II samples, where the conductivity increases on ageing (see figure 6.2b). Although

the doped and type II undoped samples show an opposite conductivity change on air admittance, the origin of the process is the same, and determined by band bending. In nominally undoped microcrystalline silicon films the Fermi level position is usually shifted from the midgap to the conduction band due to

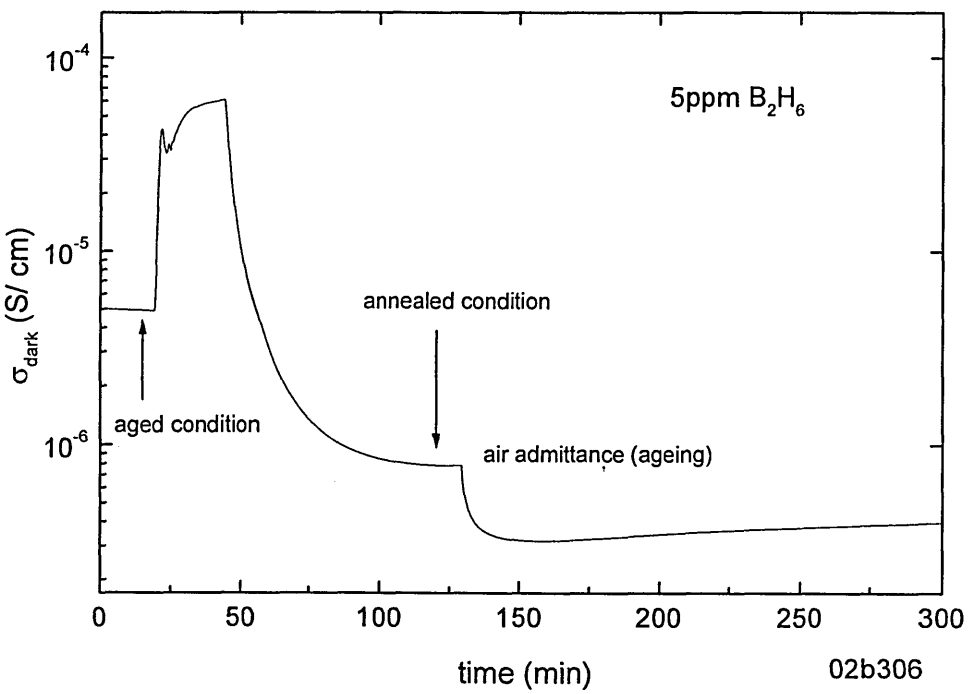

Figure 6.7. Ageing-annealing cycle of 5 vppm boron doped film.

unintentional atmospheric contaminations during deposition process [Luysberg *et al.* 1997, Finger *et al.* 1998]. In this case, for type II materials, the ageing process will result in bending of conduction band to midgap, increasing the dark conductivity. This is what normally observed in type II microcrystalline silicon films on air exposure. In the case of 5 vppm B_2H_6 film the initial conduction path is p type and the Fermi level is below midgap (see figure 6.8a). The ageing process bends conduction and valence bands. This results in initial decrease of dark conductivity on air admittance due to banding of valence band away from the Fermi level. At some point the Fermi level appears around the midgap position, as shown in figure 6.8b, yielding a minimum conductivity value. Further adsorption of atmospheric components induces a larger bending of the conduction band to the

midgap and the midgap "moves" below the Fermi level position (see figure 6.8c). This results in n-type conduction path and an increase of conductivity, revealing the dip.

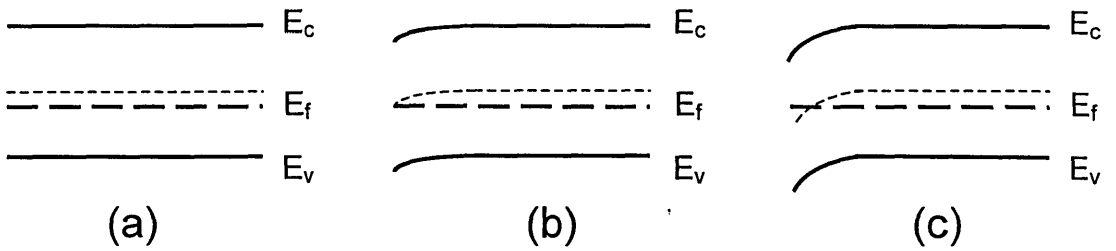

Figure 6.8. Schematic band diagram of 5 vppm boron doped film on ageing; conditions: (a) annealed, (b) dip in figure 6.7, (c) aged.

It should be noted that nominally undoped film (02b299) appeared to be highly sensitive to atmospheric adsorption – it shows some 3 orders of magnitude conductivity change on ageing. This is higher then all other samples studied here and around 2 orders of magnitude higher in comparison with films of 0.3-0.4 micron thick as shown in figure 6.3. A possible explanation could be related to increased void fraction. This sample has been grown in a different deposition reactor, optimised for doped structures deposition, which can result in microstructural modifications [Finger 2003], particularly, an increase in void fraction could occur.

It was demonstrated that for compensated microcrystalline silicon films studied here 3 different types of conductivity behaviour on air admittance could be observed:

(i) conductivity increase (such as for undoped sample)
(ii) dip for slightly doped samples (such as 5 vppm film) and
(iii) decrease for strongly doped materials (such as 10 vppm sample).

In all these cases the adsorption of atmospheric components results in same direction of band bending, but depending on the initial position of the Fermi level, the different types of behaviour take place. Although the different directions of

conductivity changes are observed in these materials, it is clear from above discussion that considering the effect of exposure to atmosphere, the materials of boron doped series studied here can be placed in type II category of microcrystalline silicon. This underlines the fact that an interpretation of the effects of atmospheric instabilities may lead to the additional information on the material properties, particularly the material morphology. However, in many cases careful observations are required in order to avoid misinterpretations.

Summary

In this section the reversible effects of atmosphere on dark conductivity of microcrystalline silicon films have been studied. It was shown that ageing could result in decrease in dark conductivity for type I films, deposited at low silane concentration and increase in dark conductivity for type II films, where large amorphous fraction presents. A difference in annealing behaviour between type I and type II films has been observed and explained in terms of rapid removal of adsorbed atmospheric components. Investigations of ageing on a series of films of varying thickness and effects of room temperature vacuum treatment led to conclusion that voids may play a significant role in the adsorption process. Particularly it was found that thinner films appear to be more sensitive to effects of ageing. Adding a small amount of diborane gas during deposition could reduce or even reverse dark conductivity changes.

6.2. Effect of atmosphere on dark and photoconductivity

From the series of microcrystalline silicon films studied here the sample 02b299 was found to be the most sensitive to ageing, so the sample was selected for more detailed investigation of the atmospheric effects. Dark and photoconductivity results, together with TPC curves have been taken several times during the ageing process to monitor material changes.

6.2.1. Dark conductivity and Fermi level position

Figure 6.9 shows the changes in dark conductivity of the film over a period of two weeks.

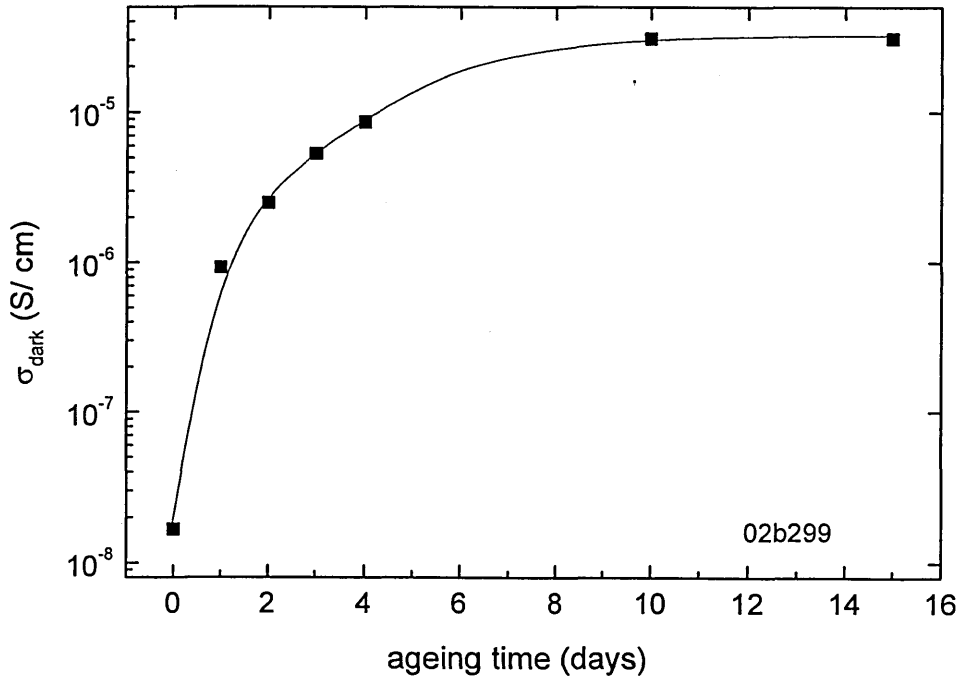

Figure 6.9. Dark conductivity changes as a function of time. The line is to guide the eye.

The first point on the graph corresponds to the annealed condition of the sample, where the dark conductivity was measured under a vacuum of about 10^{-3} torr. Subsequently the sample was left in open air conditions and the dark conductivity values were recorded. It can be seen that the dark conductivity changes by some three orders of magnitude over a period of ten days. The most significant changes take place during first days, after which the process of atmospheric ageing comes to saturation region. After ten days period further air exposure does not change significantly the dark conductivity values.

Corresponding changes in the Fermi level position relative to the transport level, calculated based on equation (1.1), are presented in figure 6.10. The figure shows that the Fermi level effectively shifts toward the conduction band by approximately 0.2 eV over the period of 10 days.

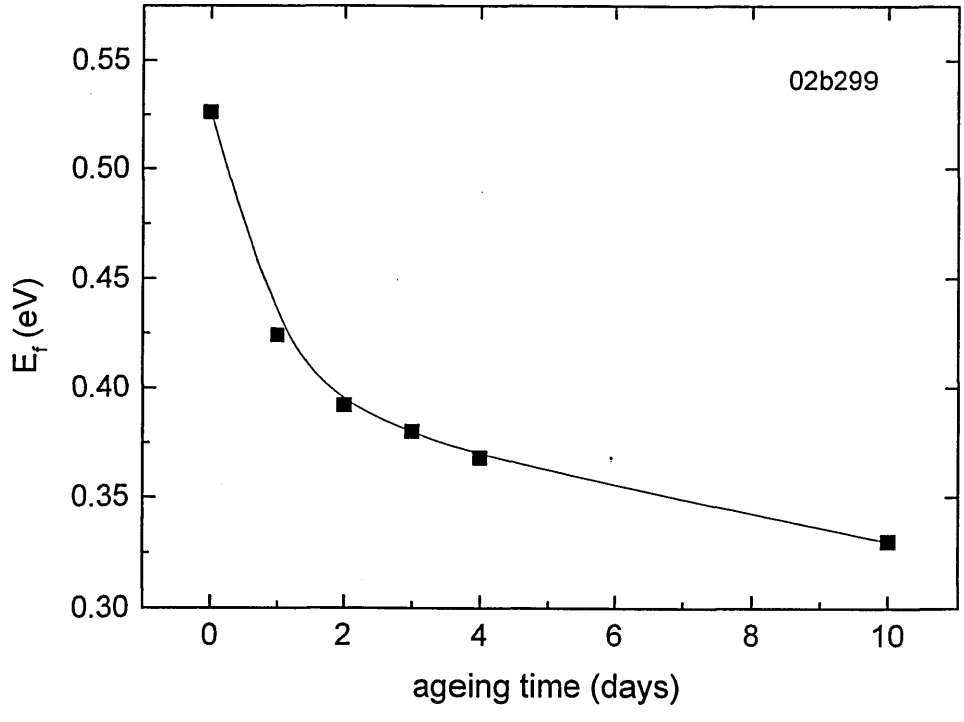

Figure 6.10. Changes in the Fermi level position on ageing. The line is to guide the eye.

Similarly to the previous graph, the greater shift takes place during first days of exposure to atmosphere. The increase in dark conductivity values and corresponding shift of the Fermi level position on ageing are associated with the

adsorption of atmospheric components on the film and subsequent band bending effect [Finger *et al.* 2003, Smirnov *et al.* 2004a]. The mechanism of band bending was described in great detail in chapter 2.

6.2.2. Steady state photoconductivity

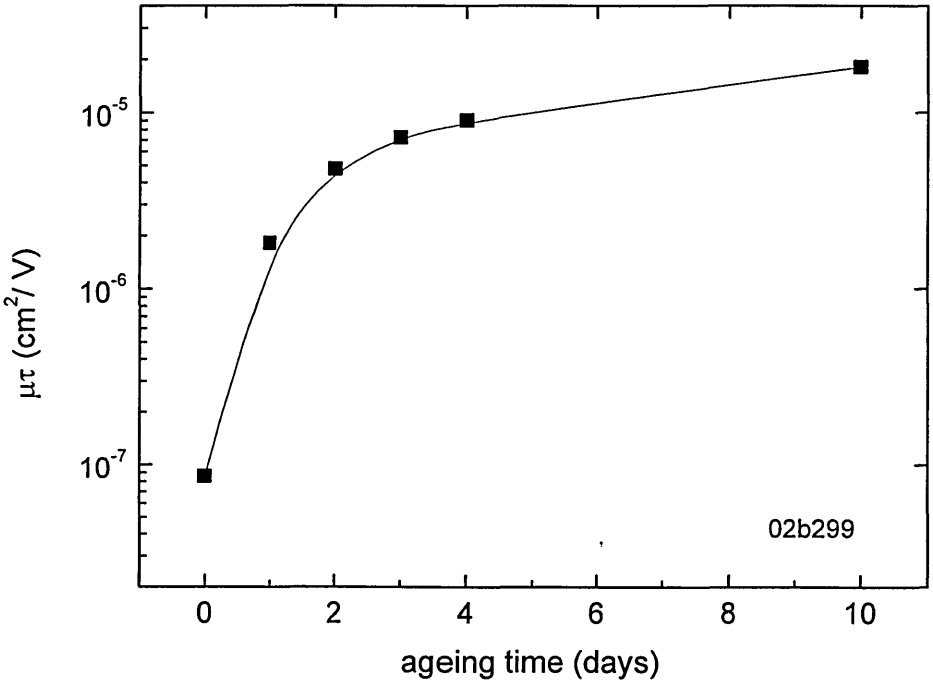

Figure 6.11. Mobility-lifetime product *vs.* ageing time for sample 02b299, measured at photon flux $\Phi=10^{14}$ $cm^{-2}s^{-1}$. The line is to guide the eye.

Changes in the mobility-lifetime product over the period of time are presented in figure 6.11. One can see that the $\mu\tau$ product increases by some two orders of magnitude over ten days ageing period. The changes in mobility-lifetime product are related to the changes in the Fermi level position [Brüggemann and Main 1998, Smirnov *et al.* 2004a], which takes place when the sample is exposed to atmosphere. The changes in the Fermi level position as shown in figure 6.10 will result in occupation of some defects by electrons, making these defects inaccessible for excess electrons, increasing the electron lifetime and $\mu\tau$ product. The mechanism of the mobility-lifetime product changes is similar to that observed for silane concentration series (see chapter 5), where the $\mu\tau$ product decreases if

the silane concentration increases. In that case the shift of the Fermi level position was introduced by changes in material deposition conditions and microstructure. In the case of ageing discussed here the changes are obtained in same sample and the changes in the Fermi level position relative to conduction band achieved by the process of adsorption of atmospheric components.

Although for the 02b299 sample the mobility lifetime product increases with ageing time, the material photosensitivity, the ratio of photo- to dark conductivities, decreases. The photosensitivity changes of the sample exposed to atmosphere are presented in figure 6.12.

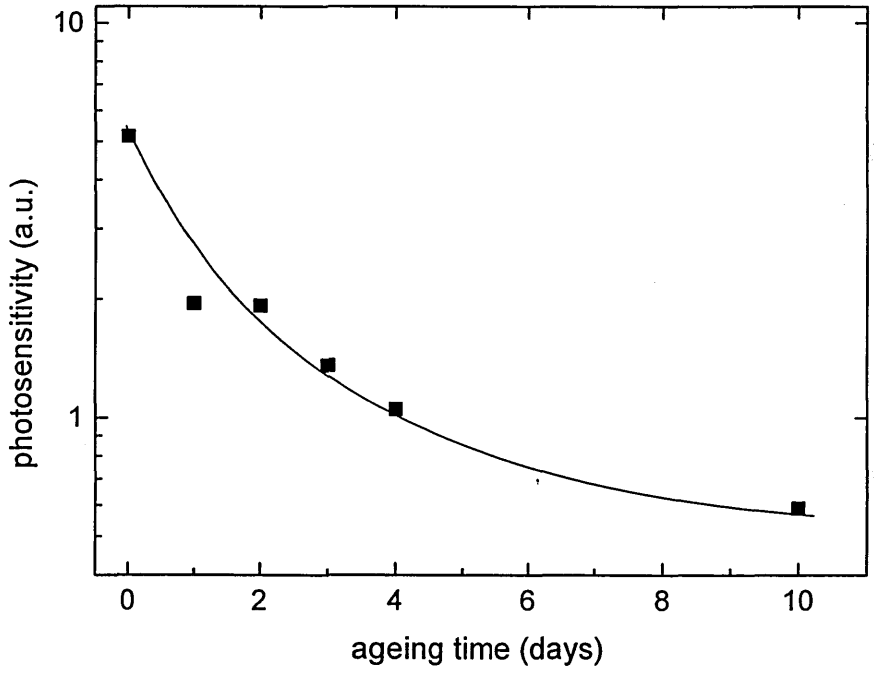

Figure 6.12. Changes in material photosensitivity *vs.* ageing time, sample 02b299. The line is to guide the eye.

Figure 6.12 shows that the material photosensitivity decreases by approximately one order of magnitude over a period of ten days ageing. It was discussed in chapter 5 that photosensitivity may be considered as an indicator of photovoltaic material quality and it is generally believed that high photosensitivity of absorber

layer is a necessary property of high efficient solar cells. Our results suggest that in general reversible ageing process may be undesirable for photovoltaic structures. Our suggestion is supported by a recent study of metastable effects in microcrystalline silicon solar cells [Sendova-Vassileva *et al.* 2005]. Although the work has not offered a detailed physical model of reversible ageing mechanism in solar cells, it was demonstrated that the adsorption of atmospheric components can result in reversible reduction of cell efficiency and particularly strong reduction of efficiency was observed for solar cells incorporated absorbed layer with larger void fraction.

Changes in the photoconductivity index, γ, over a period of 10 days are presented in figure 6.13.

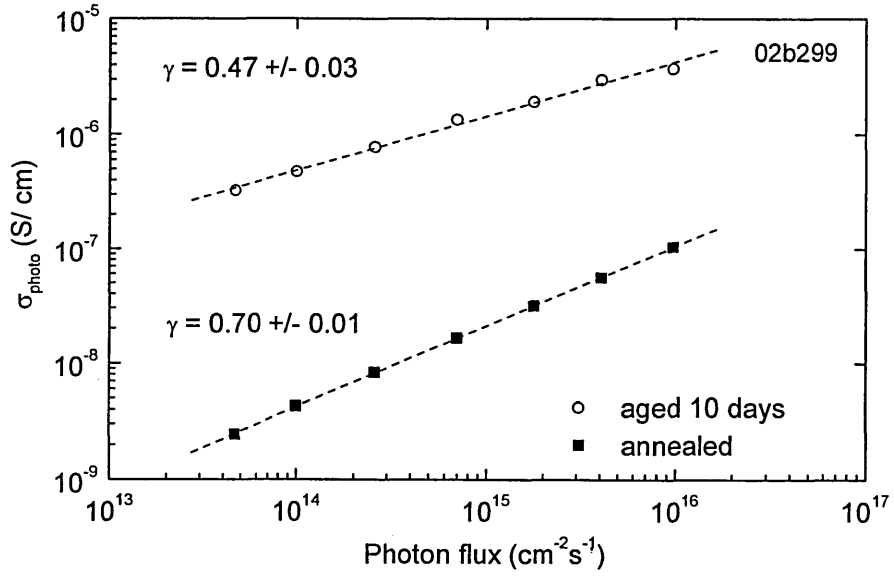

Figure 6.13. Photoconductivity σ_{photo} *vs.* photon flux for sample 02b299, in annealed state and after ageing for 10 days.

It can be seen that photoconductivity index γ changes from 0.7 in the annealed state to 0.47 after 10 days ageing. A 'standard' Rose model [Rose 1963] predicts photoconductivity index $0.5<\gamma<1$. In 10 days' aged condition photoconductivity index appears to be below 0.5. A photoconductivity index $\gamma< 0.5$ is frequently

observed in n-type amorphous silicon [Merazga 1991]. In the model proposed by Merazga to explain photoconductivity index $\gamma < 0.5$ in n type materials the recombination process is controlled by minority carriers. An observed decrease of photoconductivity index with ageing is consistent with a movement of the Fermi level towards the conduction band edge [Merazga, 1991, Main *et al.* 1996].

It was demonstrated above that the studied sample shows large variations in dark conductivity (about 3 orders of magnitude) and photoconductivity (about 2 orders of magnitude) on exposure to atmosphere. It is now interesting to compare how the variations due to ageing scale with dark- and photoconductivity data of microcrystalline silicon films grown under different deposition conditions.

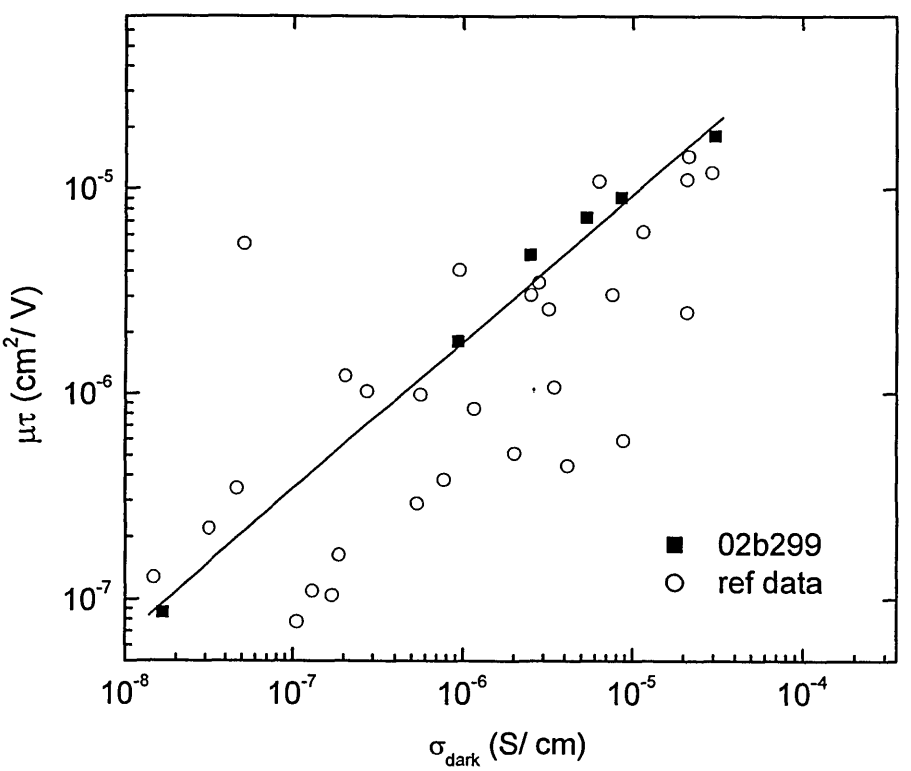

Figure 6.14. Variations of mobility-lifetime products with dark conductivity for 02b299 sample. Open cycles data presented for comparison (taken from Brüggemann *et al.* 1999, Brüggemann *et al.* 2001)

Figure 6.14 shows mobility lifetime products and dark conductivity for the 02b299 sample in annealed condition and over a period of 10 days ageing. The open circles points correspond to a series of microcrystalline silicon films grown at

various deposition conditions [Brüggemann *et al.* 1999, Brüggemann *et al.* 2001], where each data point corresponds to a single sample. Although some of the samples have been measured under vacuum conditions [Brüggemann 2004] others could be influenced by atmosphere during the measurement. The right hand side open circles correspond to the data obtained from microcrystalline silicon films with significant crystalline volume fraction, the left hand data correspond to the transitional microcrystalline silicon films. For the sample 02b299 the relationship is fitted by a power law of index approximately 0.7. The reference data show a similar trend in general, although a very large scattering of the data is observed. An important conclusion can be pointed out from the figure. It is clearly seen that a single sample, exposed to open air, can show very large variations in photoelectrical properties. Depending on the time exposed to atmosphere, the properties are in good agreement with the properties of transitional or highly crystalline microcrystalline silicon films. This underlines the relevance of the careful monitoring of atmospheric effects before any claims for the material transport properties are made. The monitoring of ageing effects can greatly reduce the scatter of the data, providing more realistic information on the true material properties.

Figure 6.15 shows the absorption coefficient of the sample measured by the Constant Photocurrent Method. The CPM experiment for these data was performed in air on the sample in aged condition and after annealing, when dark conductivity was around 3 orders of magnitude lower. No change in absorption spectrum down to 1.4 eV can be seen in the figure. An apparent increase in absorption coefficient with ageing is observed in the higher photon energy region. The apparent increase in α for aged sample could be related to changes in photoconductivity due to band bending (see figure 6.11). The effect of band bending may be particularly noticeable in the case of strongly absorbed light, because atmospheric components are adsorbed on the film surface. Brüggemann [Brüggemann 2005] reported almost no changes in absorption coefficient due to ageing for HWCVD samples, however the measurement range in the experiments was limited to 1.5 eV.

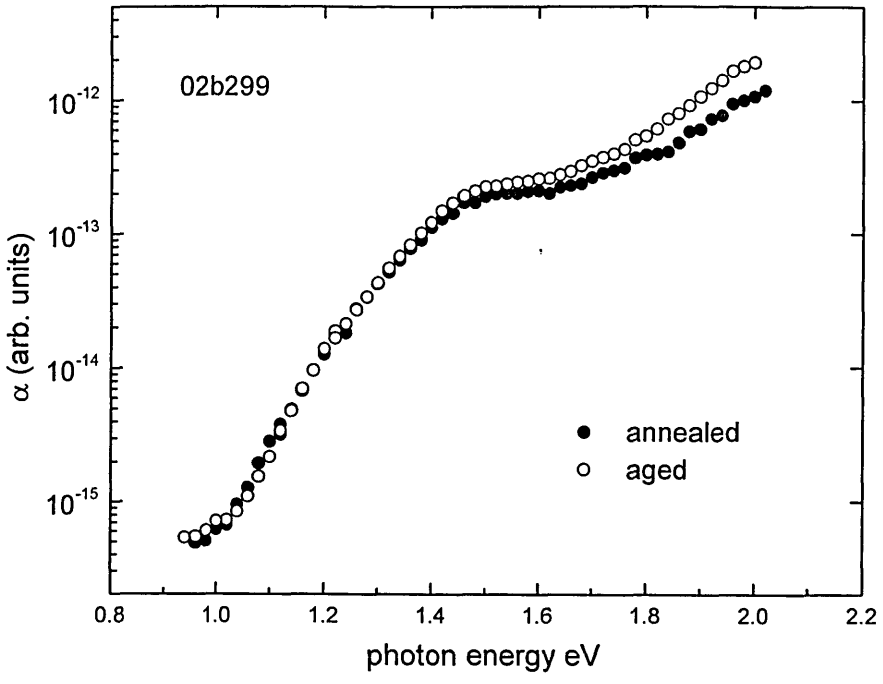

Figure 6.15. Absorption coefficient from CPM in annealed (full symbols) and aged (open symbols) conditions.

6.2.3 Transient photoconductivity

This section presents the results of transient photoconductivity measurements for 02b299 sample in annealed and exposed to atmosphere conditions. Two sets of transient photoconductivity measurements have been performed: the first set of measurements were carried out over about 2 weeks period after deposition and referred to as "as received" condition. It should be that the dark- and photoconductivity results for 02b299 sample presented earlier (sections 6.2.1 and 6.2.2) also correspond to as received condition of the sample. Second part of measurements has been carried out 6 months later. During the 6 months' period the sample was left in ambient air in the laboratory, to investigate long-term ageing effects. For both "as received" and "aged 6 months" conditions of the sample several transient photoconductivity decays were taken to investigate an effect of reversible changes.

Figure 6.16 shows a set of transient photoconductivity decays for the sample 02b299 in "as received" condition taken over a period of 10 days.

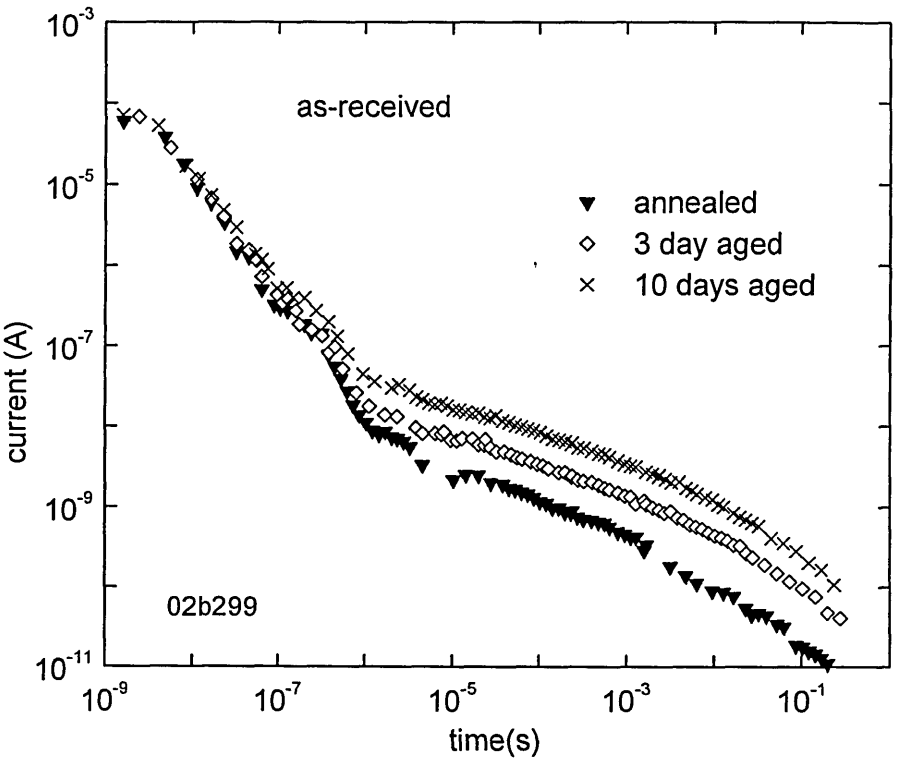

Figure 6.16. Transient photoconductivity decays for sample 02b299 in as-received condition.

Initially the sample was annealed, returned to room temperature and the photocurrent decay was recorded without breaking vacuum. This photoconductivity curve is plotted by solid triangles in the figure. Then the sample was left in the ambient air for ageing and two more photoconductivity decays were taken during the period of time. Transient photoconductivity curves taken in 6 months period are presented in figure 6.17.

The general trend observed is similar for both sets of measurements - there is an initial fall in current, steeper than t^{-1}, which reduces in gradient after approximately 1 μs. The effect of ageing is primarily to reduce the extent of the initial fall, although changes in slope also occur.

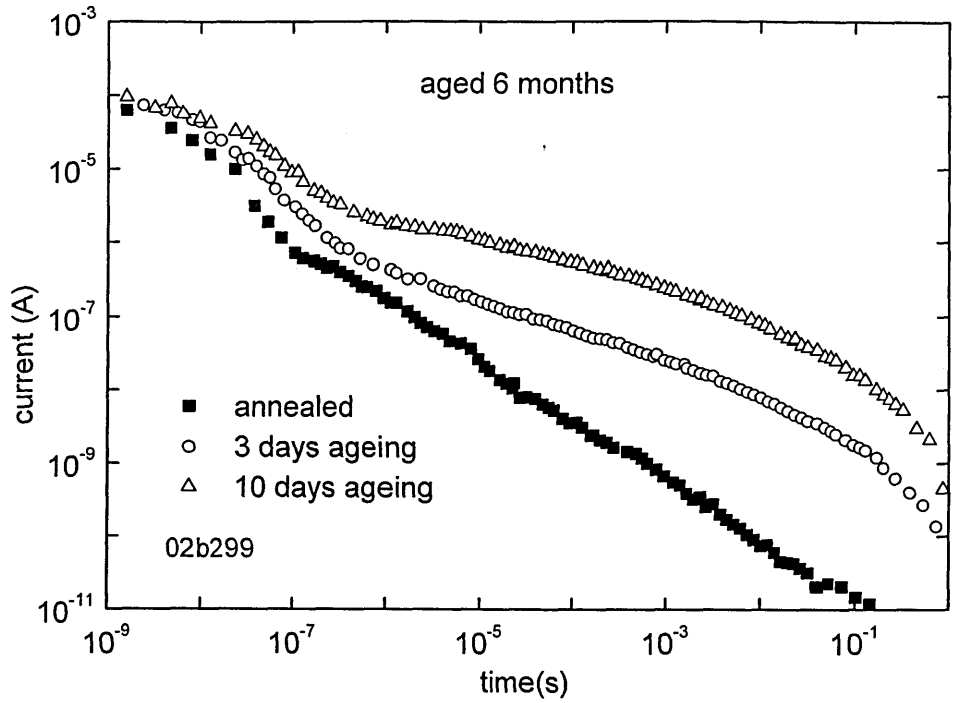

Figure 6.17. Transient photoconductivity decays for sample 02b299 in 6 months' aged condition.

The density of states corresponding to as received condition is presented in figure 6.18. The figure reveals a pronounced peak in the DOS for the as-received sample, of order 10^{17} cm^{-3} centred at about 0.5 eV. As short-term ageing proceeds, the peak moves to shallower energies. A slight increase in density of states is also observed.

However, it is unclear whether this reflects a true change in the DOS, or a change in occupancy within the same DOS caused by an effective shift in the Fermi level. A dark-current activation energy of 0.55 eV in the annealed state indicates that the Fermi level lies close to the centre of the apparent peak in the DOS, and based on relative changes in dark current it moves some 0.2 eV towards the band-edge over the ageing period. This suggests the observed effects may be accounted for solely by changes in space-charge.

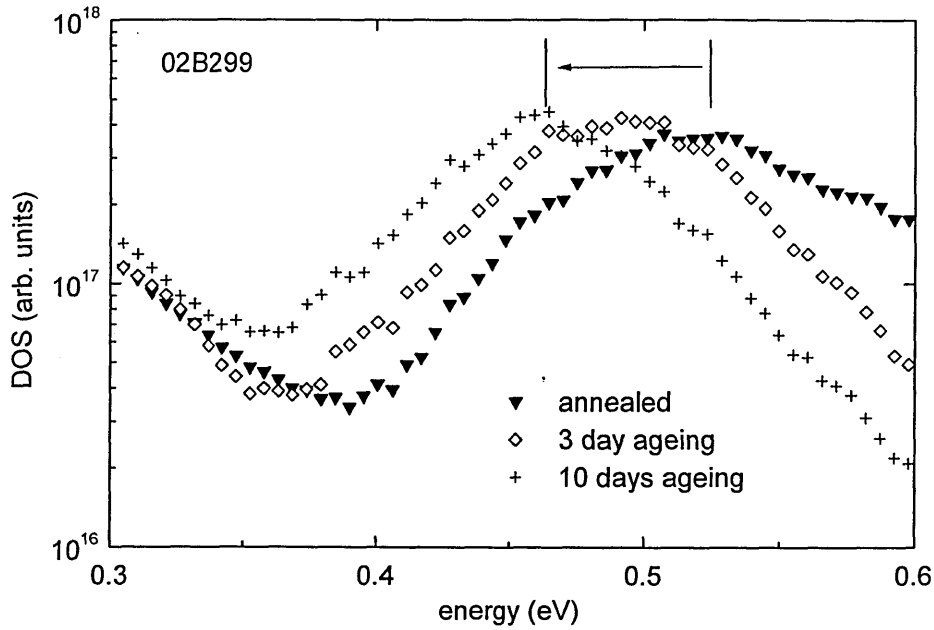

Figure 6.18. DOS curves obtained from the photoconductivity data in as received condition.

The density of states corresponding to 6 months' aged condition is presented in figure 6.19. Similarly to as-received condition of the sample, the density of states tends to decrease at deep energies as ageing proceeds. This behaviour is remarkable and similar to variations in the density of states observed for microcrystalline silicon films with varying crystalline fraction (see chapter 5). Transient photoconductivity measurements reported in previous chapter have demonstrated that the deep defect density appears to decrease with increased crystallinity. This result was attributed to the shift of the Fermi level position towards the conduction band with increasing crystallinity, that results in increased occupancy of deep states. In the present case the changes in the Fermi level position, due to atmospheric adsorption, also occur.

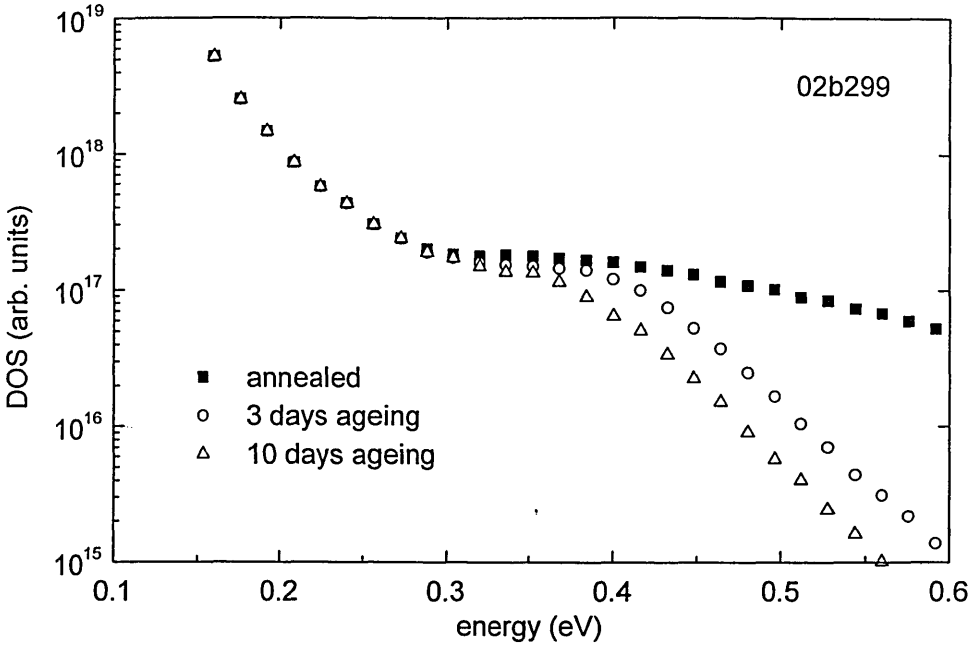

Figure 6.19. DOS curves obtained from the photoconductivity data in 6 months' aged condition.

6.2.4 Irreversible atmospheric effect

The results discussed in previous sections concerned atmospheric effects that can be reversed upon annealing at 160°C. As was already mentioned, the sample 02b299 was left in ambient air in the laboratory during 6 months. It was found that during this period dark conductivity activation energy E_a in the annealed state (excluding reversible adsorption) decreased by around 0.06 eV and an increase in dark conductivity was around 1 order of magnitude.

Figure 6.21 compares the density of states in 'as-received' and 'after 6 months' conditions in annealed state. It can be seen that after six months period the density of deeper defects (> 0.45 eV) has reduced, matched by an increase of shallower defects. If this reflects a true change in the DOS, then the sample would re-equilibrate, giving a shift in Fermi level towards the conduction band edge. This interpretation is supported by a decrease in dark current activation energy (in the

annealed state) by around 0.06 eV and an increase in room temperature dark conductivity by a factor of approximately 10 over the six-month period. Since it is widely believed [Finger *et al.* 1998, Kocka *et al.* 2003] that defects in microcrystalline silicon arise at grain boundaries, the irreversible change in the DOS may indicate a permanent reconfiguration of dangling bonds, or barrier parameters, due to oxidation.

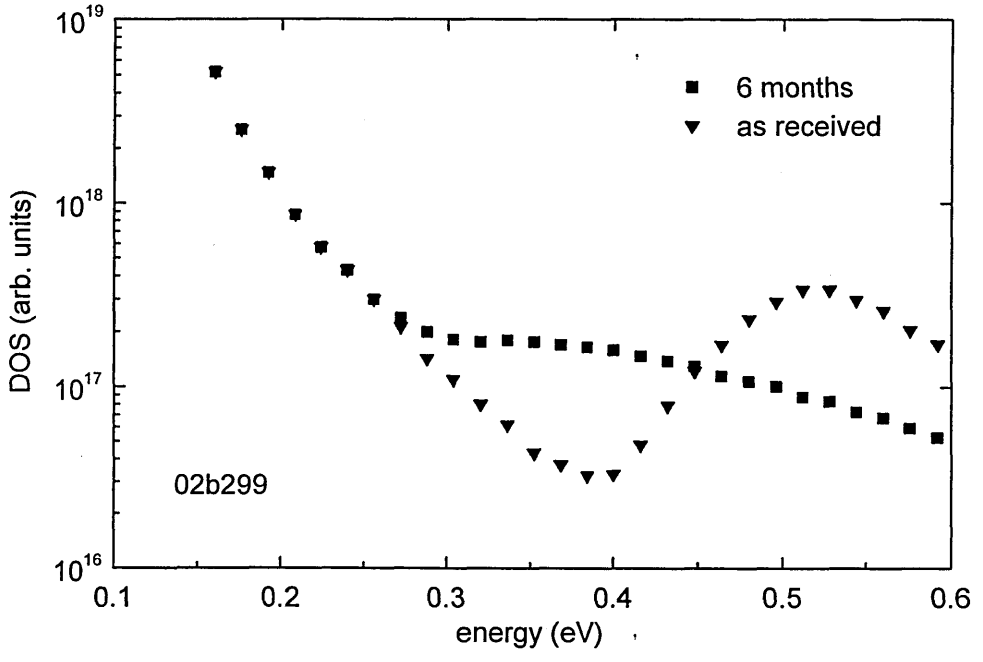

Figure 6.20. Comparison of the density of states distribution in as-received and 6 months' aged conditions in annealed state.

Summary

This section presented investigation of atmospheric effects by dark, steady state and transient photoconductivity measurements. Reversible effect results in systematic increase in dark conductivity and $\mu\tau$-product, and decrease in photoconductivity index. These results are correlated with changes in the Fermi level position and changes in the occupancy of localized states due to reversible adsorption of atmospheric components. Irreversible changes due to oxidation process over 6 months period have been observed that is reflected in the changes

in the density of states and an increase in dark conductivity value by a factor of 10.

6.3 Calculation of the density of adsorbed charge and computer modelling of atmospheric adsorption

6.3.1 Calculation of the density of adsorbed charge

It is important to estimate quantitatively the density of adsorbed charge that results in band bending and changes in dark conductivity, as shown in figures 6.9 and 6.10 for 02b299 sample. As was described in chapter 2, the equations given by Solomon [Solomon 1980] correlate the values of the band bending ΔV and the penetration depth Δ with the charge density on the film surface Q as $\Delta V = - Q/ e (\varepsilon \varepsilon_0 N_0)^{1/2}$ and $\Delta = 1/e (\varepsilon \varepsilon_0 / N_0)^{1/2}$, where ε is the dielectric constant of the material, ε_0 is the vacuum permittivity and N_o is the density of states near the Fermi level, e is the elementary charge. The values of parameters used in the calculation are summarised in Table 6.1.

Parameter	Value	Units
ε	12	-
ε_0	$8 \cdot 10^{-14}$	F/cm
e	$1.6 \cdot 10^{-19}$	C
N_0	$3 \cdot 10^{17}$	$cm^{-3}eV^{-1}$
ΔV	0 – 0.196	eV

Table 6.1. The values of calculation parameters.

The value of the penetration depth is found to be around $\Delta = 0.05$ μm that is around 15% of the film thickness. The areal density of adsorbed charge after 10 days of exposure sample to air is found to be around $Q = 4 \cdot 10^{-8}$ C/ cm^2 that is equal to $2.6 \cdot 10^{11}$ elementary charges per cm^2. This value is in agreement with given by Solomon [Solomon 1980]. The changes in the adsorbed charge density during a period of 10 days are presented in figure 6.21.

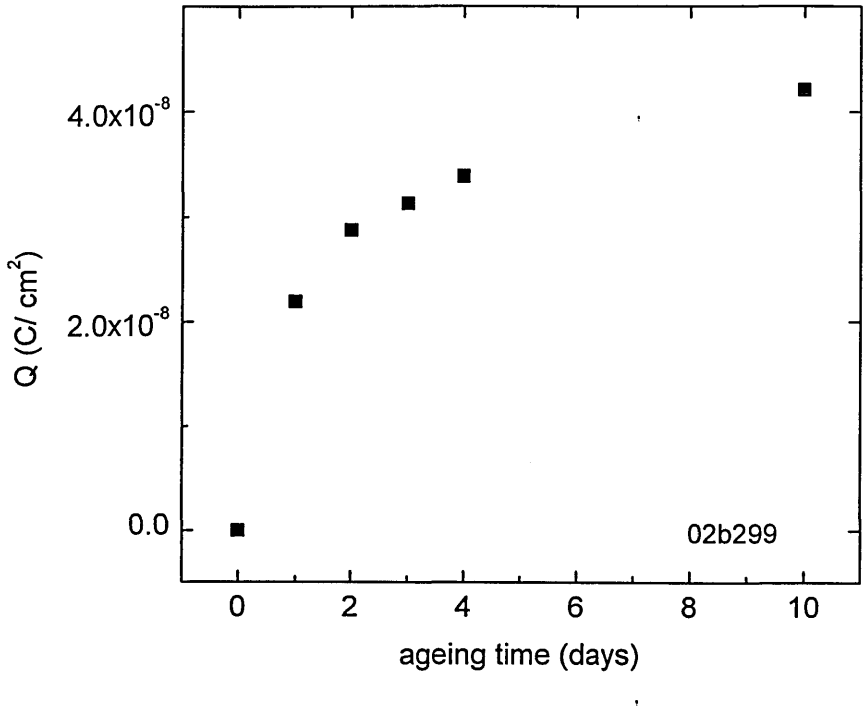

Figure 6.21. Changes in the adsorbed charge density during a period of 10 days.

6.3.2 Computer modelling of atmospheric adsorption

6.3.2.1 Basic description of the model

The program used to model the effects of atmospheric adsorption is based on code developed by W. Gao [Gao 1995] to simulate electronic processes in *pin* structures based on amorphous materials. The basic description of the simulation is given in appendix 1. While the original program was developed for solar cell simulation, it is suitable with modifications to model the case of adsorbed charge on a film. The simulation considers adsorbed atmospheric components as a charge of density Q placed in a region close to film surface and penetrated into the film for depth Δ (see figure 6.22).

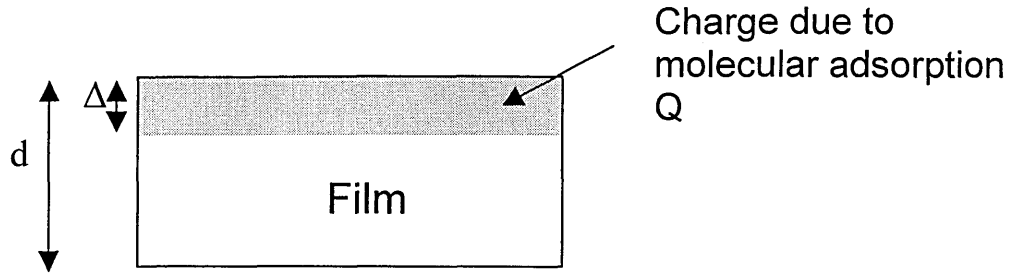

Figure 6.22. Schematic diagram of charge due to molecular adsorption.

6.3.2.2 Simulation of ageing in nominally undoped film (0 vppm)

The parameters used to simulate atmospheric adsorption for nominally undoped film are listed in table 6.2.

Table 6.2. Simulation input parameters for 0 vppm film.

Density of adsorbed charge	Q	0-2.2x10^{17}	cm^{-3}
Penetration depth	Δ_1 Δ_2	0.05 0.14	μm
Film thickness	d	0.34	μm
Fermi level position	E_f	0.53	eV
Mobility gap	E_g	1.1	eV
Band edge density of states	$g(E_c)$	4x10^{21}	$cm^{-3}eV^{-1}$
Characteristic energies for band tails	E_{CT} E_{VT}	0.025 0.030	eV
Gap centre defect density	N_0	3x10^{17}	cm^{-3}
$D^{+/0}$ energy	$E^{+/0}$-E_V	0.45	eV
Defect correlation energy	U	0.2	eV
Free electron and hole mobilities	μ_n μ_p	10 5	cm^2/Vs
Capture coefficients ratio	C_n/C_p	1	
Temperature	T	297	K

The input parameters for density of states and carrier mobilities have been selected to suit microcrystalline silicon material with large crystalline volume fraction [Dylla 2005]. The density of charge due to molecular adsorption was varied between 0 (for annealed condition) and 2.2×10^{17} cm^{-3} (10 days aged) that provides band-bending value ΔV=0.2 eV in fully aged condition. Two sets of simulations have been performed. Simulation 1 assumes penetration depth Δ_1 based on calculations performed in the previous section. For Simulation 2 the value of penetration depth Δ_2 has been selected to fit most closely experimental results.

Changes in dark conductivity depending on band-bending are presented in figure 6.23

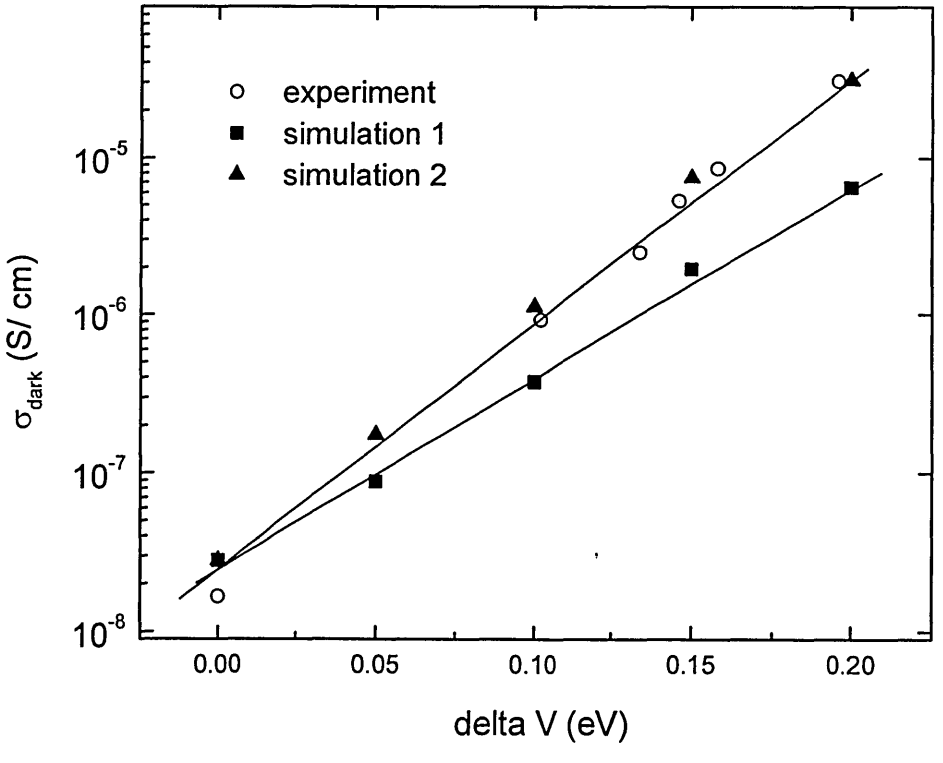

Figure 6.23. Computer modelled changes in dark conductivity with ageing for 02b299 sample (0 vppm).

Simulation 1 shows that dark conductivity increases with ageing significantly below experimental values. The value of penetration depth Δ_1 used in this

simulation is calculated based on assumption [Solomon 1980] that charge is adsorbed *on a film surface*, as one may expect for the case of amorphous silicon film. In the case of microcrystalline silicon, atmospheric components may diffuse into a film due to presence of voids, increasing penetration depth. Figure 6.23 shows that an increase of penetration depth (around 3 times) would give an excellent agreement with experimental data. This supports our view that voids in microcrystalline silicon play a significant role in the ageing process.

6.3.2.3 Simulation of ageing in 5 vppm film

Table 6.3 indicates the parameters used to simulate atmospheric adsorption for 5 vppm film. Based on dark conductivity value in annealed condition, the Fermi level position was taken to be equal to 0.51 eV. Other parameters, including the amount of charge due to molecular adsorption, are the same as for nominally undoped film.

Table 6.3. Simulation input parameters for 5 vppm film.

Density of adsorbed charge	Q	$0\text{-}2.2\text{x}10^{17}$	cm^{-3}
Penetration depth	Δ	0.14	µm
Film thickness	d	0.34	µm
Fermi level position ($E_v - E_f$)	E_f	0.51	eV
Mobility gap	E_g	1.1	eV
Band edge density of states	$g(E_c)$	$4\text{x}10^{21}$	$cm^{-3}eV^{-1}$
Characteristic energies for band tails	E_{CT} E_{VT}	0.025 0.030	eV
Gap centre defect density	N_0	$3\text{x}10^{17}$	cm^{-3}
$D^{+/0}$ energy	$E^{+/0}\text{-}E_V$	0.45	eV
Defect correlation energy	U	0.2	eV
Free electron and hole mobilities	μ_n μ_p	10 5	cm^2/Vs
Capture coefficients ratio	C_n/C_p	1	
Temperature	T	297	K

Figure 6.24 shows changes in dark conductivity depending on band-bending.

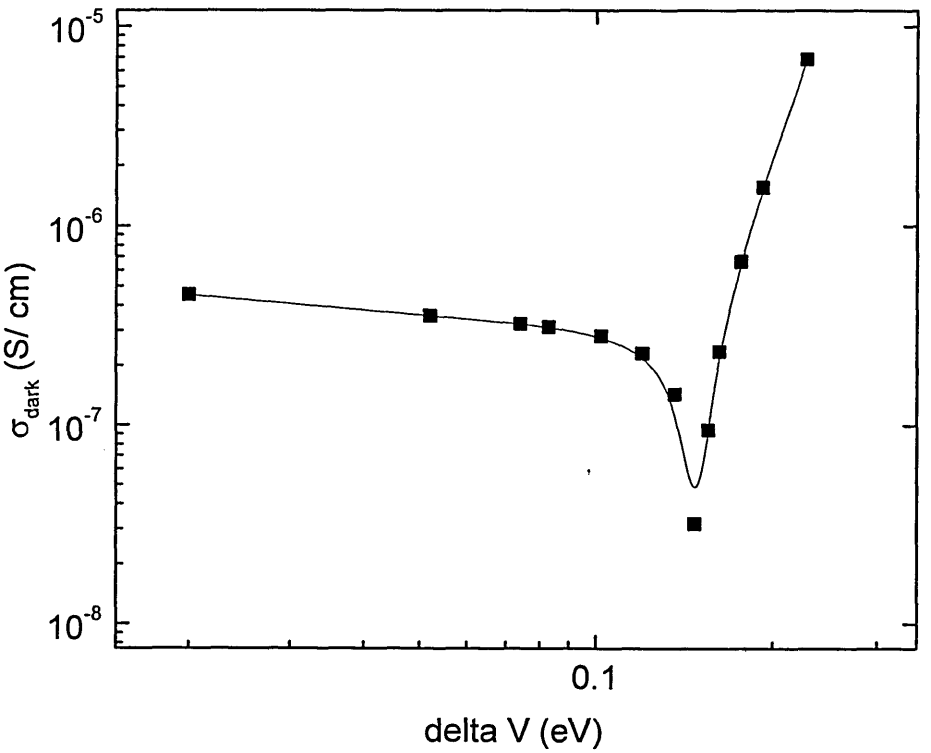

Figure 6.24. Computer modelled changes in dark conductivity with ageing for 5 vppm sample.

The simulation shows that dark conductivity initially decreases with ageing, and minimum dark conductivity is observed for ΔV=0.15 eV. The same 'conductivity dip' has been observed experimentally for 5 vppm film (see figure 6.7) as a function of ageing time. It can be seen that the same amount of adsorbed charge results in larger band bending in 5 vppm film comparatively to nominally undoped film: in the 'fully aged' condition the value of band bending is equal to 0.228 eV.

7.3.2.4 Comparison of ageing for 0 vppm, 5 vppm and 10 vppm films

The parameters used to simulate atmospheric adsorption for 10 vppm film are listed in table 6.4.

Table 6.4. Simulation input parameters for 10 vppm film.

Density of adsorbed charge	Q	0, $2.2x10^{17}$	cm^{-3}
Penetration depth	Δ	0.14	μm
Film thickness	d	0.42	μm
Fermi level position ($E_v - E_f$)	E_f	0.32	eV
Mobility gap	E_g	1.1	eV
Band edge density of states	$g(E_c)$	$4x10^{21}$	$cm^{-3}eV^{-1}$
Characteristic energies for band tails	E_{CT} E_{VT}	0.025 0.030	eV
Gap centre defect density	N_0	$3x10^{17}$	cm^{-3}
$D^{+/0}$ energy	$E^{+/0}-E_V$	0.45	eV
Defect correlation energy	U	0.2	eV
Free electron and hole mobilities	μ_n μ_p	10 5	cm^2/Vs
Capture coefficients ratio	C_n/C_p	1	
Temperature	T	297	K

Figure 6.25 presents a comparison of experimental data with the results of computer modelling for 0 vppm, 5 vppm and 10 vppm films. For all three samples the simulation assumed same penetration depth and same amount of adsorbed charge. The simulation gives a good agreement with experiment for nominally undoped and 5 vppm films. For 10 vppm film the simulation shows much smaller conductivity change than experimental data. A possible explanation may be related to the fact that the simulation assumes the same amount of charge due to molecular adsorption for all film. This may not be the case for thicker 10 vppm film, because an increase in film thickness and/ or boron doping may result in microstructural modifications, as was pointed out previously.

It is worth to note that according to simulation, same amount of adsorbed charge results in different values of band-bending. For 0, 5 and 10 vppm films the simulation gives the band-bending values equal to 0.2, 0.23 and 0.17 eV respectively. Based on DOS distribution used in simulation, the defect density at the Fermi level is found to be equal to $4.5x10^{16}$, $3x10^{16}$ and $6x10^{16}$ cm^{-3} for 0, 5 and 10 vppm films, respectively. Thus the simulation results demonstrate that an increase in defect density around the Fermi level results in smaller band bending value.

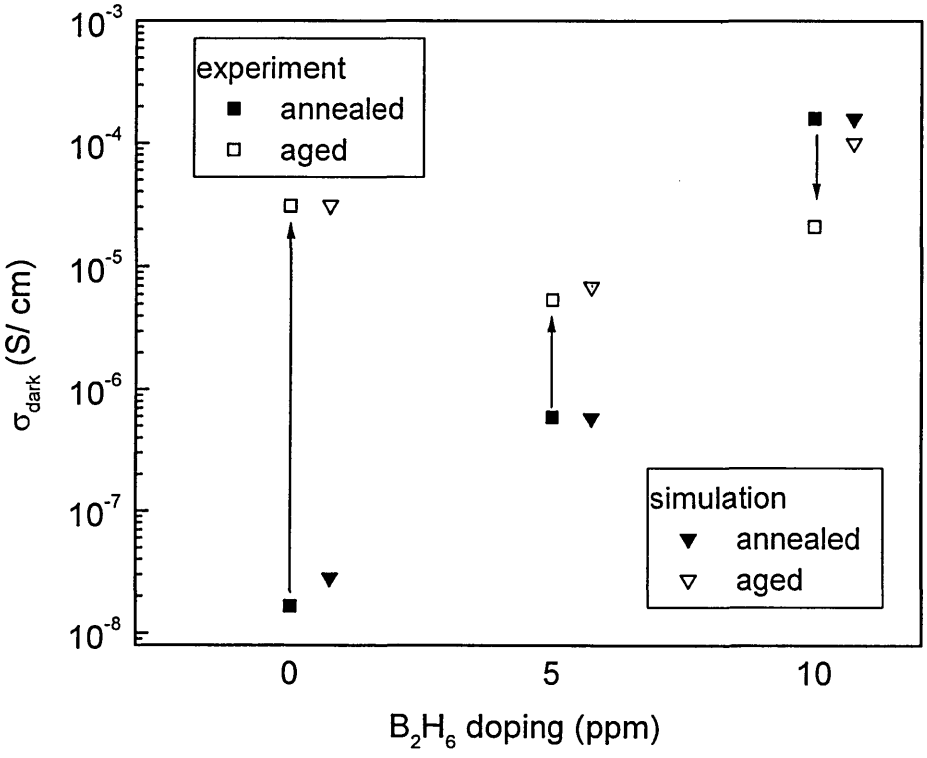

Figure 6.25 Comparison of experimental data with the results of computer modelling.

Summary

An agreement between computer modelled and experimental results suggests that the model and input parameters used in the simulations are able to describe accurately carrier dynamics in microcrystalline silicon. The simulation

confirms that the boron doping can reduce or reverse the effect of ageing and the value of band-bending decreases with increase in defect density at the Fermi level. It is also evident that the reversible effects of atmospheric adsorption are related to diffusion of adsorbed atmospheric components into the material bulk throw voids.

Chapter 7. Atmospheric effects – part II: Irreversible and reversible changes vs. composition

This section presents the study of reversible and irreversible atmospheric effects on a series of thin silicon films deposited at 3% and 5% silane concentration with thickness varied between 83 nm and 320 nm. Atmospheric effects result in reversible and non-reversible changes in dark and photoconductivity, conductivity prefactors σ_0 and activation energies for each single sample.

7.1 General conductivity behaviour under heating/ cooling cycles

The suitable materials to monitor the changes of morphology with thickness should be the films deposited under conditions where significant crystal formation is expected. Thus the silane concentrations of 3% and 5% were selected as the most appropriate for film growth at the present experiments.

Typical annealing curves obtained from a single sample are presented in figure 7.1.

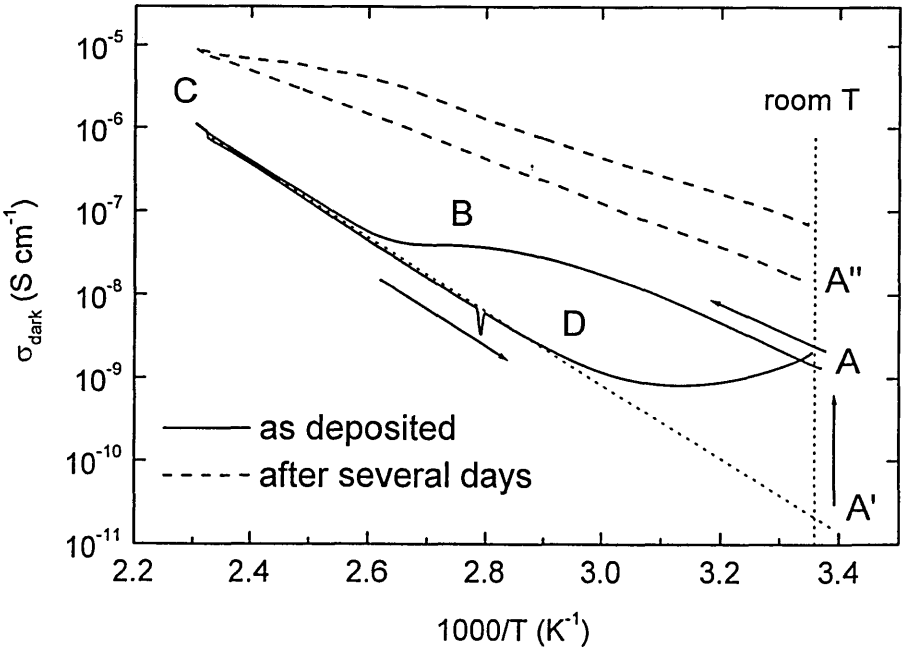

Figure 7.1. Typical annealing curves for a single film.

Point A in the figure corresponds to the current value measured soon after the sample was unpacked. Heating is presented by A-B-C path, while the cooling of the sample corresponds to C-A' path. When the temperature reaches a certain value, a desorption of atmospheric components can be observed. This region is marked by B letter in the figure 7.1. Subsequent cooling (C-A' path) of the sample enables activation energy and dark conductivity values to be determined. Similar behaviour is observed if annealing is performed in several days period, however dark conductivity in annealed condition is increased (point A'' in figure 7.1).

It should be noted that during the cooling of the sample an *increase* of current values could be observed with decreasing temperature. D in figure 7.1 indicates the starting point of this process. It is believed that this is related to the adsorption of atmospheric components starting at temperatures above room temperature and thus could increase conductivity values. Although annealing was performed under a vacuum of 10^{-3} torr, our previous experiments have demonstrated that this vacuum is able to reduce, but not able to completely remove atmospheric components (see chapter 6). Thus even if annealing is carried out at 10^{-3} torr, an interaction between atmospheric species and film could take place. This is what can be observed in the region D-A' of the graph: although temperature is decreasing the current values increase. Bearing in mind the above, the dark conductivity and activation energy values in annealed condition were calculated by extrapolating the straight line C-D to room temperature region (C-D-A').

The deviation of cooling curve from a straight line is also connected with the rate of cooling. In the above experiment the rate of cooling was kept at the average level around 0.6 K/min. Additional experiments have demonstrated that an increase of cooling rate leads to the straight line C-D-A', because in the case of fast cooling, the time when sample could interact with atmospheric components remaining in the vacuum chamber is minimized. This is shown in figure 7.2.

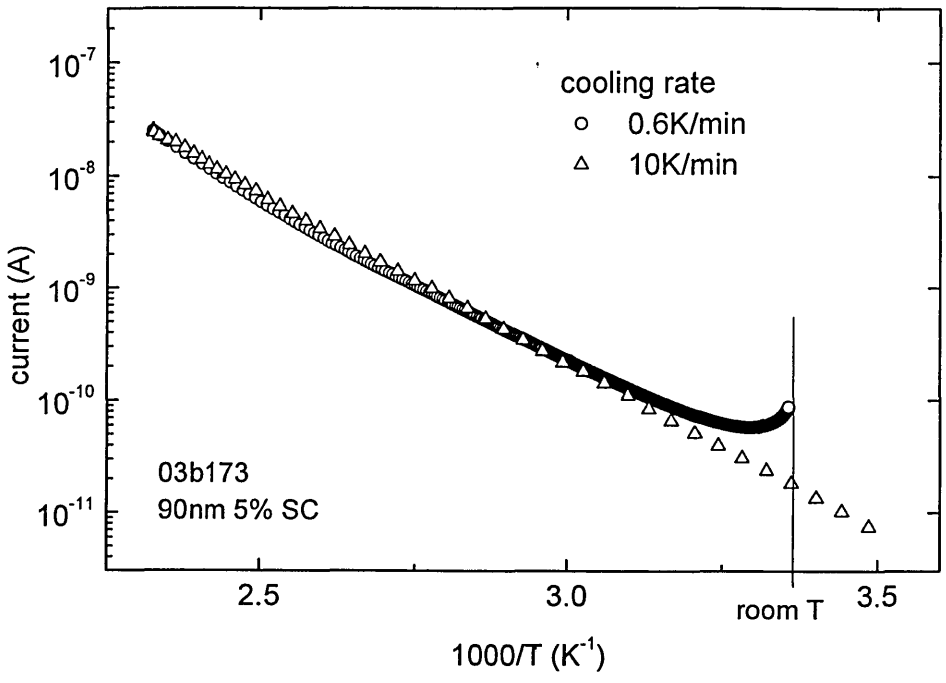

Figure 7.2. The effect of cooling rate on the cooling curves.

7.2 Irreversible ageing

7.2.1 Samples deposited at 5% silane concentration

Irreversible changes in room-temperature dark conductivity for films deposited at SC=5%, which occur on exposure of films to room air over a period of time, are presented in figure 7.3.

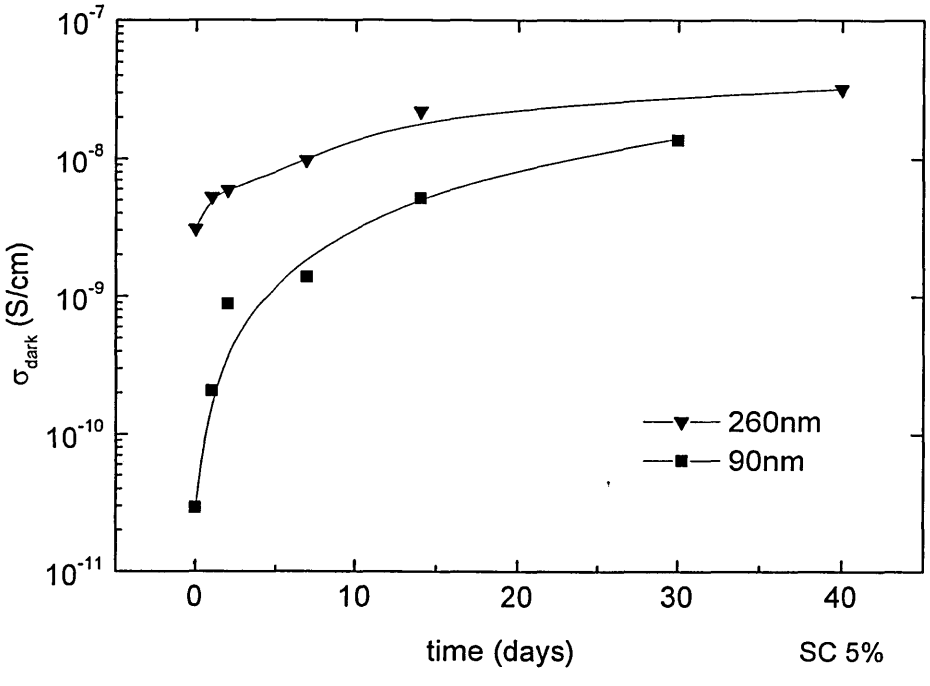

Figure 7.3. Irreversible changes in dark conductivity for 90 nm and 260 nm films. The lines are to guide the eye.

It can be seen that in both cases the dark conductivity increases with time. For 90 nm film the dark conductivity increases for some three orders of magnitude over a period of about one month, while the conductivity increase for 260 nm film is only about 1 order of magnitude. Arrhenius plots carried out on the 90 nm and 260 nm films as they undergo progressive irreversible ageing yield values of σ_0 and E_a which vary systematically. Corresponding changes in conductivity prefactor and activation energy are presented in figures 7.4 and 7.5 respectively.

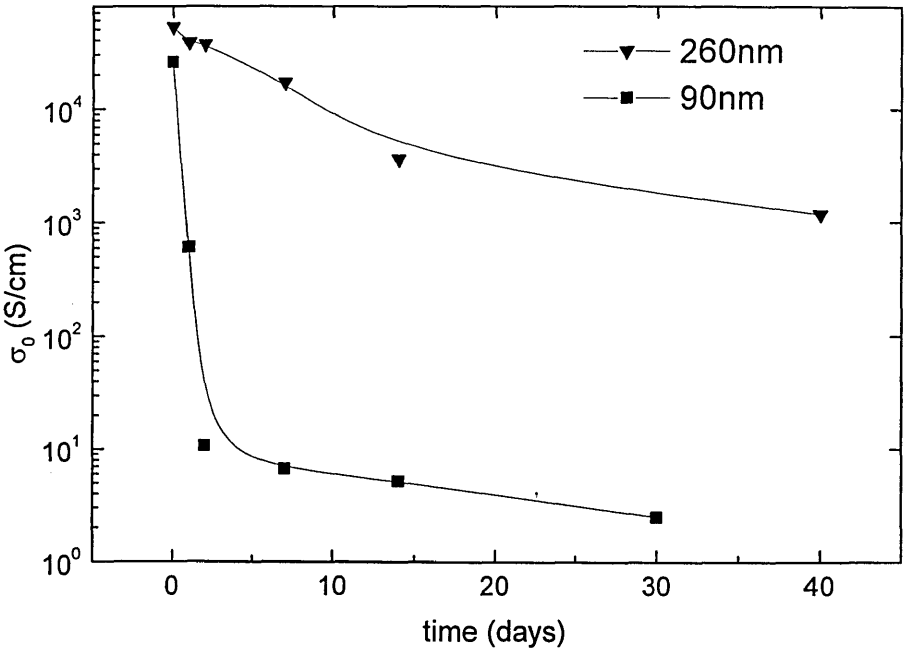

Figure 7.4. Changes in conductivity prefactor σ_0 over a period of time for 90 nm and 260 nm films. The lines are to guide the eye.

Both figures 7.4 and 7.5 show the irreversible effect is stronger for thinner film. After only 2 days activation energy has fallen from 0.9 eV to 0.6 eV in the case of 90 nm film, while for 260 nm the changes become more noticeable only after several days.

It has been reported [Yoon 2001] that annealing at temperature T=450°C shows an irreversible effect on dark conductivity activation energy of microcrystalline silicon films, without significant changes in oxygen content between annealing cycles. To check a possible relation between irreversible changes in dark conductivity and activation energy observed in the present work and annealing of samples at T=160°C, the identical 90 nm slide was studied over a period of time. For the second slide no high temperature was applied and measurements were performed at 220K-300K range. The changes of activation energy over a period of time are presented in figure 7.6.

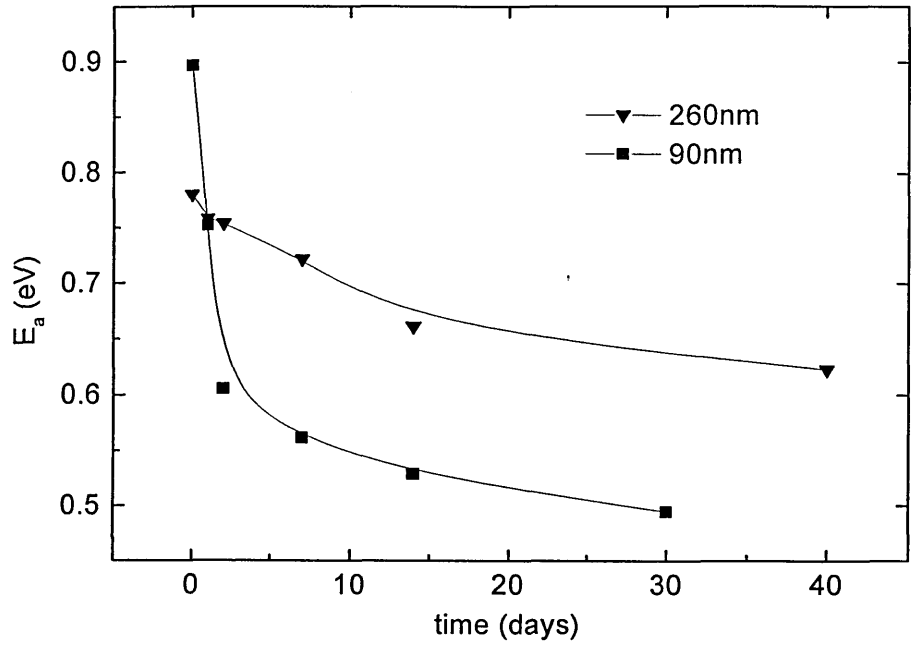

Figure 7.5. Irreversible changes in activation energy with time for 90 nm and 260 nm films. The lines are to guide the eye.

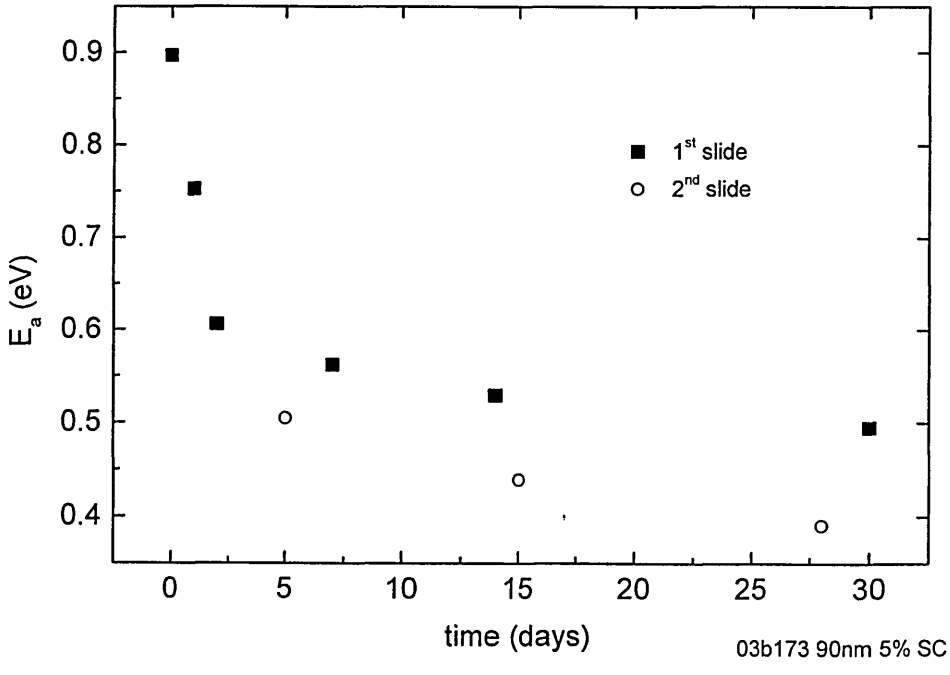

Figure 7.6. Irreversible changes in activation energy for two slides of 90 nm. Slide 2 shows the data measured below room temperature.

Although the temperature range itself influences the activation energy values, the change in activation energy are usually observed at temperatures below 200K [Kocka *et al.* 2003]. It is important for us to conclude based on figure 7.6 that activation energy is changing with time independently on temperature treatments and the changes are not influenced by applied high temperature.

Figure 7.7 presents the changes in photoconductivity measured at the photon flux of 10^{14} $cm^{-2}s^{-1}$ for 90nm and 260 nm films, and corresponding changes in photosensitivity are presented in figure 7.8.

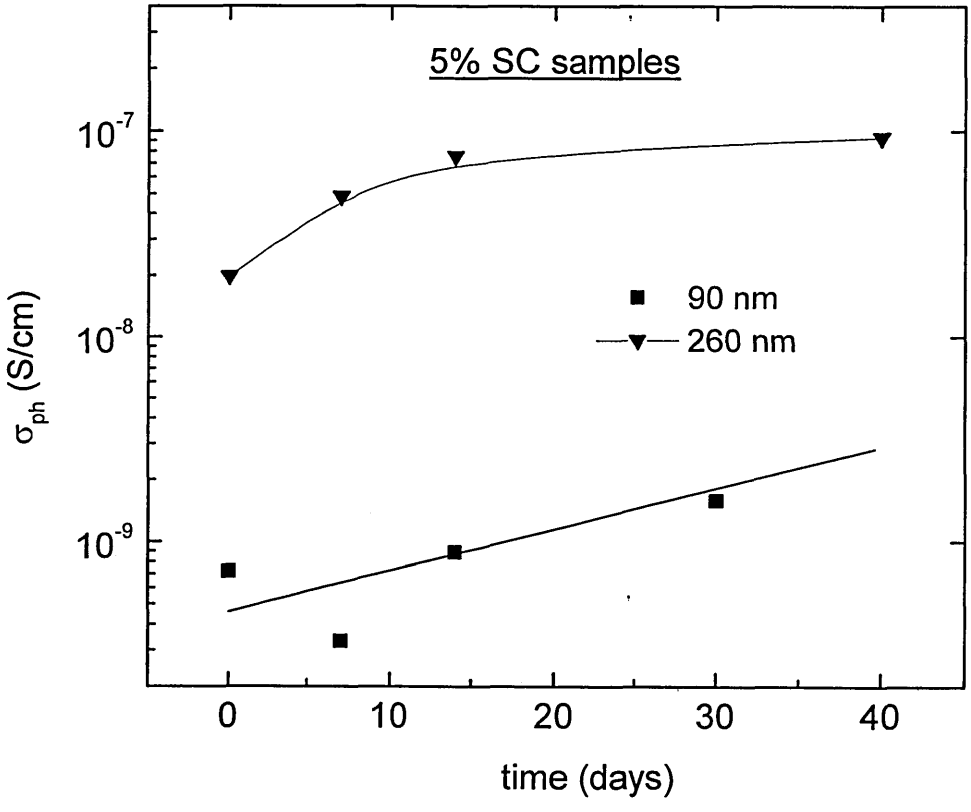

Figure 7.7. Irreversible changes in photoconductivity for 90nm and 260 nm films. The lines are to show the trend.

It can be seen that in the case of 260 nm film photoconductivity increases by less then an order of magnitude over a period of 40 days. The general trend of photoconductivity changes for 90 nm film shows a similar increase with time,

although a larger scatter of the data could be observed, particularly in the beginning of timescale, possibly due to a presence of reversibly adsorbed atmospheric components. The increase in photoconductivity is related to the changes in the Fermi level position [Brüggemann and Main 1998], that moves towards the conduction band (see figure 7.5) as the sample exposed to atmosphere.

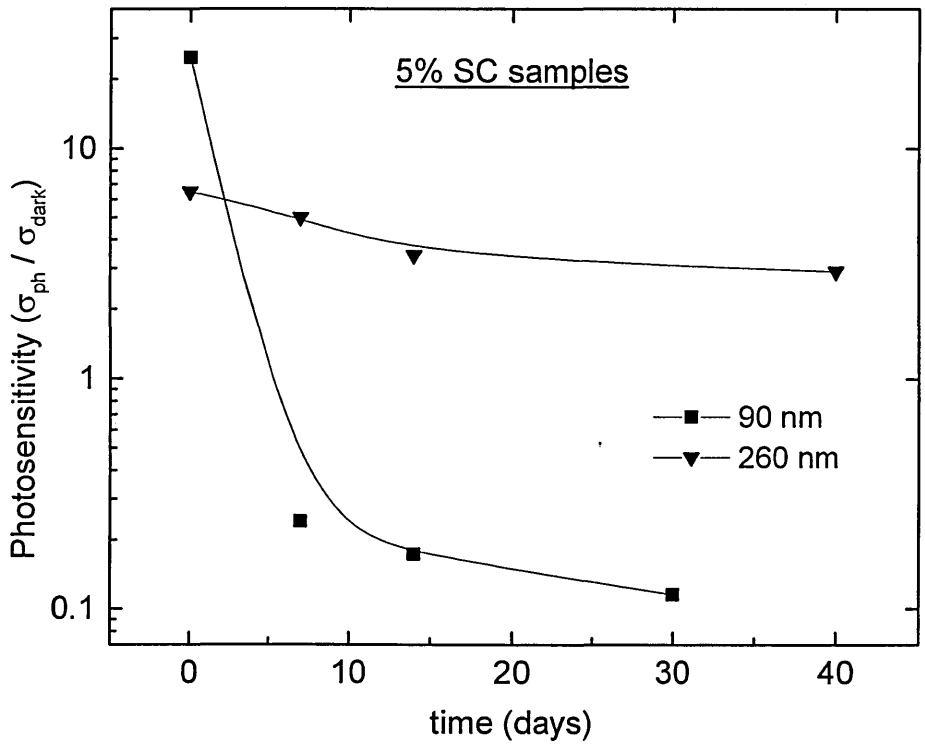

Figure 7.8. Irreversible changes in photosensitivity for 90nm and 260 nm films. The lines are to guide the eye.

Irreversible changes result in reduction of photosensitivity. For 90 nm film photosensitivity reduces by about two orders of magnitude over a period of one month, however high "as deposited" value should be considered with caution since it may be related to reversibly adsorbed atmospheric components. 260 nm film shows lighter reduction in photosensitivity. As was discussed in chapter 5, an improved photosensitivity of absorber layer is desirable for high efficiency solar cells. Our results suggest that irreversible ageing may result in reduction of solar cell efficiency, in agreement with observations of Wang *et al.* [Wang *et al.* 2003].

7.2.2 Samples deposited at 3% silane concentration

Figure 7.9 shows irreversible changes in room-temperature dark conductivity over a period of time for films deposited at 3% silane concentration.

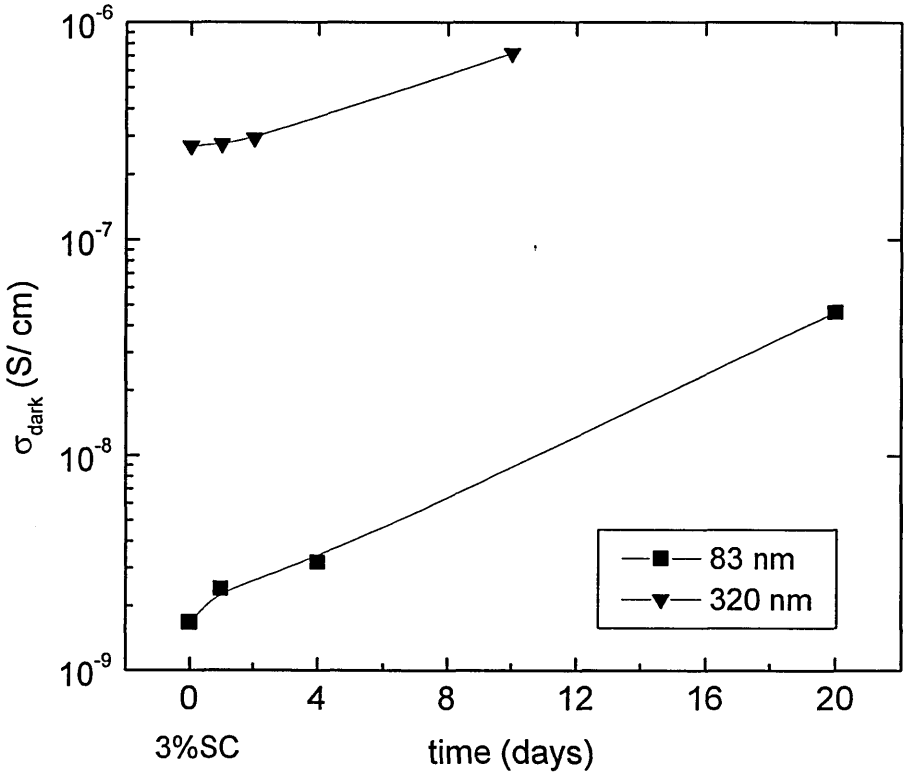

Figure 7.9. Irreversible changes in dark conductivity for 83 nm and 320 nm films. The lines are to guide the eye.

Changes in conductivity prefactor σ_0 and activation energy E_a are presented in figures 7.10 and 7.11 respectively. One can see that thinner film shows more rapid changes on ageing, similar to results of samples deposited at 5% silane concentration. For 83 nm film dark conductivity increases by more then one order of magnitude and activation energy decreases by about 0.25 eV over a period of 20 days. A comparison of results obtained for SC=3% and SC=5% films and discussion of morphological changes with film thickness are given in section 7.4.

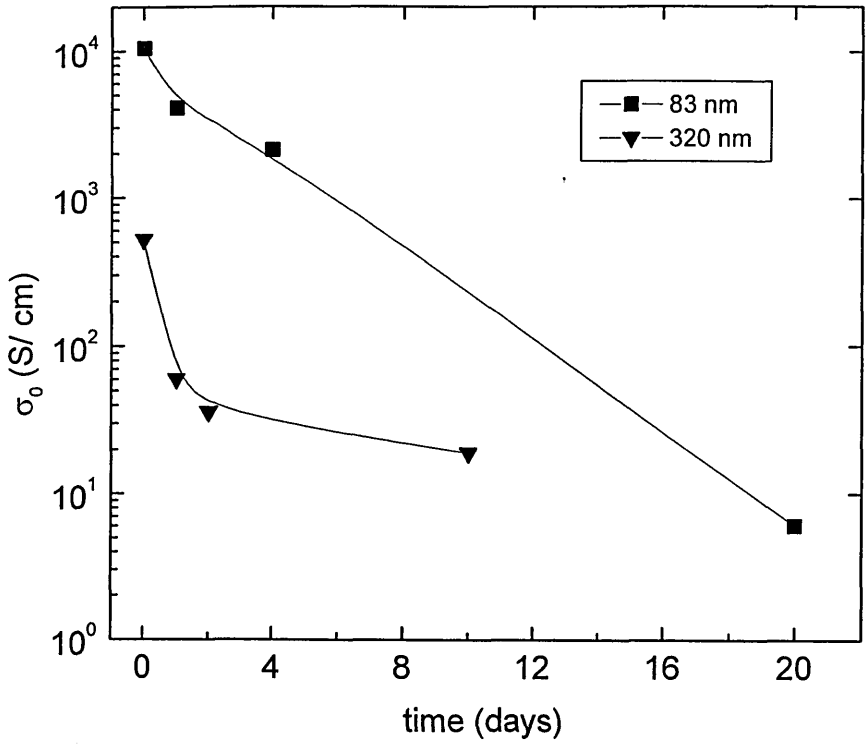

Figure 7.10. Changes in σ_0 over a period of time for 83 nm and 320 nm films. The lines are to guide the eye.

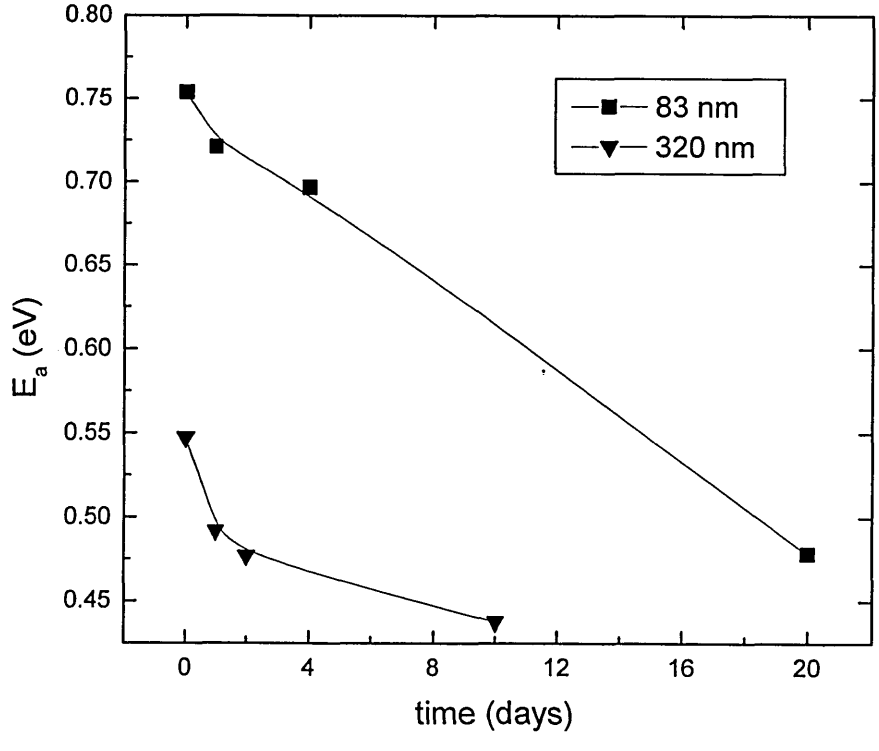

Figure 7.11. Changes in E_a over a period of time for 83 nm and 320 nm films. The lines are to guide the eye.

7.3 Reversible ageing

7.3.1 Samples deposited at 5% silane concentration

Figure 7.12 presents typical annealing curves as a function of time for both films deposited at 5% silane concentration.

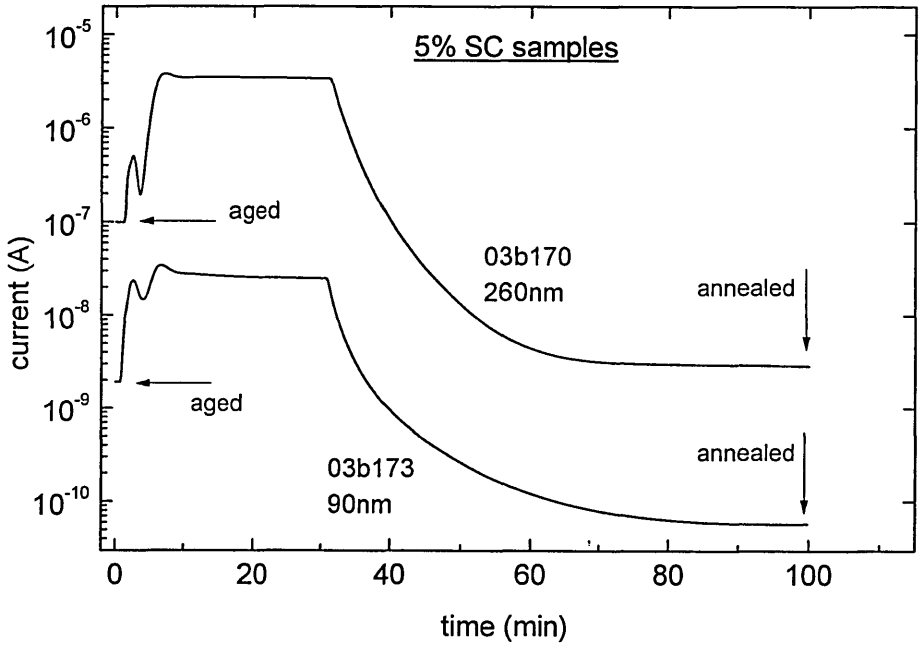

Figure 7.12. Annealing curves as a function of time for films deposited at SC=5%.

The figure shows both 90 nm and 260 nm films exhibit a similar behaviour on annealing. After exposure to ambient air the dark current increases, that is marked as "aged" condition in the figure. On annealing adsorbed atmospheric species are removed, that results in decrease of dark current ("annealed" condition). During the heating of both samples an "annealing peak" could be observed, that has been previously attributed as a specific feature of type II structures (see chapter 6).

Figure 7.13 presents reversible changes of dark conductivity for 90 nm film over a period of 30 days, compared with irreversible changes.

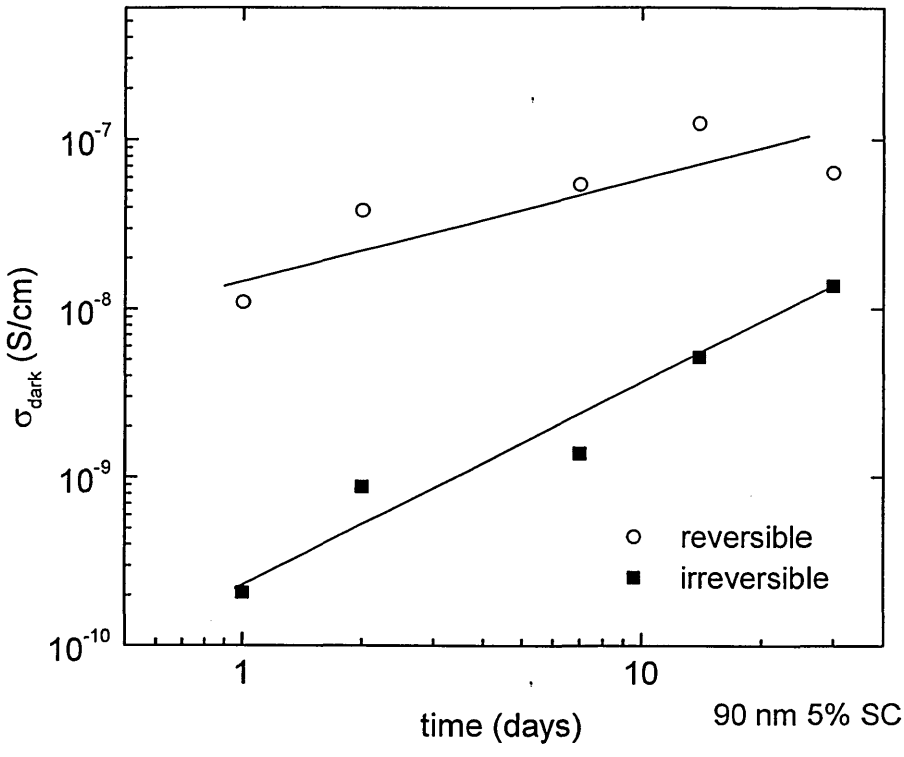

Figure 7.13. Reversible and irreversible changes in dark conductivity for 90 nm film. The lines are to show the trend.

The figure shows that dark conductivity increases due to both reversible and irreversible atmospheric effects with time. It can be seen that the slope of dark conductivity changes due to reversibly adsorbed atmospheric components does not follow the slope of irreversible changes: while irreversible changes result in dark conductivity rise roughly by two orders of magnitude, the reversible changes take place within one order of magnitude over 30 days period.

Figure 7.14 presents the changes of the ratio R of reversible changes to irreversible changes in dark conductivity. The figure shows that the ratio R reduces roughly by one order of magnitude over a period of 30 days. The reduction in the degree of reversible ageing, as expressed in the ratio R, as the sample undergoes irreversible ageing may be explained as follows. The increased conductivity and decreased activation energy indicate that the Fermi level is moving towards the conduction band edge as schematically shown in figure 7.15. It is assumed that the density of states at the Fermi level is increasing, as would

be the case if it is moving up a tail of localised states. The increase of the density of states at the Fermi level will result in reduction of band-bending [Solomon 1980] and hence a smaller fractional change in conductivity.

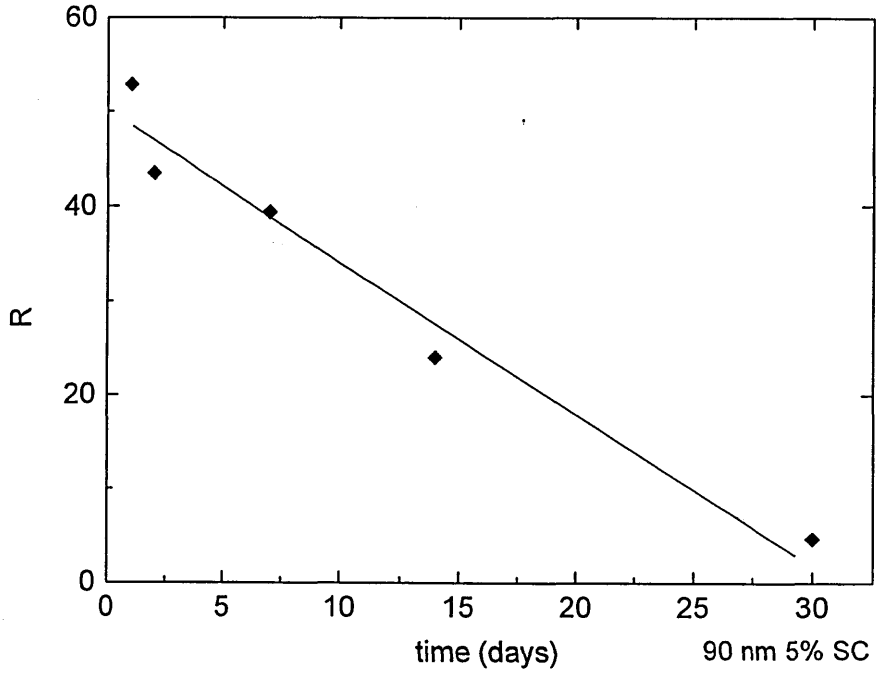

Figure 7.14. Changes in ratio R= $\sigma_{dark}^{(rev)}$ / $\sigma_{dark}^{(irrev)}$ over a period of 30 days. The line is to show the trend.

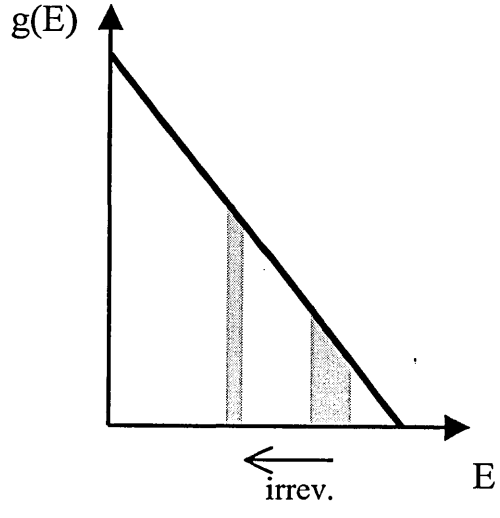

Figure 7.15. Schematic illustration of changes in R with ageing time.

7.3.2 Samples deposited at 3% silane concentration

Typical annealing curves as a function of time for both samples deposited at 3% silane concentration are presented in figure 7.16.

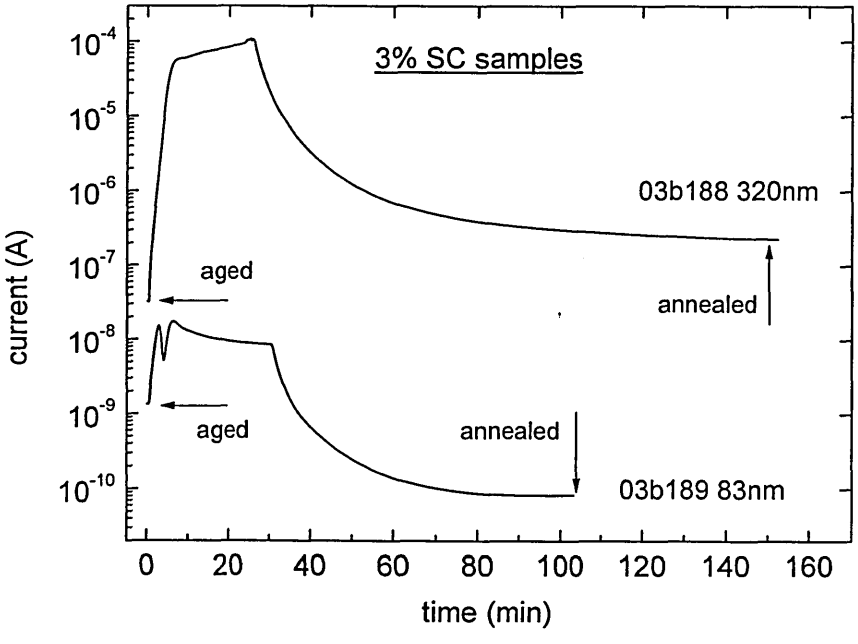

Figure 7.16. Annealing curves as a function of time for films deposited at SC=3%. The curves are offset by a factor of 50 for clarity.

The samples deposited at 3% silane concentration show a different picture on annealing. 83 nm film shows a decrease of dark conductivity on annealing and "annealing peak" that is a characteristic behaviour for type II films. Thicker 320 nm film shows a different behaviour on annealing: the adsorbed atmospheric components result in *decrease* of dark current, that results in increase of dark current after annealing, that is a behaviour generally observed for films with significant crystalline fraction (type I).

7.4. Discussion of morphological changes with silane concentration and thickness and relation to atmospheric effects

Figure 7.17 presents the data of dark conductivity in *as-deposited* condition for films studied in this chapter. The films were measured after annealing, thus are not affected by reversible ageing. It can be seen that an increase in film thickness results in increase of dark conductivity for both silane concentrations.

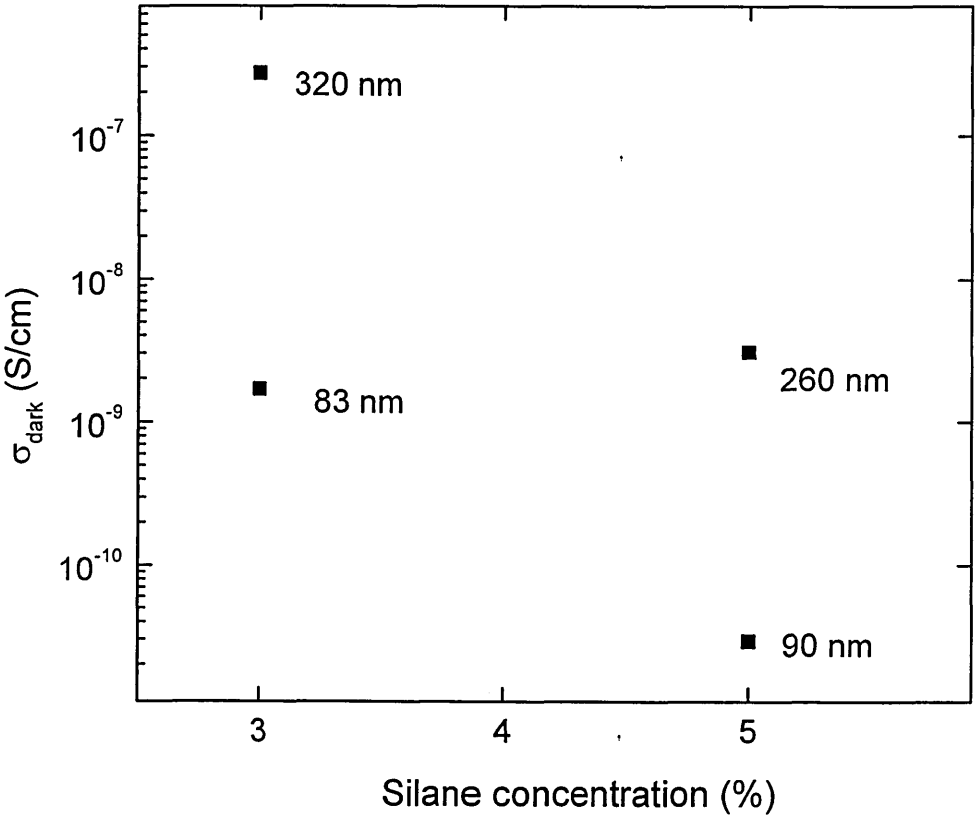

Figure 7.17. Dark conductivity values of microcrystalline silicon samples in as-deposited condition.

It is expected that film crystallinity increases with thickness [Finger *et al.* 1997, Houben *et al.* 1998, Shah *et al.* 2003], in agreement with CVF estimations based on the Raman data provided for the samples. The Raman spectra and estimated (based on equation 1.4) CVF data for the series are shown in figure 7.18.

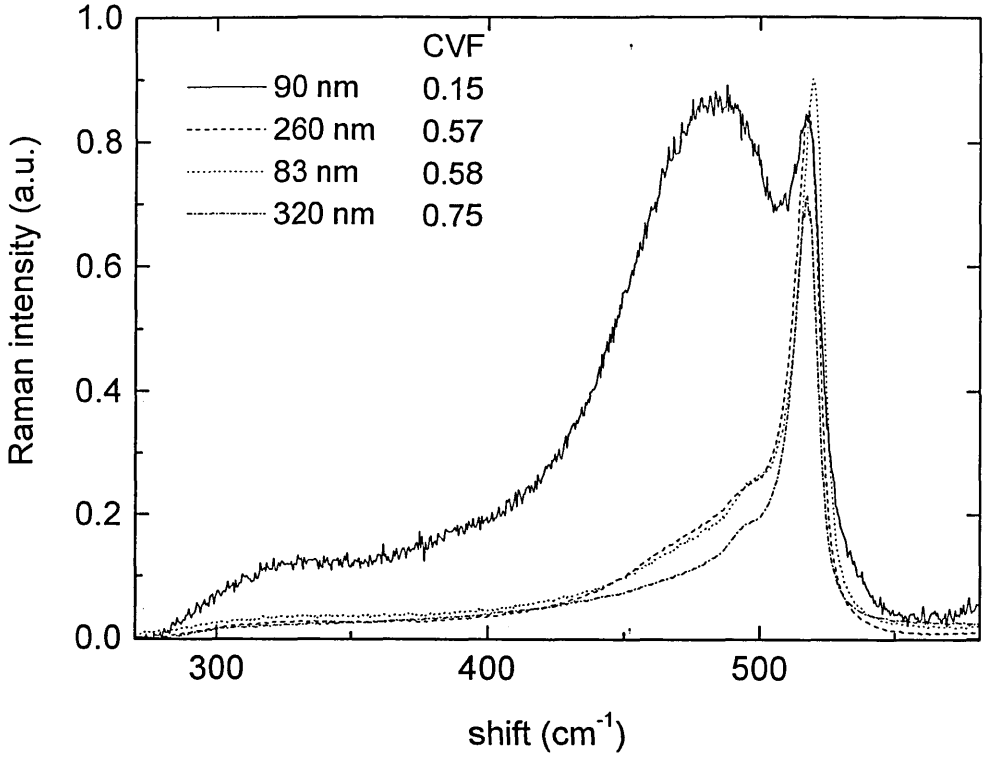

Figure 7.18. Raman spectra and estimated values of CVF for the films.

An increase in dark conductivity with thickness is thus related to anisotropy and changes in material microstructure. The 'typical' dark conductivity values reported in literature [Vetterl *et al.* 2000, Brüggemann *et al.* 2000, Baia Neto *et al.* 2002] for microcrystalline silicon films deposited at 3% and 5% silane concentrations are around 3~5 orders of magnitude higher then measured for 83nm and 90 nm films. While anisotropy in microcrystalline silicon films has been a subject of several reports [Luysberg *et al.* 1997, Tzolov *et al.* 1997, Finger *et al.* 1997, Houben *et al.* 1998, Unold *et al.* 2000, Kocka *et al.* 2003], the studies that focus on changes in transport properties with deposition conditions do not take into account reversible or irreversible atmospheric effects, which may complicate a proper comparison of various films.

The results reported in previous paragraphs of the present chapter have demonstrated irreversible (paragraph 7.2) and reversible (paragraph 7.3) ageing in films. The effect of irreversible ageing is associated with oxygen contamination

process, so-called post deposition oxidation where the oxygen atoms play the role of a n-type dopant [Veprek *et al.* 1983, Meier *et al.* 1998, Goerlitzer *et al.* 1998, Wang *et al.* 2003, Shah *et al.* 2003]. All films studied here show same tendency of systematic changes on irreversible ageing. Activation energy decreases with time, which is accompanied with an increase in dark conductivity, and as was shown for SC=5% films, an increase in photoconductivity.

Thinner films appear to be more sensitive to irreversible ageing for both silane concentrations. In a previous chapter it was shown that sensitivity to reversible ageing decreases with film thickness (fig. 6.3). These observations may have the same origin and a possible explanation of higher sensitivity of thinner films to ageing may be related to changes in microstructure with thickness, because thinner films deposited on glass are frequently found to contain larger void fraction [Houben *et al.* 1998a]. Unintentional oxygen contamination [Finger *et al.* 1998, Shah *et al.* 2000, Baia Neto *et al.* 2002] during deposition may also contribute to the rate of irreversible ageing. This is because thicker films require longer deposition time and thus larger number of oxygen atoms may be already incorporated into the film during deposition process.

Figure 7.19 presents irreversible changes in activation energy E_a for 5% silane concentration samples as a function of film thickness, compared with the data of Kocka *et al.* [Kocka *et al.* 2003] obtained for a *series* of microcrystalline silicon films grown under similar deposition conditions. Solid symbols in the figure (present work) indicate irreversible changes in activation energy for 90 nm and 260 nm films during 30 and 40 days respectively. The reference data show that activation energy decreases with film thickness, that is in agreement with expected morphological changes during film deposition. The data shows that activation energy decrease for about 0.45 eV with changes in film thickness within about 1 micron. The value of 0.45 eV is comparable with changes in films studied here due to irreversible atmospheric effect over a period of about one month. This shows that atmosphere can significantly change material properties and monitoring of atmospheric effects, particularly for thinner films, is necessary to perform an accurate comparison of various structures.

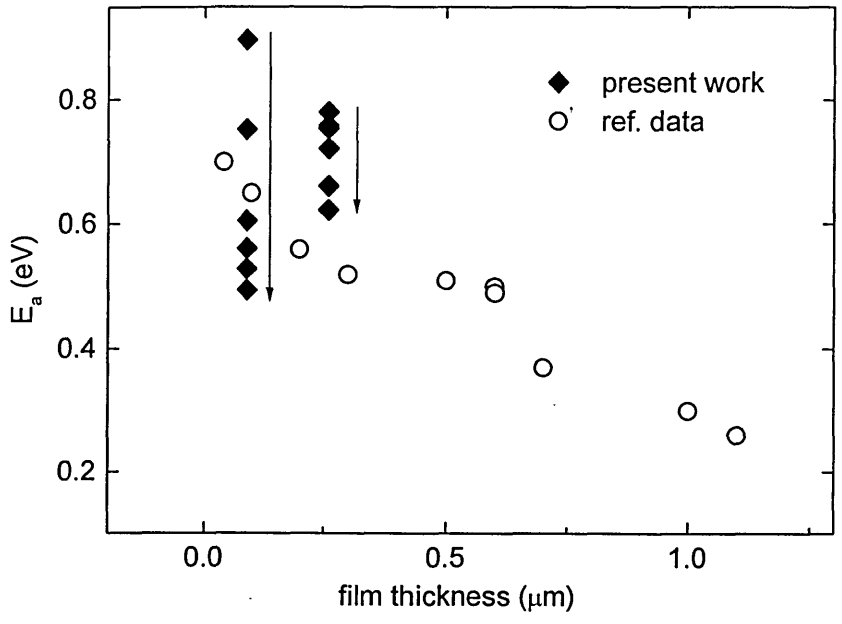

Figure 7.19. Changes in activation energy E_a with film thickness for 5% silane concentration films. The arrows are to show the direction of irreversible changes. Reference data are taken from Kocka *et al.* 2003.

While irreversible ageing has a similar effect on all films studied here, reversible ageing shows a different behaviour. Storage in ambient air results in reversible increase in dark conductivity for SC=5% films and thinner film deposited at SC=3%. Thicker 3% film shows a *decrease* in dark conductivity (figure 7.16). A decrease in dark conductivity on air exposure is commonly observed for largely crystalline films [Finger *et al.* 2003]. A different response on reversible ageing for films deposited at SC=3% thus supports the view that microcrystalline silicon films are anisotropic and material crystallinity increases with film thickness.

7.5 Meyer-Neldel Rule

7.5.1. Irreversible and reversible changes

Plots of irreversible changes of conductivity prefactor σ_0 vs. activation energy E_a are presented in figure 7.20. The relation between σ_0 and E_a is described by equation 1.2 (see chapter 1) and known as the Meyer-Neldel Rule.

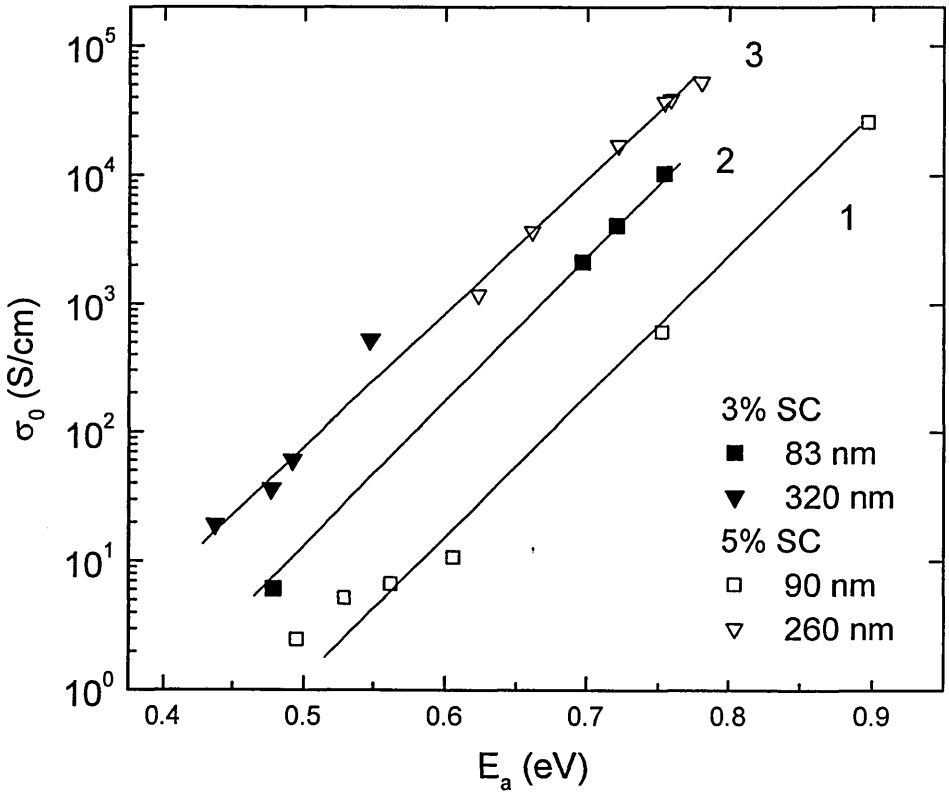

Figure 7.20. MNR plot for 3% and 5% silane concentration samples.

All four samples presented in the figure show a similar slope. Three sections of data may be identified, shifted successively by approximately two orders of magnitude of conductivity prefactor σ_0. Changes in activation energy are within the interval from 0.4 eV to 0.9 eV. The lowest curve (curve 1) corresponds to largely amorphous 90 nm film. Curve 2 corresponds to 83 nm film deposited at 3% silane concentration, that has higher crystalline fraction then 90 nm film. The data of 260 nm and 320 nm films fit curve 3. The general trend suggests that an

increase in crystalline fraction results in the shift of curves in the direction of higher σ_0 and/or smaller E_a.

Figure 7.21 shows the Meyer-Neldel plots of irreversible and reversible changes for 5% silane concentration samples.

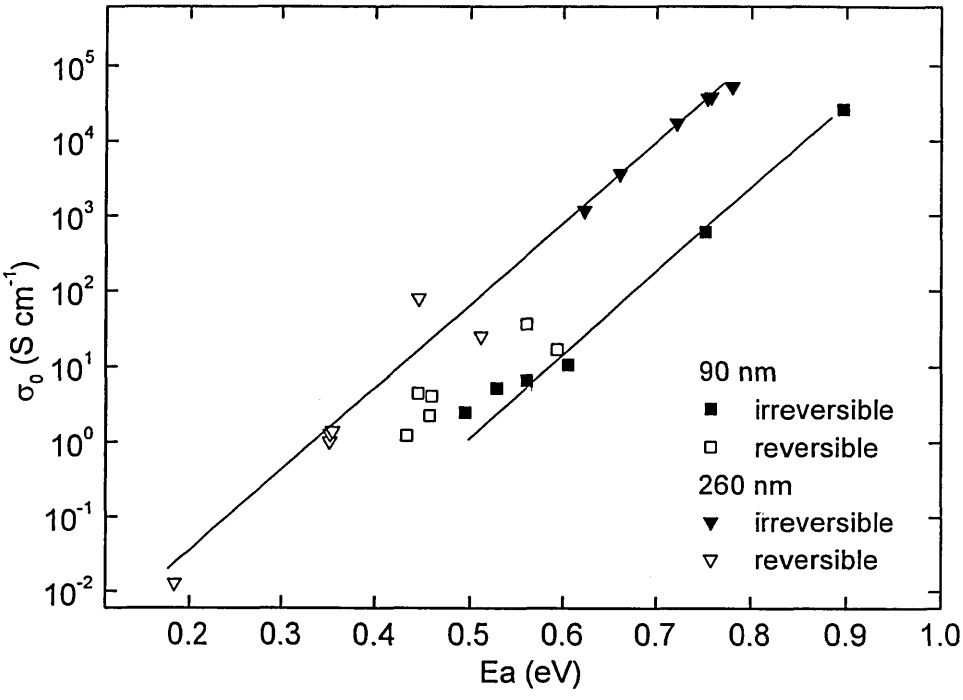

Figure 7.21. MNR plot of irreversible and reversible changes for 5% silane concentration samples.

The data of reversible changes reflects the conductivity parameters measured in the presence of adsorbed atmospheric components. In the case of 5% silane concentration samples, as was shown earlier, the reversible adsorption process results in increase of dark conductivity, associated with a shift of the Fermi level towards the conduction band. Thus the data points of reversible changes are shifted to lower activation energy region. Both reversible and irreversible changes in sample conductivity parameters fall on a similar MNR line, which suggests that their origin may be similar and associated with changes in the Fermi level position.

7.5.2. Comparison of present results with literature data

An observation of the Meyer-Neldel rule has been reported for *series* of microcrystalline or amorphous silicon films, , where the variations in dark conductivity activation energy were achieved by changes in deposition conditions, doping or film thickness [Tanielian 1982, Lukovsky *et al.* 1983, Brüggemann *et al.* 1998c, Ram *et al.* 2002,]. A comparison of our results with literature data for amorphous [Tanielian 1982] and microcrystalline silicon [Ram *et al.* 2002, Kocka *et al.* 2003] is presented in figure 7.22.

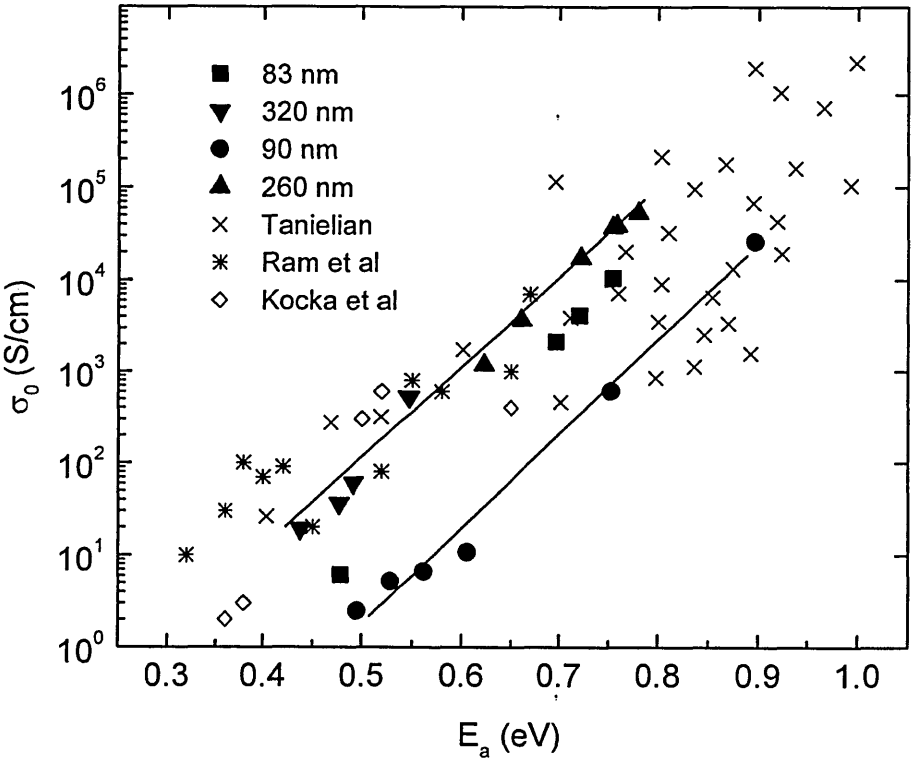

Figure 7.22. MNR plots for 3% and 5% silane concentration samples compared with literature data. The literature data taken from references: Tanielian 1982, Ram *et al.* 2002, Kocka *et al.* 2003.

The reference data presented in the figure correspond to different series of amorphous or microcrystalline silicon films where the variations in conductivity parameters were achieved by doping [Tanielian 1982] or changes in deposition

condition and film thickness [Ram *et al.* 2002, Kocka *et al.* 2003]. As can be seen, the data for amorphous silicon films are generally shifted to the direction of higher activation energy. This is in agreement with data of "as deposited" condition for 5% silane concentration films. It should be noted a large scattering of the data obtained from the various series of samples by doping or changes in thickness, while the results of the presents work scatter much less for each single film.

The data of Kocka *et al.* [Kocka *et al.* 2003], obtained on a series of microcrystalline silicon films of varying thickness tend to show a saturation of conductivity prefactor σ_0 at a level below 10^3 S/ cm. It has been reported [Irsigler *et al.* 1983] that for a series of samples subject to light-induced degradation, no further increase in conductivity prefactor σ_0 could be observed for activation energy $E_a \geq 0.6$ eV. Computer simulations performed by Overhof and Thomas [Overhof and Thomas 2001] suggest that a constant region of conductivity prefactor σ_0 may be attributed to an increase in the DOS at deeper energies, due to dangling bond defects. However, the films studied here do not show this effect. The results of Ram *et al.* on the series of varying thickness microcrystalline silicon films do not show this effect. Amorphous silicon films [Tanielian 1982] may show values of conductivity prefactor σ_0 higher 10^6 S/ cm.

Figure 7.23 presents irreversible changes for 3% and 5% silane concentration samples compared with results of 00c series, considered in chapter 5. The films of 00c series were deposited at silane concentration varied between 3% and 6.3%, that resulted in variations in crystalline volume fraction between 0.5 and 0.72. Crystalline volume fraction data are indicated in the figure for each 00c sample. The figure shows that the data of 00c series fit well the results for films deposited at 3% silane concentration. The films with crystalline volume fraction of 0.7 and 0.72 follow the general slope of 320 nm thick film deposited at 3% silane concentration. Another similar point for these films is the reversible changes due to atmospheric adsorption process. For these three films dark conductivity decreases on exposure to air. This suggests that the microstructure of 320 nm film could similar to these films. Two other films of 00c series (with crystalline volume fraction 0.5 and 0.6) follow the slope of 83 nm film, deposited at 3% silane concentration. The data of samples deposited at 5% silane concentration are shifted to the right hand side of the figure, and for 90 nm film, to

the region of lower conductivity prefactor σ_0 suggesting the films deposited at 5% silane concentration may have a different morphology from 00c films.

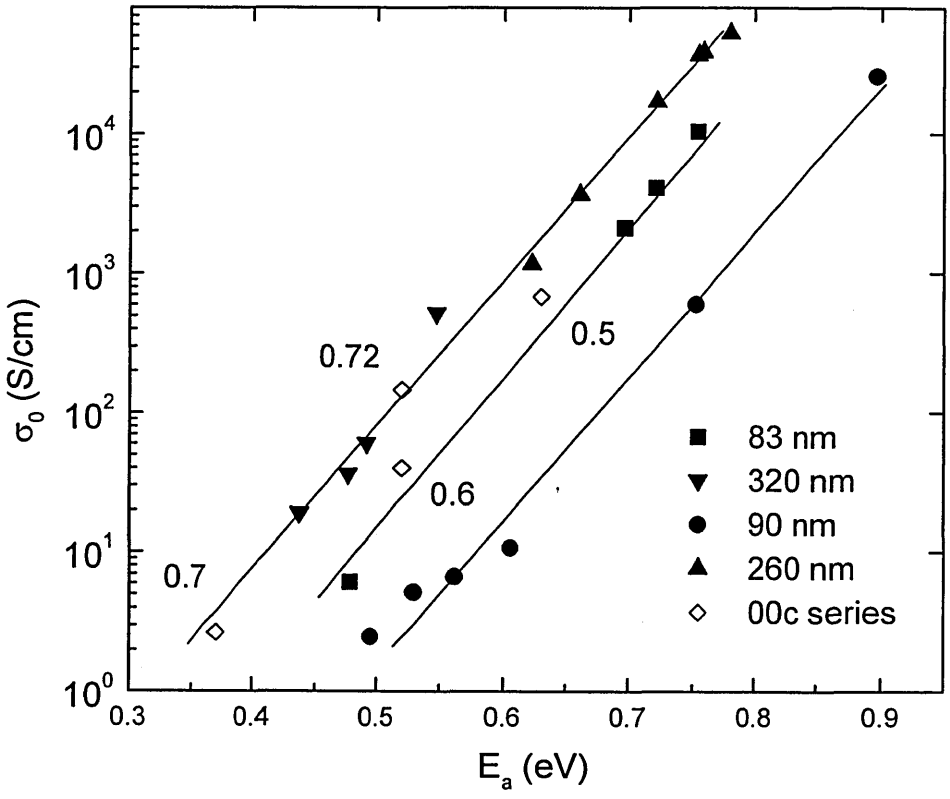

Figure 7.23. MNR plots for 3% and 5% silane concentration samples compared with 00c series data. The lines are to guide the eye.

Summary

The results presented in above paragraphs of the present chapter were aimed to investigate electronic properties of a series of microcrystalline silicon films deposited at varied SC and film thickness. It was demonstrated that in "as deposited" condition dark conductivity increases with film thickness and decreases with SC. This supports the view that microstructure of microcrystalline silicon is anisotropic.

Both reversible and irreversible post deposition atmospheric effects have been investigated. Irreversible atmospheric effects, associated with oxidation process, are found to decrease activation energy values, and increase dark and photoconductivity. For thinner film, increase in activation energy may be as large as 0.4 eV and decrease in dark conductivity around 3 orders of magnitude over a period of one month.

Both films deposited at 5% silane concentration show reversible increases in dark conductivity on exposure to air, while for films deposited at 3% silane concentration the reversible conductivity changes on ageing have opposite direction, that could be related to an increase in crystalline volume fraction with film thickness. Thinner films are found to be more sensitive to atmospheric effects. The size and rate of ageing effects is such that they may dominate over changes in transport properties produced by systematic variations in film growth parameters, and may therefore lead to complications and ambiguities when constructing transport models.

Both reversible and irreversible atmospheric effects change the film conductivity and activation energy in accordance with the Meyer-Neldel rule. The general trend suggests that an increase in amorphous fraction results in shift of the data to the direction of lower conductivity refactor σ_0 and/or larger E_a.

7.6 Thermally stimulated currents due to atmospheric effects

An interesting phenomenon has been observed during measurements of dark conductivity at temperatures below room temperature. If the sample is cooled down to temperatures around 125 K, the subsequent increase of temperature will result in *conductivity peak*, appearing at temperatures around 220 K. The experiment is performed *in dark* conditions under vacuum of 10^{-3} torr, indicating that no excess carriers are created optically. The feature has been observed for both samples deposited at 5% silane concentration. Figure 7.24 presents changes in dark conductivity observed for 90 nm and 260 nm films during heating from 125 K to room temperature.

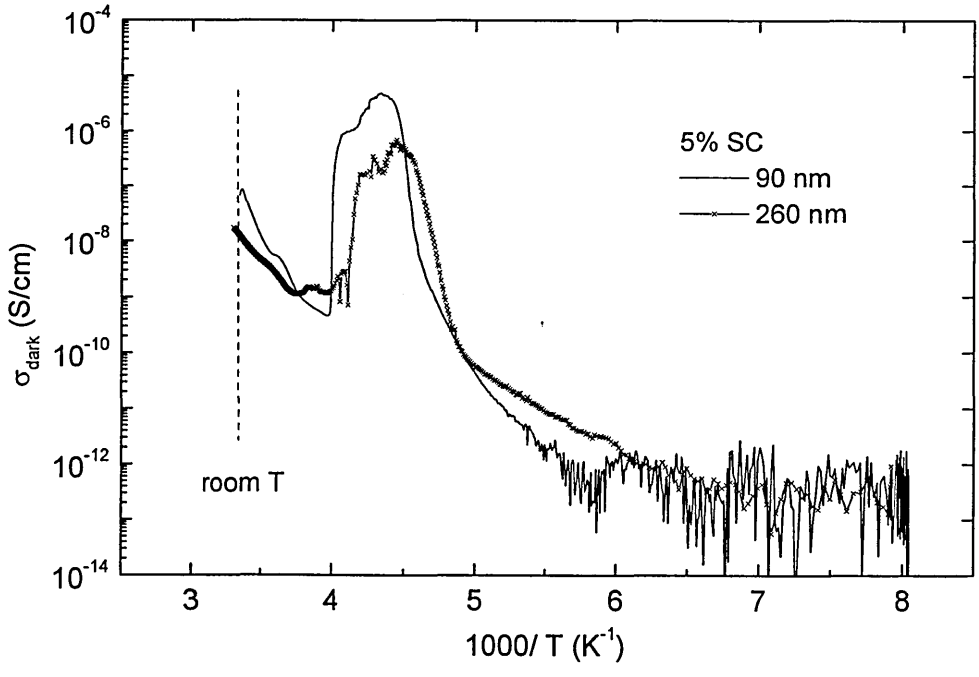

Figure 7.24. Changes in dark conductivity upon heating for SC=5% films.

It can be seen that both films show similar behaviour on heating, and the effect is stronger for 90 nm film. Although *in annealed* condition the dark conductivity values of 90 nm film are always lower then of 260 nm films (over the entire timescale of irreversible changes), it should be noted that the figure shows

the room temperature dark conductivity of 90 nm is higher, suggesting a possible presence of reversible adsorbed atmospheric components. It was shown previously that thinner films are highly sensitive to reversible ageing, even under vacuum of 10^{-3} torr, and this may explain the presence of adsorbed atmospheric components affecting room temperature conductivity.

A similar conductivity peak is usually observed during so-called 'thermally stimulated current' experiments [Fritzsche and Ibaraki 1985, Han *et al.* 2003]. It should be noted that present experiments were performed *in dark* conditions, that is a key difference from a standard TSC experiment. As the sample was not illuminated before heating, a possible reason for the rise of the TSC curve is the adsorption of atmospheric components, remaining in vacuum chamber. In a standard TSC experiment illumination splits the Fermi level and additional change carriers are created optically. In the present case the Fermi level is not split, however a shift of the Fermi level position toward the transport level with decreasing temperature can be observed [Overhof and Tomas 1989, Ruff *et al.* 1998]. To investigate the effect of molecules adsorption in more detail, the experiment on the sample, annealed prior the measurements, was performed.

Figure 7.25 shows the TSC curves for aged and annealed conditions of the sample. It can be seen that annealing of the sample prior cooling down results in reduction of conductivity peak by about 3 orders of magnitude. Annealing of the sample removes adsorbed atmospheric components, and if these components are responsible for the conductivity peak, it should modify shape of the peak. The peak is still observed, that reflects the interaction of atmosphere with sample takes place under vacuum of 10^{-3} torr. The possible mechanism to explain the observed phenomena is discussed below.

If the sample is in aged condition prior cooling down, the adsorbed atmospheric components result in some bending of the bands; the schematic diagram for this case is shown in figure 7.26a. The grey triangle represents the charge (Q_1) due to adsorbed molecules, trapped below the Fermi level. When the temperature decreases, the Fermi level moves towards the conduction band, as was discussed above. This is shown by arrow in figure 7.26b. The grey square in the figure represents the charge (Q_2), corresponding to molecules adsorbed at low temperatures. Thus the total charge (Q_1+Q_2) due to adsorbed molecules is

increased when the sample is cooled down. Subsequent increase in temperature will result in movement of the Fermi level towards the midgap. It is proposed that

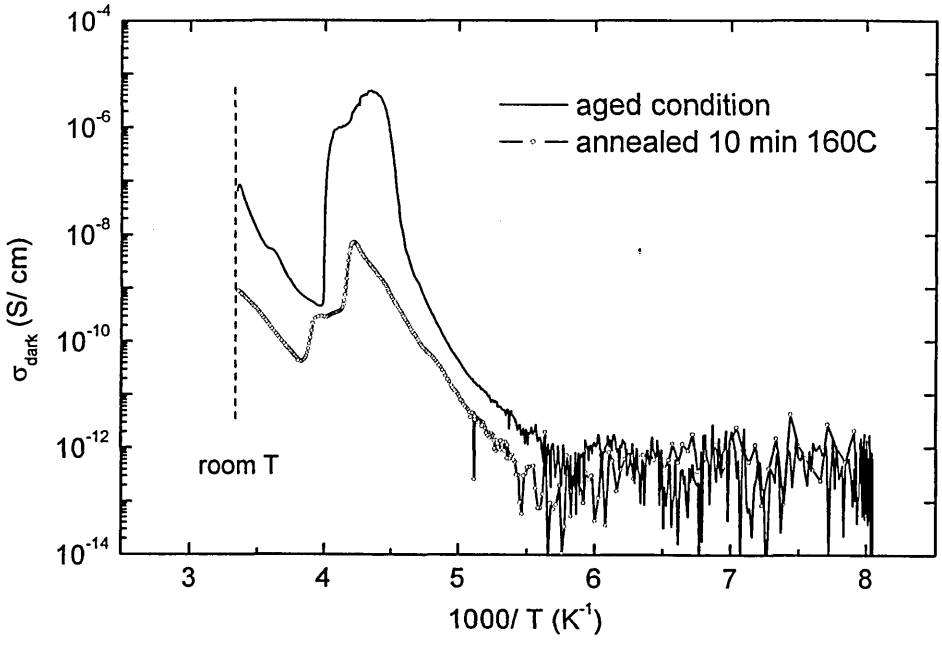

Figure 7.25. TSC curves for 90 nm film.

movement of the Fermi level with increasing temperature does not result in instant desorption of molecules, so that molecules, corresponding to charge Q_2 are still largely adsorbed. This will increase the band bending value, as shown in figure 7.26c. A larger band bending will be reflected in dark conductivity increase, as observed experimentally. At some point, desorption starts more efficiently (for example due to increase in temperature) and dark conductivity decreases.

The mechanism described above is able to explain a reduction of conductivity peak if the sample is annealed prior to cooling down (see figure 7.25). Annealing of the sample will significant reduce charge Q_1, and thus, reduce charge Q_3 as clear from above discussion. This will result in smaller band bending for the case shown in figure 7.26c, that will be reflected in smaller dark conductivity. It would be useful to perform these experiments under UHV conditions as well, however such conditions are not available in our laboratory.

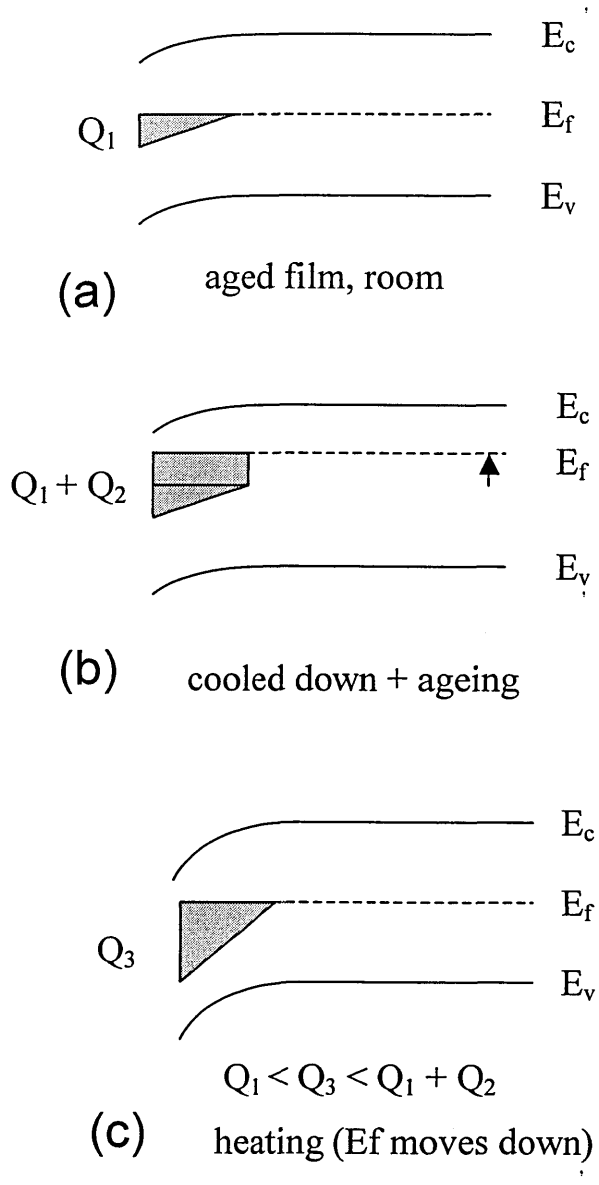

Figure 7.26. Schematic band diagram to explain the mechanism of TSC due to atmospheric adsorption. See details in the text.

Finally a standard TSC experiment was performed: the sample was annealed, then cooled to 120 K and illuminated for 1 minute by calibrated LED with photon flux $\Phi=6.3\text{x}10^{16}$ cm^{-2} s^{-1}. The results of this experiment are presented in figure 7.27. It can be seen that illumination of the sample has no significant effect on the shape of conductivity curve. This supports our view that the major

contribution to the rapid rise of conductivity could be attributed to the adsorbed atmospheric components.

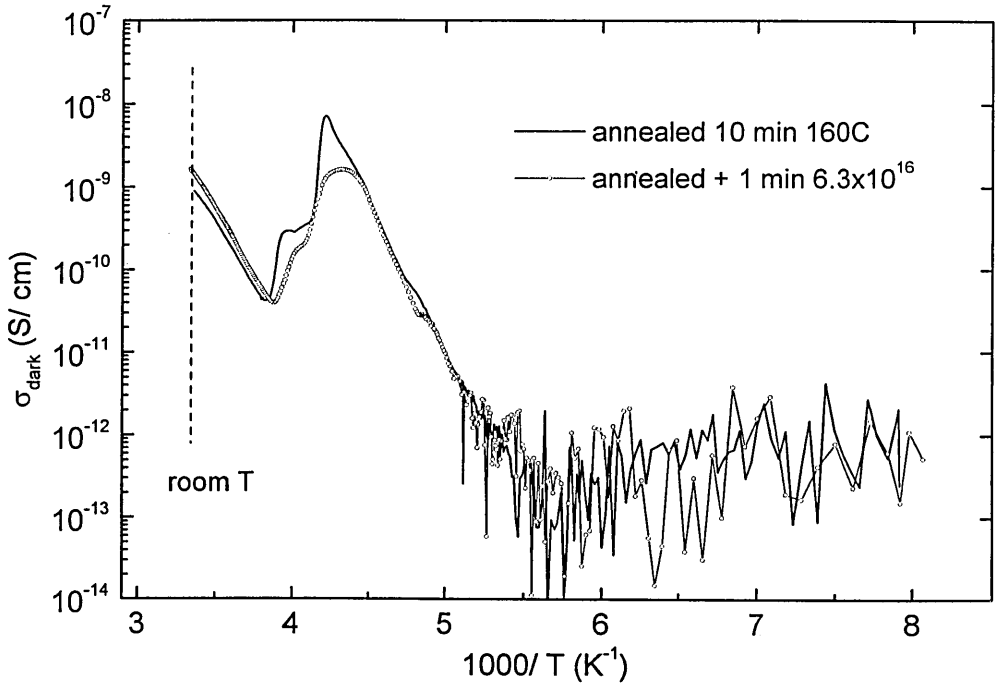

Figure 7.27. TSC curves for 90 nm film in '1 min illumination' and dark conditions.

Summary

Both films deposited at 5% silane concentration show conductivity peaks in thermally stimulated current experiments carried out in dark conditions. Our results suggest that the shift of the Fermi level with temperature and reversibly adsorbed atmospheric components are responsible for conductivity peak in TSC curves. More complete investigation of the phenomenon may require to perform measurements under UHV conditions.

Chapter 8. Light induced degradation and atmospheric adsorption

This chapter presents a study of the simultaneous effects of light soaking and atmospheric adsorption on the properties of microcrystalline silicon films. Both of the effects result in metastable changes in optoelectronic properties, such as dark- and photoconductivity, however, to the authors' knowledge, the case of simultaneous effects has not been previously considered. This work is of practical as well as scientific interest, as solar cells are exposed to the atmosphere to some extent during operation. Thus, an investigation of this case is necessary to obtain a more complete picture of instability phenomena in microcrystalline silicon.

8.1 Introduction

As was described in chapter 1, extended illumination of hydrogenated amorphous silicon structures gives rise to additional defects (Staebler- Wronski effect) that degrade the optoelectronic properties of the material. The effect seriously limits the use of amorphous silicon materials, particularly, for photovoltaic applications. A reduction in solar cell efficiency of 30% of its initial value after 100 hours of illumination has been reported [Nakata *et al.* 1991]. The number of reports [Goerlitzer *et al.* 1997, Kleider *et al.* 2001, Finger *et al.* 2003, Klein *et al.* 2003] have demonstrated that microcrystalline silicon thin films and solar cells with microcrystalline silicon active layer, in general, provide more stable photoelectrical properties under prolonged light illumination compared with amorphous silicon. However, light induced degradation of microcrystalline silicon films and solar cells containing amorphous volume fractions have been reported in several works [Ray *et al.* 2002, Klein *et al.* 2003, Finger *et al.* 2003]. It is proposed that the observed light induced degradation in these structures is associated with the amorphous phase.

Another aspect of material instabilities is related to the influence of atmosphere. As was demonstrated in previous chapters, microcrystalline silicon materials are highly sensitive to the effects of atmospheric gas adsorption. The effect is particularly pronounced in the case of coplanar structures. However, for

photovoltaic structures, changes in optoelectronic properties, such as dark- and photoconductivity and open-circuit voltage, due to adsorption of atmospheric gases have also been demonstrated [Wang *et al.* 2003, Klein *et al.* 2003, Finger *et al.* 2003, Sendova-Vassileva *et al.* 2005].

Although the effects of instabilities in thin silicon materials have attracted recent attention, to the author's knowledge no studies that investigate the case when both kinds of instabilities, e.g. light induced degradation and atmospheric gas adsorption, affect the material have been reported. Because the materials with significant crystalline volume fraction are generally stable to light induced degradation, the situation when both effects may noticeably change optoelectronic properties, is probably restricted to microcrystalline silicon films with a significant amorphous fraction. However, these are the very materials that are found to yield the highest solar cell efficiencies [Vetterl *et al.* 2000]. Consequently it was investigated a series of microcrystalline silicon films prepared under conditions that give rise to a significant amorphous fraction. For the films where crystalline volume fraction data are available, it is varied between 30% and 100%.

8.2. Atmospheric adsorption effect

Figure 8.1 shows the changes in dark conductivity observed on annealing and air exposure for the series of microcrystalline silicon films over a period of ten days. The results for a fully amorphous film (InterSolar) are also presented.

The figure shows that for the films presented here, where amorphous fraction is varied from 30% to 100%, dark conductivity increases over a period of time. The increase in dark conductivity is related to the adsorption of water molecules and the mechanism has been considered in previous sections in detail. Our observations are in agreement with results reported by Finger *et al.* [Finger *et al.* 2003], where these materials were classified as type II category (see chapter 2).

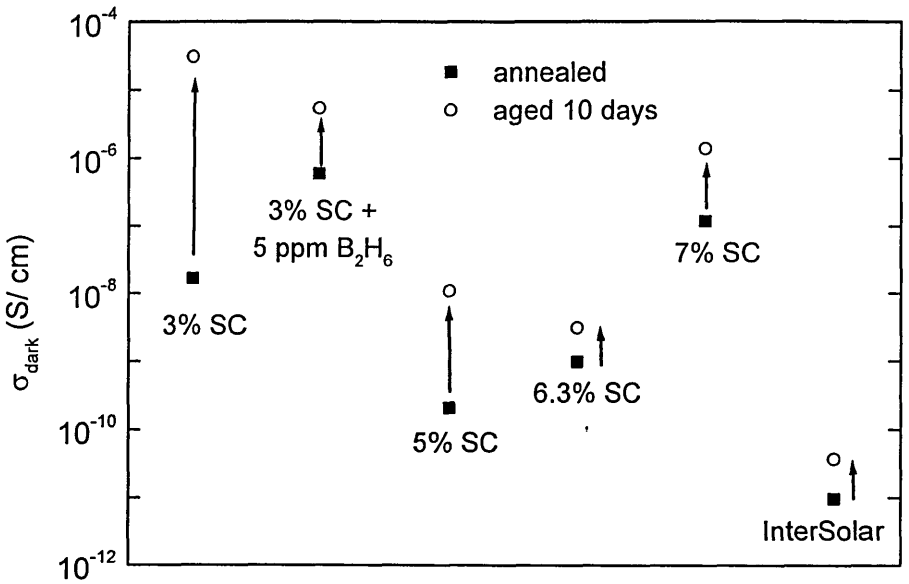

Figure 8.1. Atmospheric gas adsorption effect in microcrystalline silicon films with amorphous fraction varied between 30% and 100%.

The general trend of our results suggests that the effect of atmospheric adsorption is large when the materials are grown at lower silane concentration. However, as was shown in chapter 6, the sensitivity to atmospheric effects is determined by the material microstructure, specifically porosity and voids fraction. The material microstructure also depends on film thickness. The correlation between deposition parameters (including silane concentration and film thickness) and dark conductivity changes due to atmospheric effects and explanation of these effects have been considered in details in previous chapters. It is important now to underline the fact that type II microcrystalline silicon films, that are the most susceptible to light induced degradation due to the presence of amorphous fraction, show a dark conductivity *increase* due to exposure to atmospheric gases. On the other hand, the light induced degradation of amorphous/ microcrystalline silicon materials should result in *decrease* of dark conductivity, because the creation of additional defects will reduce carrier lifetime. Thus, in general case, the effects of light induced degradation and atmospheric adsorption could affect the material conductivity in *opposite* directions. It is clear that the presence of adsorbed atmospheric components could produce complications in the correct

estimation of light induced degradation and erroneous claims for material stability could be made. So this situation and possibilities to resolve the problems mentioned above should be investigated in detail.

8.3. Light induced degradation

For light soaking degradation experiments an 'optimal' microcrystalline silicon film (02c452) with crystalline volume fraction 0.48 was selected, and a fully amorphous sample for comparison. The effect of light-induced degradation under simulated AM1 radiation at 20°C and 50°C on the photocurrent is presented in figure 8.2.

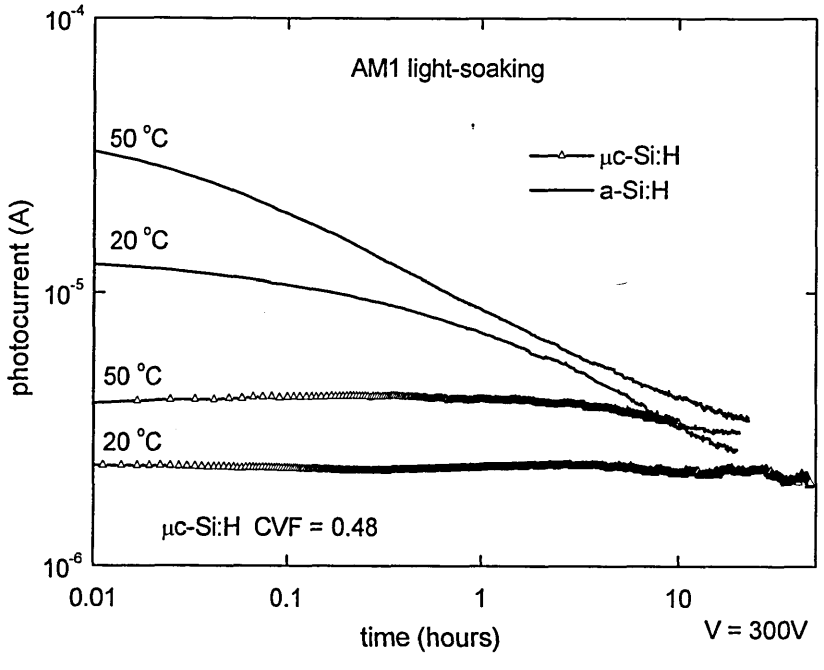

Figure 8.2. Light soaking degradation of microcrystalline and amorphous silicon films under vacuum.

The value of 20°C corresponds to ambient temperature and the temperature of 50°C was selected as a typical operating temperature of a solar cell (see for example Meier *et al.* 2003, Meier *et al.* 2004). The fully amorphous film shows significant changes in photocurrent at both temperatures. Microcrystalline silicon sample shows a higher stability against light induced degradation. Room

temperature light soaking for 50 hours has little effect on the microcrystalline silicon film. However, when the light soaking is performed at higher temperature, the small decrease in photocurrent could be observed.

8.4. Rapid and long annealing regimes

As was suggested above, the presence of atmospheric components adsorbed on the sample changes the electronic properties of the material that could mask the effect of light induced degradation. For example, in the case of the 'optimal' microcrystalline silicon sample the increase of dark conductivity due to ageing is about 1 order of magnitude that could exceed the apparent changes due to light soaking. Thus, in general, if light-soaking experiments are performed, care should be taken to avoid atmospheric effects or to separate these two distinct effects before any claims for stability are made. This could be done, for example, by maintaining the sample under high vacuum during light-soaking and all subsequent experiments, which is not always straightforward. In our experiments a high vacuum system was not available and in order to investigate the light soaked state of the sample a rapid low temperature annealing was used. The suggestion to use rapid annealing rose from monitoring of time dependence of moisture removal during annealing, where a well pronounced conductivity peak is observed for materials with significant amorphous fraction (see chapter 6). So rapid annealing may be able to remove adsorbed moisture from the light-soaked sample, whilst leaving the light-induced changes intact.

Thus, two different annealing regimes are considered in the present work:

(i) rapid annealing for about 1 minute at low temperature to remove adsorbed atmospheric species and

(ii) longer higher temperature annealing to remove light induced defects.

It was found by trial and error that 1 minute pulses between 90°C and 130°C are able to remove atmospheric moisture completely, without affecting the underlying light-soaked state. This may be successfully repeated over several cycles of atmospheric aging. Light-induced defects may be removed by annealing

for 1 hour at 160°C. Annealing curves and a schematic cartoon illustrating both annealing regimes is presented in figures 8.3a and 8.3b, respectively.

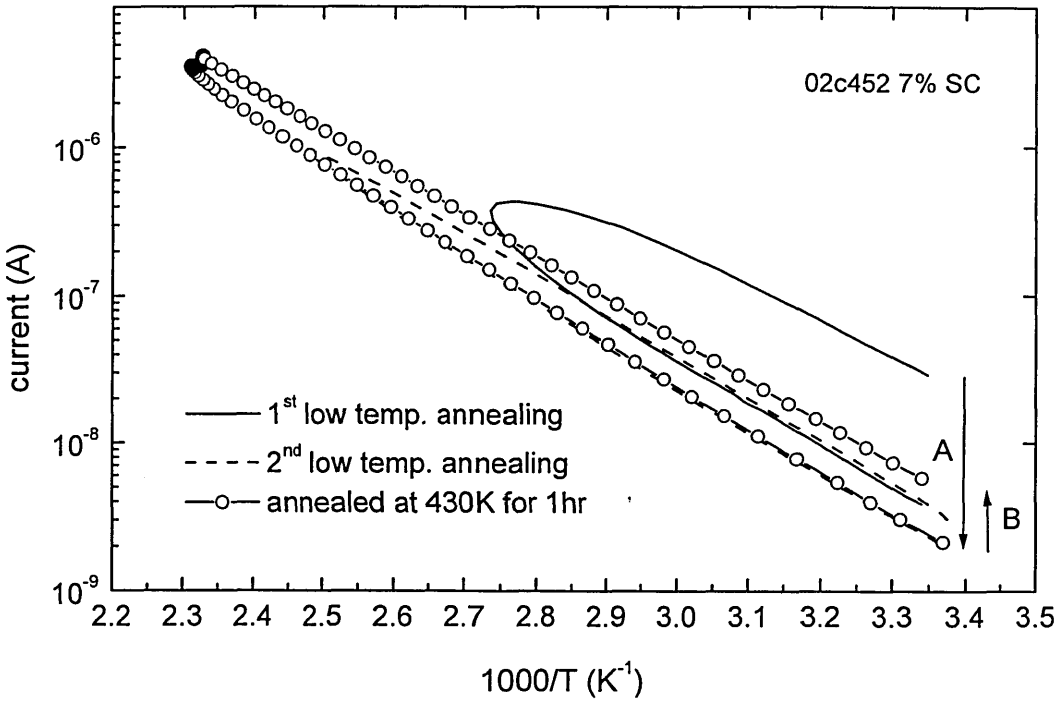

Figure 8.3a. Rapid and long annealing regimes of μc-Si:H.

The microcrystalline silicon sample was light soaked at 50°C for 20 hours. Although the light soaking was carried under vacuum of about 10^{-3} torr, such pressure is able to reduce, but not able to prevent completely the effect of atmospheric gases, as demonstrated in chapter 7.

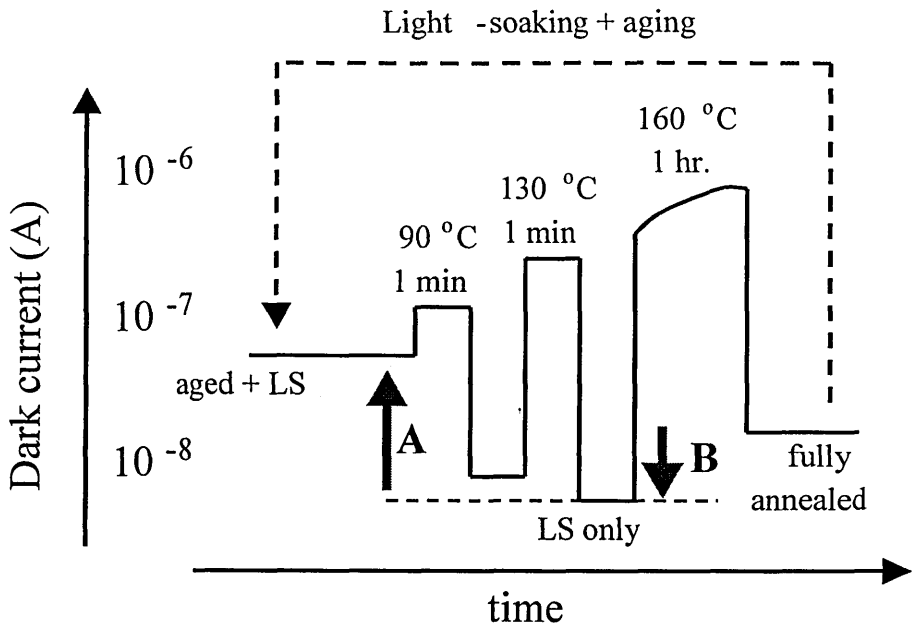

Figure 8.3b. Schematic cartoon illustrating two annealing regimes of μc-Si:H.

So, during the experiments, the light soaking degradation was carried out in vacuum to minimise the atmospheric influence on the photocurrent values, however, some atmospheric species could still be adsorbed on the sample. After the light soaking experiment the sample was left for a period of time to relax in the ambient atmosphere. As a result, the light soaked microcrystalline silicon film adsorbed atmospheric components, hiding an effect of light induced degradation. The evidence for this was the fact that the dark conductivity value was *higher* then the dark conductivity of annealed sample prior to light soaking (see also figure 8.4 and comments below in the text). After a first rapid annealing of the light soaked sample (at 90°C) a large fraction of adsorbed atmospheric moisture is removed, resulting in a reduction in dark current. To ensure the complete removal of atmospheric moisture a second rapid annealing (at 130°C) is performed. It removes the remaining adsorbate and the dark current falls to its minimum value, and may be viewed as corresponding to the light-soaked condition of the sample. Further longer annealing (1 hour at 160°C) removes light-induced defects, and consequently the dark current rises to its typical annealed level. Thus the changes in current associated with the aging process relative to the light-soaked state is

represented by arrow A, and that due to light-soaking relative to the fully-annealed state by arrow B.

8.5. Effects on dark conductivity and steady state photoconductivity

Dark conductivity values corresponding to annealed and light soaked conditions of the 'optimal' microcrystalline silicon film are presented in figure 8.4.

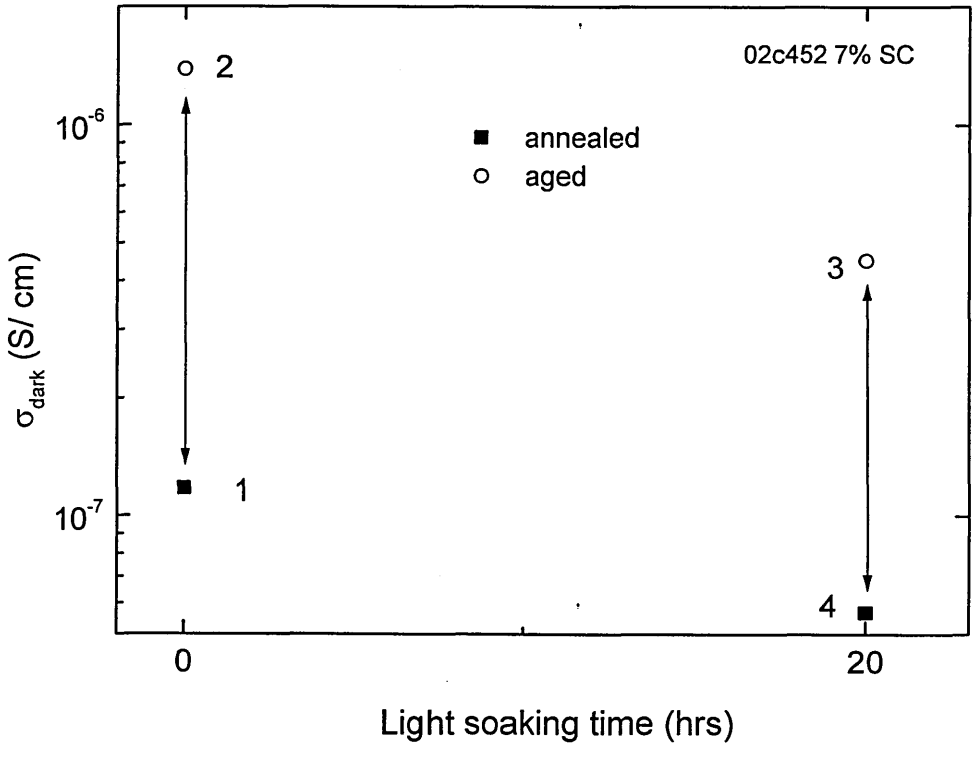

Figure 8.4. Dark conductivity of the 'optimal' microcrystalline silicon film in annealed and light soaked conditions.

Condition 1 in figure 4 corresponds to annealed state of the sample, e.g. unaffected by light soaking or atmospheric gases. When the sample is exposed to ambient atmosphere for a period of several days, the dark conductivity rises by about one order of magnitude. This condition is marked by 2 in the figure. Rapid

annealing will remove the adsorbed atmospheric components and bring the dark conductivity down to condition 1. The same effect could be achieved in this case by long annealing because no light induced defects are present in the material. The following light soaking and relaxation of the sample, as was described above, will bring the dark conductivity to position 3. In this condition the dark conductivity is affected by both light induced degradation and atmospheric gases. This condition corresponds to that state indicated by arrow A in figure 3b. It can be seen that the value of dark conductivity is higher then in annealed condition that complicates an estimation of light induced degradation. To reveal the effect of light induced degradation the rapid low temperature annealing should be applied. This brings the dark conductivity down to the minimum value corresponding to the light soaked condition of the sample. This condition is indicated by 4 in figure 4 and by arrow B in figure 3b. It can be seen that light soaking for 20 hours at 50°C was able to reduce dark conductivity, however, the effect could be easily hidden by adsorption of atmospheric gases. The long high temperature annealing will remove light induced defects and bring the dark conductivity to the condition 1.

$\mu\tau$ products corresponding to different states of the 'optimal' microcrystalline silicon sample are presented in figure 8.5. It can be seen that both light induced degradation and atmospheric adsorption affect the mobility lifetime products. Condition 1 corresponds to completely annealed state of the sample; condition 4 is light soaked state. Conditions 2 and 3 correspond to aged conditions of non-light soaked and light soaked states respectively. The effect of adsorption of atmospheric components increases dark conductivity values by approximately one order of magnitude (positions 2 and 3). It should be noted that the light soaked sample shows a smaller conductivity increase on ageing. This could be because additional defects allow extra charge to reside in traps resulting a smaller conductivity changes. This would be in agreement with suggestions described by Street regarding the band bending mechanism for materials with low and high defect densities [Street 1991].

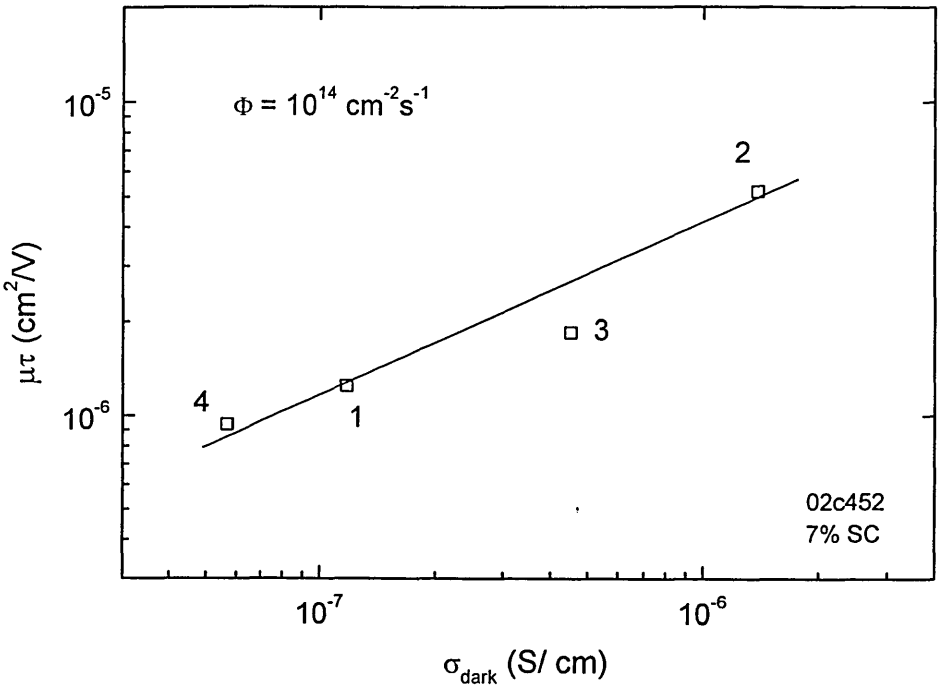

Figure 8.5. Variations of the mobility lifetime products with dark conductivity.

Light soaking slightly decreases the μτ product values. The μτ products increase by less than half order of magnitude due to adsorption of atmospheric gases. These variations could be explained as the changes in the Fermi level position, where the Fermi level shifts to the middle of the gap due to light soaking and effectively toward the conduction band on ageing, as shown in figure 8.6. The mechanism of correlation between the position of the Fermi level and mue tau products has already been discussed in chapter 5.

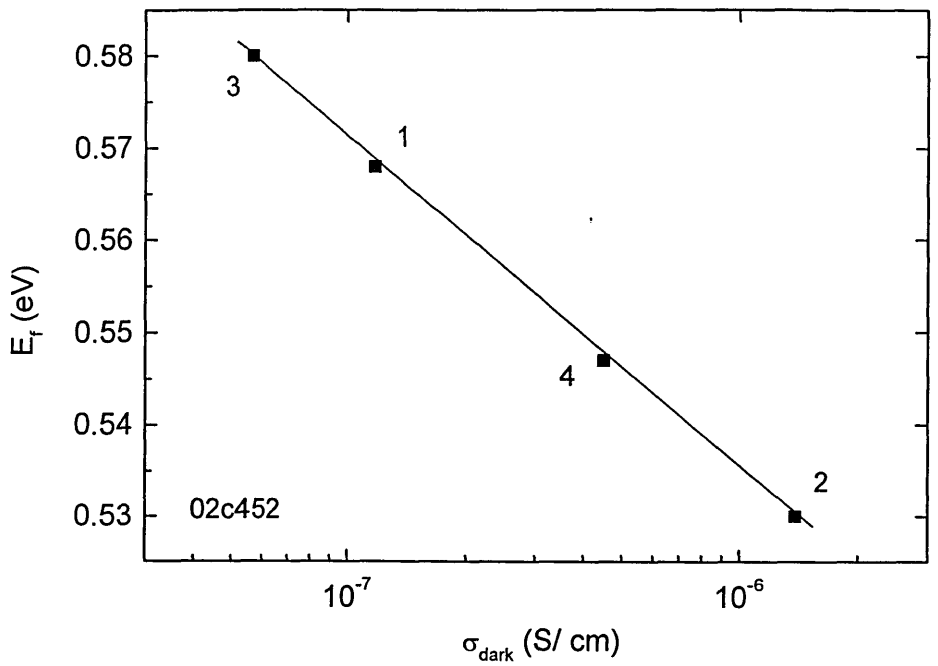

Figure 8.6. Variations in the Fermi level position correlated with different condition of the sample, see details in the text.

8.6. Effects on transient photoconductivity and density of states

To examine the effects of simultaneous aging and light soaking on the density of states, the fully amorphous sample was selected. The sample displays both significant light-induced degradation and aging effects. This sample was firstly AM1 light-soaked at 50°C for 20 hours and the TPC decay recorded. Then, as described above, rapid low temperature annealing was used to reverse the aging process, and the TPC decay recorded once more. Finally a longer high-temperature treatment was used to remove the light-induced defects and a final recording of the TPC decay made. The results are shown in figure 8.7 and the corresponding DOS plots in figure 8.8.

It can be seen that a rapid fall in the TPC decay at approximately 10^{-7} s is exhibited by the sample simultaneously light-soaked + aged. This feature is

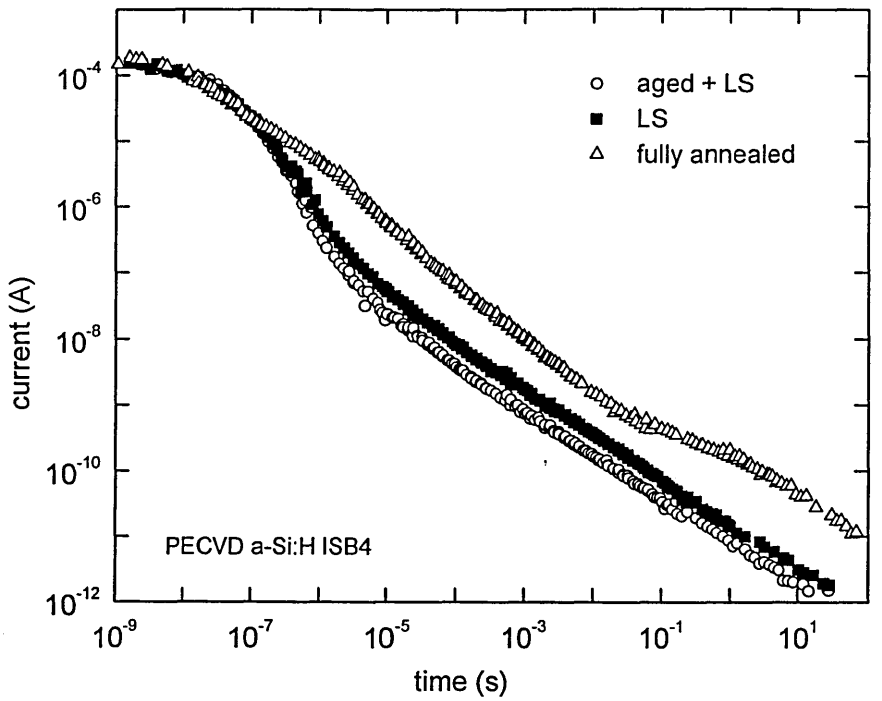

Figure 8.7. TPC decays, correlated with annealing regimes.

associated with carrier trapping into deep defect states, as is borne out in the DOS plot. Following annealing to remove aging, the deep DOS decreases slightly below 0.6 eV, suggesting that in this case the adsorbate may be introducing additional defects. A similar slight increase in the deep DOS on ageing has been observed for sample 02b299 (see chapter 6), although this sample demonstrates stronger sensitivity to atmospheric adsorption, reflected in the shift of the DOS peak to shallow energies. Stronger annealing removes the light-induced defects and the deep defect density is greatly reduced.

Summary

Both light induced and atmospheric instabilities affect the transport properties of microcrystalline silicon as reflected in changes in dark conductivity, and steady state and transient photoconductivity. It has been demonstrated that the effect of

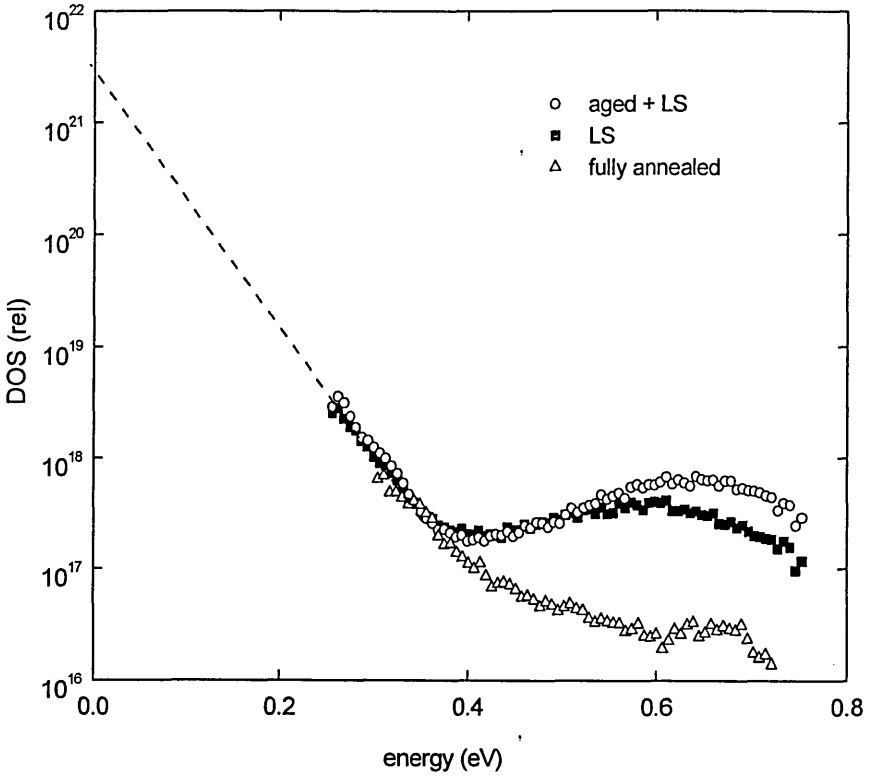

Figure 8.8. Calculated DOS correlated with annealing regimes.

atmospheric adsorption may dominate light induced degradation, particularly for the materials optimised for photovoltaic applications, and thus, the apparent effect of light soaking may be reduced or even reversed in sign by the effect of atmosphere. Unless this fact is appreciated, erroneous estimates of the influence of light-induced degradation in, for example, solar-cell material, may be made. Two annealing regimes are found to be able to *distinguish* between light induced and atmospheric metastable changes. Pulsed lower-temperature annealing can drive off adsorbed gases whilst leaving the light-induced defects largely unaffected. Transient photoconductivity confirms the presence of deep metastable defects following light-soaking, and their removal by extensive higher-temperature annealing. Adsorbed species slightly affect the shape of the DOS, that could be due to a change in occupancy within the same DOS, or a genuine change in the DOS could occur.

Chapter 9. Summary and conclusions

The primary aim of this thesis was to investigate electronic transport and stability of microcrystalline silicon films and devices to exposure to light and ambient atmosphere. Films deposited over a range of silane concentrations at various thicknesses have been investigated. In highly crystalline materials, deposited at low silane concentrations, the Fermi level position may be significantly shifted away from midgap towards the conduction band due to unintentional oxygen contamination or post deposition atmospheric effects. In these materials dark and steady state photoconductivity are found to be more similar to n-type, rather then intrinsic, amorphous silicon. In transitional microcrystalline silicon structures the Fermi level lies closer to midgap. Dark and steady state photoconductivity is found to be similar to undoped amorphous silicon films. Thickness dependence of photoelectronic properties of microcrystalline silicon films has been observed which supports the presence of morphological anisotropy in the direction of growth.

Transient photocurrent and post transit time of flight experiments on coplanar and *pin* photovoltaic structures have been made, and analysed in terms of multiple trapping transport model. The multiple trapping mechanism may be applied to explain the gross features of transient decays in transitional microcrystalline silicon. In highly crystalline material temperature and excitation dependences are inconsistent with the multiple trapping mechanism. The density of states obtained from transient photoconductivity decays using the Fourier transform technique has demonstrated that the defect density decreases with increasing crystallinity. However this is inconsistent with literature values of defect densities obtained from ESR measurements on similar materials, suggesting that the low defect density obtained for highly crystalline structures may be related to increased occupancy of deep defects due to position of the Fermi level. Transport properties are broadly similar to n-type amorphous silicon, where the influence of minority carrier kinetics must be taken into account. The general form of the density of states of transitional microcrystalline silicon structures is found to be similar to amorphous silicon, although the conduction band tail slope was found to be 30 meV, which is broader than in device quality amorphous silicon.

The analysis of post transit time of flight results on microcrystalline silicon *pin* diodes suggests that deep defects are associated with the amorphous phase, whereas the shallow defects may be assigned to crystalline columns or grain boundaries. At low crystalline volume fractions (below 0.4) the density of states was found to be broadly similar in form to that of amorphous silicon, although the deep defect density appears to be higher. At high crystalline volume fractions temperature-independent decays are observed, suggesting that at least below room temperature multiple trapping transport in band tails may not take place.

A comparison of results of coplanar and *pin* structures on microcrystalline silicon films of similar quality demonstrates that electronic transport is anisotropic. The sharper conduction band tail observed in the case of *pin* structures, where carriers travelling along the direction of growth, rather than in coplanar configuration, is consistent with a greater degree of order, as might be found within the crystalline columns. High-quality amorphous silicon appears to have a lower deep defect density than largely amorphous microcrystalline silicon, in both sample configurations, suggesting that the amorphous tissue in mixed-phase microcrystalline silicon is of poorer quality than standard 'homogeneous' amorphous silicon.

A large portion of the thesis has been devoted to investigation of effects of ambient atmosphere on the transport properties of microcrystalline silicon films and issues of material stability. It was demonstrated that atmospheric gases could result in both irreversible and reversible effects. Irreversible effects are associated with oxidation process, resulting in a shift of the Fermi level position towards the conduction band that is also accompanied by irreversible changes in the density of states, together with changes in dark and photoconductivity and conductivity prefactor. The irreversible changes were investigated as a function of material microstructure through changes in silane concentration and film thickness. Thinner films appear to be more sensitive to oxidation, possibly due to increased porosity and for these films the activation energy was found to decrease by as much as 0.4 eV over a period of one month after deposition which corresponds to an irreversible increase in dark conductivity of some three orders of magnitude. Atmospheric effects were found to change the film conductivity and activation energy in accordance with the Meyer-Neldel rule. The general trend suggests that

an increase in amorphous fraction results in shift of the data in the direction of lower conductivity prefactor and/or larger activation energy.

The reversible effect of exposure to atmospheric gases was found to result in decrease in dark conductivity for the films deposited at low silane concentration and increase in dark conductivity for the films deposited near the transition from highly crystalline to amorphous growth. The mechanism has been explained in terms of adsorption process that results in band bending, which tends to saturate over a period of several days. Vacuum treatment at a pressure of 10^{-3} torr applied at room temperature was found to reduce, but was not able to prevent, the adsorption process completely. It was demonstrated that reversible adsorption of atmospheric gases may result in an equivalent shift in the Fermi level by more than 0.2 eV over a period of 10 days. The changes in the Fermi level position relative to the transport path are correlated with reversible changes in dark conductivity by about three orders of magnitude and phoconductivity by about two orders of magnitude. Transient photoconductivity measurements have demonstrated that reversible atmospheric adsorption is accompanied by changes in the density of states that may be associated with changes in occupancy. It was found that thicker films are less sensitive to atmospheric adsorption, similarly to the case of irreversible atmospheric effects. The effect of atmospheric adsorption could be minimised or reversed by low concentrations of boron doping. At 5 vppm B_2H_6, ageing results in a change in conduction path from p-type to n-type, reflected in a 'conductivity dip', measured as a function of time and thus the dark conductivity increase after ageing is reduced when compared with the 0 vppm film. At 10 vppm the conduction path is p-type under both annealed and aged conditions, and thus ageing reverses the dark conductivity change. For the boron doped series, our interpretations are fully supported by the results of computer simulation which models the effect of atmospheric adsorption as a charge 'sheet' penetrating into the film close to the surface.

Light soaking experiments have confirmed that microcrystalline silicon films grown near the transition from crystalline to amorphous growth are significantly more stable then amorphous silicon films. 'Optimal' microcrystalline silicon shows almost no degradation during room temperature light soaking, although some degradation has been observed if temperature is increased to 50°C. It was shown that for films with significant amorphous fraction, that are the most sensitive to

light induced degradation, the effect of light soaking under room conditions may be seemingly reduced or even reversed in sign by the effect of the atmosphere. This is reflected in changes in the activation energy, dark and photoconductivity, transient photocurrents and the density of states. The results suggest that in general, the effect of ageing could oppose the effect of light soaking on dark and photoconductive properties of thin films, and thus an erroneous estimate of the light-induced degradation and material stability could be made unless each metastable effect is separated. It was shown that this could be achieved using different annealing regimes.

9.1. Directions for future work

There are several aspects of this work that would be interesting to explore in more detail. The phenomenon of morphological anisotropy of microcrystalline silicon has been studied by comparing TPC and TOF results. Another means of investigating anisotropy in the direction of growth would be to perform "depth profiling", where in the TPC experiment, strongly absorbed light is used to generate carriers in a coplanar sample separately from the front and the back. These experiments, if performed on a series of microcrystalline silicon films deposited at various silane concentrations, could provide valuable information on the distribution of defects and changes in both nucleation layer and crystalline volume fraction.

Further studies of the effects of ambient atmosphere on the transport properties of microcrystalline silicon films could prove useful. It would be interesting to extend the work presented in chapter 7 to include a wider range of silane concentration and thicknesses, to provide a more complete picture of post - deposition effects in microcrystalline silicon.

It is also important to investigate in more detail other deposition parameters that can result in minimization of the ageing effect. In particular, to what extent changes in deposition rate and substrate temperature, which are related to void fraction, may influence adsorption and oxidation processes.

Degradation of solar cells due to effects of atmosphere [Wang *et al* 2003, Klein *et al* 2003, Sendova-Vassileva *et al* 2005] requires further investigation. It is clear that materials for stable photovoltaic devices should be optimised not only with regard to light induced degradation, but also to the effects of atmospheric gases. As was demonstrated in the present work, a low doping concentration can reduce the influence of atmosphere and this could be one of the possible ways to optimise photovoltaic devices. Although doping can introduce additional defects, it may improve a photosensitivity of the active layer, that requires more detailed investigation. A comparison of effects of atmosphere on *pin* and nip photovoltaic structures could also provide more information on the mechanism of solar cell degradation. Computer modelling used in the present work can be modified to simulate the effect of atmosphere on solar cell properties.

The high sensitivity of microcrystalline silicon to atmospheric gases suggests that there may be scope for developing a new type of sensor based on the influence of selected gases on transport properties.

References

Andoh, N.,Hayashi, K.,Shirasawa, T., Sameshima, T., Kamisako, K., (2001), *Solar Energy Mater. Solar Cells* **66**, 437.

Arkhipov, V.I., Rudenko, A.I. (1978), *J. Non- Cryst. Solids* **30**, 163.

Avetard, R., Haydon, D.A. (1973), *An Introduction to the Principles of Surface Chemistry,* Cambridge University Press.

Baia Neto, A.L., Lambertz, A., Carius, R., Finger, F., (2002), *J. Non- Cryst. Solids* **299-302**, 274.

Bailat, J., Vallat-Sauvain, E., Feitknecht, L., Droz, C., Shah, A. (2002), *J. Non-Cryst. Solids* **299-302**, 1219.

Branz, H.M., (2000), *J. Non- Cryst. Solids* **266-269**, 391.

Brüggemann, R., Main, C., Berkin, J., Reynolds, S. (1990), *Phil. Mag. B* **62**, 29.

Brüggemann, R., A. Hierzenberger, A., Reinig, P., Rojahn, M., Schubert, M., Schweizer, S., Wanka, H., Zrinscak, I., (1998a), *J. Non- Cryst. Solids* **227-230**, 982.

Brüggemann, R., Hierzenberger, A., Wanka, H., Schubert, M.B. (1998b), *Mater. Res. Soc. Symp. Proc.* **507**, 921.

Brüggemann, R., Rojah, M., Rösch, M. (1998c) *Phys. Stat. Sol.* A **166,** R11.

Brüggemann, R. and Main, C. (1998), *Phys. Rev. B* **57**, R15080.

Brüggemann, R., Bronner, W., Hierzenberger, A., Schubert, M., Zrinscak, I. (1999), in *Thin Film materials and Devices – Developments in Science and Technology,* edited by J.M. Marshall *et al.*, World Scientific, Singapore, p. 1.

Brüggemann, R., Kleider, J.P., Longeaud, C., Mencaraglia, D., Guillet, J., Bouree, J.E., Niikura, C. (2000), *J. Non- Cryst. Solids* **266-269**, 258.

Brüggemann, R., Kleider, J.P., Longeaud, C., Houze, F. (2001), in *Materials for Information Technology in the New Millennium,* edited by J.M. Marshall *et al.*, Bath, p. 212.

Brüggemann, R. (2003), *J. Mater. Science - Mater. Electron.* **14 (10-12)**, 629.

Brüggemann, R. (2004), personal communication.

Brüggemann, R. (2005), *Mater. Res. Soc. Symp. Proc.* **862**, A5.1.

Cardona, M. (1982), *Light Scattering in Solids,* Springer, Berlin.

Carius, R., Mueller, J., Finger, F., Harder, N., Hapke, P. (1999), *in: Thin Film Materials and Devices – Developments in Science and Technology,* edited by J.M. Marshall et al, p. 157.

Dick, F. (1994), MSc dissertation, University of Dundee.

Droz, C., Vallat-Sauvain, E., Bailat, J., Feitknecht, L., Meier, J., Shah, A. (2004), *Solar Energy Mater. Solar Cells* **81**, 61.

Dylla, T. (2005), PhD thesis, Forschungszentrum Jülich

Dylla, T., Finger, F., Schiff, E.A. (2005) *Appl. Phys. Let.* **87(3)**, 1.

Edelman, F., Chack, A., Weil, R., Beserman, R., Khait, Yu., Werner, P., Rech, B., Roschek, T., Carius, R., Wagner, H., Beyer, W. (2003), *Solar Energy Mater. Solar Cells* **77**, 125.

Fejfar, A., Beck, N., Stuchlíková, H., Wyrsch, N., Torres, P., Meier, J., Shah A. Kocka, J. (1998) *J. Non-Cryst. Solids* **227-230**, 1006.

Finger, F., Carius, R., Hapke, P., Houben, L., Luysberg, M., Tzolov, M. (1997), *Mater. Res. Soc. Symp. Proc.* **452**, 725.

Finger, F., Mueller, J., Malten, C., Wagner, H., (1998) *Phil. Mag. B* **77** (3), 805.

Finger, F., Mueller, J., Malten, C., Carius, R., Wagner, H., (2000) *J. Non- Cryst. Solids* **266-269**, 511.

Finger, F., Vetterl, O., Carius, R., Lambertz, A., Scholten, C., Houben, L., Luysberg, M. (2001), in *Materials for Information Technology in the New Millennium,* edited by J.M. Marshall *et al.*, Bath, p. 26.

Finger, F., Carius, R., Dylla, T., Klein, S., Okur, S., Guenes, M., (2003) *IEE Proc. CDS* **150**, 300.

Finger, F. (2003), personal communication.

Fritzsche, H. (1977) *Proc. of the 7th Int. Conf. on Amorphous and Liquid Semiconductors*, edited by W.E. Spear, Edinburgh, 3.

Fritzsche, H., Ibaraki, N. (1985), *Phil. Mag.* B **52(3)**, 299.

Fujiwara, H., Kondo, M., Matsuda, A. (2004), *J. Non- Cryst. Solids* **338-340**, 97.

Gao, W. (1995), PhD thesis, University of Abertay Dundee.

Gordijn, A. (2005), PhD thesis, University of Utrecht.

Greegg, S.J., Sing, K.S.W. (1967), *Adsorption, Surface Area and Porosity*, Academic Press, London-New York.

Godet, C., (1998), *J. Non- Cryst. Solids* **227-230**, 272

Goerlitzer, M., Beck, N., Torres, P., Kroll, U., Keppner, H., Meier, J., Koehler, J., Wyrsch, N., Shah, A. (1997) *Mater. Res. Soc. Symp. Proc.* **467**, 301.

Goerlitzer, M., Torres, P., Beck, N., Wyrsch, N., Keppner, H., Pohl, J., Shah, A. (1998), *J. Non- Cryst. Solids* **227-230**, 996

Guha, S. (2000) *Multijunction Solar Cells and Modules,* in: *Technology and Applications of Amorphous Silicon*, edited by R.A. Street, Springer, p. 252.

Gummel, H.K., (1964), *IEEE Trans. Electron. Devices,* **11**, 455.

Han, D., Yue, G., Wang, Q., Shimizu, T. (2003), *Thin Solid Films* 430, 141.

Hata, M., Wagner, S. (1991) *Mater. Res. Soc. Symp. Proc.* **219**, 611.

Heintze, M., Zedlitz, R., Wanka, H. N., Schubert, M. B., (1996) *J. Appl. Phys.* **79**, 2699.

Houben, L., Luysberg, M., Hapke, P., Carius, R., Finger, F., Wagner H. (1998a), *Phil. Mag. A* **77** (6), 1447.

Houben, L., Luysberg, M., Hapke, P., Vetterl, O., Finger, F., Carius, R., Wagner H. (1998b), *J. Non- Cryst. Solids* **227-230**, 896.

Houben, L., Scholten, C. Luysberg, M., Vetterl, O., Finger, F., Carius, R. (2002) *J. Non- Cryst. Solids* **299-302**, 1189.

Hulthen, R. (1975) *Physika Scripta* **12**, 342.

Irsigler, P., Wagner, D., Dunstan, D.J. (1983) *J. Phys. C: Solid State Phys.* **16,** 6605.

Ito, M., Koch, C., Svrcek, V., Schubert, M., Werner, J. (2001), *Thin Solid Films* **383**, 129.

Itoh, T., Yamamoto, K., Harada, H., Yamana, N., Yoshida, N., Inouchi, H., Nonomura, S., Nitta, S. (2001), *Solar Energy Mater. Solar Cells* **66**, 239.

Jackson, W.B., Amer, N.M. (1982) *Phys. Rev.* **25**, 5559.

J.P. Kleider, J.P., Longeaud, C., Brüggemann, R., Houze, F., (2001), *Thin Solid Films* **383**, 57.

Klein, S., Finger, F., Carius, R., Dylla, T., Rech, B., Grimm, M., Houben, L., Stutzmann, M., (2003), *Thin Solid Films* **430**, 202.

Kluth, O., Rech, B., Houben, L., Wieder, S., Schoepe, G., Beneking, C., Wagner, H., Loeffl, A., Schock, H.W. (1999), *Thin Solid Films* **351**, 247.

Kocka, J., Stuchlikova, H., Stuchlik, J., Rezek, B., Mates, T., Svrcek, V., Fojtik, P., Pelant, I., Fejfar, A., (2002), *J. Non- Cryst. Solids* **299-302**, 355.

Kocka, J., Fejfar, A., Stuchlikova, H., Stuchlik, J., Fojtik, P., Mates, T., Rezek, B., Luterova, K., Svrcek, V., Pelant, I., (2003), *Solar Energy Mater. Solar Cells* **78**, 493.

Kondo, M., Nasuno, Y., Mase, H., Wada, T., Matsuda, A. (2002), *J. Non- Cryst. Solids* **299-302**, 108.

Ley, L. (1998) in *Properties of Amorphous Silicon and its Alloys,* edited by T. Searle, London, IEE, 113.

Lips, K., Kanschat, P., Will, D., Lerner, C., Fuhs, W., (1998), *J. Non- Cryst. Solids* **227-230**, 1021.

Liu, F., Zhu, M., Feng, Y., Han, Y., Liu J. (2001), *Thin Solid Films* **395**, 97

Liu, F., Zhu, M., Wang, Q. (2004), *Phys. Lett. A* **331**, 432.

Lukovsky, G., Wang, C. (1983), *Mater. Res. Soc. Symp. Proc.* **283**, 443

Luysberg, M., Hapke, P., Carius, R., Finger, F. (1997), *Phil. Mag. A* **75** (1), 31

Luysberg, M., Scholten, C., Houben, L., Carius, R., Finger, F., Vetterl, O., (2001), *Mater. Res. Soc. Symp. Proc.* **664**, A15.2.

McMahon, T.J., Crandall, R.S. (1990), *Phil. Mag. B* **61** (3), 425.

Main, C., Russell, J., Berkin, J., Marshall, J.M. (1987) *Phil. Mag. Lett.* **55**, 189.

Main, C., Brüggemann, R., Webb, D.P., Reynolds, S. (1992), *Solid State Comms.* **83**, 401.

Main, C., Brüggemann, R., Webb, D.P., Reynolds, S. (1993), *J. Non- Cryst. Solids* **164-166**, 481.

Main, C., Dick, F., Reynolds, S., Gao, W., Gibson, R.A.G. (1996) *J. Non- Cryst. Solids* **198-200**, 263.

Main, C. (1997), *Mater. Res. Soc. Symp. Proc.* **467**, 167.

Main, C. (2002), *J. Non- Cryst. Solids* **299-302**, 525.

Mahan, A.H., Xu, Y., Williamson, D.L., Beyer, W., Perkins, J.D., Vanecek, M., Gedvilas, B.P., Nelson, B.P. (2001), *J. Appl. Phys.* **90**, 5038.

Mahan, A.H., Xu, Y., Iwaniczko, E., Williamson, D.L., Nelson, B.P., Wang, Q. (2002), *J. Non- Cryst. Solids* **299-302**, 2.

Mahan, A.H. (2003), *Solar Energy Mater. Solar Cells* **78**, 299.

Marshall, J.M. (1977), *Phil. Mag. B* **36** (4), 959.

Marshall, J.M., Main, C. (1983), *Phil. Mag. B* **47** (9), 335.

Marshall, J.M. (1988), in: *Advances in Disordered Semiconductors: Amorphous Silicon and Related Materials (Volume B),* edited by H. Fritzsche, World Scientific, Singapore, p. 799.

Marshall, J.M., Pickin, W., Hepborn, A.R., Main, C., Brüggemann, R. (1991), *J. Non- Cryst. Solids* **137-138**, 343.

Marshall, J.M. (2000), *Phil. Mag. B* **80** (9), 1705.

Meier, J., Torres, P., Platz, R., Dubail, S., Kroll, U., Selvan, J.A., Pellaton-Vaucher, N., Hof, C., Fisher, D., Keppner, H., Shah, A., Ufert, K.D. (1997), *Solar Energy Mater. Solar Cells* **49**, 35.

Meier, J., Dubail, S., Cuperus, J., Kroll, U., Platz, R., Torres, P., Anna Selvan, J.A., Pernet, P., Beck, N., Pellaton Vaucher, N., Hof, C., Fischer, D., Keppner, H., Shah, A., (1998), *J. Non- Cryst. Solids* **227-230**, 1250.

Meier, J., Spitznagel, J., Kroll, U., Bucher, C., Fay, S., Moriarty, T., Shah, A. (2003), *3rd World Conf. Photovoltaic Energy Conv. Proc.,* Osaka, p. 2801

Meier, J., Spitznagel, J., Kroll, U., Bucher, C., Fay, S., Moriarty, T., Shah, A. (2004), *Thin Solid Films* **451-452**, 518.

Meiling H., J. van den Boogaard, M., Schropp, R. E. I., Bezemer, F., van der Weg, J., W. (1990) *Mater. Res. Soc. Symp. Proc.* **192**, 645.

Merazga, A. (1991), PhD Thesis, Dundee Institute of Technology.

Middya, A.R., Weber, U., Mukherjee, C., Schroeder, B (2001), *Mater. Res. Soc. Symp. Proc.* **664**, A25.6

Morrison, S.R. (1990), *The Chemical Physics of Surfaces*, Plenum Press, New York.

Moutinho, H.R., Jiang, C.-S., Perkins, J., Xu, Y., Nelson, B.P., Jones, K.M., Romero, M.J., Al-Jassim, M.M. (2003), *Thin Solid Films* **430**, 135.

Mueller, J., Kluth, O., Wieder, S., Siekmann, H., Schoepe, G., Reetz, W., Vetterl, O., Lundszien, D., Lambertz, A., Finger, F., Rech, B., Wagner, H. (2001), *Solar Energy Mater. Solar Cells* **66**, 275.

Nakata, Y., Yokota, A., Sannomiya, S., Moriuchi, S., Inoue, Y., Nomoto, K., Itoh, M., Tsuji, T. (1991), *Mater. Res. Soc. Symp. Proc.* **219**, 433.

Noolandi, J. (1977), *Phys. Rev. B* **16** (10), 4466.

Oheda, H. (1981), *J. Appl. Phys.* **52**, 6693.

Orenstein, J., Kastner, M.A., Vaninov, V. (1982), *Phil. Mag. B* **46** (1), 23.

Ossadnik, C., Veprek, S., Gregora, I. (1999), *Thin Solid Films* **337**, 148.

Overhof, H., Thomas, P. (1989), *Electronic Transport in Hydrogenated Amorphous Silicon,* Springer, New York.

Overhof, H., Thomas, P. (2001), *Defect and Diffusion Forum* **192-193,** 1.

Poruba, A., Schauer, F. (1994), in *Proceedings of the 8th International School on Condensed Matter Physics: Electronic, Optoelectronic and Magnetic Thin Films,* edited by J.M. Marshall et al. (Varna), p. 616.

Ram, S., Kumar, S., Roca i Cabarrocas, P. (2002), *Mater. Res. Soc. Symp. Proc.* **715**, A21.4.

Ray, S., Mukhopadhyay, S., Jana, T., Carius, R. (2002a), *J. Non- Cryst. Solids* **299-302**, 761.

Ray, S., Das, C., Mukhopadhyay, S., Saha, S.C. (2002b), *Solar Energy Mater. Solar Cells* **74**, 393.

Reynolds, S., Smirnov, V., Main, C., Carius, R., Finger, F. (2002), *Mater. Res. Soc. Symp. Proc.* **715**, 345.

Reynolds, S., Smirnov, V., Main, C., Finger, F., Carius, R. (2003), *Mater. Res. Soc. Symp. Proc.* **762**, 327.

Reynolds, S., Smirnov, V., Main, C., Finger, F., Carius, R. (2004), *Mater. Res. Soc. Symp. Proc.* **808**, 127.

Reynolds, S., Main, C., Webb, D.P., Rose, M.J. (2000) Phil. Mag. B 80, 547.

Richter, H., Wang, Z., Ley, L. (1981) *Solid State Comms.*, **39**, 625.

Roca i Cabarrocas, P., Layadi N., Drevillon B., Solomon I. (1996), *J. Non- Cryst. Solids.* **198-200**, 871.

Rose, A. (1963), *Concepts in Photoconductivity and Allied Problems,* Interscience, New York.

Ross, C., Mai, Y., Carius, R., Finger, F. (2005), *Mater. Res. Soc. Symp. Proc.* **862**, A10.4.

Ruff, D., Mell, H., Toth, L., Sieber, I., Fuhs, W., (1998), *J. Non- Cryst. Solids* **227-230**, 1011.

van Sark, W.G.J.H.M., Meiling H., Bezemer, F., Linder, M.B., Schropp, R. E. I., Weg, W.F. (1997), *Solar Energy Mater. Solar Cells* **45**, 57.

van Sark, W.G.J.H.M., (2002), Methods of deposition of hydrogenated amorphous silicon for device applications, in *Thin Films and Nanostructures, Vol. 30, Advances in Plasma-Grown Hydrogenated Films* (ed. M. H. Francombe), Academic Press, San Diego, 1.

Scher, H., Montroll, E.W. (1975), *Phys. Rev. B* **12** (6), 2455.

Schirmacher, W. (1981), *Solid State Comms.* **39** (8), 893.

Schmidlin, F.W. (1977), *Phys. Rev. B* **16** (6), 2362.

Sendova- Vassileva, M., Finger, F., Klein, S., Lambertz, A. (2005), *J. Optoelectron. Adv. Mater.* **7(1)**, 481.

Seynhaeve, G.F., Barclay, R.P., Adriaenssens, G.J., Marshall, J.M. (1989), *Phys. Rev. B* **39**, 10196.

Schubert, M.B., Brüggemann, R., Bilger, G., Hierzenberger, A. (1998), in: *Proc. 2nd World Conference on Photovoltaics and Solar Energy Conversion*, Vienna, p. 129.

Shah, A.V., Platz, R., Keppner, H., (1995), *Solar Energy Mater. Solar Cells* **38**, 501.

Shah, A., Vallat-Sauvain, E., Torres, P., Meier, J., Kroll, U., Hof, C., Droz, C., Goerlitzer, M., Wyrsch, N., Vanecek, M. (2000), *Mater. Science Engin.* B **69–70**, 219.

Shah, A.V., Meier, J., Vallat-Sauvain, Droz, C., Kroll, U., Wyrsch, N., Guillet, J., Graf, U. (2002), *Thin Solid Films* **403**, 179.

Shah, A.V., Meier, J., Vallat-Sauvain, E., Wyrsch, N., Kroll, U., Droz, C., Graf, U., (2003), *Solar Energy Mater. Solar Cells* **78**, 469.

Shepherd, J. (1998), PhD thesis, University of Abertay Dundee.

Shimakawa, K. (2000), *J. Non- Cryst. Solids* **266-269**, 223.

Shockley, W., Read, W.T. (1952), *Phys. Rev.* **87**, 835.

Siebke, F., Yata, S., Hishikawa, Y., Tanaka, M., (1998), *J. Non- Cryst. Solids* **227-230**, 977.

Silver, M., Cohen, L. (1977), *Phys. Rev. B* **15** (6), 3276.

Simmons, J.G., Taylor, G.W. (1972), *Phys. Rev. B* **4**, 502.

Smirnov, V., Reynolds, S., Main, C., Finger, F., Carius, R. (2004a), *J. Non- Cryst. Solids* **338-340**, 421

Smirnov, V., Reynolds, S., Finger, F., Main, C., Carius, R. (2004b), *Mater. Res. Soc. Symp. Proc.* **808**, 47.

Smirnov, V., Reynolds, S., Finger, F., Carius, R., Main, C. (2005), *ICANS 21,* to appear in *J. Non- Cryst. Solids.*

Solomon, I., (1980), in *Proc. Kyoto Summer Institute* (ed. F. Yonezawa), 33.

Soppe, W.J., Muffler, H.J., Biebericher, A.C., Deville, C., Burgers, A., Poruba, A., Hodakova, L., Vanecek, M (2005), in: *Proc. 20th European Photovoltaic Solar Energy Conference and Exhibition, Barcelona, Spain,* in press.

Staebler, D.L., Wronski, C.R., (1977), *Appl. Phys. Lett.* **31**, 292.

Street, R.A., (1991), *Hydrogenated amorphous silicon*, Cambridge University Press, Cambridge.

Stutzmann, M., Jackson, W.B., Tsai, C.C. (1985), *Phys. Rev. B* **32**, 23.

Tanielian, M., Chatani, M., Fritzsche, H., Smid, V., Persans, P.D., (1980), *J. Non-Cryst. Solids* **35-36**, 575.

Tanielian, M., (1982), *Phil. Mag. B* 45 (4), 435.

Tiedje, T., Rose, A. (1980), *Solid State Comms.* **37** (1), 49.

Tzolov, M., Finger, F., Carius, R., Hapke, P., (1997), *J. Appl. Phys.* **81** (11), 7376.

Vanecek, M., Kocka, J., Stuchlik, J., Trika, A. (1981), *Solid State Comms.* **39**, 1199.

van Veen, M.K., van der Werf, C.H.M., Schropp, R.E.I. (2004), *J. Non- Cryst. Solids* **338-340**, 655.

Veprek, S., Iqbal, Z., Kuehne, R.O., Capezzuto, P., Sarott, F., Gimzewski, J.K. (1983), *J. Phys. C: Solid State Phys.* **16**, 6241.

Veprek, S., Sarott, F., Iqbal, Z (1987), *Phys. Rev. B* **36**, 3344.

Vetterl, O., Finger, F., Carius, R., Hapke, P., Houben, L., Kluth, O., Lambertz, A., Muck, A., Rech, B., Wagner, H., (2000), *Solar Energy Mater. Solar Cells* **62**, 97.

Vetterl, O., Gross, A., Jana, T., Ray, S., Lambertz, A., Carius, R., Finger, F. (2002), *J. Non- Cryst. Solids* **299-302**, 772.

Wang, Q., Wang, K., Han, D. (2003), *Mater. Res. Soc. Symp. Proc.* **762**, A7.10.

Webb, D.P. (1994), PhD thesis, University of Abertay Dundee.

Wyrsch, N., Droz, C., Feitknecht, L., Goerlitzer, M., Kroll, U., Meier, J., Torres, P., Vallat-Sauvain, P., Shah, A., Vanecek, M. (2000) *Mater. Res. Soc. Symp. Proc.* **609**, A15.1.

Yoon, J-H. (2001), *Mater. Res. Soc. Symp. Proc.* **664**, A23.6.

Zrinscak, I., Reynolds, S., Main, C., Persheyev, S.K., Rose, M.J. (2001), in *Materials for Information Technology in the New Millennium,* edited by J.M. Marshall *et al.*, Bath, p. 336.

Appendix 1. Basic description of *pin* simulation program.

This is a resumé of the simulation program description given by W. Gao [Gao 1995].

The operation of the device is governed by the Poisson equation and by the continuity and current-density equations. For the amorphous silicon solar cell, it is treated as a one-dimensional device. In the steady state, no time factor is involved, and the equations can be simplified to the following form:

$$\frac{d^2\psi}{dx^2} = -\frac{e}{\varepsilon\varepsilon_0}(p - n + p_t - n_t + N_D - N_A - Dope) \quad (1)$$

$$\frac{dJ_p}{dx} = q(G - R) \quad (2)$$

$$\frac{dJ_n}{dx} = -q(G - R) \quad (3)$$

$$J_p = -q\mu_p\, p\frac{d\psi}{dx} - qD_p\frac{dp}{dx} \quad (4)$$

$$J_n = -q\mu_n\, n\frac{d\psi}{dx} + qD_n\frac{dn}{dx} \quad (5)$$

where

x is the space coordinate (*cm*)

ψ is the potential (*V*)

R is the recombination rate of electrons and holes ($cm^{-3}s^{-1}$)

G is the generation rate of electrons and holes ($cm^{-3}s^{-1}$)

J_p and J_n are the hole and electron current densities (Acm^{-2})

p and n are free hole and electron densities

p_t and n_t are the bandtail charge state densities

N_D and N_A are dangling bond charge densities (+ and - respectively)

$Dope$ is ionized dopant charge density

q is the elementary charge(*C*)

ε and ε_o are the permittivities of the semiconductor and the vacuum (Fcm^{-1})

μ_p and μ_n are the hole and electron extended-state mobilities ($cm^2v^{-1}s^{-1}$)

D_p and D_n are the hole and electron diffusion constants (cm^2s^{-1})

Variables ψ, R, G, n, p, J_p, J_n, p_t, n_t, N_D, N_A and $Dope$ are the functions of the space coordinates x, and the three basic variables $n(x)$, $p(x)$, $\psi(x)$ are coupled.

The program subdivides the device into thin layers and solves Poisson's and continuity equations with a modified Gummel's approach [Gummel 1964] after initial 'guess' of parameters. Initial parameters (n, p and ψ arrays) arise from consideration of boundary conditions. As a 'guess', potential array ψ is a straight line between the two boundaries, while for the electron and hole density distributions, a power law relation is applied. The simulation assumes exponential band tails and gaussian distribution of dangling bond defects, with correlation energy U and appropriate occupation statistics as described in section 3.1.

The ten published papers cited below have been removed from the e-thesis due to copyright restrictions

Publications and conference presentations arising from this work

Publications:

S. Reynolds, V. Smirnov, C. Main, R. Carius and F. Finger, "Transient Photocurrents in Microcrystalline Silicon Films",
in: Amorphous and Heterogeneous Silicon-Based Films - 2002, Proceedings of MRS Symposium A, Vol. ***715,*** edited by J. David Cohen, John R. Abelson, Hideki Matsumura, John Robertson (MRS, San Francisco, 2002), 345-350.

S. Reynolds, V. Smirnov, C. Main, R. Carius and F. Finger, "Localised States in Microcrystalline Silicon Photovoltaic Structures Studied by Post-Transit Time-of-Flight Spectroscopy",
in: Amorphous and Nanocrystalline Silicon-Based Films - 2003, Proceedings of MRS Symposium A, Vol. ***762***, edited by John R. Abelson, Gautam Ganguly, Hideki Matsumura, John Robertson, Eric A. Schiff (MRS, San Francisco, 2003), 327-332.

V. Smirnov, S. Reynolds, C. Main, F. Finger and R. Carius, "Aging effects in microcrystalline silicon films studied by transient photoconductivity",
J. Non-Cryst. Solids **338-340**, 421-424 (2004).

S. Reynolds, V. Smirnov, C. Main, F. Finger and R. Carius, "Interpretation of Transient Photocurrents in Coplanar and Sandwich PIN Microcrystalline Silicon Structures",
in: Amorphous and Nanocrystalline Silicon Science and Technology - 2004, Proceedings of MRS Symposium A, Vol. ***808,*** edited by Gautam Ganguly, Michio Kondo, Eric A. Schiff, Reinhard Carius, and Rana Biswas (MRS, San Francisco, 2004), 127-132.

S. Persheyev, K. O'Neill, S. Anthony, M.J. Rose, V. Smirnov and S. Reynolds, "Metastability in Undoped Microcrystalline Silicon Thin Films Deposited by HWCVD",
in: *Amorphous and Nanocrystalline Silicon Science and Technology - 2004, Proceedings of MRS Symposium A, Vol.* ***808,*** edited by Gautam Ganguly, Michio Kondo, Eric A. Schiff, Reinhard Carius, and Rana Biswas (MRS, San Francisco, 2004), 41-46.

V. Smirnov, S. Reynolds, F. Finger, C. Main and R. Carius, "The Influence of Light-Soaking and Atmospheric Adsorption on Microcrystalline Silicon Films studied by Coplanar Transient Photoconductivity",
in: Amorphous and Nanocrystalline Silicon Science and Technology - 2004, Proceedings of MRS Symposium A, Vol. ***808,*** edited by Gautam Ganguly, Michio Kondo, Eric A. Schiff, Reinhard Carius, and Rana Biswas (MRS, San Francisco, 2004), 47-52.

S. Persheyev, V. Smirnov, K. O'Neill, S. Reynolds, M.J. Rose, "Atmospheric adsorption effects in hot-wire chemical-vapour-deposition microcrystalline silicon films with different electrode configurations",
Semiconductors **39(3),** 343-346 (2005).

S. Reynolds, V. Smirnov, F. Finger, C. Main and R. Carius, "Transport and instabilities in microcrystalline silicon films",
J. Optoelectron. Adv. Mat. **7(1)**, 91-98 (2005).

S. Reynolds, V. Smirnov, F. Finger, C. Main and R. Carius, "Transport and Meyer-Neldel Rule in Microcrystalline Silicon Films",
in: *Amorphous and Nanocrystalline Silicon Science and Technology - 2005, Proceedings of MRS Symposium A, Vol.* ***862,*** edited by Robert W. Collins, P. Craig Taylor, Michio Kondo, Reinhard Carius, and Rana Biswas (MRS, San Francisco, 2005), A5.6.

V. Smirnov, S. Reynolds, F. Finger, R. Carius and C. Main, "Metastable effects in silicon thin films: Atmospheric adsorption and light-induced degradation", *J. Non-Cryst. Solids* **352**, 1075-1078 (2006)

Conference presentations without published proceedings:

S. Reynolds, V. Smirnov, C. Main, R. Carius and F. Finger, "Transient Photocurrents in Microcrystalline Silicon Films",
paper presented at Chelsea meeting on amorphous and thin film semiconductors, Cambridge, UK (April 2002)

V. Smirnov, S. Reynolds, C. Main, R. Carius and F. Finger, "Transient Photocurrents in Microcrystalline Silicon Films",
paper presented at 3rd International Conference on Amorphous and Microcrystalline Semiconductors, St Petersburg, Russia (July 2002).

S. Reynolds, V. Smirnov, C. Main, R. Carius and F. Finger. "Use of Post-Transit Time-of-Flight Spectroscopy to study Localized States in Microcrystalline Silicon Photovoltaic Structures",
paper presented at 9th Euroregional Workshop on "Thin Silicon Devices", Lisbon, Portugal (Feb 2003)

V. Smirnov, S. Reynolds, F. Finger, C. Main and R. Carius. "Effects of Light-Soaking and Atmospheric Adsorption on the Electronic Properties of Microcrystalline Silicon Thin Films",
paper presented at 10th Euroregional Workshop on "Thin Silicon Devices", Bratislava, Slovakia (Feb 2004)

V. Smirnov, S. Reynolds, C. Main, F. Finger and R. Carius "An investigation of atmospheric adsorption and light soaking effects on the electronic properties of amorphous and microcrystalline silicon thin films",
paper presented at 4th International Conference on Amorphous and Microcrystalline Semiconductors, St Petersburg, Russia (July 2004).